

Transport at Gas–Zeolite Interfaces Probed by Molecular Simulations

Vom Promotionsausschuss der
Technischen Universität Hamburg-Harburg
zur Erlangung des akademischen Grades
Doktor-Ingenieur (Dr.-Ing.)
genehmigte Dissertation

von
Nils Edvin Richard Zimmermann

aus
Buchholz in der Nordheide

2013

1. Gutachter: Prof. Dr. Dr. h. c. Frerich J. Keil

2. Gutachterin: Prof. Dr. Irina Smirnova

3. Gutachter: Prof. Dr. Berend Smit

Tag der mündlichen Prüfung: 05.08.2013

Diese Arbeit ist elektronisch unter dem URN [urn:nbn:de:gbv:830-88217409](https://nbn-resolving.org/urn:nbn:de:gbv:830-88217409) veröffentlicht.

Acknowledgments

I would like to take the opportunity here to thank those people who have significantly contributed to get me writing this doctoral thesis.

First and foremost, I am very grateful to my supervisors—Prof. Frerich Keil (Hamburg University of Technology) and Prof. Berend Smit (University of California, Berkeley)—for the opportunities that they gave me, the freedoms that they allowed me, and just the right amount of guidance with which they finally ensured that my personal trajectory would “equilibrate successfully”.

Next, I owe a great debt of gratitude to Sven Jakobtorweihen for very many different reasons. Starting with the fact that he initialized my personal trajectory in the simulation community in the summer of 2005, over the opportunity he gave me by using and extending the molecular simulation package that he has built up (`MolSim-0-Matic`), to the time and energy he spent by a thorough proofreading of important parts of this thesis, I, here, mention only some of the most important reasons. I would like to thank Sven at this point not only for research related support but also for his long and cheerful friendship that was always a source of inspiration to me.

I had the privilege to work with many people—collaborators, advisors, and students—to whom I am greatly indebted. Therefore, I would like to thank Tanin Nanok, Christian Chmelik, Dr. Siegfried Fritzsche, and Prof. Jörg Kärger for many inspiring discussions. Furthermore, I owe gratitude to Manju Sharma, Bei Liu, Jocelyn Rodgers, Ayelet Benjamini, Joseph Swisher, Maciej Haranczyk, Forrest Abouelnasr, and Frédéric de Meyer for many fruitful discussions and the joyful atmosphere in Berkeley. Also, I am very grateful to Alexander Rudenko for innumerable discussions in our office and, in particular, for the joint efforts on electronic structure calculations. Of course, I wish to thank the Bachelor and Master students who I advised for the great time and good work; they are Ana Popovic, Stephan Bendt, Sayee Balaji, and Timm Zabel.

Because this thesis is a simulation study I am extraordinarily indebted to Klaus Mandel who managed to build up a most reliable and stable computer cluster at the Institute for Chemical Reaction Engineering, representing one of the pivotal requirements for this thesis. Furthermore, I wish to thank Klaus for his patience to help me with small and big technical problems. At this point, I thank all other dear colleagues from the institute for the good times we had: Achim Bartsch, Aykut Argönül, Christina Laarmann, Denis Chaykin, Diana Tranca, Niels Hansen, and Till Brüggemann. I wish to

thank our secretary, Hermine Oppelaar, in particular because she was always a great support with respect to administration issues.

The book covers are charcoal drawings by Ronny Lischinski. I am deeply indebted to him because he took the time and passion to find another access to my work apart from the purely scientific route.

The primary funding source of this work was the German Research Foundation [Deutsche Forschungsgemeinschaft (DFG), priority program SPP 1155 under contracts KE 464/8-1 and KE 464/10-1], to which I am very grateful.

I would like to thank my friends who always stood at my side. Particularly, Frank was a continuous source of power to me.

My family has always supported me in an unconditional manner and with great, great passion for which I will be indebted forever. Thank you so much: Mama and Papa, Sagitta, Steffi, Björn, and Nico, Mike and Tanja, Jan, Nora, Nele, and Lenja.

At last, I wish to thank my beloved wife, Minke, for thorough proofreading of large parts of this thesis but primarily for her patience, support, criticism, understanding, and, simply, for her love.

Jag älskar er!

“No man adds very much to the body of knowledge.

Why should we expect more of a machine?”

Alan Turing

Contents

I	Exposition	1
1	Introduction	3
1.1	Outline	5
2	Zeolites	9
2.1	Historical Review	10
2.2	Structure and Nomenclature	12
2.3	Synthesis	16
2.4	Properties and Applications	19
2.5	Materials Used in this Work	22
2.6	Other Nanoporous Materials	22
2.6.1	Carbon Nanotubes	22
2.6.2	Metal–Organic Frameworks	24
II	Background	27
3	Transport Processes	29
3.1	Convective Mass Transport	30
3.2	Diffusion	31
3.2.1	The Mathematics of Diffusion	33
4	Molecular Simulations	39
4.1	Statistical Mechanics	39
4.2	Monte Carlo	43

4.2.1	Grand-Canonical Monte Carlo	46
4.3	Equilibrium Molecular Dynamics	48
4.3.1	Thermostats	53
4.4	Transition State Theory	56
4.4.1	Free-Energy Contribution	56
4.4.2	Reactive Flux Contribution	59
4.4.3	Other Properties from DCTST	62
4.4.4	First-Passage Times—an Alternative Approach	64
4.5	Transient Molecular Dynamics	65
4.6	Models	70
4.6.1	Force Field	70
4.6.2	Host Structure	76
4.7	Simulation Details	77
5	Review of Experimental Techniques	81
5.1	Uptake Rate Measurements	81
5.2	Interference Microscopy	82
5.3	Infrared Microscopy	83
5.4	Pulsed Field Gradient Nuclear Magnetic Resonance	84
III	Preliminary Results	87
6	Verification of Methodology	89
6.1	Force Field	90
6.2	Crystal Structure	91
6.3	Framework Flexibility	100
6.4	Thermostats	101
6.5	Simulations vs Experiments	102
6.5.1	LTA	103
6.5.2	AFI	104
7	Quantification of Surface Barriers	107
IV	Results	115
8	In-Depth Analysis of Interface Dynamics	117

8.1	Introduction	118
8.2	Methodology	120
8.2.1	Zeolite Description and Simulation Box	120
8.2.2	Simulation Details	123
8.2.3	Extended Dynamically Corrected Transition State Theory	124
8.3	Simulation Results	128
8.3.1	Free-Energy Profiles	128
8.3.2	Transmission Coefficient	133
8.3.3	Critical Crystal Thickness	138
8.4	Discussion	141
8.5	Conclusions	142
8.6	Supplementary Data	143
8.6.1	Transition State Locations and Free-Energy Landscapes	143
8.6.2	Committer Probability and Correlation Plots of RF simulations	146
9	The Nature of Surface Barriers	151
9.1	Introduction	152
9.2	Methodology	152
9.2.1	Zeolites	153
9.2.2	Assessment of Surface Barriers	155
9.3	Results	157
9.3.1	One-Dimensional Pores	157
9.3.2	Intersecting Channels	160
9.3.3	Temperature	161
9.4	Discussion	164
9.5	Conclusions	170
9.6	Supplementary Data	172
9.6.1	Methodology Details	172
9.6.2	Isotherms and Heats of Adsorption	173
9.6.3	Transmission Coefficients	175
9.6.4	Critical Membrane Thickness—Remaining Surfaces	177
9.6.5	Temperature and Chain-Length Dependence of Henry Coefficient	180

10 Predicting Surface Permeabilities	183
10.1 Introduction	184
10.2 Methodology	185
10.3 Results	188
10.3.1 One-Step Release Mechanism	188
10.3.2 Two-Step Release Mechanism	193
10.4 Discussion	194
10.5 Conclusions	196
10.6 Supplementary Data	198
10.6.1 Comparison Tracer Release and Uptake	198
10.6.2 Transmission Coefficients in the Boundary Layer	198
10.6.3 Impact Factors of Permeability Influences	200
11 Transport into Nanosheets	205
11.1 Introduction	206
11.2 Methodology	208
11.3 Results	213
11.4 Conclusions	219
11.5 Supplementary Data	221
11.5.1 Methodology Details	221
11.5.2 Parameter Tests	223
11.5.3 Transport Diffusion Coefficient from EMD	223
11.5.4 LTA Tracer-Exchange Surface Permeability	228
11.5.5 Concentration-Dependent Corrected Diffusivity from TrMD	231
12 Binary Transport	235
V Resolution	241
13 Summary	243
14 Outlook	249

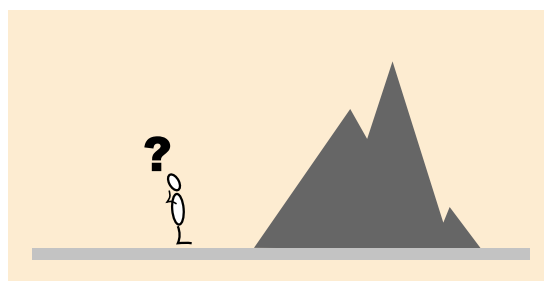
Appendices	253
A Nomenclature	253
A.1 List of Symbols	253
A.2 List of Abbreviations	264
B Zeolite Unit Cells	267
B.1 AFI from Qiu <i>et al.</i>	267
B.2 ITE from Cambor <i>et al.</i>	269
B.3 ITE from IZA	271
B.4 LTA from Corma <i>et al.</i>	273
B.5 LTA from IZA	274
B.6 LTA from Pluth and Smith	275
B.7 LTL from Barrer and Villiger	280
B.8 MFI from van Koningsveld <i>et al.</i>	282
B.9 SAS from IZA	285
B.10 SAS from Patinec <i>et al.</i>	286
B.11 SAS from Wragg <i>et al.</i>	287
C Continuum Calculations of Tracer Exchange	289
Bibliography	293
Publications	311
Conferences	313
Lebenslauf	315

Part I
Exposition

Introduction

1

Research is defined as a process of knowledge acquisition and refinement through observation and deduction. The first step, historically based on pure visual inspections, has undergone major transformations in recent years. Owing to the development of instruments with orders-of-



magnitude higher spatial resolution than the human eye and the occurrence of digital computers investigation of effects that take place at sub-micrometer length scales have become possible. One field that has taken major advantage of these accomplishments is research on zeolites. These solid materials excel with pores of usually nanometer size so that conventional gas molecules (e.g., hydrocarbons, aromatics, oxygen, carbon dioxide) just fit into them. Their significance stems mainly from the fact that they are widely used in chemical industry as thermostable catalysts. To design a corresponding reactor or to improve the performance of an existing one a good qualitative understanding of reaction, diffusion, and adsorption phenomena is as indispensable as accurate measurements or predictions of corresponding parameters quantifying these processes. In this respect, diffusion of molecules in zeolite nanopores represents such a large research area that single issues have kept scientists around the world busy for decades, and they are continuing to do so.

One of these issues are so-called surface barriers, which originates from the assumption that the transport through the interface between gas phase and zeolite space (Figure 1.1) is particularly slow. Speculations have persisted over many years whether these barriers exist, under which circumstances their effect might be especially strong, and what the origin of the

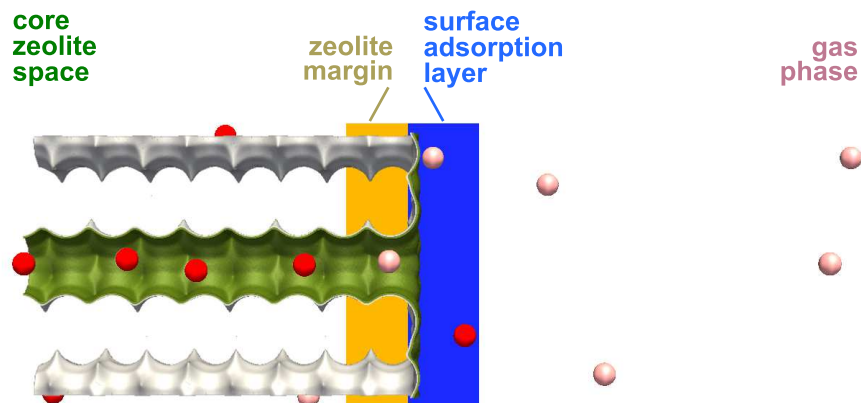


Figure 1.1: The interface between the core of a zeolite on the left-hand side and gas phase on the right-hand side consists of two subregions: the zeolite margin and the surface adsorption layer.

barriers is. Differences in crystal samples, nonideality effects (e.g., blocked pore entrances), heat release problems, and potential barrier differences to leave the pores have been the most frequently hypothesized reasons.^{1,2} Most importantly, however, they have been repeatedly speculated to bias diffusion measurements because of the superposition of the (presumably) much slower transport rate in the interface in comparison to the transport rate inside the zeolite interior. Using novel microscopy techniques, the group of Jörg Kärger and Christian Chmelik has significantly contributed to this debate in the past ten years. In their studies, they have highlighted the importance of blocked pore entrances. This was primarily made possible by the unprecedented high spatial resolutions of the measurement techniques,³ which have, however, not reached the scale to directly observe the reason to pore blockage. Instead, the studies usually followed a top-down approach, where experimental data on the micrometer scale⁴ were compared to model results at the nanometer scale,⁵ thus, giving rise to a separation of length scales of several orders-of-magnitude.

The significance of digital computers to zeolite science in general is mirrored by the efforts made at the frontier of electronic structure calculations and molecular simulations. Two recent examples illustrate the particular power of such approaches. The work by Lin *et al.*⁶ showed that screenings of structure-property relationships including hundred thousands of different zeolite materials have become possible. Because of the enormous number and the fact that hypothetical, yet not synthesized structures were investigated,

experiments could not have accomplished this task at present. As a second example of the emerging possibilities triggered by simulations, Hansen and Keil⁷ successfully designed an entire lab reactor from bottom up. That is, quantum chemical calculations yielded data on reactions and molecular simulations provided adsorption and diffusion properties, which were subsequently merged in a continuum reactor model of lab-scale size. This multiscale simulation approach nicely reproduced measurements from literature.

Despite the possibilities of theoretical approaches, most molecular simulation studies conducted prior to the present thesis pointed at a negligible influence of highly ideal surfaces in the context of surface barriers.^{8,9} However, these studies left an aspect unconsidered, so-called barrier recrossings, which had been shown to be important to intracrystalline barrier hopping at that time.¹⁰ This shortcoming represented the rationale for a reassessment and, in particular, the motivation of this thesis. Furthermore, advances in zeolite synthesis opened the possibility to produce ultrathin, highly oriented, dense, and stable zeolite membranes.¹¹ While financial penalties to fabricate such membranes persist to date, these are largely related to the support materials rather than to the separation-active zeolite films and their production.¹² Therefore, two golden threads run through the present work and they can be condensed to following questions.

- **Can surface barriers located in the gas–zeolite interface lead to substantial deviations in diffusion coefficients from different measurement techniques?**
- **Are the effects probed in the present work relevant to novel applications using ultrathin zeolite membranes or nanosheets?**

To answer these questions the present work pursues the opposite course in comparison to the above mentioned measurements.^{4,5} That is, molecular simulations (small length scale) in conjunction with continuum calculations (large length scale) are exploited to shed light into the nature of surface barriers and to spot consequences of technological significance.

1.1 Outline

The present thesis consists of five parts. In Part I, the reader is introduced into the topic of transport at the gas–zeolite interface from a broad perspective (Chapter 1). The necessity of the present study is given as well as the reason why simulations are employed rather than experiments. Furthermore, Chapter 2 describes the solid materials investigated (zeolites) from different perspectives (historical, structure, synthesis, properties, and appli-

cations). The detailed presentation shall underline that fundamental research on zeolites is still important, in spite of a long research history and, thus, enormous efforts already made.

Part II of this thesis provides the theoretical background necessary to follow subsequent chapters on the simulation results and corresponding discussions. Chapter 3 highlights the transport processes that can occur when guest molecules are adsorbed inside zeolites. The standard mathematical description is given, where the focus lies on different analytical solutions with different boundary conditions. In Chapter 4, fundamentals of the molecular simulations performed in this work are given as well as detailed descriptions of the various types of the simulations themselves (Monte Carlo, molecular dynamics, transient molecular dynamics). Furthermore, transition state theory is explained in the context of diffusion of guest molecules in well-ordered nanoporous materials. Moreover, Chapter 4 specifies the models used in and central approximations made for the here performed molecular simulations. Part II concludes with a short review about experimental measurement techniques (Chapter 5), where it is instructive to mention that no experiments were conducted. However, two reasons make the review inevitable. First, simulation results are, of course, compared to experimental results for validation. And second, one of the main aims of the present work is to provide an explanation for differences of diffusion coefficient obtained from different measurement techniques.

Part III of this thesis justifies the methodology chosen. For this reason, Chapter 6 investigates and discusses aspects of the simulation methodology, such as force-field influences, zeolite lattice flexibility, and thermostat issues. The main focus of that chapter lies however on the sensitivity of adsorption and diffusion results in response of using different crystal structures of the same topology type during the simulations. Chapter 6 concludes with a comparison of results obtained from simulations performed in the present work with experimental data from literature to validate the chosen approach. Because the tacit working hypothesis of the present work is that surface barriers can cause differences in measured diffusion coefficients, Chapter 7 describes how these barriers were quantitatively assessed to permit systematic comparison for different guest–host systems. The verification of the corresponding criterion is based on complementing continuum calculations, which are described in Appendix C.

Part IV represents the core of the present work, where the results of the simulations are presented, discussed, and analyzed for their significance to the main aims. While the chapters are usually self-contained, methodology details are provided only if they differ from previous chapters to avoid re-

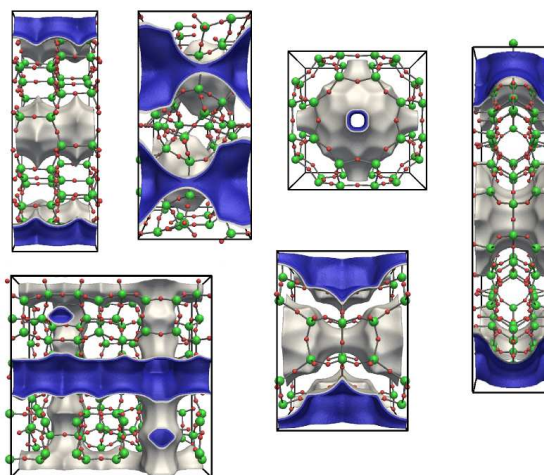
dundancy. In what follows is a short overview of the individual foci of these chapters. Chapter 8 investigates the equilibrium dynamics of methane and ethane at the interface between the fluid phase and the interior of an ultrathin AFI-type zeolite crystal. Subsequently, a screening of the influence of surface barriers is performed in Chapter 9 using various hydrocarbons in three different zeolites. Here, additional electronic structure calculations complement the molecular simulations in view of the nature of surface barriers. Chapter 10, which considers methane tracer release from an AFI-type zeolite, presents an accurate prediction of the surface permeability. This coefficient describes the local transport at the gas–solid interface. Nonequilibrium transport of methane into LTA and AFI-type zeolite nanosheets is studied in Chapter 11. A computationally demanding simulation method (transient molecular dynamics) is used here to test the transferability of insights from the preceding equilibrium simulations to instationary conditions and, first and foremost, to test whether conventional diffusion equations are applicable to well-ordered nanoporous materials of nanometer size. Finally, Chapter 12 gives the proof-of-principle that transient molecular dynamics is extendable to mixtures.

Part V highlights the conclusions of the present work. Chapter 13 summarizes all central insights gained and deduces the logical consequences in regard on the goals of this work. At last, Chapter 14, apart from highlighting future research in consequence of the outcomes of this thesis, provides a first rough sketch of a modulated principle to measure surface barriers.

Zeolites

2

A class of crystalline solids, zeolites stand out by a more than 250 years lasting research history which started with the discovery by Swedish chemist Axel Cronstedt in 1756 and which will be briefly reviewed in Section 2.1. Their highly ordered three-dimensional crystal structure, which will be elucidate in more detail in Section 2.2, consists primarily of silicon, aluminum, and oxygen, for which reason most zeolites



are strict aluminosilicates. Current accomplishments in nanotechnology opened the way for ultrathin, highly oriented, and well-intergrown zeolite membranes¹³ and record thin zeolite nanosheets¹⁴ so that Section 2.3 will outline a few general facts and highlight some current breakthroughs in zeolite synthesis. Owing to the fact that they possess micro- and mesopores,¹⁵ zeolites may contain guest molecules such as ions, hydrocarbons, and other atoms and molecules. It is this ability of accommodating structure-foreign matter together with the possibility of tailoring the composition of synthetic zeolites to meet individual needs which makes zeolites ideal candidates for implementation in adsorption¹⁶ and separation⁶ processes, for catalysis,^{14,17-20} and drug-supply coatings;²¹ Section 2.4 elaborates more on the application possibilities. More than 200 approved zeolite framework types are known to date,²² and millions more are possible based on theoretical considerations.^{23,24} Therefore, Section 2.5 highlights the

structures that were investigated in this work. The chapter will conclude with a brief presentation of two further groups of porous materials relevant to this work.

Note that following material laid out the basis of the present chapter: the book chapters by Flanigen *et al.*, McCusker and Baerlocher, and Doesburg *et al.* about the history,^{25,28} structural details,²⁶ and synthesis of zeolites²⁷ as well as definitions²⁹ and nomenclature^{15,30} proposed by the International Union for Pure and Applied Chemistry (IUPAC), and a very recommendable review by Caro and Noack about developments in zeolite membrane research.¹¹ Furthermore, some parts of the present chapter are borrowed from or inspired by the Master's Thesis of the author.³¹

2.1 Historical Review

The first scientific report about zeolites can be attributed to Baron Axel Fredrik Cronstedt.* In 1756 he worked on the mineral stilbite with an apparatus he himself had invented: the blowpipe. A long, rejuvenating tube, blowing into the broad end of the blowpipe produced a concentrated jet of air at the other, the narrow end. When directed into a flame, the blowpipe facilitated heating minerals to very high temperatures, which allowed drawing conclusions about the composition and nature of the minerals studied. Curiously, when Cronstedt rapidly heated up stilbite, the particles began to “fume”, for the reasons of which he named the new class of minerals *zeolites*. The word is in fact derived from two Greek words: *zeo* (to boil) and *lithos* (stone).

After the discovery of naturally occurring zeolites by Cronstedt, the new mineral class did not get much attention from the scientific community for the next 120 years. In the middle of the 19th century, however, zeolites were found to be reversibly hydrated and they showed ion-exchange potential. Then, in 1862 and 1896, two important milestones were set. On the one hand, St. Claire-Deville produced a zeolite in his laboratory which represented the first documented synthesis of a zeolite. On the other hand, Friedel proposed that the inner structure of a zeolite had to consist of an open, sponge-like framework because of the ability to adsorb (i.e., accommodate in their pores) vapors and liquids, such as alcohol, benzene and chloroform.^{25,28} As the adsorption behavior was observed after dehydration only, the term “activated zeolite” was introduced which still refers to the dehydrated state.

*Cronstedt, Baron Axel Fredrik: *December 23, 1722, in Ströpsta, Sweden; † August 19, 1765, in Stockholm, Sweden; chemist and mineralogist. Apart from his discovery of zeolites, he is also recognized for the discovery of the element nickel.³²

In 1925, seven years before McBain introduced the term *molecular sieve*, Weigel and Steinhoff found that chabazite was capable of adsorbing certain compounds, such as water, methyl and ethyl alcohol, while others, such as acetone, ether and benzene, were expelled. It was the first time that zeolites became known for their selective adsorption and therefore for their separation capabilities. Note that the term molecular sieve is hereby related to materials that are capable of selectively sorbing molecules, primarily based on size exclusion. The idea of a sponge-like structure within zeolite materials was confirmed by Taylor and Pauling in 1930 by means of X-ray experiments. From this time on, the interest in zeolites grew steadily and rapidly.

By systematically studying the sorption of polar and non-polar gases in zeolites (1938), Barrer began his career in the new field of zeolite science. Until his passing away in 1996, he actively formed the novel field by, for example, proposing a naming scheme for the different types of zeolites in 1945 and chairing the first International Zeolite Conference in 1968 in London. Therefore, it seems justified to consider him as the "founding father" of zeolite science today.

Another breakthrough in zeolite science was achieved between 1949 and 1954 when Milton and Breck, who worked for the Union Carbide Corporation, developed the so-called *reactive gel crystallization* method to produce synthetic zeolites. Al_2O_3 and SiO_2 were here mixed with an alkali hydroxide to yield a reactive gel in which the zeolite crystallized. This method still is the basis for the majority of current synthesis procedures from solution. In addition, Union Carbide was the first to use zeolites for major bulk processes. The so-called ISOSIV process for normal and iso-paraffin separation was marketed by Union Carbide in the same year (1959) as they introduced a Y-based zeolite as an isomerization catalyst.

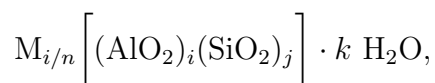
The 1960s were coined by synthesizing zeolites with a high silica-to-alumina ratio, mainly by introducing alkyl ammonium cations into the reactive gel. These highly siliceous zeolites were particularly interesting for the petrochemical industry, because hydrophobic/organophilic environments were desired in separation processes. ZSM-5, the most prominent and probably most thoroughly studied high-silica zeolite, was introduced at the end of the 1960s. Up to that date, the so-called FISCHER-TROPSCH process was the only known conversion path for methanol to gasoline and included many intermediate steps. With the advent of ZSM-5, this changed however because the catalyst enabled the conversion in one single step. That fact was and is still the most striking reason for the strong interest in ZSM-5 over most other zeolites.

From the late 1970s to the mid of the 1990s zeolite science increasingly

looked beyond all-silica structures and turned its attention to structures with compositions other than SiO_2 and AlSiO_4 , such as aluminophosphates, metallosilicates and metallophosphates. Last but not least, computational studies on zeolites became more and more available since the 1970s, owing to the steadily increasing computer capacities and speeds. The computational studies complemented the experimental investigations²⁰ by providing molecular insights into processes and mechanisms which are occurring inside the zeolite structures.

2.2 Structure and Nomenclature

As mentioned at the beginning of this chapter, zeolites mainly consist of silicon, aluminum, and oxygen atoms* that form a well-defined three-dimensional crystal structure. The general composition formula of such aluminosilicates is given by



where i , j , and k denote integer values, M represents a cation species for charge compensation of the framework in the case when trivalent aluminum is present ($i > 0$), and n is the cation's valency. Other than these elements are usually found in natural zeolites, too, and can be incorporated into synthetic structures so to even completely replace silicon and aluminum (e.g., GaPO_4 -LTA³³). Obviously, a feature that all zeolite materials share is that oxygen occurs. Because of the vast chemical diversity of the other atoms that truly belong to the crystal structure (i.e., not extra-framework cations M) they are named *T atoms* in the following.

The second feature common to all zeolites is that the crystal structure is built up by TO_4 tetrahedrons, representing the smallest repetitive structure unit and therefore called *primary building unit* (PBU). The four oxygen atoms are located at the four corners of a given tetrahedron and the tri-, tetra-, or pentavalent T atom (e.g., Si, Al, P, Ga) in its center (Figure 2.1a). PBUs are connected by sharing oxygen atoms to form *secondary building units* (SBUs). These are finite units, such as four-rings (Figure 2.1b), five-rings, six-rings (Figure 2.1c), double four-rings (Figure 2.1d), and double

*Some authors prefer to consider the crystal species as ions due to the fact that the outermost electrons of Si and Al are thought to be taken by the O atoms. The notion *atoms* instead of *ions* was adopted here to avoid confusion with extra-framework cations that balance the framework charge in aluminosilicates.

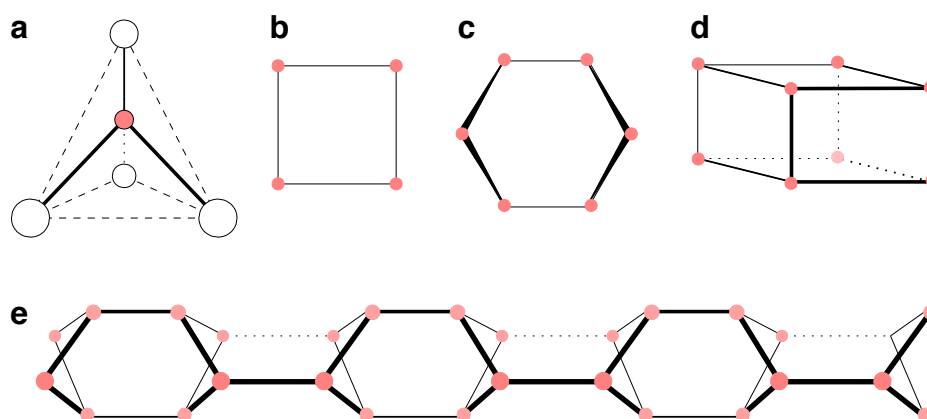


Figure 2.1: Schematic drawing of a primary building unit (a), where oxygen atoms (unfilled circles) occupy the corners of a tetrahedron in whose center a T atom (red circle) is located. The figure furthermore shows three examples for secondary building units (SBUs): four-ring (b), six-ring (c), and double four-ring (d). For reasons of clarity oxygen bridges were omitted within the SBUs. The T atoms in the four-ring lie in a plane; the T atoms of the six-ring, by contrast, form a three-dimensional structure. The Narsarsukite chain (e) is an example for a structural element built up by SBUs; here: double six-rings.

six-rings. Because each pair of T atoms is connected via exactly one oxygen atom, the T–O–T connection is also referred to as *oxygen bridge*. SBUs occur repetitively in the zeolite framework and they are used to characterize similar parts of the framework. Mirror images of SBUs are identical, that is, they are invariably nonchiral.

A zeolite structure may be viewed as an assembly of different and similar SBUs. However, the SBUs form larger regular structural components which occur repetitively and may be finite (e.g., cages) or infinite (e.g., channels, sheets, chains) in size. Figure 2.1e presents a schematic drawing of an infinite element: the *Narsarsukite* chain, which consists of double-six rings. Note that six-rings and wraps of these are often the basis for one-dimensional zeolite pores.

SBUs link together to finally form a *framework type*. The term refers to the description of the connectivity of the framework's tetrahedrally coordinated T atoms in the highest possible symmetry.²⁶ This implies that the actual chemical composition, observed symmetry, and the actual (unit cell) dimensions are not considered.²⁶ The advantage of this definition is that zeolites with different composition but similar arrangement of O and T atoms can

be comprised to a “group”. For example, $\text{AlPO}_4\text{-5}$, CoAPO-5 , FAPO-5 , SAPO-5 , and SSZ-24 all are of the same framework type while their compositions differ. The framework type usually determines relative pore sizes and pore dimensionality of a channel system.²⁶ Both features are crucial for the properties of a given zeolite. While millions of hypothetical framework types are possible,^{24,34} the internet database²² provided by the International Zeolite Association (IZA) lists those 201 framework types which were so far officially confirmed to exist by experimental evidence. An approved framework type is given a three-letter code which usually hints at the name of the first material of that framework to have been characterized. For example, AFI originates from “**al**uminophosphate-**fi**ve” ($\text{AlPO}_4\text{-5}$), LTA and LTL stand for “**L**inde **t**ype **A**” and “**L**inde-**t**ype **L**”, respectively, and MFI reflects that the framework is identical to “zeolite Socony **M**obil-**fi**ve” (ZSM-5).

A *unit cell* (UC) is defined by the IUPAC²⁹ as the smallest, regularly repeating material portion contained in a parallelepiped from which a crystal is formed by parallel displacements in three dimensions. Therefore, a unit cell can be regarded as the chemical implementation of a given framework type. That does however not necessarily imply that it contains the same number of T atoms as its framework type. While this T atom correspondence is usually observable in the case of siliceous zeolites and their framework types, the unit cells of aluminosilicates are always larger than the framework type definition. Consider, for example, zeolites ITQ-29 and 4A, both structures exhibiting framework type LTA. The unit cell of the purely siliceous material ITQ-29 consists of 24 Si atoms,³⁵ just as many T atoms as in the framework definition.²² On the other hand, the 4A unit cell accommodates eight times as many T atoms; specifically, 96 Si and 96 Al atoms.³⁶ Importantly, the 4A unit cell cannot be subdivided anymore without violating Loewenstein’s rule. The rule, also known as the principle of Al avoidance, states that no two aluminum atoms in a aluminosilicate are connected via the same oxygen bridge due to the high instability of such Al–O–Al complexes.³⁷

The positions of T and O atoms within the unit cell are usually described in terms of fractional coordinates of the parallelepiped. That is, the atom coordinates vary between zero and one and they are related to the unit cell vectors **a**, **b**, and **c**, forming a basis in Euclidean space. The first vector describes the \hat{a} axis which is usually collinear with the x axis whereas the \hat{b} axis (second basis vector) lies in the x - y plane.³⁸ Conversion of \hat{a} - \hat{b} - \hat{c} coordinates into x - y - z is possible by applying the standard transformation matrix when the angles between the unit cell vectors are known.³⁹

Apart from the framework type and the chemical composition of the (ideal) crystal, a zeolite structure is also characterized by (possible) extra-

framework cations and sorbed molecules. The chemical formula of zeolite-type aluminosilicate given at the beginning of the present section has already hinted at these conditions. Furthermore, departure from ideality (i.e., lattice distortions²⁹) represents another important feature of a “real” zeolite material. These defects will be of as central importance to this work as the ideal crystal structure. Furthermore, note that large crystals are most frequently in fact intergrown poly-crystallites and not perfect single crystals.⁴⁰

In accordance with IUPAC recommendations,³⁰ following terms will be used in this work as described below. The *host* or *host structure* refers to the zeolite atoms that are linked by chemical bonds to form the solid material. The voids between the zeolite atoms are called *pores*, no matter whether they are accessible or not. Following the recommendations for the characterization of porous solids by the IUPAC,¹⁵ pores can be classified based on their size, where

- micropores have widths $l_{\text{pore}} < 2$ nm,
- mesopores $2 \text{ nm} \leq l_{\text{pore}} \leq 50$ nm, and
- macropores $l_{\text{pore}} > 50$ nm.

The pore size (or pore width) is hereby defined as the distance between two opposite walls of the pore.¹⁵ It should, however, be pointed out that the term *micropore* is nowadays often substituted by the term *nanopore*, which much more exactly reflects the scale involved (a few nanometers rather than a few micrometers).

Within a pore, *guest* species, such as cations, water, and hydrocarbons, may be accommodated.³⁰ Because this work deals exclusively with siliceous zeolites, counter ions balancing charged frameworks are not required due to the absence of aluminum, which, in turn, causes also water to not adsorb any significantly. Consequently, hydrocarbons are the only adsorbate molecules referred to as guests or guest molecules in the present work.

Windows denote the structural rings that form a polyhedral pore. For example, eight-rings (8R) are prominent windows. They consist hence of eight silicon (or more generally T) atoms linked via eight oxygen atoms and are found in such important zeolite types as LTA. *Cages* are pores that are not accessible for water and larger molecules such as sodalite cages in LTA. By contrast, a *cavity* refers to accessible pores such that one window, at least, is large enough to allow guest molecules to slip in. Note however that the term cage is used in this work as a synonym for cavity. Finally, *channel* denotes an in one dimension infinitely extended pore which is accessible to guest molecules.

The categorization of zeolites introduced by Beerdsen *et al.* is of immedi-

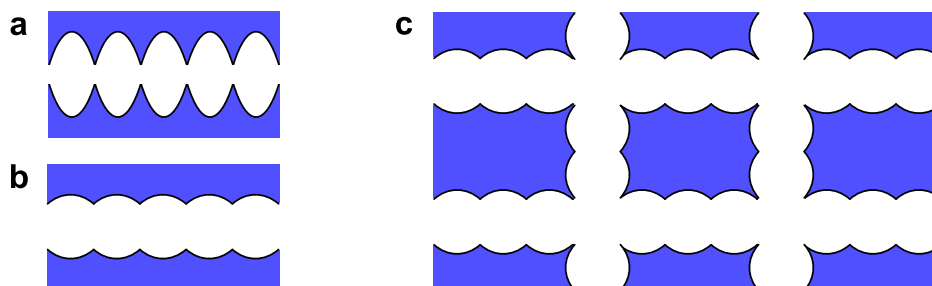


Figure 2.2: Illustration of differences between zeolite types according to the categorization by Beerdsen *et al.*:⁴¹ (a) cage type, (b) channel type, and (c) intersecting channel type.

ate relevance to the present work because it is based on diffusion characteristics of guest molecules within zeolite channels.⁴¹ In that categorization, *cage-type* zeolite refers to a channel whose windows connecting adjacent cavities are so small (Figure 2.2a) that they trigger large entropic diffusion barriers for guest molecule jumps from one cavity to an adjacent one (cf., Section 6.2). *Channel-type* zeolites, on the contrary, stand out due to smooth channel walls and rather broad windows (Figure 2.2b), giving rise to much smaller diffusion barriers than seen for cage-type structures. Lastly, an *intersecting channel-type* zeolite denotes smooth channels running along different directions but intersecting at some point (Figure 2.2c). Whereas cavities, themselves, are not as bulky such as in cage-type structures, the intersections are characteristic in this third class because they form entropic traps to diffusing guest molecules.⁴¹

2.3 Synthesis

The significance of zeolite synthesis comes mainly from two facts. First, the number of known natural zeolites is rather small (40),⁴² which severely limits the optimization possibilities of a process by variation of the zeolite employed. And second, natural zeolites are usually not uniform and phase-pure enough for implementation in most industrial applications where, however, synthetic structures have in fact been successfully incorporated. As a strong indicator of its importance, the global synthetic zeolite industry is worth about \$1.9 billion a year.⁴³

Because TO_4 tetrahedrons are primary building units, SiO_4^{4-} and AlO_4^{5-} have to be present in any synthesis mixture to produce an aluminosilicate

zeolite.²⁷ Aluminum ions are only stable at high pH so that the synthesis solution is usually alkaline; the reactive gel crystallization is therefore also known as *sol-gel processing*. As a rule of thumb, the higher the silicon-to-aluminum ratio is, the more difficult will be the synthesis and the more severe the conditions.²⁷

The first synthesis step represents the preparation of the so-called *synthesis gel* at low temperature ($T < 60^\circ\text{C}$).²⁷ Silicate and aluminate monomers and oligomers are here in equilibrium with condensed silicate aluminate units. Subsequently, the temperature is raised to the crystallization temperature ($100\text{--}200^\circ\text{C}$), representing the second step. Silicate and aluminate oligomers dissociate now so that the monomer concentration increases. Crystallization begins, as soon as the crystallization temperature is finally reached and a certain induction time exceeded. The entire process of nucleation and crystallization usually shows a typical S-shaped curve when the amount of matter already crystallized is plotted versus time. Depending on the specific system and conditions, it can easily take several hours up to days until the crystallization has completed.* The post-synthesis treatment represents the third and last step, where the mother liquor usually undergoes decantation, filtration or centrifugation, washing, drying, and calcination.²⁷ Sometimes special post-synthesis treatments, such as acid leaching, high temperature steaming, and chemical treatments, are necessary to fine-tune the properties of a zeolite for its target application.⁴⁵

Typical zeolite A (LTA framework with composition $\text{Na}_2\text{OAl}_2\text{O}_3 \cdot 2\text{SiO}_2$) is obtained by mixing sodium aluminate and sodium silicate in aqueous solution (water glass) in stoichiometric amounts ($\text{Al}:\text{Si} = 2:1.95$).²⁷ The solid yield is approximately 10 % and the crystals are $1\text{--}10\ \mu\text{m}$ in size. Synthesis of zeolite Y usually gives more solid (25 %). However, this FAU-type zeolite needs extra SiO_2 because of the higher silicon-to-aluminum ratio. Furthermore, ageing of the gel is necessary before crystallization can begin, and crystallization takes much time (2–4 days). As a last important example, ZSM-5 is obtained by using a large alkaline ion which ensures high pH to facilitate crystallization of this high-silica zeolite but which also directs the formation of the zeolite pore. Tetrapropylammonium (TPA) hydroxide is almost always used for ZSM-5. Long crystallization of some 2–5 days results in 10 % solid material, in which the template molecule is still present and has therefore to be burned off.²⁷

Steady progress and recent breakthroughs have enabled the fabrication

*In this context, it is noteworthy that natural zeolites are usually found in volcanic deposits.⁴⁴ This is, because fine-grained volcanic ash, rich in aluminosilicate glass, had been reacting under the influence of percolating hot water to form the zeolite. Importantly, this process may have taken tens to thousands of years.

of ultrathin, highly oriented, and dense zeolite films. For example, Lai *et al.* have developed a procedure to produce siliceous MFI membranes on α -alumina support.⁴⁶ Seed crystals were synthesized by conventional hydrothermal growth and then attached to the support by covalent bonding with the functionalized support surface. The functionalization triggered the orientation in crystallographic \hat{b} direction. Secondary growth with a different structure directing agent (trimer-TPA rather than TPA) then favored further growth along \hat{b} over \hat{a} and \hat{c} direction to yield a well-intergrown, dense film. The use of zeolite growth modifiers to tailor desired crystal morphologies (i.e., obtaining control of anisotropic growth) has indeed become a hot topic in zeolite synthesis.⁴⁷

Another important milestone in zeolite synthesis was also achieved with silica-rich MFI films. Choi *et al.* succeeded in synthesizing ZSM-5 nanosheets of single unit-cell thickness which was possible due to the use of a special, very long surfactant molecule.¹⁴ That molecule contained a hydrophilic part, around which the zeolite crystallized, and a hydrophobic part, which prevented ripening of the crystal by micellar inhibition.¹⁴ Furthermore, the same synthesis strategy was transferable to MTW nanosheets.¹⁴ A more recent work by Yoo *et al.* highlighted the possibility of considerably reducing the production time of these ultrathin MFI membranes by a few changes in the procedure.⁴⁸ Fabrication of thin films is however not limited to MFI-type membranes and sheets. Veziri *et al.*¹³ produced ultrathin ($< 1 \mu\text{m}$), highly \hat{c} -oriented and very continuous AlPO_4 -5 films. The exceptional films were obtained by systematically screening for optimal synthesis conditions (mixture preparation and dilution as well as precrystallization).

Besides these size-reduction accomplishments, attaching mesoporous layers onto zeolite crystals is yet another current focus of the synthesis community. Such combined meso-microporous materials are usually referred to as hierarchical structures. As an exception to most of them, García-Martínez *et al.* succeeded in introducing controlled mesoporosity directly into the crystal structure of zeolite Y via a surfactant templating approach.⁴⁹ The controlled adjustment of the mesopore size and morphology was here achieved by varying the surfactant molecule length and synthesis conditions.⁴⁹

Despite current breakthroughs and a long research history, the understanding of zeolite synthesis is still somewhat limited. Evidence to this conjecture is found in the database by Michael Deem²² which contains more than two million hypothetical but unique siliceous zeolite structures.³⁴ Even though Pophale *et al.* posited that the vast majority (85–90 %) is thermodynamically unstable,³⁴ that fraction leaves some 100 000 structures feasible to produce. However, the number clearly contrasts the few structures officially

approved by the International Zeolite Association²² (201) so that the large discrepancy (hypothetical vs truly observed structures) may be regarded as a low degree of understanding. In this context, a recent report by Li *et al.* should be mentioned because it underlines the deficiency.⁵⁰ The authors investigated new criteria for predicting the feasibility of synthesizing a given zeolite framework.⁵⁰ In most cases, the energy of the structure is employed to state whether or not a certain hypothetical zeolite can in fact be synthesized: low energy per silicon atom = synthesis feasible; α -quartz serves hereby usually as a reference value. For example, Pophale *et al.* made use of the energy criterion.³⁴ However, too many exceptions to this approximate rule have been observed. Li *et al.* showed by structure optimization with classical potentials,⁵⁰ and therefore by similar means as Pophale *et al.*,³⁴ that local atomic distances of nearest neighbors (T-O) and next-nearest neighbors (T-O-T as well as O-T-O) unambiguously pinpoint feasible structures. Using all approved²² zeolite frameworks in their siliceous form and 665 hypothetical frameworks, Li *et al.* concluded that the feasibility of synthesizing a given hypothetical zeolite framework was determined by the intrinsic structural nature.⁵⁰ This confirms an earlier conjecture by Davis who postulated that a certain synthesis procedure does not necessarily give the most stable material from a purely thermodynamic stance.⁵¹ The diversity of kinetic pathways was instead speculated to play a central role for the final product.⁵¹

2.4 Properties and Applications

Most zeolite properties that arouse technological interest stem from the fact that the materials possess nanopores. The ability of adsorbing gases and liquids, that is, to accommodate guest molecules in the pores, can be considered as the first and foremost property (*adsorption**). The stronger the interaction between guests and host is, the larger is the amount of adsorbed molecules. In the case of mixtures, *selective adsorption* denotes the property of a zeolite to adsorb a single (or a few) component(s) much stronger than the other. Second, the ability to prohibit access of certain guests that are simply too large to enter the pore network is central to zeolite science and referred to as *molecular sieving*. Third, zeolites, if not purely siliceous, can exchange their extra-framework ions with other ions from the surrounding (*ion-exchange* capabilities). Fourth, Brønstedt and Lewis acid sites inside the

*The accumulation of molecules by a zeolite is an adsorption rather than an absorption process because the molecules reside at the pore walls (surface) rather than dissolving in the volume.⁵²

pores define the *catalytic* activity of zeolites. Clearly, the adsorption capability triggers all other properties. Furthermore, any technological application will, in one way or another, have to consider guest transport between the pores and the bulk (fluid) phase, and thus across a solid-fluid interface, for process design purposes.

A classical example for practical use of zeolites is the separation of oxygen from air by means of pressure swing adsorption with zeolite 5A (LTA) or 13X (FAU).⁵³ Nitrogen adsorbs selectively in these zeolites so that separation factors of 3–3.5 can be achieved. Oxygen is obtained in purity of 95–96% and can be used for domestic medical purposes at a scale of a few liters per minute or in industry with some 10 000 tons per day.⁵³

The most prominent example of exploiting the ion-exchange capabilities is the domestic use in detergents for water softening purposes, where calcium ions in water are exchanged by sodium ions contained in the zeolite. Henkel introduced zeolite A in detergents in 1974,²⁵ because the standard softener, sodium tripolyphosphate, was found to be of environmental concern as it caused eutrophication in lakes.⁵⁴ Today, this application represents the largest single market of zeolites by volume with 72%.²⁵ The affinity of the zeolites towards calcium ions is indeed so strong that other ion-exchange applications such as lead adsorption at mining sites⁵⁵ suffer from too low efficiencies. However, zeolites, presumably natural ones such as clinoptilolite, served as an “ad-hoc clean-up medium” in several nuclear power plant accidents, including the most recent in Fukushima, Japan.⁵⁶ Sandbags filled with zeolites were dumped into the sea close to the troubled plant to adsorb radioactive cesium.⁵⁶ Also invoked by the ion-exchange property, natural zeolites are found in agriculture as nutrient storage systems. Before being spread on the soil, they are loaded with ammonium. When it starts raining the ammonium is (partially) washed out and thus delivered to the roots of the plants. Because zeolites in general, and natural ones in particular, are non-toxic, it is environmentally safe to introduce them to the soil.

The key needs for a successful cracking catalyst are strong acid activity and high thermal and hydrothermal stability.⁴⁵ Therefore, zeolites rich in silicon are preferable over structures with low Si:Al ratios.⁵⁴ The importance of synthetic zeolite catalysts to industry crystallizes in the fact that they constitute the largest market by value (55%) because of a roughly ten times higher price compared to those zeolites added to detergents.²⁵ Silica-enriched zeolite Y amounts here to 95% of total zeolite catalyst consumption, which is primarily employed in fluid catalytic cracking (FCC).²⁵ Despite the maturity of this technology, there is still room for optimization, as two studies by García-Martínez *et al.* from 2012 indicate.^{17,49} The direct introduction of con-

trolled mesoporosity into a conventional zeolite Y catalyst (cf., Section 2.3) yielded high hydrothermal stability and superior FCC performance due to the reduction of diffusion limitation.⁴⁹ The quick entrance of reactants and exit of products prevented overcracking.⁴⁹ Starting with a commercially available zeolite Y from Rive Technology⁴³ to introduce mesoporosity, this route is in fact attractive from an industrial perspective, in contrast to the vast majority of hierarchical zeolites.⁴⁹ The project was further pursued to test the novel catalyst in a refinery.¹⁷ The mesostructured zeolite Y was produced at a scale of 30 tons and then processed to yield 52 tons of FCC catalyst microspheres.¹⁷ A 70-days trial showed two positive effects. The selectivity slightly increased and less coke formed at same catalyst activity when compared to the purely microporous analogous.¹⁷

An emerging opportunity for zeolite catalysis appears in the growing field of biotechnology where biomass is currently being tested for conversion into valuable products.* Cheng *et al.* have succeeded to perform catalytic fast pyrolysis of ground pinewood in fluidized-bed lab reactors with the aid of different ZSM-5 zeolites. 32% of the input carbon could be converted to valuable aromatics.¹⁸ Importantly, the commercially purchased spray-dried ZSM-5 catalysts had to be modified by incipient wetness impregnation with $\text{Ga}(\text{NO}_3)_3$ to yield the high conversion.¹⁸ The group fine-tuned the catalyst in a follow-up study and unraveled that surface treatment by chemical liquid deposition of tetraorthosilicate led to an increase in paraxylene selectivity from 51% to 72%.¹⁹ The improvement was attributed to shape selectivity. Narrower pore openings at the surface (*pore mouth*) of the modified catalyst reduced the fraction of bulkier ortho and metaxylene leaving the solid.¹⁹

The shape selectivity of the last example can be even “transformed” into a molecular sieving potential as the works by Lai *et al.* and Pham *et al.* highlighted.^{46,58} Central to this switchover is the change from high-silica to purely siliceous MFI-type zeolites⁵⁸ and the fabrication of ultrathin, highly oriented, and dense zeolite films.^{46,58} Using such thin MFI films on different supports, both groups showed that orthoxylene could be separated from a mixture with paraxylene at very high separation factors (> 100).^{46,58} In addition, the role of ultrathin films seems attractive to membrane reactors¹¹ for methanol-to-gasoline conversion. This is, because MFI nanosheets of single unit-cell thickness have been proven to be an active and longer-lived catalyst than conventional ZSM-5.¹⁴

Finally, notice that zeolites are potential candidates as carriers of contrast agents for diagnostic magnetic resonance imaging⁵⁹ and as microlasers,⁶⁰

*Underlining current efforts to establish biomass as a chemical feedstock, Green Dot, a U.S.-based company, has recently started offering a soft bio-plastic to the toy industry.⁵⁷

among others.⁵¹

2.5 Materials Used in this Work

The unit cells of the six zeolite materials investigated in this work are displayed in Figure 2.3, where silicon atoms are represented by large green spheres and oxygen atoms by small red ones. For reasons of simplicity, the different materials are referenced by their respective framework types in the remainder of this work because they are all purely siliceous and thus distinct. The exception is Section 6.2, in which different siliceous structures of the same framework type will be investigated. But the local labeling should be unambiguous. The unit cells used were taken from References 22,35,36,61–66 and can be found in Appendix B. Within the categorization of Beerdse *et al.*,⁴¹ the selection comprises all structure types: cage type (ITE, LTA, LTL, SAS), channel type (AFI), and intersecting channel type (MFI).

2.6 Other Nanoporous Materials

Although zeolites are investigated in the present work only, some results will be compared to other nanoporous materials in a conceptual manner. Therefore, this section gives a short description of the two groups of porous solids in question: carbon nanotubes and metal–organic frameworks.

2.6.1 Carbon Nanotubes

Exhibiting strict one-dimensional channels, carbon nanotubes (CNTs) can be regarded as “wrapped-up” graphene, as seen in Figure 2.4a. The nomenclature is thereby indeed derived from the way how the nanotube is rolled up. Two vectors, **a** and **b**, serve as basis on the two-dimensional sheet. An (i, j) CNT is, for example, constructed by laying the carbon atom at $(0, 0)$ on top of that carbon found at position (i, j) with respect to the just described basis and origin $(0, 0)$. Nanotubes obtained by following basis vector **a** only [i.e., $(i, 0)$] are called zigzag CNTs (Figure 2.4b) whereas carbon nanotubes constructed by proceeding in the same number of steps along **a** and **b** [i.e., (i, i)] are labeled armchair structures.

As an incidental connections between zeolites and carbon nanotubes, CNTs can be produced by means of AFI-type zeolites.⁶⁷

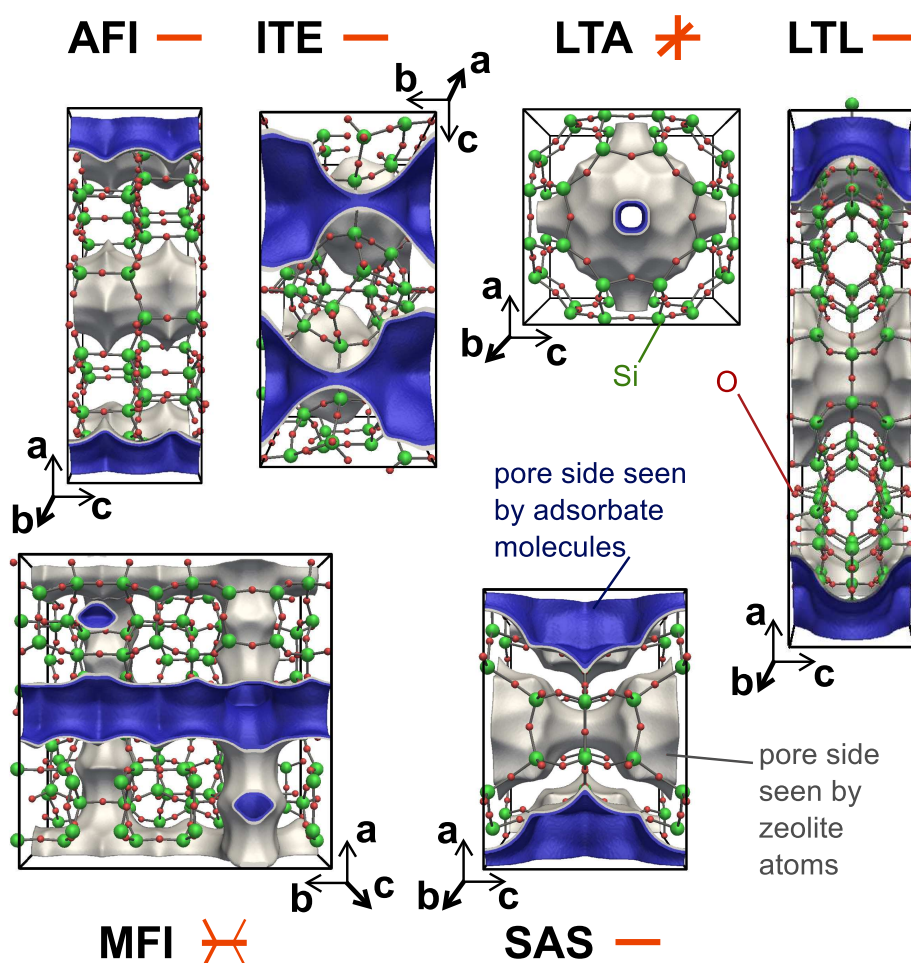


Figure 2.3: Compilation of the unit cells of those zeolite structures investigated in the present work. Orange drawings to the right of the three-letter structure names schematically display respective channel connectivities.

Most current applications of CNTs are related to their mechanical strength.⁶⁸ Nonetheless, Mirica *et al.* have recently shown that commercially available single-walled carbon nanotubes can be used as sensors for NH_3 .⁶⁹ Surprisingly simple, the sensors were fabricated by drawing: gold electrodes on conventional paper substrate were connected by a line of abraded CNT pellets.⁶⁹ The measuring principle relies hereby on the dependence of the electrical current measured with varying amount of ammonia adsorbed when a constant voltage is applied.⁶⁹

For more details on carbon nanotubes, particularly in regard on theoretical transport aspects, the reader is referred to the excellent dissertation by

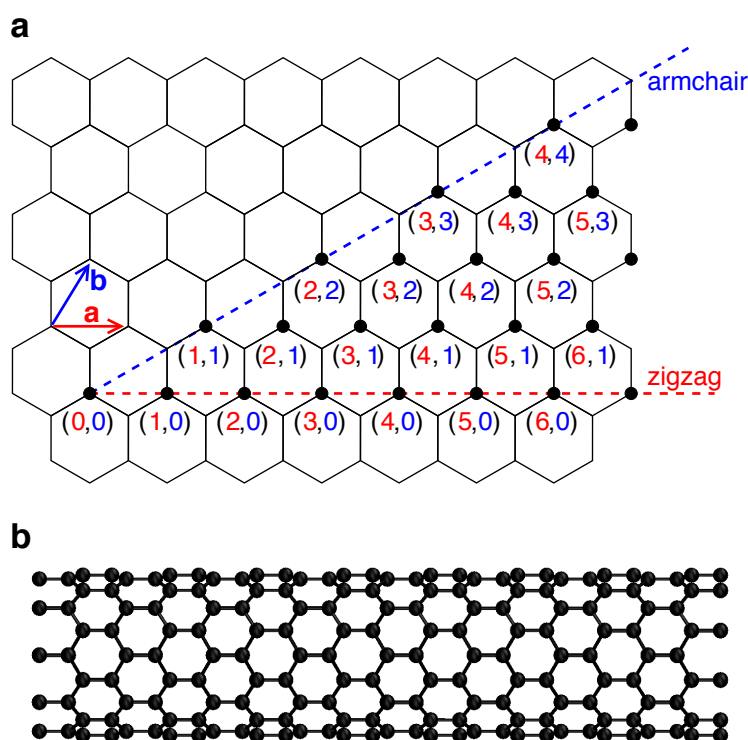


Figure 2.4: (a) Scheme of the derivation of the carbon nanotube nomenclature based on vectors **a** and **b**. (b) A zigzag (10, 0) CNT of 3.4 nm length and 0.39 nm diameter as calculated by atomic coordinates.

Jakobtorweihen.⁷⁰

2.6.2 Metal–Organic Frameworks

Metal–organic frameworks (MOFs) consist of metal ions, or clusters thereof, that are connected via rather rigid organic entities (*linkers*) to usually form a three-dimensional, porous crystal structure.^{71,72} Therefore, MOFs are more similar to zeolites than (single-walled) carbon nanotubes. However, the vast chemical diversity of both linkers and metal ions triggers a correspondingly much larger number of possible structures due to the far larger variety in bridges and connectivity compared to zeolites. Recall that zeolite linkers are always oxygen bridges and the T atoms always four-coordinated. Clearly, this fact calls for the necessity of archiving and there are, in analogy to zeolites, well-maintained databases for metal–organic frameworks. For example, the Cambridge Structural Database⁷³ today lists more than half a million of

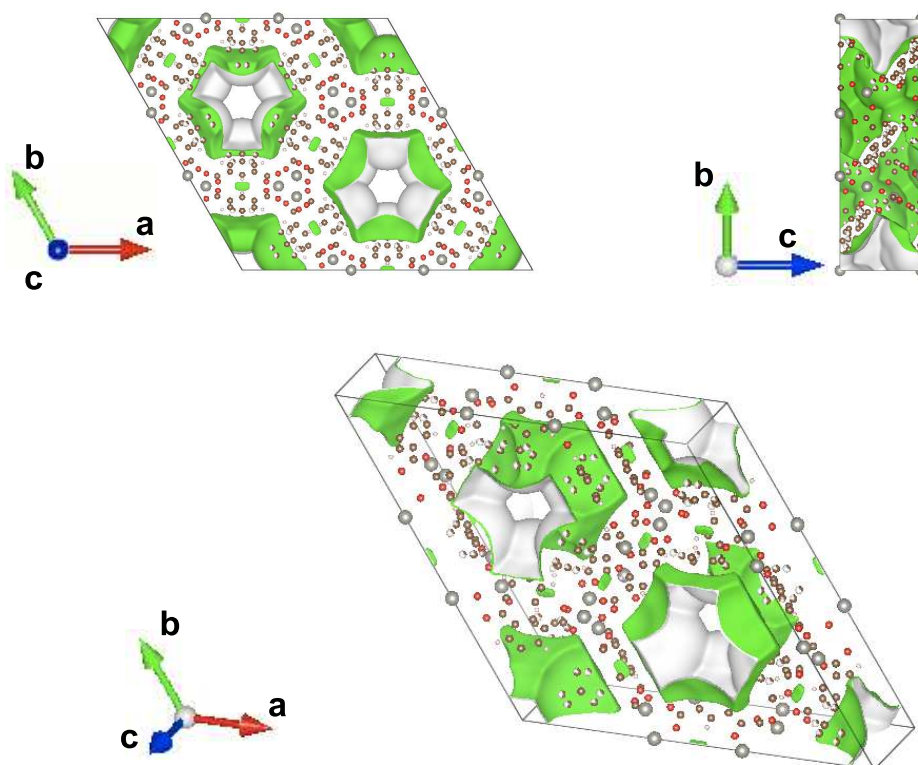


Figure 2.5: Three different projections of the Zn(tbip) unit cell;⁷⁵ snapshots were obtained with VESTA.⁷⁶

organic molecules and metal–organic compounds.⁷⁴

Research interest in metal–organic frameworks has grown extraordinarily rapidly over the past 15 years so that “consensus is [still] lacking about what they really are”.⁷⁷ As a result, the IUPAC has so-far provided provisional recommendations about MOF nomenclature only, at the time this chapter is being written.⁷² In a sense, history seems to be repeating because the situation resembles the one in zeolite science in the late 1970s. Indeed, the parallel between the developments in the two material classes is reflected by the strong recommendation of the IUPAC to use the topology (“framework type”) and related descriptors for describing a given MOF crystal structure.⁷² Not only from a structural point of view, but also with regard on the properties (e.g., possessing meso- and micropores) and resulting applications do the two material classes reveal similarities. Apart from hydrogen storage purposes,⁷⁸ one of the most promising uses of MOFs delineates currently in the area of carbon capture and storage (CCS) from flue gas,⁷⁹ which is also

true for new zeolite applications.⁶

Representing the first report on polymer-supported, large-scale free-standing MOF membranes, Ben *et al.* have recently shown that such membranes of HKUST-1 type can be cheaply produced. The membranes revealed promising separation factors for H₂/N₂ as well as CO₂/CH₄ mixtures (9–11).⁸⁰

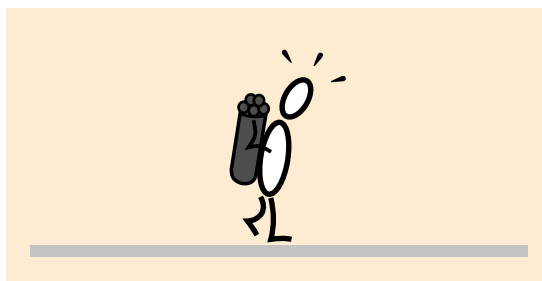
The MOF that is most relevant to this work is Zn(tbip).⁷⁵ The name reflects the chemical composition of the material because it consists of zinc cations that are tetrahedrally connected via 5-*tert*-butyl isophthalate (tbip) linkers.⁷⁵ The unit cell⁷⁴ is monoclinic and gives rise to one-dimensional channels along crystallographic \hat{c} axis, which can be seen in Figure 2.5.

Part II
Background

Transport Processes

3

Transport of energy and matter is essential to any type of living (e.g., plants) to function at all (transferring water from the roots into the leaves); to commercial companies for delivering goods (gas) to consumers (via a pipeline); to chemical industry (for ensuring that the



reactants reach the active site of a porous catalyst and the products can exit the pores); to researchers for obtaining their daily dose of caffeine or theine (extraction of natural products with water); and to the universe to have taken the form that we all witness. Clearly, a good understanding about transport phenomena is crucial for a good understanding of both nature and technological applications.

Because different process, and therefore transport, modes exist, they shall be briefly recalled. *Instationary* or *transient* processes are defined by the fact that the variables involved (here: concentrations and transport rates) depend on both time and space. *Stationarity* or *steady state** is achieved as soon as the variables of the system do not depend on time anymore. They do, importantly, still vary in space, which is the crucial difference to the third mode. An *equilibrium* process denotes the situation when each (intensive) variable (e.g., temperature, pressure, chemical potential) achieves the same value at any point in time and space, where a homogeneous environment has been tacitly assumed. That implies from a rather macroscopic perspective that the net flux of heat or particles is strictly zero at any point and time. On

*Steady-state situations are not covered by the present work. They are included for reasons of completeness only.

the molecular scale, however, the notion that the transport rate in forward direction of any of the (three Cartesian) coordinates equals the backward rate at any time is more adequate (microscopic reversibility).

Two main types of mass transport are distinguishable: convection and diffusion. Section 3.1 briefly describes the former type which is not being investigated in the present work. Subsequently, diffusion phenomena are highlighted (Section 3.2) and the mathematical description of diffusion is provided, together with analytical solutions to Fick's laws. A special focus lies here on surface-barriers boundary conditions which are of central importance to this work.

3.1 Convective Mass Transport

*Convective mass transport** relates to the phenomenon where a macroscopic flow—no matter if laminar, turbulent, or circulating—is observable. That is, a directed, non-negligible movement of any one volume element establishes for the system in question. Importantly, the flow is the result of one of the two possible *driving forces*, or both together: potential differences due to height differences in the gravitational field of the earth and mechanical forces.

Classical examples of flow caused by potential differences are rivers descending from mountains toward the sea and ancient aqueducts for fresh water supply from a lake to a village or town. Mechanically caused flow is usually due to pressure differences and can, for example, be generated by fans and pumps (Figure 3.1a) in a pipeline or by a stirrer in a reactor (Figure 3.1b). Macroscopic convective mass transport may be described by the Navier–Stokes equations⁸³ or simplifications thereof: the Euler equations, the Stokes equations, and the Bernoulli equation. All of these equations share the starting point of their derivation: the momentum balance of the fluid.⁸³ Furthermore, they all encompass both influences, potential and pressure differences and are indeed approximations of the Boltzmann equations.

The Euler equations describe flow of incompressible fluids (“inviscid”) and can be applied to important design problems such as flow around airplane wings and to crucial natural processes like ocean currents.⁸³ On the other hand, swimming microbes and flow through macroporous media can

*The more simple terms “fluid flow”⁸¹ and “fluid dynamics”⁸² are frequently adopted instead of convective mass transport.⁸³ The author of this work chose the latter to underline the equivalence of heat and mass transfer problems because convection or convective transport, as a standalone expression, is usually related to heat transfer phenomena.

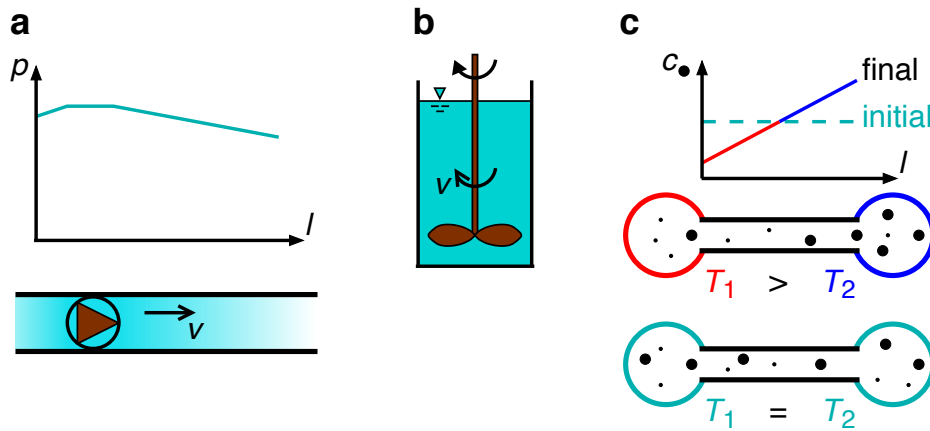


Figure 3.1: Convection can, for example, be caused by generating an excess pressure by a pump along a pipeline (a) or by a stirrer rotating in a vessel (b). Thermal diffusion is nonconvective transport triggered by temperature differences (c).

be modeled with the Stokes equations.⁸³ Because the Stokes equations assume negligible acceleration, they are also known as “creeping flow equations”.⁸³ On the other hand, the fact that the Navier–Stokes equations incorporate an additional friction term compared to the Euler equations gives them the byname “viscous flow”.

3.2 Diffusion

Diffusion or diffusional mass transport is in the simplest and most original way defined as transport caused by concentration differences. That assumes the condition of negligible pressure, height, and temperature differences and, furthermore, the presence of a fluid mixture. Transport takes here place from regions of higher concentration toward lower concentrations and is exclusively caused by random molecular movements similar to Brownian motion.⁸³ Diffusing molecules are therefore said to perform a *random walk*. The scheme in Figure 3.2 highlights an important aspect in this context: the center of mass of all diffusing molecules together does not move; in contrast to convective mass transport.

Temperature and pressure differences as well as external forces can also trigger diffusion which gives the individual phenomena their respect-

ive names: *thermal diffusion** (Figure 3.1c), *pressure diffusion*, and *forced diffusion*.⁸³ Ordinary diffusion is consequently also known as *concentration diffusion*⁸³ and it is thus instructive to mention that the term diffusion will always relate to this type in the upcoming chapters. Finally, it should be pointed out that a rigorous description of diffusion encompassing all of these effects exists. It utilizes chemical potential differences as driving force and it is known as *Maxwell–Stefan* (MS) formulation.² Importantly, multicomponent diffusion can be modeled in a straightforward manner by the MS formulation,⁹⁰ which makes possible the flawless incorporation into reaction-diffusion problems.²⁰

Diffusion can be subdivided into transport diffusion and self-diffusion. Consider Figure 3.2 to realize the difference between the two types. In the case of *transport diffusion*, the two species (blue dots and red circles) are truly different molecules. That is, they should (significantly) differ in their molecular weight and/or structure. *Self-diffusion*, on the other hand, relates to the special situation when a substance is diffusing in itself. In that case, the dots and circles in Figure 3.2 represent in fact the same type of molecule. Because the dots carry a tag, mark, or tracer (blue color) that does yet not change molecular properties, self-diffusion is also known as tracer diffusion.

Single-component transport diffusion into a porous host material resembles convective transport because of a directed movement of the fluid molecules' center-of-mass. However, such cases should rather be viewed as exceptional binary diffusion situations, where the immobile porous host is species one and the mobile fluid molecules represent the second component.¹ The flux is here defined with respect to the coordinates of the solid which usually rests at a fixed position in the experimental cell.¹ Because the mass of the host is much larger than the mass of the guests, it is obvious that the combined center-of-mass (host+guests) hardly moves, thus indicating diffusional rather than convective transport. Also, the fact that pressure is not definable in a micropore⁹¹ hints at diffusive transport. Finally, height influences vanish simply because of the small host size and the much stronger

*Thermal diffusion,^{84,85} sometimes also referred to as thermodiffusion,^{86,87} thermophoresis^{86,87} or Soret effect,^{85–87} denotes mass transport that is caused by the presence of temperature gradients. Consider a binary gas mixture that is initially uniformly distributed between two bulbs which are connected with an isolated capillary (Figure 3.1c). Both bulbs experience immediate temperature jumps so that the left bulb is hotter than the right one. As a reaction to this perturbation, the heavier species (larger molecular weight) usually tends to go to the colder region and the lighter one to the hotter; particularly when dilute gas mixtures are considered.⁸³ Promising applications exploiting this phenomenon are currently emerging such as microscale thermophoresis.^{88,89} That is an equilibrium technique for experimental analysis of molecular interactions of a broad range of molecules in bulk solution.⁸⁹

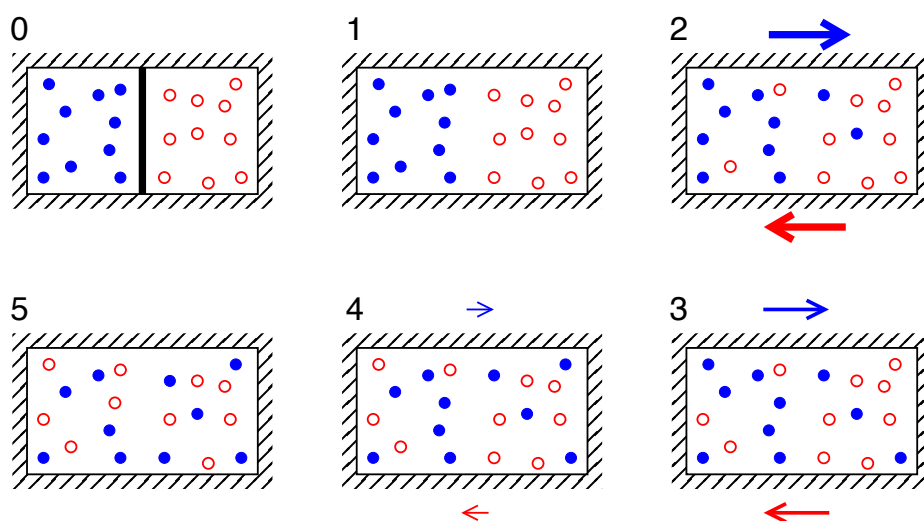


Figure 3.2: Schematic representation of two (fluid molecule) species, blue dots and red circles, diffusing in one another. At step 0, the species are separated by an impermeable wall which is removed in step 1. The largest flux of blue dots (from left to right) and red circles (from right to left) is observable at the earliest stage (2). The fluxes decrease as time proceeds which is represented by vanishing arrow size (2–4). Finally, the system reaches equilibrium (5) so that both species are uniformly distributed over the entire container. Note that pressure and temperature differences within the container did not contribute to the exchange of different species.

force field experienced by the fluid molecules inside the pores compared to the strength of earth’s gravitational field.

3.2.1 The Mathematics of Diffusion

The description of diffusion was hitherto based on a molecular model of the fluid because this seemed more intuitive to picture and thus to help understand the phenomena. For the following mathematical treatment, it has to be pointed out that a continuum model forms the basis. As a result, a homogeneous structureless environment is assumed,⁹² which seems to contrast molecular diffusion in a nanoporous host structure. In Chapter 11, this discrepancy will be investigated. Furthermore, note that instationary diffusion in a plane sheet will be covered in this subsection only and that the corres-

ponding analytical solutions were taken from Section 4.3 of Reference 92.*

The most basic diffusion equations are Fick's[†] laws. The first law connects the rate of transport at any point along the sheet [i.e., flux $j(z)$ in molecules or moles per unit area and unit time at position z] with the driving force (concentration gradient $dc(z)/dz$) via a constant of proportionality (diffusion coefficient D):

$$j(z) = -D \cdot \frac{dc(z)}{dz}. \quad (3.1)$$

The minus sign reiterates that Fickian diffusion always proceeds in the direction of lower concentrations.

Fick's second law states how concentration fluctuations decay with time t .⁹⁵

$$\frac{\partial c(t, z)}{\partial t} = D \cdot \frac{\partial^2 c(t, z)}{\partial z^2}. \quad (3.2)$$

Accumulation of matter [$\partial c(t, z)/\partial t$] is directly proportional to the degree of convexity of the concentration profile [$\partial^2 c(t, z)/\partial z^2$]. Consequently, any concave part of a concentration profile will give rise to negative accumulation so that matter will diffuse out of this segment.

The first analytical solution to Fick's second law in a plane sheet considered in this work assumes that the initial concentration throughout the sheet is zero except for the surface. There, a constant concentration value (c_{final}) is maintained during the entire diffusion process (boundary condition). The resulting solution of the symmetric concentration profiles (Figure 3.3a) follows:

$$\frac{c(t, z)}{c_{\text{final}}} = 1 - \frac{4}{\pi} \sum_{i=0}^{\infty} \frac{(-1)^i}{2i+1} \cdot \exp \left[-D(2i+1)^2 \pi^2 t / \delta^2 \right] \cdot \cos \frac{(2i+1)\pi z}{\delta}, \quad (3.3)$$

where δ denotes the thickness of the sheet. These concentration profiles, although analytical in nature, have to be determined with the aid of a computer because of the infinite sum. The present work used as an abort criterion the detection of the first instance (i.e., addition of a further summand) when

*The title of Subsection 3.2.1 deliberately coincides with the title of the seminal book by Crank⁹² in recognition of his contributions to diffusion theory and the impact that they had on this work.

[†]Fick, Adolf Eugen: *September 3, 1829, in Kassel, Germany; † August 21, 1901, in Blankenberge, Belgium; physician and physiologist. Apart from his diffusion laws, Fick is known for another important principle: the Fick principle. It quite intuitively states that the blood flow to an organ can be calculated using a marker substance consumed by that organ.^{93,94}

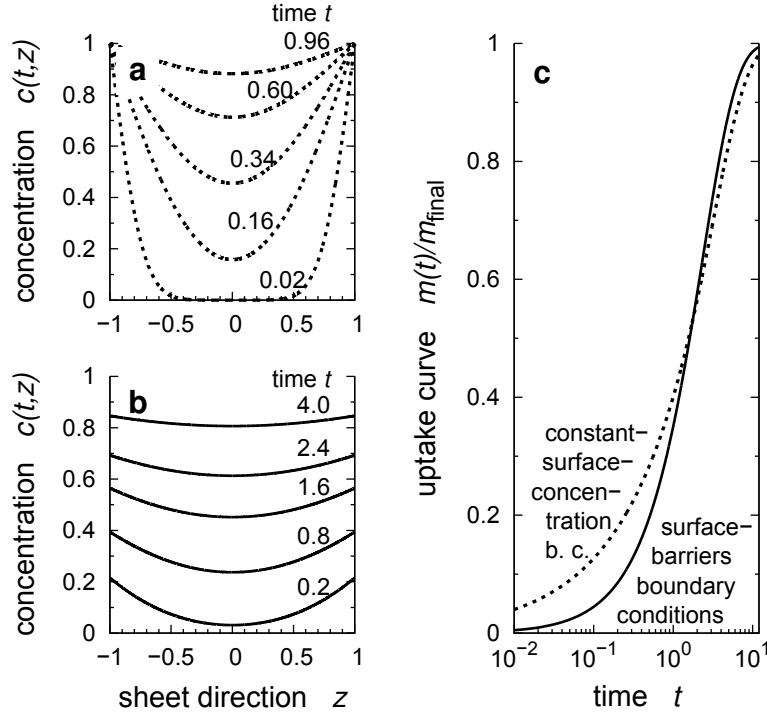


Figure 3.3: Analytical solutions of the diffusion equations: concentration profiles obtained with constant-surface-concentration boundary conditions (a) and with surface-barriers boundary conditions (b), respectively, as well as uptake curves under the use of both boundary conditions (c); $c_{\text{final}} = 1$, $D = 1$, $\alpha = 0.5$, $\delta = 2$.

the maximal relative change in the normalized c -profile (and uptake curve as described below) was smaller than 10^{-12} .

Diffusive transport can also be monitored in an integral manner. Instead of concentration profiles, that can be regarded as a local (because spatially resolved) way of rating the transport progress, so-called uptake curves are frequently used in diffusion experiment analysis and process design. An uptake curve gives the amount of mass that has already entered the sheet, $m(t)$, in comparison to the saturation value of diffusing substance, m_{final} , that is, after infinite time. It is in fact the spatial integral of the above concentration profiles (Equation 3.3) and thus reads:

$$\frac{m(t)}{m_{\text{final}}} = 1 - \sum_{i=0}^{\infty} \frac{8 \cdot \exp \left[-D(2i+1)^2 \pi^2 t / \delta^2 \right]}{(2i+1)^2 \pi^2}. \quad (3.4)$$

An example uptake curve is displayed in Figure 3.3c (dotted line).

The boundary conditions of constant surface concentration is only an approximation. A more realistic approach is to explicitly model the transport at the surface via a phenomenological ansatz such as:

$$j(t, \pm\delta/2) = \alpha \cdot [c(t, \pm\delta/2) - c_{\text{final}}]. \quad (3.5)$$

Similar to Equation 3.1, the flux* equals the driving concentration difference multiplied by a constant of proportionality: the surface permeability α . That are these boundary conditions of the diffusion equations that represent the core of the present work. Crank called them *surface evaporation* conditions.⁹² In the present work, they are however referred to as *surface barrier* boundary conditions or simply surface barriers because that term is predominantly encountered in the current literature. Furthermore, it puts emphasis on the fact that the flux at the sheet boundary is usually (much) smaller than a comparable flux in the interior of the sheet, under otherwise similar conditions.

The resulting analytical concentration profiles using the surface barrier boundary conditions follows:

$$\frac{c(t, z)}{c_{\text{final}}} = 1 - \sum_{i=1}^{\infty} \frac{2L \cdot \exp[-\gamma_i^2 Dt / (\delta/2)^2]}{(\gamma_i^2 + L^2 + L) \cos \gamma_i} \cdot \cos[\gamma_i z / (\delta/2)], \quad (3.6)$$

where γ_i is the i -th positive root of $\gamma \tan \gamma = L$ with $L = (\delta/2)\alpha/D$. Figure 3.3b shows example profiles. The corresponding analytical uptake curve (solid line in Figure 3.3c) is given by:

$$\frac{m(t)}{m_{\text{final}}} = 1 - \sum_{i=1}^{\infty} \frac{2L^2 \cdot \exp[-\gamma_i^2 Dt / (\delta/2)^2]}{\gamma_i^2 (\gamma_i^2 + L^2 + L)}. \quad (3.7)$$

Finally, an important equation to diffusion of adsorbed matter links the transport diffusion coefficient, D_T , to the corrected diffusion coefficient, D_C :¹

$$D_T = \Gamma \cdot D_C. \quad (3.8)$$

The conversion factor Γ , known as the thermodynamic correction factor, is defined for single component adsorption under isothermal conditions by the change in the logarithm of the fugacity, $\partial \ln f$, with change in logarithm of equilibrium concentration in the adsorbed zeolite phase, $\partial \ln c_{\text{eq}}$:

$$\Gamma \equiv \left. \frac{\partial \ln f}{\partial \ln c_{\text{eq}}} \right|_T. \quad (3.9)$$

*Here, two fluxes are in fact highlighted: the flux at the left-hand end of the sheet (i.e., at $z = -\delta/2$) and the one at the right side ($z = +\delta/2$).

The thermodynamic correction factor can, for example, be obtained from an adsorption isotherm by numerical differentiation.

Equation 3.8 originates from deriving the diffusion equations on the basis of an energy balance where the chemical potential driving force is opposed by a friction force,¹ and because of sharing the same starting point the corrected diffusivity equals the Maxwell–Stefan diffusivity.

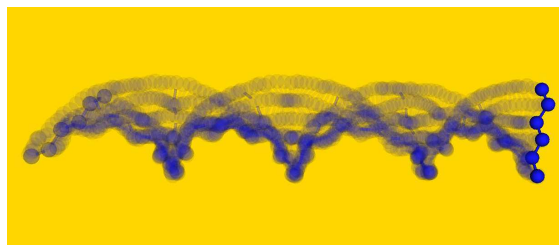
From a scientific point of view, Equation 3.8 provides an ideal means to investigate diffusion phenomena because the relative significance of thermodynamic effects (Γ) and mobility effects (D_C) on the transport diffusivity can be extracted.¹ The particular importance of Equation 3.8 to the present work stems however from the fact that conventional equilibrium molecular dynamics simulations provide data that can be analyzed for the corrected diffusion coefficient (Section 4.3). On the other hand, experimental techniques such as uptake rate measurements (Section 5.1) and interference microscopy (Section 5.2) yield transport diffusion coefficients. Hence, the equation can be regarded as an interface between measurements and molecular simulations, making possible a direct comparison.

All three quantities, that is, D_T , D_C , and Γ , are usually (strong) functions of guest molecule concentration c_{eq} . Therefore, it is noteworthy that many authors in zeolite science prefer to present diffusion coefficients as functions of loading (θ), that is, in molecules per unit cell or cavity, and that both quantities are directly related ($\theta \propto c_{\text{eq}}$). Clearly, Equation 3.8 does not change if c_{eq} is substituted by θ .

Molecular Simulations

4

Molecular simulations performed by a computer are similar to experiments conducted by a person in a laboratory. In both cases, an observation space has to be defined or created. In both cases, one needs to carefully prepare and conduct a measurement. In



both cases, measurements are usually carried out in a timely manner where a detector (or sampling routine) continuously records the property of interest. And in both cases, the raw data usually have to be further processed to finally yield the target quantity. Therefore, the present chapter will introduce the fundamental principles to link the behavior of many-particle systems of atoms or molecules to chemico-physical properties (Section 4.1). Subsequently, Sections 4.2, 4.3, and 4.5 will describe the different types of molecular simulations performed in this work and highlight specific preparation issues and sampling aspects. Because the first two simulation types have been exhaustively used in this work and because a special theory was predominantly employed to analyze the data, Section 4.4 is devoted to that theory. Finally, Sections 4.6 and 4.7 provide information about the models used to describe molecules and atoms as well as simulation details.

4.1 Statistical Mechanics

Connecting the behavior of atomic and molecular systems with properties that are accessible from macroscopic (or mesoscopic) measurements represents the key function of statistical mechanics to a computational scientist.

The generation of such assemblies will be the focus of subsequent sections, as much as specific aspects of statistical mechanics such as sampling procedures. In this section, the most fundamental points shall be reviewed only, where the seminal textbook by Chandler served as primary source and basis.⁹⁶

As the term suggests, statistical mechanics analyzes the dynamics of a many-body system by applying the principles of probability statistics, where classical systems are considered in the present work only. An individual state of such a system is fully defined by the N coordinate vectors $\mathbf{r}_1, \mathbf{r}_2, \dots, \mathbf{r}_N$ (i.e., a point in *configuration space*) and their N conjugated momenta $\mathbf{p}_1, \mathbf{p}_2, \dots, \mathbf{p}_N$ (a point in *momentum space*) of the N atoms, together defining a point in the so-called *phase space*:

$$(\mathbf{r}^N, \mathbf{p}^N) \equiv (\mathbf{r}_1, \mathbf{r}_2, \dots, \mathbf{r}_N; \mathbf{p}_1, \mathbf{p}_2, \dots, \mathbf{p}_N). \quad (4.1)$$

Assuming that an initial state is provided and that successive states can be generated in a physically meaningful manner enables the generation of a trajectory of the system on a surface of phase space by fixing a small number of variables. For example, when the number of particles N , the volume V , and the energy E of the system are being given values, an MD simulation can compute the trajectory of the system from the starting point onwards. Hence, N , V , and E control the entire further behavior of the high-dimensional system. If the trajectory visited all states of phase space consistent with the constraints imposed (N , V , E) and the property of interest A had been measured N_{samp} times then one would calculate the observed (time) average value \bar{A} as:

$$\bar{A} = \frac{1}{N_{\text{samp}}} \cdot \sum_{i=1}^{N_{\text{samp}}} A_i, \quad (4.2)$$

where A_i is the value from the i -th measurement.

The N_{samp} single measurements can now be divided into N_{groups} groups, each of which is characterized by comprising measurements that yielded the same value A_ν . Hence, each measurement group has a well-defined number of members, N_ν , or, in other words, each group value A_ν exhibits a characteristic probability, $P(A_\nu)$, to have been observed:

$$P(A_\nu) = P_\nu = \frac{N_\nu}{N_{\text{samp}}}. \quad (4.3)$$

Equation 4.2 can now be rewritten to:

$$\bar{A} = \sum_{\nu=1}^{N_{\text{groups}}} P_\nu \cdot A_\nu \equiv \langle A \rangle, \quad (4.4)$$

which defines $\langle A \rangle$, the *ensemble* average of A . An ensemble is the collection of all microstates consistent with the constraints imposed on the experiment (here: fixed N, V, E). Equation 4.4 has therefore tacitly introduced a central theorem of statistical mechanics: ergodicity. The ergodicity theorem states that if one takes samples (or makes measurements) very often (or over a very long period) the corresponding average, \bar{A} , will equal the ensemble average $\langle A \rangle$, that is, time average and ensemble average are equivalent. Of course, successive samplings (or measurements) should be uncorrelated so that the time needed to take an individual sample (or perform the measurement) is required to be (much) shorter than the interval between two successive samplings.

The most central point of statistical mechanics also follows directly from Equation 4.2 and 4.4: each microstate in a isolated system of fixed N, V , and E is equally likely to occur when the system rests at thermodynamic equilibrium. Hence:

$$P(\mathbf{r}_1^N, \mathbf{p}_1^N) \Big|_{N,V,E} = P(\mathbf{r}_2^N, \mathbf{p}_2^N) \Big|_{N,V,E} = \dots \quad (4.5)$$

If $\Omega(N, V, E)$ denotes the number of microstates that conform with the macroscopic constraints of fixed (or rather chosen) N, V , and E , then the probability, P_ν , of each and every microstate of that ensemble is given by:

$$P_\nu = 1/\Omega(N, V, E). \quad (4.6)$$

Before continuing with implications following from Equation 4.6, two definitions have to be given. First, the statistical mechanical definition of entropy, S :

$$S = k_B \cdot \ln \Omega(N, V, E), \quad (4.7)$$

which is consistent with the variational statements of the second law of thermodynamics.⁹⁶ Furthermore, the thermodynamical definition of temperature, $(\partial S/\partial E)|_{N,V} \equiv 1/T$, leads to the introduction of β , which is usually referred to as the reciprocal temperature:

$$\beta = \frac{1}{k_B T} = \frac{\partial \ln \Omega}{\partial E} \Big|_{N,V}. \quad (4.8)$$

In the two preceding equations, k_B is the Boltzmann constant.* Because temperature can only be positive, $\Omega(N, V, E)$ has to be a monotonic increasing function of E .

*Boltzmann, Ludwig Eduard: *February 20, 1844, in Vienna, Austria; † September 5, 1906, in Duino, Italy; physicist. Boltzmann is recognized as the “inventor” of statistical mechanics. It is thus not surprising that Equation 4.7 is engraved on his tombstone in Vienna, using only slightly different variables ($S = k \cdot \log W$).⁹⁷

The relations and concepts presented form the basis from which all other thermodynamic equilibrium properties can be derived.⁹⁶ The hitherto considered ensemble with fixed variables N , V , and E is called *micro-canonical* ensemble. Usually, it is however desirable to investigate systems with different constraints, where the *canonical* ensemble with fixed temperature instead of energy (NVT ensemble) is probably the most exhaustively studied one. Its statistical mechanical behavior can be derived by imagining a large micro-canonical ensemble of total energy E . In this system, there is a small subsystem (the actually considered NVT ensemble) with “instantaneous” energy E_ν . The remainder of the large system is called heat bath and has obviously an energy of $E_{\text{bath}} = E - E_\nu$. Its number of states $\Omega_{\text{bath}}(E - E_\nu)$ determines now the probability that the subsystem is in a state of energy E_ν :

$$P_\nu = \frac{\Omega_{\text{bath}}(E - E_\nu)}{\sum_j \Omega_{\text{bath}}(E - E_j)}. \quad (4.9)$$

The fact that $E_{\text{bath}} \gg E_\nu$ yields together with Equation 4.8 and an normalization:

$$P_\nu = \frac{\exp(-\beta E_\nu)}{\sum_j \exp(-\beta E_j)} = \frac{\exp(-\beta E_\nu)}{Q}, \quad (4.10)$$

which is known as the Boltzmann distribution function and which defines the canonical partition function, Q :

$$Q \equiv \sum_j \exp(-\beta E_j). \quad (4.11)$$

The relationship between the average energy, $\langle E \rangle$, and the partition function highlights its central importance to statistical mechanics:

$$\langle E \rangle = - \left. \frac{\partial \ln Q}{\partial 1/(k_B T)} \right|_{N,V}. \quad (4.12)$$

An important aspect is that both energy and temperature fluctuate about a mean value in the canonical ensemble. The respective magnitudes of fluctuations can be estimated so that one obtains for the energy, for example:

$$\frac{\sqrt{\langle [E - \langle E \rangle]^2 \rangle}}{\langle E \rangle} \propto \mathcal{O}\left(\frac{1}{\sqrt{N}}\right). \quad (4.13)$$

This indicates also that the energy attains a strictly constant value for a large enough system. In other words, results from the micro-canonical and

the canonical ensemble of same N and V and comparable E and $\langle E \rangle$ become the more alike the larger the systems get.

The canonical partition function in the form of Equation 4.11 is applicable to cases with discrete energy levels (quantum systems). The corresponding definition in the limit of classical mechanics is obtained by integrating over phase space and assuming that the potential energy is independent of the momenta, which is true for the models used in this work (cf., Section 4.6):

$$Q \equiv \frac{1}{h^{3N} N!} \cdot \int \exp[-\beta K(\mathbf{p}^N)] d\mathbf{p}^N \cdot \int \exp[-\beta U(\mathbf{r}^N)] d\mathbf{r}^N, \quad (4.14)$$

where h denotes the Planck constant and K and U the kinetic and the potential energy of the system, respectively. The configurational part of the partition function, Z , is therefore given by:

$$Z \equiv \int \exp[-\beta U(\mathbf{r}^N)] d\mathbf{r}^N. \quad (4.15)$$

The term $\exp[-\beta U(\mathbf{r}^N)]$ is also known as Boltzmann factor which is proportional to the probability of observing the particular configuration. Note that the factor preceding the integrals in Equation 4.14 accounts for the quantum mechanical nature of the many-body system (here: N indistinguishable particles).

In addition to the two mentioned ensembles, the *grand-canonical* (GC) ensemble is of relevance to the present work. Fixed chemical potential μ , volume V , and temperature T represent the thermodynamic constraints characterizing the GC ensemble. Its partition function, Ξ , can be derived in a similar manner to the canonical ensemble and reads:⁹¹

$$\Xi \equiv \sum_{N=0}^{\infty} \frac{\exp(\beta\mu N) V^N}{\Lambda^{3N} N!} \int \exp[-\beta U(\mathbf{r}^N)] d\mathbf{r}^N. \quad (4.16)$$

Again, N indistinguishable particles were here assumed and Λ denotes the de Broglie wavelength.

4.2 Monte Carlo

Monte Carlo (MC) methods are applicable to a wide variety of scientific, industrial, and even economic and financial problems.⁹⁸ Their usability stems from the possibility to determine numerical solutions to mathematical problems that are otherwise not manageable (e.g., high-dimensional integrals with

unknown analytical solutions). The procedure is entirely random in nature as the name suggests (gambling in Monte Carlo), which, however, raises problems when MC is applied in a direct manner to (finite) molecular systems, as the ones studied in the present work. What is usually done in such cases is the generation of successive configurations (a chain) by perturbing either the position, rotational orientation and conformation of a single molecule (or atom) from one configuration to the next one in the chain. To illustrate the problem emerging with just any random perturbation to the configuration and definitive acceptance of this trial perturbation or move, consider the example of a canonical ensemble and the aim to calculate a reliable estimate of the ensemble average of A . $\langle A \rangle$ can be expressed in the limit of classical mechanics as following phase-space integral:⁹¹

$$\langle A \rangle = \frac{\int A(\mathbf{r}^N, \mathbf{p}^N) \exp\left[-\beta \mathcal{H}(\mathbf{r}^N, \mathbf{p}^N)\right] d\mathbf{r}^N d\mathbf{p}^N}{\int \exp\left[-\beta \mathcal{H}(\mathbf{r}^N, \mathbf{p}^N)\right] d\mathbf{r}^N d\mathbf{p}^N}. \quad (4.17)$$

where $\mathcal{H}(\mathbf{r}^N, \mathbf{p}^N)$ denotes the Hamiltonian, which gives the total energy [$U(\mathbf{r}^N) + K(\mathbf{p}^N)$] of the system on the basis of the coordinates and momenta. Properties that depend on the momentum part alone can be treated analytically, thus not posing any severe problems. However, properties that depend on the configuration part have to be evaluated differently because they cannot be solved analytically. A valid, yet naive approach would, for example, span a grid over configuration space and calculate all individual values of A and the potential energy U of the grid points and then numerically integrate those according to Equation 4.17. But that approach is not efficient at all.

As the previous section uncovered, any microstate with high Boltzmann factor and thus low energy is, first, more likely to be observed than a microstate with lower Boltzmann factor and thus higher energy, and, second, it has therefore a higher contribution on the average of A than the high-energy microstate. In other words, the weight of a given microstate on the average value of some property A increases with decreasing energy. This realization opens a promising route how successive microstates (i.e., a chain of states) should be generated. Instead of creating entirely new microstates so that most states will exhibit a negligibly small weight, generate a chain that consists of as many microstates with high weights as possible. That is achieved with so-called *importance sampling*, where the weight is generally some arbitrary function.⁹¹ The idea to specifically use the Boltzmann factor as weight is due to Metropolis *et al.*⁹⁹

The *Metropolis* method, in essence, casts the original problem of comput-

ing a configuration-space integral into the problem of obtaining an uncorrelated chain of significant, similarly probable microstates (*Markov chain*). The arithmetic average of all $A(\mathbf{r}_i^N)$ of that chain equals (in good approximation) the ensemble average $\langle A \rangle$. The method can be derived by imposing the strong detailed balance condition, which requires that the average number of accepted moves from an old state o to a new state n [$\mathcal{N}(o) \cdot \pi(o \rightarrow n)$] exactly equals the reverse moves $n \rightarrow o$ [$\mathcal{N}(n) \cdot \pi(n \rightarrow o)$]. Here $\mathcal{N}(i)$ denotes the probability density of state i and $\pi(i \rightarrow j)$ the transition probability to go from state i (\mathbf{r}_i^N) to state j (\mathbf{r}_j^N). As the probability of any transition $i \rightarrow j$ is given by the product of the probability, $\alpha(i \rightarrow j)$, to perform the respective *trial* move and the probability, $\text{acc}(i \rightarrow j)$, to accept this trial move and because the simulations usually ensure that $\alpha(i \rightarrow j) = \alpha(j \rightarrow i)$, detailed balance yields:

$$\mathcal{N}(o) \cdot \text{acc}(o \rightarrow n) = \mathcal{N}(n) \cdot \text{acc}(n \rightarrow o). \quad (4.18)$$

Therefore and because $\mathcal{N}(i) \equiv \exp[-\beta U(i)]/Z$ the ratio of acceptance probabilities is given by:

$$\frac{\text{acc}(o \rightarrow n)}{\text{acc}(n \rightarrow o)} = \frac{\mathcal{N}(n)}{\mathcal{N}(o)} = \exp\left\{-\beta[U(n) - U(o)]\right\}. \quad (4.19)$$

Although other choices are possible,⁹¹ Metropolis *et al.* set $\text{acc}(o \rightarrow n) = \mathcal{N}(n)/\mathcal{N}(o)$ and thus $\text{acc}(o \rightarrow n) = \exp\{-\beta[U(n) - U(o)]\}$ if $\mathcal{N}(n) < \mathcal{N}(o)$ and thus if $U(n) > U(o)$; otherwise, that is, if $U(n) \leq U(o)$, the acceptance probability was unity.

In summary, Metropolis-type Monte Carlo methods provide a compelling means to generate a chain of random yet important microstates of the molecular system under study. The remainder of this section briefly provides the trial types and the respective acceptance probabilities used in the present work, as well as properties sampled during the simulations. For more theoretical details and a good guide for implementation of MC (and MD) algorithms, the textbook by Frenkel and Smit can be recommended,⁹¹ which was the primary source for writing the present and the next section.

Translational displacement trials have been performed in all MC simulations, which, first, selected one of the N molecules at random (i) and, then, calculated the energy of the system, $U(\mathbf{r}_o^N)$. The old position of molecule i , $\mathbf{r}_{i,o}$, was changed by a small displacement $\Delta\mathbf{r}_i$ to $\mathbf{r}_{i,n} = \mathbf{r}_{i,o} + \Delta\mathbf{r}_i$, and the energy $U(\mathbf{r}_n^N)$ of the new configuration was calculated. Finally, this trial displacement was accepted with a probability $\text{acc}_{\text{displ}}(o \rightarrow n)$:

$$\text{acc}_{\text{displ}}(o \rightarrow n) = \min\left(1, \exp\left\{-\beta[U(\mathbf{r}_n^N) - U(\mathbf{r}_o^N)]\right\}\right). \quad (4.20)$$

Rotational trials were performed for all molecules consisting of more than a single bead (e.g., ethane, ethene, propane), where a random rotation about the center of mass yielded the new relative position of the randomly picked molecule. The procedure and the acceptance probability, acc_{rot} , for such a trial is thus analogous to translational displacement trials.

An essential aspect of Metropolis-type Monte Carlo methods represents the multi-counting requirement of properties of the old state for calculating simulation averages, when new states are progressively declined. This is, because, otherwise, the correct equilibrium probability distribution of micro-states will not be reproduced and the computed average may thus differ from the true ensemble average.

4.2.1 Grand-Canonical Monte Carlo

A constant chemical potential that fluctuates around an imposed value is achieved by making possible a varying number of molecules. Therefore, molecule insertion and molecule deletion trial moves have to be included into the Monte Carlo event library. It is common practice to use the so-called configurational-bias Monte Carlo method (CBMC),⁹¹ which inserts a new molecule atom by atom into the simulation box. Central to applying CBMC is the generation of multiple trial positions for each atom and the differentiation between internal (u^{intern}) and external (u^{extern}) contributions to the molecule's potential energy (see Section 4.6).

Usually, a single trial is performed for the very first atom of the molecule. The rest of the molecule is then grown atom by atom along the chain, where k trial positions are generated per atom according to the Boltzmann weight of the internal interactions. One out of the k trial positions $\mathbf{r}_{i,1}, \dots, \mathbf{r}_{i,k}$ is chosen for atom i , say trial j , with a probability $P(\mathbf{r}_{i,j})$ to further grow the molecule, which is given by:

$$P(\mathbf{r}_{i,j}) = \frac{\exp[-\beta u^{\text{extern}}(\mathbf{r}_{i,j})]}{\sum_{l=1}^k \exp[-\beta u^{\text{extern}}(\mathbf{r}_{i,l})]}. \quad (4.21)$$

The denominator is known as the Rosenbluth weight (w_i) of atom i . After the entire molecule has been grown the Rosenbluth factor, W_{ros} , of the trial insertion is computed:

$$W_{\text{ros}} = \prod_{i=1}^{N_{\text{atoms}}} w_i, \quad (4.22)$$

and the normalized Rosenbluth factor as well:

$$\mathcal{W}_{\text{ros}} = \frac{W_{\text{ros}}}{k^{N_{\text{atoms}}-1}}. \quad (4.23)$$

The acceptance probability of the current trial insertion is then given by:⁷⁰

$$\text{acc}_{\text{ins}}(o \rightarrow n) = \min \left[1, \frac{V}{\Lambda^3(N_A + 1)} \cdot \exp(\beta\mu) \cdot \frac{\mathcal{W}_{\text{ros},A}(n)}{\langle \mathcal{W}_{\text{ros},A}^{\text{IG}} \rangle} \right] \quad (4.24)$$

$$= \min \left[1, \frac{V\beta f}{(N_A + 1)} \cdot \frac{\mathcal{W}_{\text{ros},A}(n)}{\langle \mathcal{W}_{\text{ros},A}^{\text{IG}} \rangle} \right]. \quad (4.25)$$

The transition $o \rightarrow n$ could also be indicated for by $N_A \rightarrow N_A + 1$ because the transition is characterized by adding to the simulation box a new molecule (+1) of type A to the N_A already existing molecules of type A . $\langle \mathcal{W}_{\text{ros},A}^{\text{IG}} \rangle$ represents the average normalized Rosenbluth factor of growing a molecule of type A in vacuum (ideal gas), which has to be determined by a separate simulation prior to using the insertion trial. Note that, because GCMC is used in this work for adsorption isotherm determination, it is more practical to impose the fluid-phase pressure p instead of the chemical potential μ . The pressure needs, however, first to be converted into the corresponding fugacity, f , by an equation of state (here: Peng-Robinson) before it is incorporated into the acceptance probabilities (Equation 4.25).⁹¹

An GCMC deletion trial begins with randomly selecting the molecule to be removed. The acceptance probability for the deletion trial ($o \rightarrow n = N_A \rightarrow N_A - 1$) reads:⁷⁰

$$\text{acc}_{\text{del}}(o \rightarrow n) = \min \left[1, \frac{N_A}{V\beta f} \cdot \frac{\langle \mathcal{W}_{\text{ros},A}^{\text{IG}} \rangle}{\mathcal{W}_{\text{ros},A}(o)} \right], \quad (4.26)$$

which requires the calculation of the Rosenbluth factor of the molecule to be deleted in the old configuration. This is achieved by performing $k - 1$ instead of k trial positions per atom. The atom position in the old configuration is then used as the missing k th trial positions for determination of the Rosenbluth weights.

CBMC trials are in fact also used in NVT -MC simulations for partial and full regrow trials. The acceptance probability is:

$$\text{acc}_{\text{regr}}(o \rightarrow n) = \min \left[1, \frac{\mathcal{W}_{\text{ros}}(n)}{\mathcal{W}_{\text{ros}}(o)} \right]. \quad (4.27)$$

Adding such trials enables the sampling of different molecule configurations and can help the systems to escape metastable regions of configuration space. Furthermore, CBMC forms the basis of other MC trial moves.¹⁰⁰

The importance of grand-canonical Monte Carlo (GCMC) lies in the fact that the average number of molecules in the simulation box can be computed as a function of (external) pressure, which facilitates the determination of adsorption isotherms. Importantly, mixture isotherms can be obtained in a straightforward way, which is not as easily done in experiments.

If the low pressure regime is of interest only, the Henry coefficient, K_H , can be calculated instead of the entire (single-component) isotherm, representing in fact the slope of the isotherm. This is achieved by sampling the ratio of the average normalized Rosenbluth factors in the adsorbed phase, $\langle \mathcal{W}_{\text{ros}} \rangle$, to the one in the ideal gas phase, $\langle \mathcal{W}_{\text{ros}}^{\text{IG}} \rangle$, with the help of CBMC molecule insertion trials:⁹¹

$$K_H = \frac{1}{RT} \frac{\langle \mathcal{W}_{\text{ros}} \rangle}{\langle \mathcal{W}_{\text{ros}}^{\text{IG}} \rangle}, \quad (4.28)$$

where R denotes the ideal gas constant. It is important to stress that both simulations, in the ideal gas phase and in the adsorbed phase, are carried out with a single molecule. Another important adsorption quantity, the isosteric heat of adsorption, ΔH_{ads} , can be obtained in a similar manner:

$$\Delta H_{\text{ads}} = \langle U \rangle - \langle U^{\text{IG}} \rangle - k_B T. \quad (4.29)$$

$\langle U \rangle$ denotes the average potential energy of the single molecule in the adsorbed phase and $\langle U^{\text{IG}} \rangle$ the average potential energy in the ideal gas state.

4.3 Equilibrium Molecular Dynamics

Similar to Monte Carlo, equilibrium molecular dynamics (EMD)—or, short, molecular dynamics (MD)—is used in the present work to generate trajectories of molecular assemblies. The striking difference between the two methods is that trajectories generated by MC are probabilistic in nature whereas MD yields deterministic trajectories. This difference represents the main reason why dynamic processes can be investigated with MD but not with MC. To start the description of conventional equilibrium molecular dynamics those aspects of classical dynamics that are most important to MD are briefly reviewed.

Dynamics, denoting the study of bodies in motion and the reason why they move, is founded on Newton's equations of motion:

1. A moving body will continue to move in exactly the same manner as it is just doing [i.e., magnitude and direction of the velocity vector remains the same: $\mathbf{v}(t) = \mathbf{v}(0)$] unless a force \mathbf{f} starts acting on it.
2. If a force, $\mathbf{f}(t)$, acts on a body, the force invokes a proportionate change in momentum, $d\mathbf{p}(t)/dt$:

$$\mathbf{f}(t) = \frac{d\mathbf{p}(t)}{dt} = \frac{d}{dt} \left(m(t) \cdot \mathbf{v}(t) \right) = m(t) \cdot \frac{d\mathbf{v}(t)}{dt} + \frac{dm(t)}{dt} \cdot \mathbf{v}(t), \quad (4.30)$$

where $m(t)$ denotes the mass of the body at time t . This law, also known as the action principle, simplifies for MD because relativistic effects are usually neglected [$dm(t)/dt = 0$]:

$$\mathbf{f}(t) = m \cdot \frac{d\mathbf{v}(t)}{dt} \quad (4.31)$$

Noting that $\mathbf{v}(t) = ds(t)/dt$, Equation 4.31 suggests that both the velocity $\mathbf{v}(t)$ and the position $\mathbf{s}(t)$ of a body can be determined at any instance of time by (analytical or numerical) integration. Only, the (evolution of the time-dependent) force and initial values [$\mathbf{v}(0)$, $\mathbf{s}(0)$] need to be known.

3. The last law—the interaction principle—states that a force never occurs alone. Therefore, any force $\mathbf{f}_{i,j}$ acting on a body i due to the presence of body j always evokes a reaction: a force, $\mathbf{f}_{j,i}$ with same magnitude but opposite direction.

Analytical solutions to Newton's equations of motions can be obtained for very simple cases including few bodies only, hence, indicating the importance of numerical approaches. The laws require that any numerical integrator has to be time-reversible, area-, and energy-conserving (or rather exhibiting as little drift as possible*).⁹¹ From an efficiency point of view, the integrator should additionally be simple to implement and computationally inexpensive and it should allow for as large a time step size Δt as possible while maintaining as high accuracy as possible.⁹¹ *Verlet*-like integration schemes meet these requirements because they are symplectic. They usually exhibit moderate short-time and small long-time energy drift, are time-reversible, fast and in general do not need much memory capacities.⁹¹ In the present work, the *velocity Verlet* algorithm was used only, which works as follows. First, the new positions $\mathbf{r}_i(t + \Delta t)$ of all N bodies are computed from the

*Minimizing the drift is so important because the *Lyapunov instability* states that any integration error, no matter how small, will cause the computed trajectories to diverge exponentially from the true ones.⁹¹

current positions $\mathbf{r}_i(t)$, the current velocities $\mathbf{v}_i(t)$, and the current forces $\mathbf{f}_i(t)$ acting on each body i via:

$$\mathbf{r}_i(t + \Delta t) = \mathbf{r}_i(t) + \mathbf{v}_i(t) \cdot \Delta t + \frac{\mathbf{f}_i(t)}{2m_i} \cdot \Delta t^2. \quad (4.32)$$

Then, the forces at the new positions can be calculated. Subsequently, the new velocities $\mathbf{v}_i(t + \Delta t)$ can be calculated from the old velocities $\mathbf{v}_i(t)$, the new force $\mathbf{f}_i(t + \Delta t)$, and the old force $\mathbf{f}_i(t)$ by:

$$\mathbf{v}_i(t + \Delta t) = \mathbf{v}_i(t) + \frac{\mathbf{f}_i(t + \Delta t) + \mathbf{f}_i(t)}{2m_i} \cdot \Delta t. \quad (4.33)$$

The applicability of molecular dynamics stems from the assumption that classical dynamics of conservative systems may be rigorously extrapolated from the macrocosm to the microcosmos. Specifically, the definition of a conservative force, \mathbf{f} , is central to MD:¹⁰¹

$$\mathbf{f} = -\nabla U(x, y, z). \quad (4.34)$$

At this point, it has to be stressed that trajectories computed by MD do not represent the natural evolution of the molecular system under study. Instead, they are good approximations of *possible* trajectories (so-called shadow trajectories).^{91,102} However, the large number of case studies found in literature that have indicated good agreement between experiments and MD simulations is a strong indicator of the accuracy, reliability, and reproducibility of the method.

The most important purpose of MD simulations is to compute dynamical properties of the molecular system. In almost every case, the link between a (macroscopic) dynamical property and the molecular behavior is grounded on the assumption that Onsager's regression hypothesis, a consequence of the fluctuation dissipation theorem,⁹⁶ applies to the specific problem. The hypothesis states that spontaneous fluctuations of a system in equilibrium decay in the same manner as perturbations of the system away from equilibrium that are caused by an external force.⁹⁶ A requirement is however that the fluctuations/perturbations are not too severe (i.e., within the linear response regime).⁹⁶ Usually, the fluctuations are measured in terms of correlation functions which are then further processed or analyzed to yield the dynamical property of interest.

Consider, for example, self-diffusion and thus the Einstein equation connecting the average mean squared displacement (MSD), $\langle |\mathbf{r}_i(t) - \mathbf{r}_i(0)|^2 \rangle$, of

a single tagged molecule i with the “macroscopic” self-diffusion coefficient, D_S :

$$\left\langle |\mathbf{r}_i(t) - \mathbf{r}_i(0)|^2 \right\rangle = 6 \cdot D_S \cdot t. \quad (4.35)$$

This relationship can be obtained by considering Fick’s second law (Equation 3.2) and a correlation function, $C(\mathbf{r}, t)$, of fluctuations in the instantaneous density of the considered molecule type, $\delta\rho(\mathbf{r}, t)$:⁹⁶

$$C(\mathbf{r}, t) = \langle \delta\rho(\mathbf{r}, t) \cdot \delta\rho(\mathbf{0}, 0) \rangle. \quad (4.36)$$

Assuming that Onsager’s regression hypothesis applies here and noting that $\langle \rho(\mathbf{r}, t) \cdot \rho(\mathbf{0}, 0) \rangle \propto P(\mathbf{r}, t)$, the latter being the conditional probability distribution that the tagged molecule is found at position \mathbf{r} at time t given that it started at the origin $\mathbf{0}$ at time 0, yields:⁹⁶

$$\frac{\partial P(\mathbf{r}, t)}{\partial t} = D_S \nabla^2 P(\mathbf{r}, t). \quad (4.37)$$

The mean squared displacement is connected with the probability distribution by:

$$\left\langle |\mathbf{r}_i(t) - \mathbf{r}_i(0)|^2 \right\rangle = \int r^2 P(\mathbf{r}, t) \, d\mathbf{r}. \quad (4.38)$$

Taking the time derivative, substituting Equation 4.37 into Equation 4.38, integrating by parts twice, and realizing that $P(\mathbf{r}, t)$ is normalized, the time derivative of the MSD is given by:⁹⁶

$$\frac{d}{dt} \left\langle |\mathbf{r}_i(t) - \mathbf{r}_i(0)|^2 \right\rangle = 6 \cdot D_S, \quad (4.39)$$

which is obviously equivalent to Equation 4.35. Hence, establishing the link between Fick’s second law, which describes the dissipation of nonequilibrium concentration disturbances, with concentration fluctuations of a molecular system in equilibrium has provided an important dynamical property of the fluid molecules: the self-diffusion coefficient.

The mean squared displacement is a quantity that can be directly determined from an MD trajectory of a molecule. Therefore, the MSD opens a straightforward route to calculating the self-diffusion coefficient: fitting a linear function to the data (Figure 4.1). However, it has to be stressed that the MSD behaves initially not ideally diffusive, that is, $\langle |\mathbf{r}_i(t) - \mathbf{r}_i(0)|^2 \rangle \not\propto t$. This is, because any force acting on the tagged molecule takes a finite amount of time to change the molecule’s motion.⁹⁶ In the meantime, the molecule moves as if located in an inert space so that the displacement varies linearly with

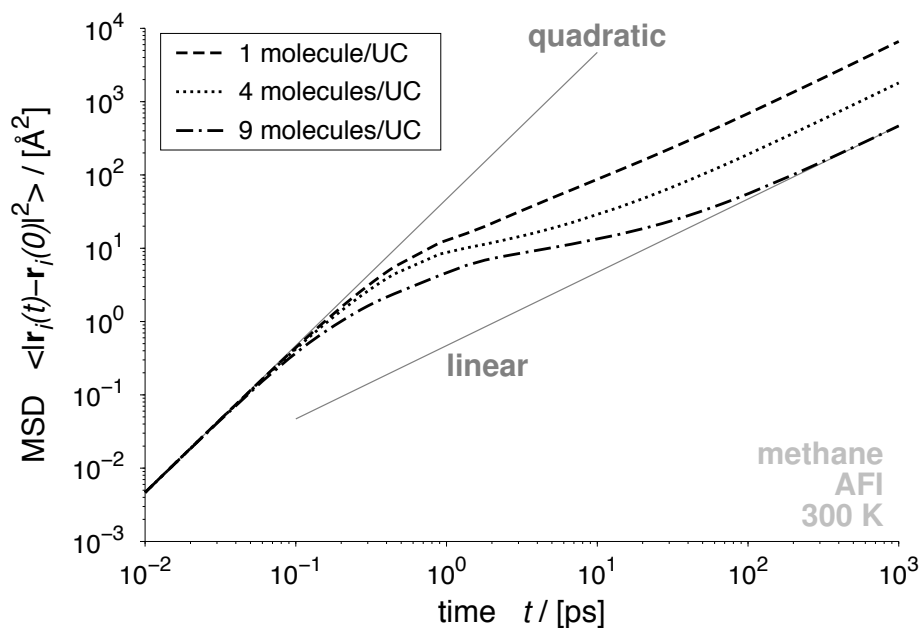


Figure 4.1: Mean squared displacement (MSD), $\langle |\mathbf{r}_i(t) - \mathbf{r}_i(0)|^2 \rangle$, of single tagged molecules as a function of time, t ; methane diffusing in a periodic AFI-type zeolite at 300 K and various loadings. A quadratic and a linear function (thin solid lines) are plotted along with simulation data to highlight the inertial and diffusive regime, respectively.

time and the mean squared displacement increases thus in a quadratic manner with time. The switchover from inertial (sometimes also referred to as ballistic) regime to the truly diffusive regime where the molecule performs a random walk⁹⁶ takes additional time. Even more so, this transition regime and its characteristic time can depend on further parameters such as the average concentration (or loading), as is appreciable by the different plots in Figure 4.1. Therefore, analysis of the MSD should always include careful visual inspection to ensure that data fitting was actually performed in the diffusive region.

To conclude the current presentation of diffusion in molecular systems note the following points. The mean squared displacement can be sampled separately for each of the three Cartesian coordinates. If ξ denotes one of the coordinates x , y , or z , the self-diffusion coefficient of the N molecules

under study in that direction is given by:

$$D_{S,\xi} = \frac{1}{2} \cdot \lim_{t \rightarrow \infty} \frac{d}{dt} \left\langle \frac{1}{N} \sum_{i=1}^N [\xi_i(t) - \xi_i(0)]^2 \right\rangle, \quad (4.40)$$

Note that the difference of the pre-factor (1/2) in comparison to the original Einstein relation (rearranged Equation 4.35: 1/6). stems from the fact that the original self-diffusivity was averaged over all three dimensions. The dimensionally averaged self-diffusion coefficient can be obtained by:

$$D_S = \frac{D_{S,x} + D_{S,y} + D_{S,z}}{3} \quad (4.41)$$

Finally, the corrected diffusion coefficient, $D_{C,\xi}$, can be computed in a similar way as the self-diffusion coefficient:

$$D_{C,\xi} = \frac{1}{2} \cdot \lim_{t \rightarrow \infty} \frac{d}{dt} \left\langle \left\{ \frac{1}{N} \sum_{i=1}^N [\xi_i(t) - \xi_i(0)] \right\}^2 \right\rangle. \quad (4.42)$$

The average over all three coordinates, D_C , (trace of diffusion tensor) is calculated in analogy to D_S (Equation 4.41).

4.3.1 Thermostats

The natural ensemble of MD simulations is the micro-canonical (constant NVE) ensemble. The transition to the canonical (constant NVT) ensemble can be achieved by using special methods that mimic a heat bath, for which reason they are also called *thermostats*. The methods slightly perturb the velocities of the molecules so that, on an average, the imposed temperature (instead of the imposed energy) is maintained because of the relationship between kinetic energy (K), molecule velocities (\mathbf{v}_i), and temperature (T):

$$K = \frac{1}{2} \cdot \sum_{i=1}^{N_{\text{atoms}}^{\text{tot}}} m_i \cdot |\mathbf{v}_i|^2 = \frac{1}{2} \cdot k_B T N_f, \quad (4.43)$$

where $N_{\text{atoms}}^{\text{tot}}$ denotes the total number of atoms ($N_{\text{atoms}}^{\text{tot}} = \sum_{j=1}^N N_{\text{atoms},j}$) and N_f the number of degrees of freedom which is usually $3N_{\text{atoms}}^{\text{tot}}$.^{*} Equation 4.43

^{*}The number of degrees of freedom was always $3N_{\text{atoms}}^{\text{tot}}$ for guest molecule temperature calculation, unless globally acting thermostats such as velocity scaling or the Nosé–Hoover chain were used where $N_f = 3(N_{\text{atoms}}^{\text{tot}} - 1)$.

may lead to the impression that the best way to maintain T is rigorous scaling of the velocity vectors by a factor so as to exactly match the imposed temperature. This rather naive approach is in fact pursued in the very first phase of each MD simulation performed in this work but only with the intention to pre-equilibrate the initial configuration;⁷⁰ not for the purpose of harvesting data! That is an important point because it has been shown that this *velocity scaling* method does not yield the correct canonical distribution function.⁹¹ However, the method is still being widely used in present day simulation studies because the influence of the distribution deviation vanishes as the number of degrees of freedom approaches several hundreds to thousands.

The velocity-scaling method is an example of the class of *global deterministic* thermostats, because it works on the velocity vectors of all atoms simultaneously and in a well-defined way without introducing any randomness.⁷⁰ Another example of this class is the Nosé–Hoover chain (NHC) thermostat.^{103–105} In contrast to the scaling method, the NHC thermostat is based on an extended Lagrangian, meaning that fictitious particles (positions and velocities) are introduced in addition to the N molecules that are truly present in the simulation box. The fictitious particles take part in the interaction of the entire system because they contribute to the Hamiltonian. Therefore, the molecules are coupled to the fictitious particles via a coupling constant so that all molecules do in fact interact with one another at any time via the thermostat particles. The coupling constant quantifies here how “tightly” the molecules are coupled to the thermostat, where two points should be mentioned. First, simulating more than 100 atoms or molecules leads usually to the equivalence of results obtained from the micro-canonical and from the canonical ensemble.⁹⁶ In such a case, the influence of the coupling constant is thus expected to be minor. Second, if the coupling constant turns out to yet have a (strong) influence, which can be uncovered by a simple parameter study, that is a clear indicator that the constant was chosen inappropriate and has to be readjusted. While that may, at first sight, seem trivial but also arbitrary, the reader is reminded that an experimenter in the laboratory would go for precisely the same route with her/his experimental system and setup parameters. The implementation of the thermostat⁷⁰ followed the instructions given by Martyna *et al.*¹⁰⁵

Apart from the first class of thermostats (deterministic and global),⁷⁰ a popular second class exists that is characterized by locally acting on individual molecules in a stochastic (i.e., random) manner. An example is the Lowe–Andersen fluid-interface collision (LA IFC) thermostat.^{106,107} Originally developed by Jakobtorweihen *et al.*^{106,107} for the specific purpose of guest diffusion in carbon nanotubes, the thermostat’s intuitive idea is that heat is

transferred from the pore atoms to the guest molecules. This is achieved by collisions which are assumed to introduce some degree of randomness into the motion of the guest molecules. The extent of this randomness can be exactly extracted^{106,107} from simulations with a flexible framework which are however much shorter than the final simulations for diffusion coefficient determination.¹⁰⁶ At this point, the striking advantage of the method comes into play: a rigid lattice can be used during the long diffusion simulations if the LA IFC thermostat is coupled to the guest molecules. That approach yields equivalent diffusion coefficients compared to flexible-framework simulations^{106,107} which can yet be obtained much faster (factor of 25 or even five orders of magnitude, depending on loading and implementation¹⁰⁶) indicating that the thermostat is both accurate and efficient.

In its original proposition,¹⁰⁶ two collision frequencies have to be determined for the LA IFC to work:

1. The parallel collision frequency Γ_z^{LAIFC} rates how often a guest molecule collides parallel to the channel axis (z) with a pore atom. It is obtained by fitting an analytical equation to the velocity autocorrelation function in z direction of a single molecule diffusing in a vibrating CNT.¹⁰⁶
2. The orthogonal collision frequency, $\Gamma_{xy}^{\text{LAIFC}}$, rates collisions perpendicular to the channel axis and is usually much larger than Γ_z^{LAIFC} in the case of CNTs.¹⁰⁶ The most reliable way to determine $\Gamma_{xy}^{\text{LAIFC}}$ represents the computation of heating curves with a flexible CNT, where the temperature response of the guest molecules to a T jump of the pore atoms is monitored in a timely manner.¹⁰⁶ The curves are compared to corresponding data from rigid CNT simulations with Γ_z^{LAIFC} as described above and varying $\Gamma_{xy}^{\text{LAIFC}}$, where minimization of the root mean square deviation of the guest molecule temperature resembles the objective function.

Provided that it is found within a cutoff distance, $r_{\text{cutoff}}^{\text{LAIFC}}$, from the nearest pore atom, every guest molecule has after each MD step a certain probability, $\Gamma_{\xi}^{\text{LAIFC}} \cdot \Delta t$, to exchange momentum with the pore atoms in ξ direction via a “model collision”. If such a model collision occurs, the new relative velocity is taken from a Gaussian distribution, thus yielding for the ξ component of the velocity vector of molecule i ($v_{i,\xi}$):

$$v_{i,\xi}(t + \Delta t) = v_{i,\xi}(t) + \frac{m_i \cdot m_{\text{pore}}}{m_i \cdot (m_i + m_{\text{pore}})} \cdot \left(\chi_{g,1} \sqrt{\frac{k_B T}{m_{\text{pore}}}} - v_{i,\xi}(t) \right) + \chi_{g,2} \sqrt{\frac{m_i \cdot m_{\text{pore}} \cdot k_B T}{(m_i + m_{\text{pore}}) \cdot m_i^2}}, \quad (4.44)$$

where $\chi_{g,1}$ and $\chi_{g,2}$ represent independent random numbers drawn from a Gaussian distribution with zero mean and unit variance.

Again, the textbook by Frenkel and Smit⁹¹ but also the PhD thesis by Jakobtorweihen⁷⁰ shall be mentioned here because they served as superb references and guides for this section.

4.4 Transition State Theory

Transition state theory (TST) was originally developed to describe and understand the phenomenology of chemical reactions and is therefore also known as the theory of the *activated complex*.¹⁰⁸ Today TST denotes however rather a framework to describe *activated processes* in general. These processes are characterized by the system under study remaining in well-defined states for very long times and only very rarely making a transition from the current state to another (directly accessible) state. Computing frequencies of such transitions (k) is the central aim of TST. Because of this broad definition, transport of single tagged guest molecules along the pore network of a regularly ordered porous host structure with well-defined adsorption sites seems to fulfill the requirements of TST.^{109,110} Therefore, the present section takes such type of process immediately as a basis for all further explanation. Moreover, the entire presentation reflects the view of TST from the so-called *Bennett–Chandler approach*,^{111,112} where the transition frequency equals the product of two terms: the “static” free-energy and the “dynamic” reactive-flux contribution.

4.4.1 Free-Energy Contribution

Before turning to the computation of transition, hopping, or transport frequencies, a frame for measuring the progress of a transition from one state to an adjacent one has to be given. This represents in fact the first task, the calculation of free-energy profiles along the process coordinate q , which is mostly called reaction coordinate for historical reasons. Here, q denotes however the transport coordinate of a molecule hopping between adsorption sites, cages, and intersections of zeolite structures. In the following, it is assumed that the center-of-mass of the *entire* molecule identifies q rather than one specific atom (cf., References 113 and 114). In general, the coordinate is one-dimensional in the present work (more complicated cases are explicitly indicated in the later chapters) and thus coincides with one of the three Cartesian coordinates, as seen in Figure 4.2. The profiles make decisions

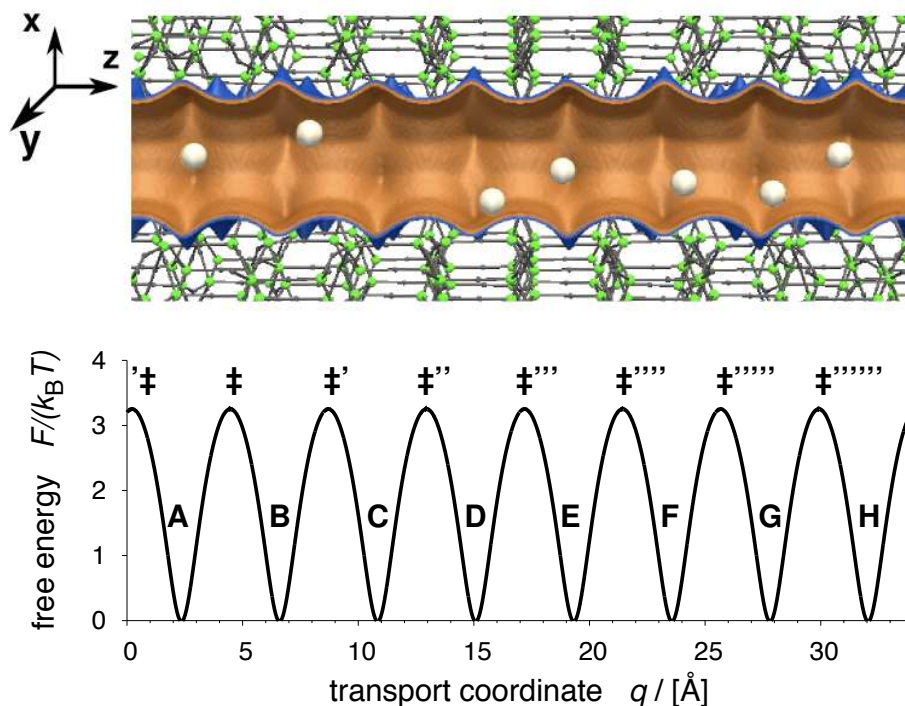


Figure 4.2: Top: snapshot of guest molecules in an AFI pore. Bottom: corresponding free-energy profile [$F/(k_B T)$] along the transport coordinate q (i.e., along pore axis z).

about stable states (adsorption sites) and dividing surfaces separating adjacent states (almost) unambiguous. Every well forming a local minimum represents the central location of a site (e.g., B in Figure 4.2). The two maxima to the left and right of a given site (\ddagger and \ddagger') identify the dividing surfaces to the neighboring two other sites (A and C). At this point it is crucial to realize that the state (B) is not represented by the well alone but rather the entire region between the two barriers (\ddagger and \ddagger') comprise the state. While the example chosen considers hopping on a one-dimensional lattice, the methodology and terms are straightforwardly extendable to more complex pore dimensionalities and connectivities.

Self-diffusive motion of molecules confined in well-ordered, periodic pore structures can be regarded as a cascade of infrequent random hops from one cage to an adjacent one. Thus, the applicability of TST to a specific diffusion problem is intertwined with the assumption of a random walk. That imposes the condition that a molecule immediately loses any memory of the previous hop or transition, as soon as it has arrived in an adjacent cage. For that reason, it is however sufficient to focus on a single transition; for

example, consider hopping from cage A to cage B (region between q^\ddagger and q^\ddagger in Figure 4.2). The probability of an elementary A \rightarrow B hop has now to be computed. Three functions are introduced to identify whether the hopping molecule is currently found in cage A, $n_A(t)$, in cage B, $n_B(t)$, or within their dividing surface (transition state), $n^\ddagger(t)$:

$$n_A(t) = \text{H}[q^\ddagger - q(t)], \quad (4.45)$$

$$n_B(t) = \text{H}[q(t) - q^\ddagger], \quad (4.46)$$

$$n^\ddagger(t) = \widehat{\delta}[q^\ddagger - q(t)], \quad (4.47)$$

where q^\ddagger denotes the position of the dividing surface, H the Heaviside function [$\text{H}(x) = 1$ for $x > 0$ and $\text{H}(x) = 0$ if $x < 1$], and $\widehat{\delta}$ represents the Dirac delta function [$\widehat{\delta}(0) = \infty$ and $\widehat{\delta}(x) = 0$ otherwise]. On the basis of the functions, the relative conditional probability, $P(q^\ddagger)|_{q(0) < q^\ddagger}$, of finding the tagged molecule within the dividing surface q^\ddagger provided that it has been initially found in cage A [$q(0) < q^\ddagger$] can be obtained by:

$$P(q^\ddagger)|_{q(0) < q^\ddagger} = \frac{\langle n^\ddagger \rangle}{\langle n_A \rangle}. \quad (4.48)$$

The functions can be expressed for a closed system⁹⁶ in terms of free energies, F , along the transport coordinate, which yields:

$$P(q^\ddagger)|_{q(0) < q^\ddagger} = \frac{\exp[-\beta F(q^\ddagger)]}{\int_{q^\ddagger} \exp[-\beta F(q)] dq}. \quad (4.49)$$

Because the free-energy profile depends upon the zeolite-adsorbate system, but, for one and the same system, also changes with loading, θ , different probabilities, $P(q^\ddagger)|_{q(0) < q^\ddagger}$, will, in general, be calculated at different loadings. Also, the temperature has an impact on the free-energy profile. Hence $F(q)$ is in fact $F(q, \theta, T)$, and $P(q^\ddagger)|_{q(0) < q^\ddagger} = P(q^\ddagger, \theta, T)|_{q(0) < q^\ddagger}$. It is worthwhile noting that there are several schemes for extrapolating $F(q, \theta, T_1)$ to $F(q, \theta, T_2)$, see for example Reference 115 and references therein.

Free-energy profiles can be obtained from either Widom particle insertion or histogram sampling. The latter was used in the present work because Widom particle insertion is known to give erroneous results at higher densities.^{91,116} Histograms are computed in such a way that the simulation box is divided into small bins of usually $\Delta q \leq 0.1 \text{ \AA}$. During a simulation, the number of instances are counted that the tagged molecule was located in each of the N_{bins} bins, where configurations may be generated by either MC

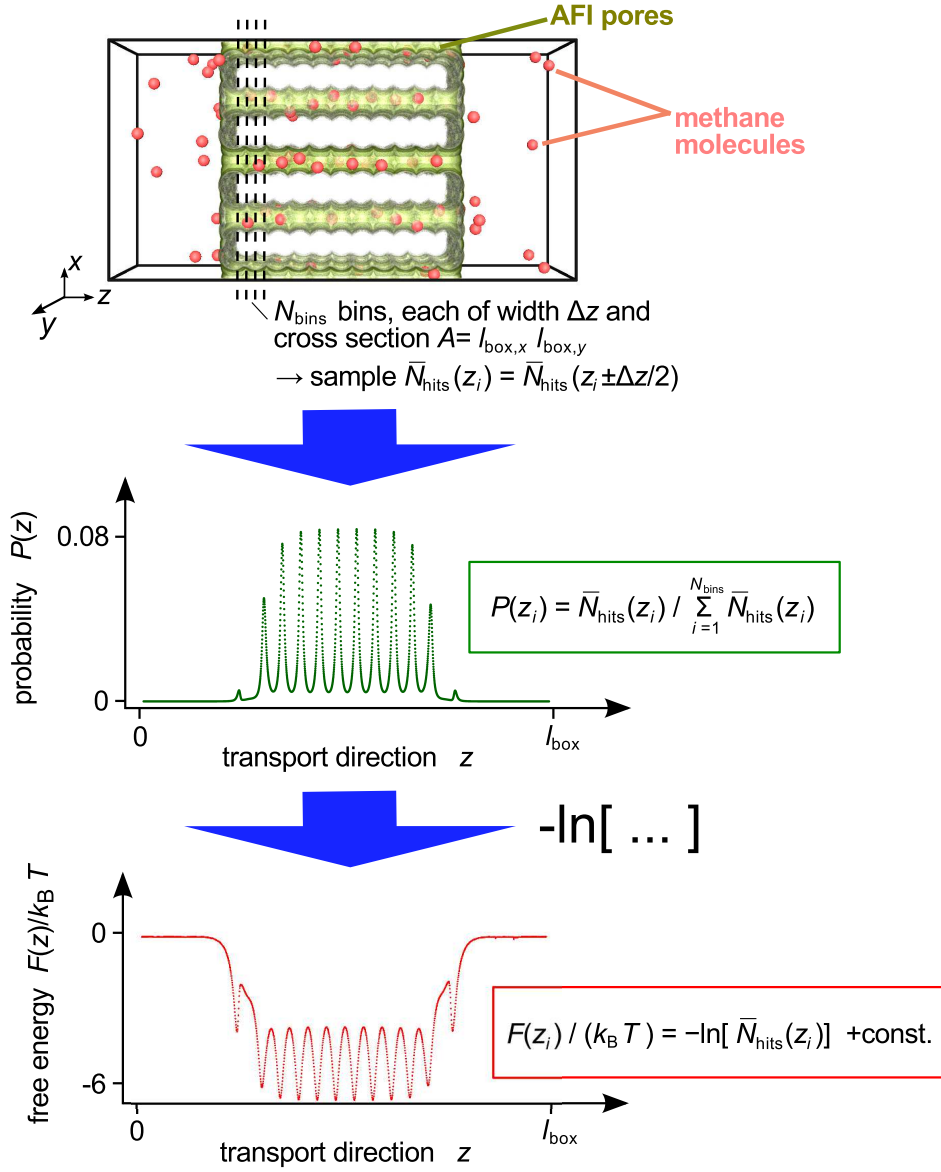


Figure 4.3: Top: snapshot of an MC simulation. Center: histogram along q . Bottom: resulting free-energy profile along q .

or MD. Normalization of the histograms obtained gives the residence probability distribution $[P(q)]$ which, in turn, yields the normalized free-energy profile via:

$$\frac{F(q)}{k_B T} = -\ln[P(q)]. \quad (4.50)$$

Figure 4.3 summarizes the procedure schematically.

4.4.2 Reactive Flux Contribution

Up to this point, the mere probability of finding a molecule within the transition state region (on top of the barrier) has been determined. In order to obtain hopping frequencies the time frame involved has to be assessed. It is composed of two contributions: the average uncorrected flux through the dividing surface and a factor that accounts for spurious crossings known as transmission coefficient or dynamical correction factor.

By assuming that the velocity of the tagged molecule follows a Maxwell–Boltzmann distribution, the average flux through the transition state region in any one of the two directions (i.e., either towards cage A or towards cage B), $\langle 0.5 \cdot |\dot{q}| \rangle_{q^\ddagger}$, can be calculated to $\sqrt{k_B T / (2\pi m)}$; \dot{q} denotes the time derivative of q , that is, the velocity of the tagged molecule projected onto q , and m is the molecule’s mass. The TST hopping frequency, $k_{A \rightarrow B}^{\text{TST}}$, is thus:

$$k_{A \rightarrow B}^{\text{TST}} = \sqrt{\frac{k_B T}{2\pi m}} \cdot P(q^\ddagger) \Big|_{q(0) < q^\ddagger}. \quad (4.51)$$

The tacit assumption in the equation is that, once a molecule reaches the transition state, conventional TST predicts that it will eventually equilibrate in the target cage. However, it could be shown^{110,116,117} that this is not true per se. Hopping molecules may, particularly at finite loadings, have some likelihood to recross the transition state before having reached q_B . The TST frequency is therefore an upper bound for the true frequency $k_{A \rightarrow B}$. The introduction of the so-called transmission coefficient^{111,112} defined as:

$$\kappa \equiv \frac{k_{A \rightarrow B}}{k_{A \rightarrow B}^{\text{TST}}} \quad (4.52)$$

gives the correction to those unsuccessful hopping attempts. Moreover, if the choice of the transport coordinate is not optimal, because q is, in general, a function of the *entire* configuration space [i.e., $q(t) = q(\mathbf{r}_1, \mathbf{r}_2, \dots, \mathbf{r}_N; t)$], κ will be the *exact* correction to this inappropriate definition.¹¹²

The transmission coefficient is usually identified as the plateau value of the reactive flux correlation function (RFCF) defined as:^{91,111,112}

$$\kappa(t) = \frac{\langle \dot{q}(0) \cdot \text{H}[q(t) - q^\ddagger] \cdot \widehat{\delta}[q(0) - q^\ddagger] \rangle}{\langle 0.5 \cdot |\dot{q}(0)| \cdot \widehat{\delta}[q(0) - q^\ddagger] \rangle}, \quad (4.53)$$

where $q(0)$ and $\dot{q}(0)$ denote the initial ($t = 0$) position and velocity of the molecule in terms of the transport coordinate, respectively. This time-dependent

correlation function can be interpreted as the velocity-wise $[\dot{q}(0)]$ weighted likelihood that, after some time t , a molecule that has started its trajectory from the transition state region $\{\widehat{\delta}[q(0) - q^\ddagger]\}$ with a velocity toward the target cage B (0.5 in denominator of Equation 4.53) has already reached B. The transmission coefficient may attain values between zero and unity.

The correlations probed by the RFCF during the jump are usually short-term back-correlations due to particle-particle interactions. At some finite loading, it is very likely that a molecule attempting to reside in the new cage B hits on another adsorbate molecule. Hence, the probability to jump back to the old cage is high because that cage is very likely empty. The plateau value of the RFCF, κ , is therefore attained in a time, $\tau_{\text{mol}} \approx |q_{\text{B}} - q^\ddagger| / \langle |\dot{q}| \rangle$, much shorter than the average hopping time, $\tau_{\text{hop}} = 1/(k_{\text{A} \rightarrow \text{B}} + k_{\text{B} \rightarrow \text{A}})$.⁹⁶ The latter is *not* expected to be a *constant* for varying loading.¹¹² A new time frame, τ_{col} , will set in as a consequence of increasing molecular collisions if loading increases, which most likely retards $\kappa(t)$ in reaching the plateau value. At this point, it should be pointed out that other correlations exist apart from recrossings; for example, kinetic jump correlations, cooperative jump phenomena, and concerted motion of clusters,^{118–121} the first of which will be part of the present work (cf., Chapter 11).

As indicated by the ensemble brackets, the RFCF is to be computed for many initial starting configurations that are distributed according to the Boltzmann distribution. For harvesting these starting configurations, two different simulation strategies were adopted. In Chapter 8, a modified version of the BOLAS¹²² algorithm, called equilibrium path sampling¹²³ (EPS), was used. As has been shown in Reference 122, the configurations sampled by BOLAS/EPS are distributed according to the (canonical) equilibrium distribution. Using the BOLAS/EPS method for sampling starting configurations causes yet a problem at low loadings. As the density is low and the shoots quite short (200–300 fs), it is sampled in a region of configuration space that is too correlated. Therefore, there is an imperative for generating starting configurations from several independent runs where the BOLAS/EPS starts with entirely different initial configurations. At intermediate loadings this problem levels off. Latter chapters follow a different route. Instead of an MD-based approach, Monte Carlo simulations are performed where a specific atom (or bead) of the tagged chain molecule (usually the most central atom/bead) was restricted to the dividing surface. The remainder of the molecule was then grown with configurational-bias Monte Carlo. Importantly, the mass in Equation 4.51 is no longer the mass of the molecule but the mass of the atom (or bead) that is restricted to the dividing surface.

After the generation of starting configurations, all molecules were as-

signed velocities from a Gaussian distribution. The initial configuration was propagated in time by standard MD and the RFCF was sampled on-the-fly. When the tagged molecule reached either of the free-energy wells before the maximum trajectory time exceeded the shoot was stopped because the hop attempt was successful. This procedure ensures that only short-term correlations are accounted for in the transmission coefficient. After the forward shoot has been performed, the initial configuration is reused with reverted velocities and thus the entire system propagated backward in time, where it has to be mentioned that the transport coordinate was also reverted ($q \equiv -\xi$ instead of $q \equiv +\xi$). The two resulting transmission coefficients κ_{forw} and κ_{backw} are identical even if the barrier is asymmetric. Figure 4.4 illustrates the procedure of the reactive flux (RF) simulations (here: at an AFI crystal surface).

Finally, the dynamically corrected transition state theory (DCTST) hopping frequency, $k_{\text{A} \rightarrow \text{B}}^{\text{DCTST}}$, follows:

$$k_{\text{A} \rightarrow \text{B}}^{\text{DCTST}} = \kappa \cdot k_{\text{A} \rightarrow \text{B}}^{\text{TST}} = \kappa \cdot \sqrt{\frac{k_{\text{B}}T}{2\pi m}} \cdot P(q^\ddagger) \Big|_{q(0) < q^\ddagger}. \quad (4.54)$$

Note that the term *extended* dynamically corrected transition state theory, coined by Dubbeldam *et al.*,¹¹⁰ denotes the rigorous extension of DCTST from infinite dilution cases (single molecule in the pore) to cases of finite loadings. The additional guest molecules can therefore be regarded as an additional contribution to the external field applied on the single tagged molecule (i.e., in addition to the zeolite framework).

4.4.3 Other Properties from DCTST

A characteristic transition property that can be regarded even more direct than the frequency is the flux through the dividing surface, $j_{\text{A} \rightarrow \text{B}}$. This is, because a transition or reaction frequency is always derived from the assumption of a specific phenomenological rate law.^{96,108} Because the residence histograms of the present work exhibited very little noise, it was possible to directly obtain smooth concentration profiles along the transport coordinate. The concentration profiles, $c(q)$, permitted the calculation of equilibrium fluxes through dividing surfaces by:

$$j_{\text{A} \rightarrow \text{B}} = \kappa \cdot \sqrt{\frac{k_{\text{B}}T}{2\pi m}} \cdot c(q^\ddagger). \quad (4.55)$$

The present work made in fact more use of the rate-law independent flux than of any rate-law bound transition frequency because this allows consistent

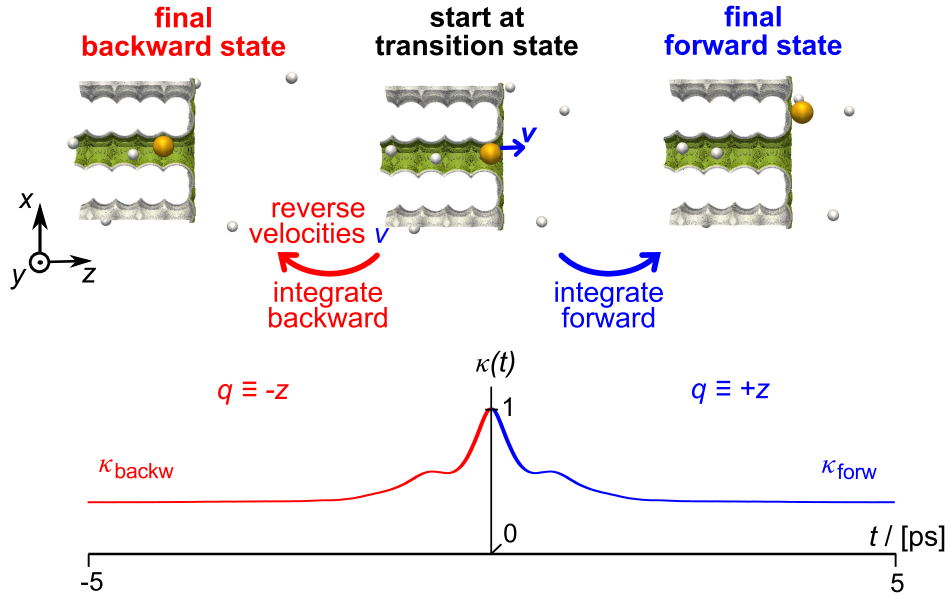


Figure 4.4: Top: snapshots from a reactive flux simulation. The tagged molecule is indicated by a golden sphere. Bottom: reactive flux correlation function, $\kappa(t)$, for the forward ($q \equiv +z$) and the backward integration ($q \equiv -z$), respectively.

comparisons between different barriers even if one (or some) of these barriers is (are) asymmetric.¹¹³

As TST was presented using the example of self-diffusive motion of adsorbate molecules in porous host materials, the self-diffusion coefficient in terms of TST follows:

$$D_S^{\text{TST}} = \sqrt{\frac{k_B T}{2\pi m}} \cdot \frac{\exp\left[-\frac{F(q^\ddagger)}{k_B T}\right]}{\int_{q^{\ddagger'}}^{q^\ddagger} \exp\left[-\frac{F(q)}{k_B T}\right] dq} \cdot l_{A-B}^2. \quad (4.56)$$

where l_{A-B} denotes the separation between cage (well) A and cage (well) B. The DCTST self-diffusion coefficient is correspondingly given by:

$$D_S^{\text{DCTST}} = \kappa \cdot \sqrt{\frac{k_B T}{2\pi m}} \cdot \frac{\exp\left[-\frac{F(q^\ddagger)}{k_B T}\right]}{\int_{q^{\ddagger'}}^{q^\ddagger} \exp\left[-\frac{F(q)}{k_B T}\right] dq} \cdot l_{A-B}^2. \quad (4.57)$$

Approximations to the self-diffusion coefficients can be computed on the basis of the potential energy profile by simply substituting $F(q)$ with $U(q)$ in Equations 4.56 [$D_S^{\text{TST}}(U)$] and 4.57 [$D_S^{\text{DCTST}}(U)$], which enables quantitative statements about energetic and entropic contributions to D_S .

As a last important property, the committor probability, $P_A^\ddagger = \text{H}[q^\ddagger - q(t)]$, can be extracted from reactive flux simulations, which gives the *uncorrelated* fraction of molecules that have started from the transition state at $t = 0$ and arrived in cage A at some (short) time later. The RFCF also rates arrivals but under the additional requirement that the molecule was heading toward that specific cage when it started on the barrier. By contrast, the committor probability (CP) does not correlate the end state with the initial motion. Therefore, it should equal 0.5 for cage A and 0.5 for cage B provided that the free-energy profile is symmetric.

4.4.4 First-Passage Times—an Alternative Approach

As an alternative to separate free-energy and reactive flux simulations, single EMD simulations can be conducted to extract both free-energy profiles and transmission coefficients on the basis of trajectory data, the possibility of which ultimately results from the ergodicity theorem. Of course, the trajectory needs first to be analyzed for the free-energy profiles (identification of locations of wells and barriers) before the RFCF can be computed, and transitions/hops have to take place during the (long) trajectory. However, that opens a route to an alternative approach for a quantitative assessment of recrossings: first-passage times.

To compute first-passage times (FPT), information about locations of wells and barriers are still required so that the procedure substitutes in fact the second step of the Bennett–Chandler approach only (i.e., transmission coefficient calculation). The important difference is a slight shift in perspective. Instead of following the tagged molecule from the barrier “downward” to either the target site or the starting site (as to be judged on the basis of the velocity vector), the time t^{FPT} of a full transition from the starting site to any one of the adjacent sites is measured (over the barrier). Averaging over many such transitions yields the trajectory and therefore ensemble average ($\bar{t}^{\text{FPT}} = \langle t^{\text{FPT}} \rangle$). Assuming that half of the transitions will have proceeded to the neighboring site located to the left of the starting site and the remaining 50% to the right (one-dimensional diffusion lattice) leads to the first-passage time transition frequency, k^{FPT} :

$$k^{\text{FPT}} = 0.5 \cdot \frac{1}{\bar{t}^{\text{FPT}}}, \quad (4.58)$$

which can be directly compared to the DCTST frequency k^{DCTST} . In analogy to the transmission coefficient, it seems therefore convenient to introduce a first-passage time correlation factor, f^{FPT} , defined as:

$$f^{\text{FPT}} \equiv \frac{k^{\text{FPT}}}{k^{\text{TST}}} = \frac{0.5}{\bar{t}^{\text{FPT}} \cdot k^{\text{TST}}}. \quad (4.59)$$

It has to be stressed that these equations are strictly speaking valid for symmetric free-energy profiles only. Provided this symmetry exists, deviation between f^{FPT} and κ are most likely due to either inhomogeneous temperature distributions or the fact that the barrier was too small. The latter case would imply that the hopping cannot be considered as truly activated so that the time to hop on the barrier may not be neglected as in DCTST.

4.5 Transient Molecular Dynamics

Transient molecular dynamics (TrMD), sometimes also referred to as nonequilibrium molecular dynamics (NEMD),^{124,*} is a combination of equilibrium molecular dynamics (EMD) with spatially restricted grand-canonical Monte Carlo (GCMC) trials (Figure 4.5), the latter enabling a nonconstant number of molecules in contrast to ordinary EMD. As this type of simulations was employed in the present work to investigate the transient filling of ultrathin zeolite membranes (nanosheets) with guest molecules, this specific example forms the basis for describing the working principle of transient molecular dynamics. Of course, the method is of general applicability so that it should be transferable to other instationary transport processes (e.g., gas-liquid).

The simulation box was set up in such a way that the zeolite atoms were placed in the center of the simulation box and void space (gas phase) was added in the z direction (Figure 4.5b). At the uttermost left and right end of the gas phase, control volumes (CVs) were placed which joined indeed to

*Transient MD was preferred because the author of this work thinks that it is slightly more specific. Non-equilibrium MD, in his view, encompasses also dual control volume grand-canonical molecular dynamics (DCV GCMC; cf., Reference 8 and references therein) which resembles steady-state and thus also nonequilibrium situations. Transient MD, by contrast, immediately signifies the process modus: transient or instationary. Single control volume transient molecular dynamics seems even more distinct but for reasons of brevity the short notation “transient MD” was adopted. The naming issue indicates that the formalisms and therefore the theoretical foundations of nonequilibrium molecular dynamics techniques are usually not covered by standard textbooks on molecular simulations which, in turn, highlights limited understanding of the method. Therefore, Chapter 11 investigates TrMD specific aspects and parameters.

an unbiased fluid behavior in the control volume.

The setup mimics situations encountered in diffusion measurements, such as uptake experiments as well as interference⁴ and infrared microscopy,⁴ where the zeolite crystal is initially empty and then filled with gas molecules as time proceeds. In the experiments, the huge surrounding that is several magnitudes larger than the pore volume forms practically an infinite reservoir of gas molecules that can enter the pores of the solid. In the simulations, the control volume, which is of similar size as the pore volume, takes over the task of steady molecule supply because it is coupled to a hypothetical infinite gas reservoir via the GCMC trials.

A constant chemical potential, μ_{CV} , was imposed on the control volume (spatial restriction) by standard grand-canonical insertion and deletion trials. After having performed the preset number of trials, N_{ins} and N_{del} , (GCMC phase) and after all atoms of newly inserted molecules have been given velocities from a Gaussian distribution that corresponded to the imposed T , the simulation switched back to the MD modus which numerically integrated the motion of *all* molecules (forward in time) for a preset number of MD steps (N_{steps}). Subsequently, the simulation switched back into the GCMC modus; and so on and so far (Figure 4.5a).

The acceptance probability of an insertion trial restricted to the control volume, $\text{acc}_{ins}^{\text{TrMD}}(o \rightarrow n) = \text{acc}(N_{CV} \rightarrow N_{CV} + 1)$, reads:^{91,124}

$$\begin{aligned} & \text{acc}(N_{CV} \rightarrow N_{CV} + 1) \\ &= \min \left[1, \frac{V_{CV}}{\Lambda^3(N_{CV} + 1)} \cdot \exp \left\{ \beta [\mu_{CV} - U(N_{CV} + 1) + U(N_{CV})] \right\} \right] \end{aligned} \quad (4.60)$$

$$= \min \left[1, \frac{V_{CV}\beta f}{(N_{CV} + 1)} \cdot \exp \left\{ -\beta [U(N_{CV} + 1) - U(N_{CV})] \right\} \right], \quad (4.61)$$

where N_{CV} denotes the number of molecules in the control volume, V_{CV} its size, and $U(N_{CV})$ and $U(N_{CV} + 1)$ the total potential energy of the old (N_{CV}) and new ($N_{CV} + 1$) state, respectively. Apart from N_{CV} and V_{CV} , the equations differ slightly from the original GCMC acceptance probabilities because the Boltzmann factors have substituted the Rosenbluth factors of the new and old configuration (cf., References 124 and 125). Thus, they are valid for single-bead molecules in this form only. Furthermore, notice that Equation 4.61 indicates a similarity to GCMC simulations because the fluid-phase pressure converted by the Peng-Robinson equation of state to the corresponding fugacity was again used to (indirectly) set the chemical potential. The corresponding acceptance probabilities of a trial for molecule

deletion from the control volume, $\text{acc}_{\text{del}}^{\text{TrMD}}(o \rightarrow n) = \text{acc}(N_{\text{CV}} \rightarrow N_{\text{CV}} - 1)$, are:

$$\begin{aligned} & \text{acc}(N_{\text{CV}} \rightarrow N_{\text{CV}} - 1) \\ &= \min \left[1, \frac{\Lambda^3 N_{\text{CV}}}{V_{\text{CV}}} \exp \left\{ -\beta [\mu_{\text{CV}} + U(N_{\text{CV}} - 1) - U(N_{\text{CV}})] \right\} \right] \quad (4.62) \end{aligned}$$

$$= \min \left[1, \frac{N_{\text{CV}}}{V_{\text{CV}} \beta f} \exp \left\{ -\beta [U(N_{\text{CV}} - 1) - U(N_{\text{CV}})] \right\} \right]. \quad (4.63)$$

As concerns the MD part of the TrMD simulations, no specific adaptations were made.

The most relevant properties measured during TrMD simulations were concentration profiles, $c(t, z)$, of guest molecules across the zeolite membrane or nanosheet. They were obtained by dividing the zeolite into equally sized slabs with respect to the z coordinate (Figure 4.6). The slab width was set to the cage size, l_{cage} , of the respective structure. The slab borders were set to the window locations where molecules “feel” the diffusion bottleneck. At each c -profile sampling time, the numbers of molecules that were found (strictly speaking whose centers-of-mass were found) in the individual slabs were determined and divided by $N_{\text{A}} \cdot V_{\text{slab}} = N_{\text{A}} \cdot l_{\text{box},x} \cdot l_{\text{box},y} \cdot l_{\text{cage}}$, with N_{A} being the Avogadro constant. Note that the X’s in the figure indicate that the concentration profile data points that represent the outermost cages were not included in simulation analysis for reasons explained in Chapter 11.

In addition, uptake curves, $m(t)/m_{\text{final}}$, could be determined on the basis of the transient concentration profiles by numerical integration along the transport direction z . Normalization with the integral at saturation (c_{final}) yielded:

$$\frac{m(t)}{m_{\text{final}}} = \frac{\int_{-\delta/2}^{+\delta/2} c(t, z) \, dz}{\int_{-\delta/2}^{+\delta/2} c_{\text{final}} \, dz}. \quad (4.64)$$

The integration limits highlight that the origin was located in the center of the nanosheet whose thickness was δ .

It is instructive to note that the concentration profiles described here differ in two ways from those obtained with EMD or MC. First, the profiles from TrMD are transient profiles whereas the EMD and MC profiles do crucially not vary with time. Second, the spatial resolution is much more coarse in the case of TrMD c profiles than in EMD because of different aims. EMD and MC are performed to unravel different residence probabilities at different

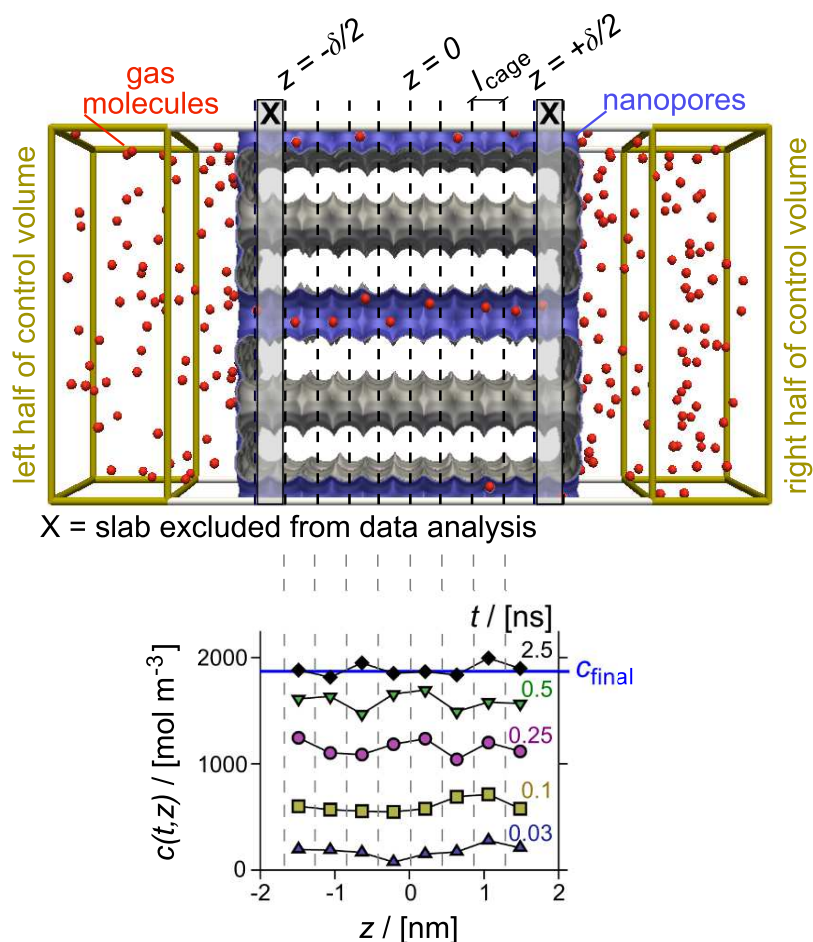


Figure 4.6: Scheme illustrating sampling of concentration profiles in TrMD simulations. Note that each curve is in fact an average from 40 independent TrMD simulations because single simulation data are very noisy.

locations within just one cage to then estimate, for example, the transition state theory self-diffusivity. Concentration profiles from TrMD, on the other hand, shall monitor instationary filling of the pores and thus guest molecule distribution across (several) cages.

Finally, the concentration profiles and uptake curves were analyzed in this work by fitting analytical solutions of Fick's diffusion equations to the TrMD data in order to obtain transport diffusion coefficients (and, possibly, surface permeabilities).



Figure 4.7: Representations of an n -hexane molecule in both approaches: fully atomistic (left) and united atoms (right).

4.6 Models

4.6.1 Force Field

Hydrocarbon molecules were modeled by a united atom (UA) approach, as depicted in Figure 4.7, because hydrogen atoms are known to have negligible influence on adsorption^{126,127} and diffusion¹²⁸ of guest molecules in nanoporous host materials. The important degrees of freedoms (i.e., positions and velocities of carbon atoms), and the insignificant ones (hydrogen atoms bonded to C-atoms) are comprised together to single CH _{i} beads in the UA approach, where $i = 0-4$. A molecule consists hence of several, possibly different CH _{i} beads. The striking advantage of the model is that it tremendously saves computing time* while simultaneously maintaining a realistic physical description of the systems.¹²⁹

Several UA force fields for guest molecule simulation in zeolites exist. Most of them took as a starting point the transferable potentials for phase equilibria (TraPPE) force field which has been introduced and is still maintained by Ilja Siepmann and co-workers.¹³⁰ The present work uses however the force field developed by Dubbeldam *et al.* for alkanes¹²⁷ and extended by Liu *et al.* to alkenes.¹³¹ This is, because the TraPPE force field aims

*The calculation of energies and forces usually represents the heaviest computational burden of a simulation so that the number of floating point operations performed in the force subroutine may well serve as a measure of the total computing time. A simple system consisting of N atoms that interact via a pair-wise additive potential such as the Lennard-Jones type will give rise to $N(N-1)/2$ terms to be calculated in the subroutine per MD cycle.⁹¹ Reducing the amount of atoms will obviously decrease the computing time overproportionately. For example, comparing a fully atomistic simulation with N methane molecules with a corresponding UA simulation decreases the number of relevant floating point operations in first order approximation by a factor of $[N(N-1)/2]/[4N(4N-1)/2] \approx 1/16$. It has to be stressed that this number does yet not include the gain achieved by neglecting intramolecular interactions.

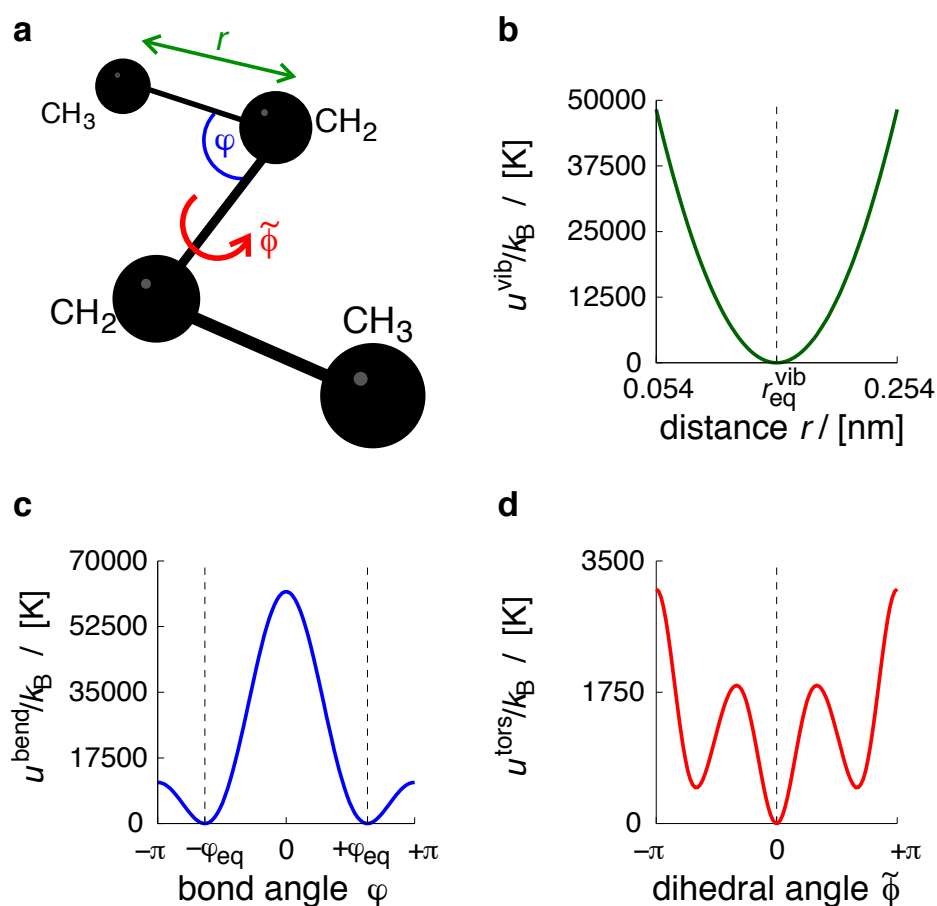


Figure 4.8: Intramolecular potentials; here *n*-butane (a) interactions with parameters from Dubbeldam *et al.*¹²⁷ Bond vibration (b), bond-angle bending (c), and torsion (d). Note that subscripts “CH₃,CH₂” etc. have been omitted for reasons of clarity.

at predicting a wide variety of systems and, first and foremost, fluid phase equilibria. By contrast, Dubbeldam’s and Liu’s force field was specifically developed to match adsorption isotherms of hydrocarbons in zeolites.^{126,127,131} In the remainder of this chapter, the force field will be described and the parameters relevant to the present work provided.

The force field is based on five contributions to the total potential energy, U^{tot} :

$$U^{\text{tot}} = U^{\text{vib}} + U^{\text{bend}} + U^{\text{tors}} + U^{\text{LJ}} + U^{\text{elec}}, \quad (4.65)$$

where superscripts vib, bend, tors, LJ, and elec refer to bond vibration, bond-angle bending, torsion, dispersive Lennard–Jones, and electrostatic interac-

tion, respectively. Each contribution is either pair-, triple-, or quadruple-wise additive. Consider a pair-wise additive interaction type U^i . All possible pairs j and k of (united) atoms participating in that interaction have their individual contribution, $u_{j,k}^i$. The separate contributions are then simply summed up to yield the final value of U^i :

$$U^i = \sum_{j=1}^{N-1} \sum_{k=j+1}^N u_{j,k}^i, \quad (4.66)$$

where N is the number of atoms and/or beads relevant to the interaction type i . The functional forms of the different interaction types will be given in the following.

Vibration of two bonded beads in the same molecule (Figure 4.8a) was modeled by a harmonic potential (Figure 4.8b):

$$u_{i,j}^{\text{vib}} = 1/2 \cdot k_{i,j}^{\text{vib}} \cdot (r_{i,j} - r_{i,j,\text{eq}}^{\text{vib}})^2, \quad (4.67)$$

where $k_{i,j}^{\text{vib}}$ denotes the vibrational spring constant of the bond between beads i and j , $r_{i,j}$ the current distance between the two beads, and $r_{i,j,\text{eq}}^{\text{vib}}$ the (constant) equilibrium bond length of that (type of) bond.

Two bond-angle bending terms were used, depending on the type of beads:

$$u_{i,j,l}^{\text{bend1}} = 1/2 \cdot k_{i,j,l}^{\text{bend1}} \cdot (\varphi_{i,j,l} - \varphi_{i,j,l,\text{eq}}^{\text{bend1}})^2, \quad (4.68)$$

$$u_{i,j,l}^{\text{bend2}} = 1/2 \cdot k_{i,j,l}^{\text{bend2}} \cdot (\cos \varphi_{i,j,l} - \cos \varphi_{i,j,l,\text{eq}}^{\text{bend2}})^2. \quad (4.69)$$

Again, $k_{i,j,l}^{\text{bend}m}$ represents a potential constant that is specific for the bond angle considered, $\varphi_{i,j,l}$ the current bond angle between atoms or beads i , j , and l , as well as $\varphi_{i,j,l,\text{eq}}^{\text{bend}m}$ the equilibrium bond angle. In Figure 4.8c, the second bending potential is displayed as a function of angle. In contrast to the vibrational term, the bending potential is periodic with two equally stable states that are separated by two differently high barriers.

The torsional potential is given by a cosine power series of the dihedral angle, $\tilde{\phi}_{i,j,l,m}$:

$$u_{i,j,l,m}^{\text{tors}} = \sum_{n=0}^5 \eta_n \cdot \cos^n \tilde{\phi}_{i,j,l,m}, \quad (4.70)$$

where each η_n is a constant. Similar to the bending potential, the torsional term is periodic (Figure 4.8d), exhibiting however three stable states and thus three barriers between them. The parameters of the just described intramolecular terms are provided in Table 4.1.

Table 4.1: Bond vibration, bond-angle bending, and torsion parameters taken from References 127 and 131. R_1 and R_2 represent any possible alkyl remainder [e.g., $\text{CH}_3(\text{sp}^3)$ and $\text{CH}_3(\text{sp}^3) - \text{CH}_2(\text{sp}^3)$].

potential	bond pattern	$k^{\text{vib}}/k_{\text{B}}$	$r_{\text{eq}}^{\text{vib}}$
		$k^{\text{bend}}/k_{\text{B}}$	$\varphi_{\text{eq}}^{\text{bend}}$
		η_i/k_{B}	i
u^{vib}	$\text{CH}_3(\text{sp}^3) - \text{CH}_3(\text{sp}^3)$	96 500 K/Å ²	1.54 Å
	$\text{CH}_3(\text{sp}^3) - \text{CH}_2(\text{sp}^3)$		
	$\text{CH}_2(\text{sp}^3) - \text{CH}_2(\text{sp}^3)$		
	$\text{CH}_2(\text{sp}^2) = \text{CH}_2(\text{sp}^2)$	786 873 K/Å ²	1.33 Å
	$\text{CH}_2(\text{sp}^2) = \text{CH}(\text{sp}^2)$	785 050 K/Å ²	1.33 Å
	$\text{CH}(\text{sp}^2) - \text{CH}_3(\text{sp}^3)$	251 549 K/Å ²	1.54 Å
u^{bend1}	$\text{CH}_2(\text{sp}^2) - \text{CH}(\text{sp}^2) - \text{CH}_3(\text{sp}^3)$	70 400 K/rad ²	119.7°
u^{bend2}	$\text{CH}_3(\text{sp}^3) - \text{CH}_2(\text{sp}^3) - \text{CH}_3(\text{sp}^3)$	62 500 K	114.0°
	$\text{CH}_3(\text{sp}^3) - \text{CH}_2(\text{sp}^3) - \text{CH}_2(\text{sp}^3)$		
	$\text{CH}_2(\text{sp}^3) - \text{CH}_2(\text{sp}^3) - \text{CH}_2(\text{sp}^3)$		
u^{tors}	$R_1 - \text{CH}_2(\text{sp}^3) - \text{CH}_2(\text{sp}^3) - R_2$	1204.654 K	0
		1947.740 K	1
		-357.845 K	2
		-1944.666 K	3
		715.690 K	4
		-1565.572 K	5

Interactions between two beads of different molecules were described by a Lennard–Jones type potential:

$$u_{i,j}^{\text{LJ}} = 4 \cdot \varepsilon_{i,j} \cdot \left[\left(\frac{\sigma_{i,j}}{r_{i,j}} \right)^{12} - \left(\frac{\sigma_{i,j}}{r_{i,j}} \right)^6 \right], \quad (4.71)$$

where $r_{i,j}$ denotes the distance between the interacting beads i and j and $\varepsilon_{i,j}$ and $\sigma_{i,j}$ are the respective Lennard–Jones parameters (well-depth and zero-potential distance). Figure 4.9 depicts the potential as a function of inter-bead distance, using the example of two methane united atoms. The

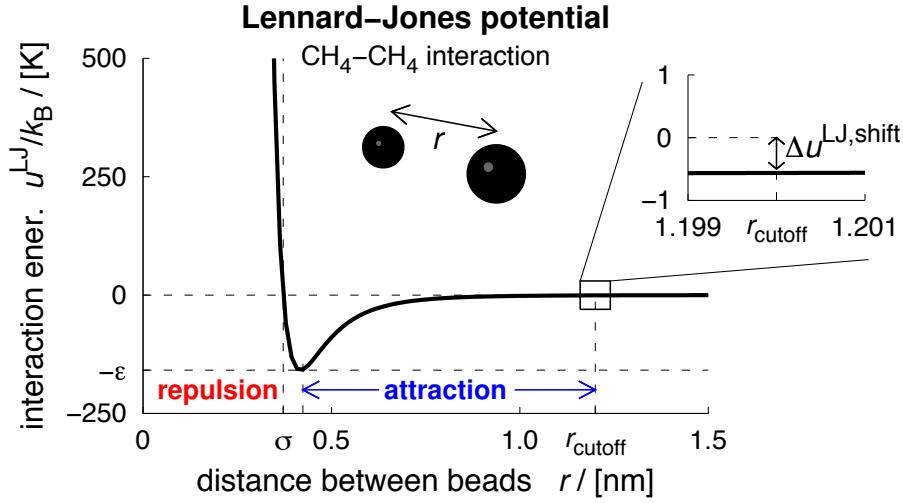


Figure 4.9: Lennard–Jones potential; here for methane-methane interaction with parameters from Dubbeldam *et al.*¹²⁷ Note that subscripts “CH₄,CH₄” have been omitted for reasons of clarity.

Lennard–Jones potential has a large region of attractive character, which causes the typical strong adsorption of hydrocarbons in siliceous zeolite structures and is therefore of central importance to this work.

The energies and forces due to the Lennard–Jones potential were only explicitly calculated up to a certain cutoff distance. To avoid any singularities in the potential energy, the cut potential was shifted to zero at the cutoff distance [i.e., by a value of $\Delta u_{i,j}^{\text{LJ,shift}} = -u_{i,j}^{\text{LJ}}(r_{\text{cutoff}})$], thus yielding:

$$u_{i,j}^{\text{LJ,cut,shift}} = \begin{cases} 4 \cdot \varepsilon_{i,j} \cdot \left[\left(\frac{\sigma_{i,j}}{r_{i,j}} \right)^{12} - \left(\frac{\sigma_{i,j}}{r_{i,j}} \right)^6 \right] + \Delta u_{i,j}^{\text{LJ,shift}} & , \text{ if } r < r_{\text{cutoff}} \\ 0 & , \text{ otherwise.} \end{cases} \quad (4.72)$$

A value of 1.2 nm for r_{cutoff} seems appropriate, considering the vanishing interaction energy at that distance; compare zoom in Figure 4.9.

Intra- and intermolecular forces have to be calculated on the basis of the potentials chosen in order to move a given system forward in an MD simulation. The force acting on bead j due to a pair-wise interaction of type i with bead k is given by:⁷⁰

$$\mathbf{f}_{j,k}^i = -\frac{\partial u^i(|\mathbf{r}_{j,k}|)}{\partial \mathbf{r}_{j,k}} = -\frac{\partial u^i(|\mathbf{r}_{j,k}|)}{\partial |\mathbf{r}_{j,k}|} \cdot \frac{\mathbf{r}_{j,k}}{|\mathbf{r}_{j,k}|} = -\frac{\partial u^i(r_{j,k})}{\partial r_{j,k}} \cdot \frac{\mathbf{r}_{j,k}}{r_{j,k}}. \quad (4.73)$$

For example, the x component of the force due to a Lennard–Jones interaction is:⁹¹

$$f_{x,j,k}^{\text{LJ}} = \frac{48 \cdot \varepsilon_{j,k} \cdot x_{j,k}}{r_{j,k}^2} \cdot \left[\left(\frac{\sigma_{j,k}}{r_{j,k}} \right)^{12} - 0.5 \cdot \left(\frac{\sigma_{j,k}}{r_{j,k}} \right)^6 \right], \quad (4.74)$$

where $x_{j,k}$ is the distance between the two beads along the x coordinate and the shift part has been omitted for clarity. Functional forms of the forces corresponding to the intramolecular interaction potentials are listed in the excellent PhD thesis by Jakobtorweihen,⁷⁰ which has in fact inspired a large part of the present chapter.

Interactions between molecule beads and oxygen atoms of the siliceous zeolite structure consisted also of a Lennard–Jones potential only.¹²⁷ In accordance with the original force field proposal,^{127,131} interactions between guest molecules and silicon atoms of the host structure were neglected, which is common practice in zeolite research of hydrocarbon adsorption and transport with molecular simulations.¹³² The physical reason lies in the fact that the oxygen atoms are indeed large negatively charged ions that effectively shield the small silicon ions (cf., Chapter 2). Because hydrocarbons were studied only and extra-framework cations were not present (siliceous structures) a Lennard–Jones description of the guest–host interaction was sufficient so that the term u^{elec} could be entirely neglected in the present work. Furthermore, intramolecular Lennard–Jones interactions were calculated for beads separated by more than three bonds only. That is, so-called 1-4 interactions were excluded. Table 4.2 lists the remaining parameters used in this work.

Although electrostatic interactions and polarizability were neglected due to the nature of the guest–host systems, it should be noted that these interaction types become important for molecules such as carbon dioxide and water. In this respect, much research effort is currently being spent on improving existing force fields by multiscale simulation approaches. As a typically example, density functional theory based electronic structure calculations provide partial charges of host atoms derived from a single unit cell.¹³³ The charges are then transferred to atomistically detailed GCMC simulations with much larger super cells to determine adsorption isotherms of guest molecules (e.g., CO₂).¹³³ The need for a more accurate description of the electrostatic guest–host interaction was already indicated by the work of Clark and Snurr in 1999.¹³⁴ But it was not until recently that increasing computer resources facilitated the rigorous combination of electronic structure methods and classical molecular modeling.

Table 4.2: Lennard–Jones parameters taken from References 127 and 131.

bead/ atom		CH ₄	CH ₃ (sp ³)	CH ₂ (sp ³)	CH ₂ (sp ²)	CH(sp ²)
CH ₄	$\frac{\varepsilon_{i,j}}{k_B}$ [K]	158.50				
	$\sigma_{i,j}$ [Å]	3.72				
CH ₃ (sp ³)	$\frac{\varepsilon_{i,j}}{k_B}$ [K]		108.00	77.77		
	$\sigma_{i,j}$ [Å]		3.76	3.86		
CH ₂ (sp ³)	$\frac{\varepsilon_{i,j}}{k_B}$ [K]		77.77	56.00		
	$\sigma_{i,j}$ [Å]		3.86	3.96		
CH ₂ (sp ²)	$\frac{\varepsilon_{i,j}}{k_B}$ [K]				93.000	70.210
	$\sigma_{i,j}$ [Å]				3.685	3.710
CH(sp ²)	$\frac{\varepsilon_{i,j}}{k_B}$ [K]				70.210	53.000
	$\sigma_{i,j}$ [Å]				3.710	3.740
O(zeol)	$\frac{\varepsilon_{i,j}}{k_B}$ [K]	115.00	93.00	60.50	82.050	55.215
	$\sigma_{i,j}$ [Å]	3.47	3.48	3.58	3.530	3.502

4.6.2 Host Structure

The zeolite structures were frozen so that the atoms remained at their crystallographic positions and guest molecules were allowed to move only. Section 6.3 will however discuss the influence of framework flexibility (i.e., vibrating zeolite atoms).

A zeolite super cell was obtained in the conventional manner by translationally placing unit cells side by side. Zeolite surfaces were created by cutting through a given super cell perpendicular to one of the three Cartesian coordinates (usually z) and adding void space to the simulation box in that direction. The influence of the cutting plane and thus the impact of the surface nature will be investigated in Chapters 8 and 9.

4.7 Simulation Details

Because the simulation boxes attained sizes of 30 nm along a single coordinate at maximum in the present work, they were several orders of magnitude smaller than experimental observation cells. Hence, the treatment of the simulation box boundaries deserved some care. Any hard boundary would immediately have introduced a bias to the behavior of the molecules, and also a soft, yet impermeable boundary would have unwanted side-effects to the study of “bulk” properties. Therefore, periodic boundary conditions (PBC) were employed to avoid such disturbing effects. The conditions can be imagined as replicating the simulation box infinitely in all three dimensions, as depicted in Figure 4.10 for a simplified two dimensional case. The important point for the interaction calculation of, say, the filled particle with the shaded one is that the closest mirror image of the latter (dotted rectangular) is considered instead of the true one within the simulation box itself. An important implication follows for MD simulations, where particles can in fact cross the border of the simulation box and enter one of the mirror image boxes. In such a case, the true position of the molecule is not changed in the program because some quantities such as the mean squared displacement rely on that genuine position. However, when the program computes (intra- and) intermolecular forces and interaction energies, it uses a second position variable for each atom and bead which is mapped back to the simulation box. The second position variable is then used to determine the closest mirror images for force and energy calculation, where it has to be noted that the simulation boxes were chosen such that each of the three lengths (i.e., $l_{\text{box},x}$, $l_{\text{box},y}$, and $l_{\text{box},z}$) were at least twice as large as the potential cutoff radius.

Although PBC can also be prone to side-effects when the box gets too small, increasing the size and comparing the results provides a straightforward means to test the sensitivity of the quantity of interest against PBC. If that is not possible due to limited computer resources, the vice versa approach (i.e., decreasing the box size) serves the same purpose.⁹¹

In the remainder of this section, a summary of details is presented that generally applied to all MC, EMD, and TrMD simulations performed in this work, if not explicitly stated otherwise.

After having build up the host structure as outlined in Subsection 4.6.2, the guest molecules were randomly distributed throughout the simulation box. That was achieved by using GCMC insertion moves until the target number of molecules was attained, unless 10 000 000 trials had been performed for the current molecule to be inserted. In that case, the simulation program stopped with an error message indicating too dense a system to be

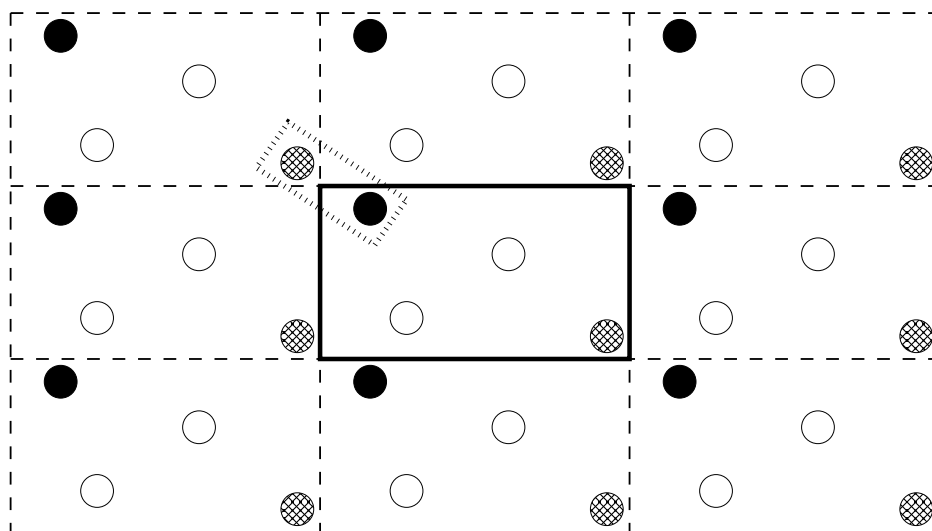


Figure 4.10: Periodic boundary conditions: the simulation box (thick solid rectangular) can be viewed as being infinitely replicated with mirror images (dashed rectangulars) in all directions. The dotted rectangular highlights the closest shaded-particle mirror image with respect to the filled particle.

created with this approach. Molecules of the initial configuration were assigned random velocities drawn from a Gaussian distribution. Subsequently, the main part of the simulations began, which is the numerical integration (EMD), the Monte Carlo trial loop, and their combination (TrMD), respectively. Equilibration of the systems was necessary in all cases, where EMD simulations performed in fact two equilibration phases. Typically, 1 ns velocity scaling succeeded by a short 0.1 ns equilibration in the NVE ensemble ensured stable behavior of the systems in terms of energy and temperature because the two quantities were subject to fluctuations of anticipated extent only. Minor energy drift was observable in expected limits.⁹¹ Note that the time step sizes amounted to 1 fs for methane simulations and to 0.5 fs for simulations containing any chain molecules (e.g., ethane), respectively. As for MC simulations, the equilibration consisted of some 1000 to 10 000 additional MC cycles performed prior to the production phase, in the latter of which the observables of interest were sampled. Of course, the program discarded any data from the equilibration phases, that is, they did not contribute to any observables presented in this work. Each MC cycle consisted of 2–50 displacement, rotation, regrow, and, if applicable, insertion and deletion trials. It was *a priori* estimated how many trials in total would be necessary to have changed the position of each molecule in the simulation at

least once per MC cycle on an average. The exact number of trials was not ultimately important because the aim was only to ensure that the sampling of the properties of interest performed after any one MC cycle was meaningful because the configuration has substantially changed.

After the equilibration the production phase began, the length of which depended on the purpose and on the number of independent simulations with the same macroscopic constraints (applies also to MC). Usually, several tens to hundreds of nanoseconds were conducted at least. Key quantities such as temperature, total energy, kinetic energy and potential energy were saved in regular intervals of at least some tens to hundreds picoseconds. More specific observables such as the mean squared displacement were sampled more frequently but also on-the-fly rather than by post-simulation processing of a trajectory file. Residence histograms were updated every time step (NVT-MC simulations: every MC cycle).

Monte Carlo displacement and rotation trials were subject to dynamic adjustment of the maximal displacement and quaternion to obtain an *a priori* set acceptance rate on an average (in this work 50 % in both cases).⁹¹ For this to work, actual acceptance rates were computed in regular intervals during the MC simulation (usually every 10–100 MC cycles) and the maximum values correspondingly increased (actual acceptance rate higher than desired rate) or decreased (actual rate smaller than desired rate).

Decision of acceptance of a single MC trial move (of type i) was achieved by drawing a random number between zero and unity and comparing this decimal number with the acceptance probability $\text{acc}_i(o \rightarrow n)$. If the random number was smaller than $\text{acc}_i(o \rightarrow n)$, the move was accepted; otherwise the old configuration remained unchanged. The random number generator required a seed value given as an input; that is, no automatic seed generation (e.g., clock time based) was used.

Periodic crystal simulations (e.g., for isotherm determination and diffusion coefficient calculation on the basis of the mean squared displacement) employed potential energy grids to speed up the computation of guest-host interactions. By contrast, simulations with interfaces/surfaces used neighbor lists (MD) or cell lists (MC) for improving the efficiency of the calculations.

As for TrMD simulations, some specific setup aspects follow. Each half of the control volume (cf., Figure 4.5) was 16 Å in width in z direction, if not indicated otherwise. Hence, the size of the single control volume was $2 \cdot 16 \text{ \AA} = 32 \text{ \AA}$. The total void space added to the centered zeolite sheet amounted to 56.01 Å so that the intermediate buffer zone between the end of the CV and the position of the first zeolite atoms in z direction was 12.005 Å in thickness.

100 000 GCMC trials prior to the transient MD simulation itself ensured equilibration of the control volume where the probability to perform an insertion trial was equal to the one of a deletion trial (50 %). In the production phase, five molecule insertion as well as five molecule deletion trials were performed inside the control volume every ten MD steps. A Nosé-Hoover chain thermostat maintained the temperature imposed. Although the maximum length of the simulations were always set to 2 μs , the simulations were usually stopped as soon as the uptake curve showed a well appreciable plateau at unity.

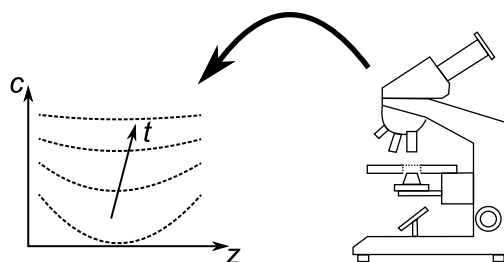
Concentration profiles from single TrMD simulations were very noisy. Therefore, 40 separate, independently initialized simulations were performed per system in order to average the noisy single-simulation concentration profiles. In this respect, it has to be added that the time origin was shifted to the last concentration-profile sampling instance at which all concentrations of the averaged profile were zero.

Review of Experimental Techniques

5

This chapter briefly introduces experimental techniques for determining diffusion coefficients of guest molecules in zeolites. Of course, there are many more methods around, such as zero-length column¹³⁵ (ZLC), confocal laser scanning microscopy¹³⁶ (CLSM),

and fluorescence correlation spectroscopy¹³⁶ (FCS). However, molecular simulation results are compared in the present work to data from following techniques only: uptake rate measurements by gravimetric means,¹³⁷ interference microscopy (IFM),^{4,138,139} infrared microscopy (IRM),⁴ and pulsed field gradient nuclear magnetic resonance (PFG NMR).^{140,141} Uptake measurements and IFM yield transport diffusion data whereas IRM and PFG NMR provide self-diffusion results.



5.1 Uptake Rate Measurements

Representing the “coarsest” technique considered in this chapter because of zero spatial resolution, uptake rate measurements are most frequently carried out by gravimetric means. Due to the simplicity of the underlying principle, the measurements are one of the most straightforward ways for determination of single-component diffusion data.¹

A batch of the adsorbent crystallites is placed on a balance in a closed chamber. After initial evacuation, some amount of gas is quickly introduced. The gas molecules enter the adsorbent which causes an increase in weight. The transient mass increase is monitored until it attains a constant value. The curve obtained divided by the final value of mass taken up (i.e., at equilibrium) gives the uptake curve. Diffusion coefficients (and surface permeabilities) can be determined by fitting corresponding analytical solutions (e.g., Equations 3.4 and 3.7).

After having reached equilibrium, the measurement can be repeated by introducing more gas. In this way, transport coefficients can be measured as a function of pressure or loading, if the isotherm is available, where small pressure steps need yet to be applied.¹

Extraneous heat and mass transfer resistances can cause problems, for which reason it is recommendable to use small samples.¹ Small adsorbent batches and thus small pore volumes are also necessary in regard on minimizing the pressure drop in the chamber due to adsorption. Because of the requirement of highly sensitive balances, most uptake measurement studies use tapered element oscillating microbalances today.¹

As an alternative to gravimetric measurements, piezometric methods can be used to obtain the uptake curve. They monitor however the pressure change rather than the mass change in a constant volume system after a pressure step has been applied.¹ Piezometric methods can be exploited, in particular, to investigate uptake of liquids.¹

5.2 Interference Microscopy

Interference microscopy (IFM) relies on the principle that the refractive index of a transparent porous solid changes with varying guest molecule concentration.¹³⁸ A single adsorbent crystal is placed in a chamber under an interference microscope. Two light beams are used: one is sent through the pure gas surrounding the crystal and the other passes through the adsorbent crystal in which molecules gradually adsorb. After having left the observation chamber, the beams are superimposed to give rise to interference patterns.

The primary quantity accessible is the change in optical path length integrated over the direction of observation.¹⁴² That quantity is directly related to the integral of the change in refractive index¹ which, in turn, is directly proportional to the integral of change in guest molecule concentration along the direction of observation.¹⁴³ Normalizing the data by means of an isotherm (e.g., from gravimetric measurements or infrared microscopy¹³⁸)

yields therefore mean concentration values of guest molecules in lateral directions (concentration “surfaces”). Two striking differences to uptake rate measurements are immediately clear. First, transport is monitored in a spatially resolved manner, for the reason of which IFM is a direct experimental technique for diffusion studies. Second, the method investigates transport in a single adsorbent crystal rather than in a batch (or bed) of crystals.

Despite the fact that this method has led to valuable insights into a particular type of surface barriers, as will be discussed in Chapter 9, it suffers from not being adaptable to slightly more complicated but practically much more relevant systems. The reasons are the following. Large single crystals of several to some tens micrometer are necessary because the spatial resolution is limited to $0.5\ \mu\text{m} \times 0.5\ \mu\text{m}$.¹⁴³ That confines the determination of transport parameters to some extent because the surface nature of ultrathin films, membranes, and nanosheets may differ dramatically from those of giant crystals, given that the respective synthesis procedures usually differ. But these thin solid structures are precisely the wanted “zeolite form” for practical purposes.¹² Furthermore, temporal resolutions of below 10 s are not achievable with IFM,¹⁴³ which limits the application to rather slow diffusing molecules. Also, IFM has not been proven to be capable of measuring multicomponent transport to date, and it seems very unlikely that the experimental setup can be modified in a straightforward way to do so any soon. Finally, IFM studies of dense fluids (liquids or supercritical fluids) have yet not been reported either, indicating a further severe restriction of the method.

5.3 Infrared Microscopy

Conceptually similar to interference microscopy, infrared microscopy (IRM) measures the change of the concentration integral along the direction of observation in an indirect manner. Here, the change in the integral under the infrared band characterizing the guest molecule is used however. The spectra can be acquired in two different modes: integral and spatially resolved. Both beds of crystals and a single crystal can be investigated in the integral mode. Single crystal studies are particularly interesting because they are not as prone to heat release problems upon adsorption as studies of zeolite beds;¹ on the other hand, single-crystal studies suffer more from disturbing influences induced by impurities.¹

The spatially resolved mode is limited by a resolution of $2.7\ \mu\text{m} \times 2.7\ \mu\text{m}$, which is five times more coarse than the resolution achievable with IFM.¹ The advantage of IRM over IFM is yet that IRM can track multicomponent

transport by exploiting different bands associated with different molecular species. The bands may not overlap significantly, limiting the application to multicomponent systems of “sufficiently” distinct molecules. Both techniques, IRM as well as IFM, are called microimaging techniques for obvious reasons.¹⁴⁴

5.4 Pulsed Field Gradient Nuclear Magnetic Resonance

Pulsed field gradient nuclear magnetic resonance (PFG NMR) exploits the fact that a magnetic field—be it constant or gradient-like—does usually not disturb the motion of a (gas) molecule or atom to a considerable extent, unless deep temperatures are visited.¹ Two further points are central to use PFG NMR for determination of molecular displacements. First, a magnetic field gives rise to precession of a spin about the field direction with a characteristic (Larmor) frequency. Second, this frequency depends on the position as soon as the magnetic field becomes position-dependent (gradient). Applying a magnetic pulse perpendicular to a field gradient decreases the magnetization (= vector sum of all individual spins) in field direction, M_{\parallel} , and increases the one perpendicular to the field, M_{\perp} . If all atoms that carry a spin rest at their individual positions, another pulse with the opposite sign will lead to the original magnetizations. On the other hand, if the atoms move in the meantime the magnetizations will not fully resume their initial values. This results in an attenuation of the transverse magnetization, $\psi = M_{\perp}/M_{\perp,init}$, the signal of which is directly accessible from the measurement.¹ Importantly, the spin echo attenuation depends exponentially on the self-diffusion coefficient, D_S :¹

$$\psi(t_{\text{interval}}, t_{\text{pulse}} g) = \exp(-\hat{\gamma}^2 t_{\text{pulse}}^2 g^2 D_S t_{\text{interval}}), \quad (5.1)$$

where t_{interval} denotes the time between the two pulses, t_{pulse} the length of each pulse, g the magnetic field gradient, and $\hat{\gamma}$ the gyromagnetic ratio of the atom whose spin echo is being followed (e.g., ^1H , ^2H , ^{13}C , ^{129}Xe).¹ Hence, fitting of attenuation curves to exponential functions with varying pulse interval t_{interval} provides a straightforward way¹⁴¹ of self-diffusivity determination. Notwithstanding a high apparent spatial resolution (down to some ten nanometer),¹ it has to be stressed that PFG NMR cannot directly pinpoint molecules. It is an *indirect* method to molecule displacement and thus self-diffusion measurements.

While former PFG NMR studies usually employed beds of zeolite crystals (powders),¹⁴⁵ a large single crystal is preferable today^{4,141} because of similar reasons as in the case of IRM.

Part III

Preliminary Results

6

Verification of Methodology

The present chapter investigates pivotal aspects of the methodology chosen. First, the sensitivity of key properties of this work to changes in the guest molecule model parameters is assessed in Section 6.1, which, in analogy to experiments, can be viewed as the sensitivity of the results towards the degree of purity of purchased fluids. The guest molecule sensitivity assessment is followed by the main focus of the current chapter: the influence of the input crystal structure. Many theoretical works on zeolite adsorption and diffusion from the past, including one by the author himself,¹⁴⁶ used crystal structures derived from materials of the same framework type but of different composition. Whether or not this has been an underrated issue will therefore be elucidated in Section 6.2 and, in keeping on with the analogy to experiments, might be interpreted as the sensitivity towards different zeolite batches. Furthermore, Section 6.3 will justify the rigid-lattice assumption. Section 6.4 will provide indication for the equivalence of the two thermostats employed in different molecular dynamics simulations of this work (analogy to experiments: two heat baths that work similarly). Finally, the quality of the methodology will be assessed in Section 6.5 by comparison of simulation results with experimental data from literature, naturally including some limitations.

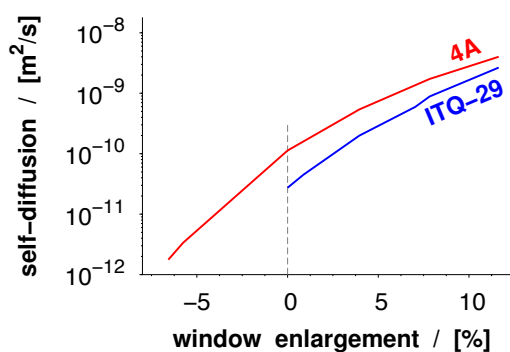


Table 6.1: Perturbed Lennard–Jones parameters and the corresponding relative deviations from the original parameters.

interacting beads	ε/k_B [K]	$\Delta\varepsilon$ [%]	σ [Å]	$\Delta\sigma$ [%]
CH ₂ (sp ³)-CH ₂ (sp ³)	77.770	+38.9	3.860	-2.5
CH ₂ (sp ²)-CH ₂ (sp ²)	85.000	-8.6	3.675	-0.3
CH(sp ²)-CH ₂ (sp ²)	63.206	-10.0	3.703	-0.2

6.1 Force Field

To investigate the sensitivity of the force field small random perturbations from the original parameters^{127,131} were given to some Lennard–Jones interaction parameters (Table 6.1).¹¹⁴ The perturbations affected results of ethene, propene, propane, butane, pentane, and hexane and the relative differences in the guest–guest Lennard–Jones parameters varied between -10% and +39%. To assess whether or not the partly large differences in the model parameters imply similarly strong deviations in the simulation results, two “probe” properties have been chosen that are of central importance to this work: the ratio of equilibrium transport fluxes prevailing at intracrystalline diffusion barriers and at the surface barrier, respectively (i.e., $j_{\text{zeol}}^\ddagger/j_{\text{surf}}^\ddagger$), and intracrystalline transmission coefficients, κ_{zeol} . The two properties were determined with both the original and the perturbed force field, thus providing data for parity plots.

As can be seen from Figure 6.1, the vast majority of the results from the two parameter sets agree very well with each other. In those very few cases when the deviation is larger than $\pm 10\%$ (dashed lines), the error bars are usually so large that the uncertainty region of a given data point overlaps again with the 10%-agreement region. The absence of any considerable systematic deviation can be explained by the domination of the zeolite force field over the interaction that guest molecules exert on one another. The Lennard–Jones parameters of a given CH_{*i*} bead to interact with another bead of the same kind is similar to the interaction parameters with the zeolite oxygen. There are usually only few other fluid molecule beads surrounding any CH_{*i*} bead because low to moderate loadings are primarily investigated in this work. However, the situation is entirely different in regard to the oxygen atoms of the zeolite which surround the CH_{*i*} under consideration by hundreds. Hence, the guest–host interaction vastly dominates over any other contribution to

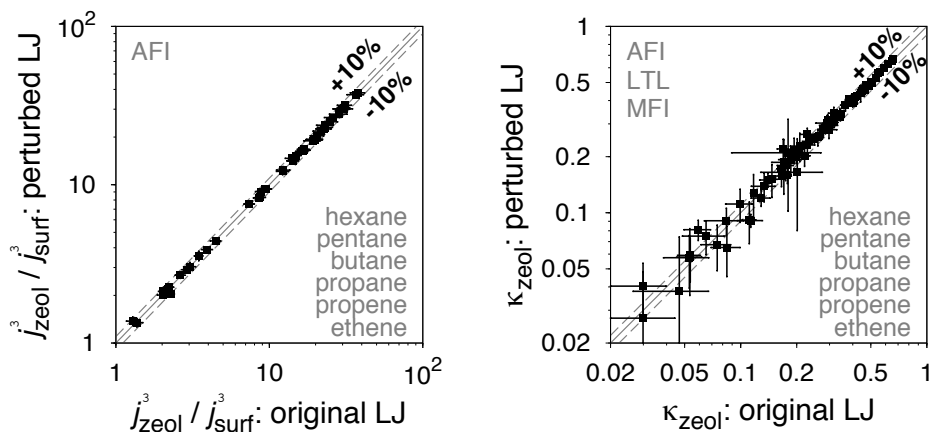


Figure 6.1: Parity plots: flux ratio, $j_{\text{zeol}}^{\ddagger}/j_{\text{surf}}^{\ddagger}$, of all molecules affected by the parameter perturbation in AFI (left); transmission coefficients of hopping in the periodic structure, κ_{zeol} , of all affected molecules in AFI, LTL, and MFI (right).

the potential, and the results do thus not show any significant sensitivity towards small to moderate deviations in the guest-guest parameters.

6.2 Crystal Structure

Apart from the force field,¹⁴⁷ the crystal structure represents an important input to molecular simulations of guest adsorption and diffusion in porous host materials, where it should be mentioned that all-silica zeolites are investigated most frequently. Crystallographic studies on the true siliceous structure provide the atoms' positions in the unit cell (procedure 1). If experimental data are yet not available, two principle routes exist for obtaining the input structure. Either, the database of the International Zeolite Association²² (IZA) can be accessed which, for every framework type, offers a prediction of the siliceous material on the basis of theoretical considerations (procedure 2). Or, a synthesized structure which is not purely siliceous can be converted by, for example, substituting the aluminum atoms of an aluminosilicate by silicon atoms (procedure 3). Of course, the latter two procedures give rise to (small) structural differences from the true siliceous structure. In this context, it is interesting that a PFG NMR study by Hedin *et al.*¹⁴⁸ has indicated that the self-diffusion coefficient of propene in different LTA-type

zeolites is quite sensitive to compositional *and* structural differences.

To investigate the influence of these structural differences on both the adsorption and the diffusion behavior of guest molecules in zeolites, Monte Carlo and reactive flux simulations of methane in different zeolite structures of the same framework type—following procedure 1, 2, and 3—have been performed. The simulations provided Henry coefficients, isotherms, transmission coefficients, and self-diffusion coefficients of methane in siliceous structures of the LTA, SAS, and ITE frameworks (cf., Figure 2.3). Apart from the IZA structures,²² the zeolites investigated here included the all-silica materials as experimentally determined by Corma *et al.* (LTA),³⁵ Wragg *et al.* (SAS),⁶⁵ and Cambor *et al.* (ITE),⁶² as well as an aluminosilicate (LTA) by Pluth and Smith³⁶ and a magnesioaluminophosphate (SAS) by Patinec *et al.*⁶⁶ The latter two are converted to purely siliceous structures according to procedure 3 mentioned above. The all-silica structures by the IZA, although published only if the framework in any composition has been confirmed by experimental means, represent hypothetical all-silica zeolites because the atomic positions are determined by refinement using fixed weighted atomic distances between nearest Si–O, O–O and Si–Si atoms. However, these structures and results obtained with them shall serve as reference in the following.

Providing an impression of how much the atomic positions in different structures of the same framework can vary, Figure 6.2 shows fractional coordinates of the oxygen atoms in different crystallographic projections. The plots include the per-atom deviation in fractional atomic positions, δr , of the experimental structures from the IZA structure:

$$\delta r = \frac{1}{N_{\text{atoms}}} \cdot \sum_{i=1}^{N_{\text{atoms}}} \sqrt{\left(\frac{\hat{a}_i}{\hat{a}_{\text{UC}}} - \frac{\hat{a}_i^{\text{IZA}}}{\hat{a}_{\text{UC}}^{\text{IZA}}}\right)^2 + \left(\frac{\hat{b}_i}{\hat{b}_{\text{UC}}} - \frac{\hat{b}_i^{\text{IZA}}}{\hat{b}_{\text{UC}}^{\text{IZA}}}\right)^2 + \left(\frac{\hat{c}_i}{\hat{c}_{\text{UC}}} - \frac{\hat{c}_i^{\text{IZA}}}{\hat{c}_{\text{UC}}^{\text{IZA}}}\right)^2}, \quad (6.1)$$

where the sum runs over all N_{atoms} oxygen atoms in the unit cell and \hat{a}_i , \hat{b}_i , and \hat{c}_i represent the position of atom i in the unit cell while subscript “UC” refers to the unit cell length along the respective crystallographic coordinate. The per-atom deviation considerably exceeds 1% only in a single case (LTA structure by Pluth and Smith³⁶). Hence, relative atom distances seem to be usually comparable among structures of the same framework type.

Figures 6.3 and 6.4 show relative differences of the adsorption isotherms (loading θ vs pressure p) and diffusion quantities (TST self-diffusivity and transmission coefficient, respectively, vs loading) of methane in the two experimentally confirmed LTA structures from the corresponding IZA values.

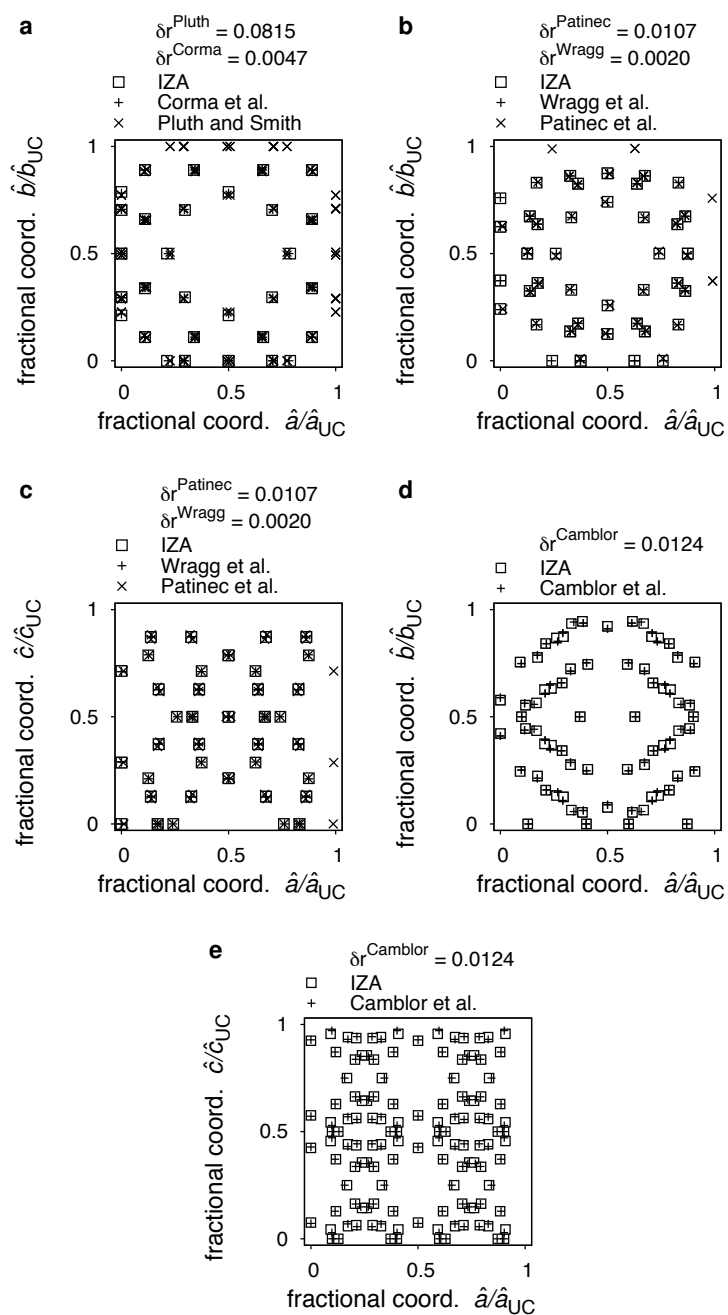


Figure 6.2: Two-dimensional projections of fractional coordinates, $\hat{a}/\hat{a}_{\text{UC}}$, $\hat{b}/\hat{b}_{\text{UC}}$, and $\hat{c}/\hat{c}_{\text{UC}}$, of oxygen atoms in different LTA^{22,35,36} (a), SAS^{22,65,66} (b, c), and ITE^{22,62} (d, e) zeolite structures.

While the adsorption differences between the structure by Corma *et al.*³⁵ and the IZA structure²² are rather small, those between Pluth and Smith³⁶ and IZA structure²² are larger; especially at low pressure ($p \leq 0.3$ bar) and low temperature ($T = 200$ K), where a maximal discrepancy of around -40% is observable (Figure 6.3). Therefore, it can be concluded that the smaller the cages (Corma *et al.* < IZA < Pluth and Smith), the stronger is the adsorption at low pressures. This is likely due to a denser and thus more attractive potential-energy field inside the smaller cages. On the other hand, the larger a cage is, the stronger is the adsorption at high pressures because the cages are simply geometrically larger and can thus accommodate more methane molecules (larger saturation loading).

Self-diffusion data were calculated at 300 K and low loadings (Figure 6.4). In contrast to the isotherm differences, the largest discrepancies (-65%) are observed between the structure by Corma *et al.* and the IZA. Over the loading range studied here, this difference is practically constant, indicating that the qualitative trend of D_S^{TST} over loading is the same (top of Figure 6.4). Although the absolute value of $D_S^{\text{TST}}(U)$ (diffusivity calculated from a potential-energy profile) is, for a given structure and state point, consistently larger than D_S^{TST} (diffusivity calculated from a residence histogram, i.e. from a free-energy profile) by a factor of approximately 100, the relative difference of D_S^{TST} and $D_S^{\text{TST}}(U)$ between two structures is the same. This supports the assumption that entropic barriers of different structures of the same framework type are equal; only the potential-energy barrier changes significantly between two structures.

The obvious insensitivity of the zeolite crystal structure on the transmission coefficient, as highlighted in the bottom part of Figure 6.4, stems most likely from the fact that this coefficient is mainly influenced by guest molecules adsorbed in neighboring cages.¹¹⁶ An analysis of cage occupancy distributions revealed that the distributions were equivalent for all three structures at the same average loading (Figure 6.5). Hence, the transmission coefficients are the same.

To allow a comparison of the crystal structure influence between different framework types, Henry coefficients and TST self-diffusivities at infinite dilution were calculated because the LTA results suggested that the influence was strongest at low loadings and transmission coefficients were hardly affected. All three framework types studied (LTA, SAS, ITE) belong to the group of cage-type zeolites.⁴¹ Their diffusion windows are in fact so small that a methane molecule just fits into them (kinetic diameter of a methane bead: $\sigma_{\text{CH}_4, \text{CH}_4} = 3.72$ Å; diameter of the windows determined as the largest hard sphere that fits:¹⁴⁹ $d_{\text{wind}} \approx 4$ Å; cf., Table 6.2).

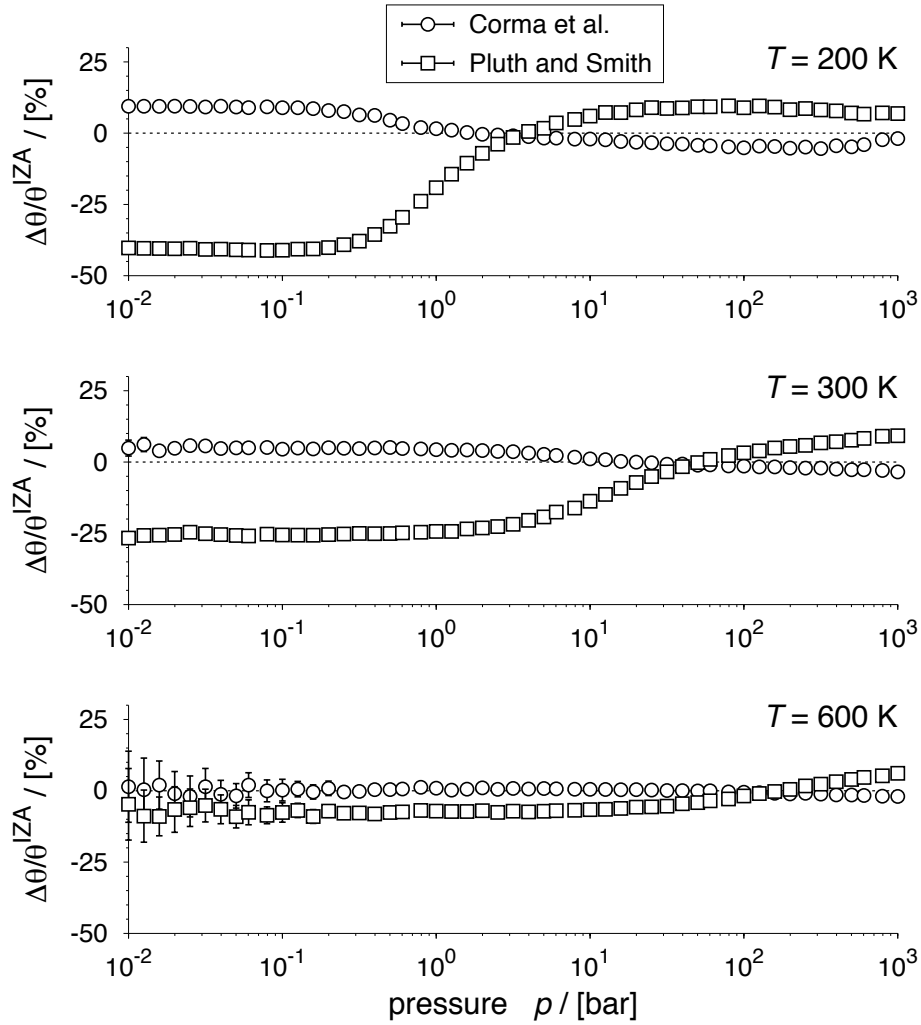


Figure 6.3: Structure influence on adsorption (loading θ) of methane in LTA-type zeolites as a function of pressure, p , and for different temperatures, T . The values obtained from the IZA structure are taken as reference values (i.e., $\Delta\theta^{\text{Corma}} = \theta^{\text{Corma}} - \theta^{\text{IZA}}$).

The influence of the crystal structure on adsorption is moderate, as Table 6.2 shows. Henry coefficients differ between -32% (LTA: Pluth and Smith) and $+23\%$ (ITE: Cambior *et al.*) from the corresponding $K_{\text{H}}^{\text{IZA}}$ of a given framework type. A larger Henry coefficient indicates stronger adsorption at low loadings and can be correlated with a smaller unit cell (cf., Appendix B) and thus cage size. In this context, the earlier conjecture that the average potential in the zeolite cage becomes denser but more attractive

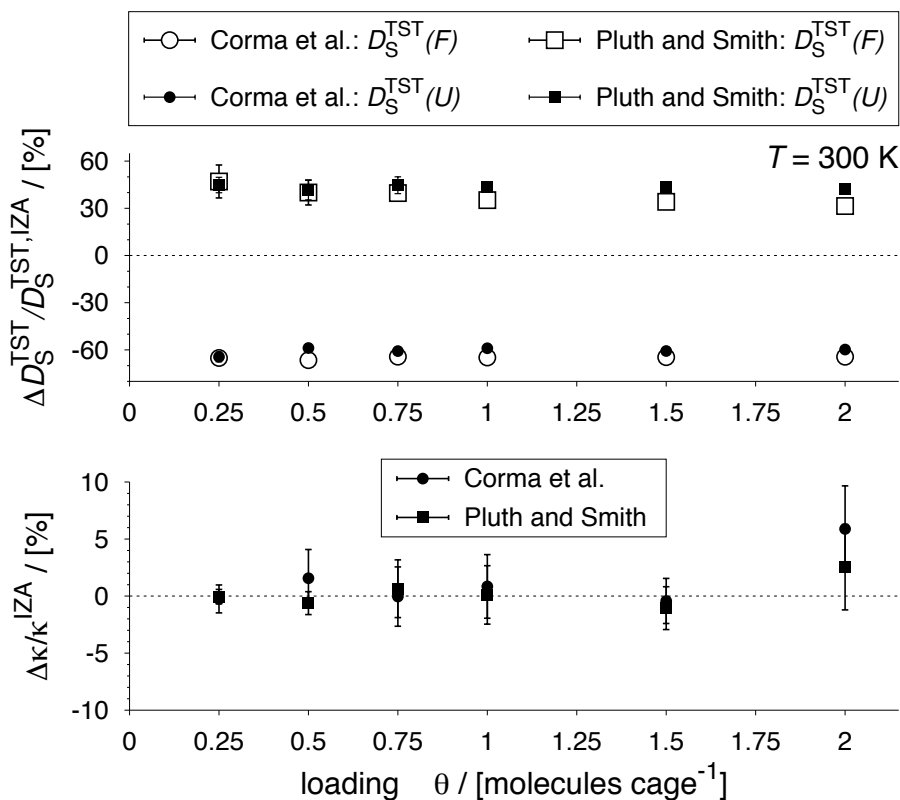


Figure 6.4: Structure influence on the TST self-diffusivity, D_S^{TST} , (top) and on the transmission coefficient, κ , (bottom) of methane in LTA-type zeolites as a function of loading, θ , at 300 K; analogous to Figure 6.3. Note that D_S^{TST} was calculated on the basis of both free-energy, F , and potential-energy, U , profiles of single tagged methane molecules.

in consequence of decreasing cage size is confirmed by Figure 6.6.

Clark and Snurr¹³⁴ as well as Castillo *et al.*¹⁵⁰ have shown that the crystal structure (silicalite) can strongly influence benzene as well as water adsorption because of the importance of electrostatic guest-host interactions. However, Castillo *et al.* have also shown that propane adsorption in silicalite was not influenced by the crystal structure.¹⁵⁰ To sum up, it might thus be concluded that the sensitivity of adsorption to structure variations is weak as long as relatively small non-polar molecules are considered.

The impact of structure variations on the diffusivity is much stronger than on adsorption. In particular, the differences between the diffusion coefficients obtained with the IZA structures and the “true” all-silica crystals are

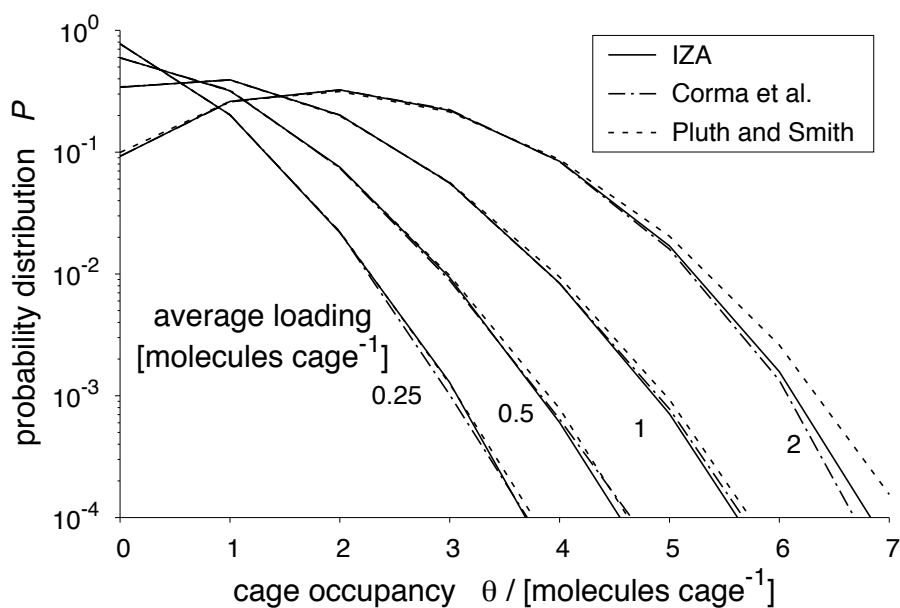


Figure 6.5: Probability distribution of cage occupancy; methane in three different LTA-type zeolites at 300 K and various loadings.

large; the latter ones are smaller by factors of 2.9, 15.3, and 161 for LTA, SAS, and ITE, respectively. As has been already mentioned, the analysis of the free-energy and potential-energy profiles (Figure 6.6) revealed that the entropic diffusion barriers observed in different structures of the same framework type [$-\Delta S/k_B = (\Delta F - \Delta U)/(k_B T)$] hardly varied. Significant changes manifested only for the potential-energy barriers.

In order to better understand the structure sensitivity of the guest diffusivity a parameter study was conducted using the LTA zeolites. Either the unit-cell parameters ($\hat{a}_{UC} = \hat{b}_{UC} = \hat{c}_{UC} = l_{UC}$) were scaled proportionately or the Lennard–Jones size parameter of the guest–host interaction (σ_{O,CH_4}) was changed. From the results shown in Figure 6.7 it can be concluded that enlarging the window area by increasing the unit-cell size by a given fraction (filled symbols) has *precisely* the same effect on the diffusion coefficient as reducing the Lennard–Jones parameter by the same fraction (open symbols which, for a given structure and thus symbol type, lie on the same trend line as the filled ones). Furthermore, the diffusivity is extremely sensitive to only small window-area changes because an enlargement of $\approx 4\%$ can result in an order of magnitude larger diffusion coefficient. Most importantly, however, the differences between diffusion coefficients obtained in different structures

Table 6.2: Henry coefficients and TST self-diffusivities at zero loading of methane at 300 K. Note that the errors are given along with the diffusivities as subscripts and that the maximal relative error amounts to only 11 %.

framework type	d_{wind}	K_{H}	$D_{\text{S}}^{\text{TST}}$
structure	[10^{-10} m]	[10^{-3} mol Pa $^{-1}$ m $^{-3}$]	[10^{-12} m 2 s $^{-1}$]
LTA			
IZA ²²	4.14	4.18	78.08 _{4.30}
Corma <i>et al.</i> ³⁵	4.00	4.45	27.39 _{1.60}
Pluth and Smith ³⁶	4.00	2.85	112.91 _{4.05}
SAS			
IZA ²²	4.21	6.87	118.06 _{5.70}
Wragg <i>et al.</i> ⁶⁵	4.02	9.29	7.72 _{0.83}
Patinec <i>et al.</i> ⁶⁶	4.16	6.94	160.84 _{12.23}
ITE			
IZA ²²	4.15	56.75	155.72 _{0.89}
Camblor <i>et al.</i> ⁶²	3.79	69.99	0.97 _{0.09}

decrease with increasing window size. In other words, the structure sensitivity becomes the more prominent, the tighter the guest molecule fits into the window and the sensitivity will very likely be observed for any cage-type zeolite into which non-polar guest molecules diffuse.

The occurrence of window-area differences between different structures of the same topology type stem partially from different unit-cell sizes, as the (almost) parallel trends of $D_{\text{S}}^{\text{TST}}$ over l_{cage}^2 in the inset of Figure 6.7 suggest. On top of this “scaling effect”, differences in individual crystal atom positions can lead to even more pronounced deviations in diffusivities. This is indicated by the discrepancies between diffusivities obtained with the 4A structure by Pluth and Smith³⁶ and the other two LTA structures. As has been indicated earlier, the 4A structure exhibits much larger differences in atom positions from the IZA structure than the siliceous structure by Corma *et al.*³⁵ does.

In comparison to the previous section, the here investigated structure effect is much stronger. Because the parameter study included also variation of the guest-host Lennard–Jones interaction parameters it is clear that the

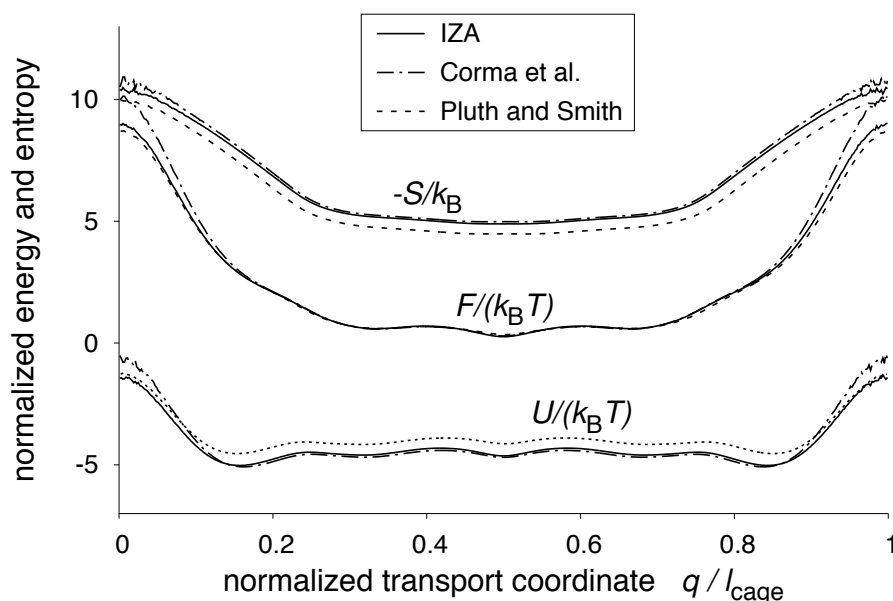


Figure 6.6: Normalized free-energy, $F/(k_B T)$, potential-energy, $U/(k_B T)$, and entropy profile, $-S/k_B$, of a single methane molecule in LTA structures from IZA,²² Corma *et al.*,³⁵ and Pluth and Smith.³⁶ The profiles are based on residence-probability histograms across the unit cells which gave rise to slightly varying cage sizes $l_{\text{cage}}^{\text{IZA}}$, $l_{\text{cage}}^{\text{Corma}}$, and $l_{\text{cage}}^{\text{Pluth}}$.

results of this work are in general very sensitive to the (guest-host) force field parameters. Therefore, Section 6.5 will demonstrate that the force field realistically describes the systems studied in this work by comparing simulation results with experimental data.

In summary, it is concluded that the self-diffusion coefficient can, in fact, be extremely sensitive to very small structural differences supporting experimental observations.¹⁴⁸ This effect might have been underestimated in the past. Therefore, and because there is no standard procedure to create all-silica structures when experimental data are still lacking, it is suggested to always include the actual crystal structure data used in a simulation study, for example in the supporting information accompanying a research article or in the appendix of a monograph.

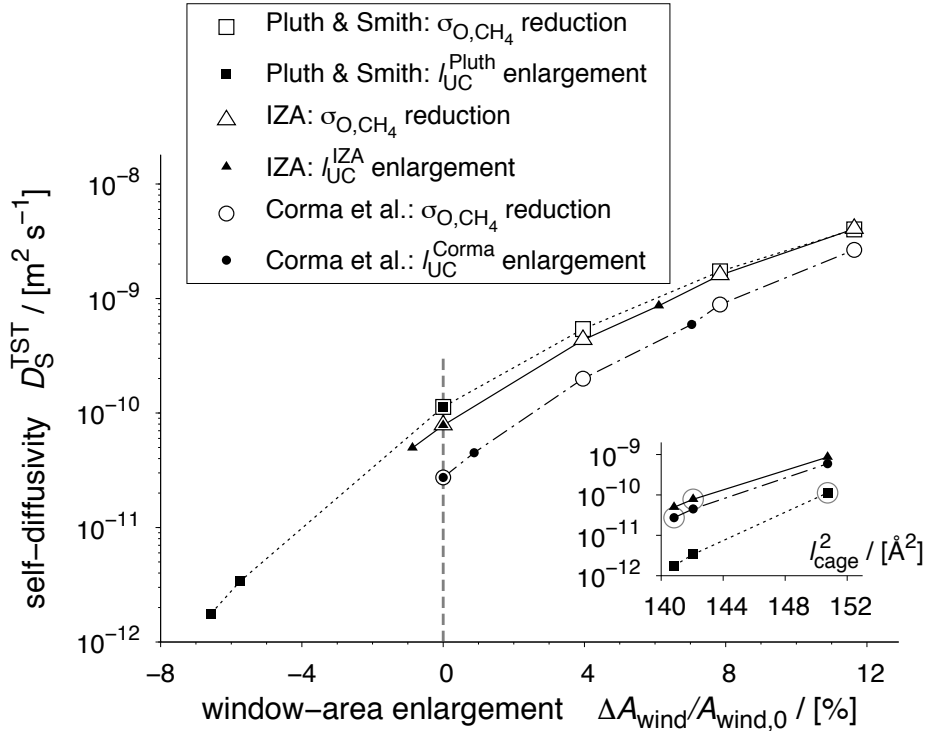


Figure 6.7: Transition state theory self-diffusion coefficient, D_S^{TST} , of methane in LTA structures from IZA,²² Corma *et al.*,³⁵ and Pluth and Smith³⁶ for varying relative window-area enlargement, $\Delta A_{\text{wind}}/A_{\text{wind},0}$. Note that $A_{\text{wind},0}$ represents the window area of the original structure (i.e., with size $l_{\text{UC},0}$) and original Lennard–Jones parameter ($\sigma_{\text{O,CH}_4,0}$). Thus $\Delta A_{\text{wind}}/A_{\text{wind},0} = [(l_{\text{UC}})^2 - (l_{\text{UC},0})^2]/(l_{\text{UC},0})^2$ for unit-cell enlargement and $\Delta A_{\text{wind}}/A_{\text{wind},0} = -[(\sigma_{\text{O,CH}_4})^2 - (\sigma_{\text{O,CH}_4,0})^2]/(\sigma_{\text{O,CH}_4,0})^2$ for interaction parameter reduction. The errors in D_S^{TST} are at maximum in the range of the largest symbol size. The inset shows the variation of D_S^{TST} with squared cage length, l_{cage}^2 ; the large open circles highlight here results obtained with the original structures.

6.3 Framework Flexibility

The role of zeolite-lattice flexibility has been a controversial topic since the very beginnings of simulation studies on guest-molecule adsorption¹⁵¹ and transport^{152,153} in these nanoporous host materials. But most evidence points today at the fact that the influence is minor, particularly for small and/or linear molecules such as *n*-alkanes and *n*-alkenes.^{146,154–156} Purely dynamic

effects, such as the “breathing window”,¹⁵² do most likely not have any significant influence. The term refers to the idea that the window atoms of a zeolite structure move as soon as a guest molecule appears so that the window size increases and the passage of the guest molecule is considerably facilitated. However, “static” effects, such as the average window size, have been proven to be pivotal to transport in zeolites, as the previous section highlighted and References 146,154–156 confirm. In this light, the modeling approach of keeping the zeolite atoms frozen at their crystallographic positions is realistic enough for drawing valid “real-world” conclusions while being efficient for the computationally demanding purposes of this work.

6.4 Thermostats

The main focus of the present work lies on the interface between gas and zeolite space. Newsome and Sholl argued in this context that it is important to account for energy exchange between fluid molecules and zeolite atoms at the external surface.⁸ As rigid zeolite-lattices were always used for reasons given in the previous section an appropriate treatment should be employed to ensure constant temperature at the surface. *NVT* Monte Carlo simulations do by construction not suffer from this issue because the atomic velocities are not explicitly calculated; the influence of the temperature manifests here within the acceptance rules and the temperature distribution can thus be regarded as perfectly homogenous. In molecular dynamics simulations, the situation is however different because the velocities are calculated so that the temperature may show an inhomogeneous distribution along the transport coordinate. To model the energy exchange between fluid molecules and the lattice oxygen atoms and thus to ensure relatively smooth temperature distributions in the vicinity of the gas-solid interface the Lowe–Andersen fluid-interface collision^{106,107} (LA IFC) thermostat was applied in Chapter 8.

The parameters of the thermostat—the collision cutoff radius, $r_{\text{cutoff}}^{\text{LAIFC}}$, and the (here isotropic) collision frequencies in x , y , and z , Γ^{LAIFC} —were roughly estimated from Reference 157 on the basis of a pore size comparison: $r_{\text{cutoff}}^{\text{LAIFC}} = 3.6 \text{ \AA}$ and $\Gamma^{\text{LAIFC}} = 10^{11} \text{ s}^{-1}$. Tests in a *periodic* AFI crystal (methane and ethane at 300 K and infinite dilution) have been performed in order to check the validity of the parameters. On the one hand, the collision frequencies should be chosen as large as possible in order to allow for efficient energy exchange at the crystal surface. On the other hand, too large a Γ^{LAIFC} will result in too much decorrelation of the fluid particle dynamics by an unrealistically high number of collisions which, in turn, will lead to

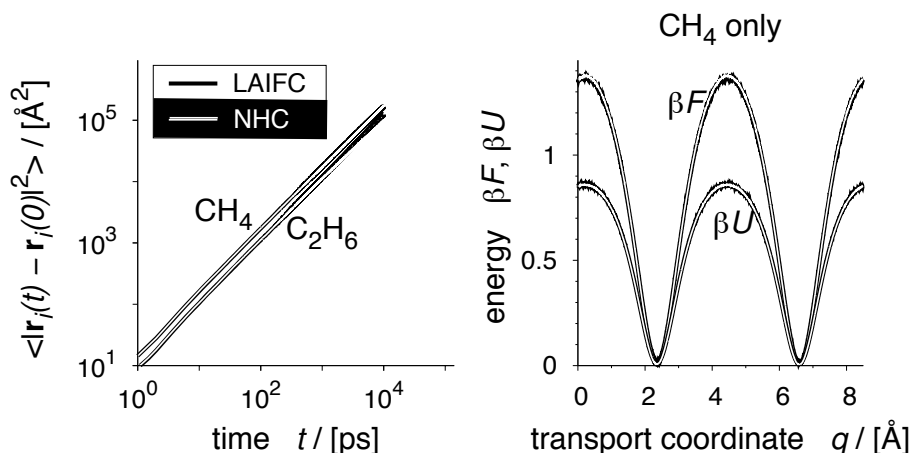


Figure 6.8: Mean squared displacement, $\langle |\mathbf{r}_i(t) - \mathbf{r}_i(0)|^2 \rangle$, over time, t , for methane and ethane (left) as well as free-energy, βF , and potential-energy, βU , profile of tagged molecules as a function of transport coordinate, $q = z_{\text{UC}}$, for methane only (right). The simulations were conducted in a periodic all-silica AFI crystal at 300 K and infinite dilution. The two different thermostats—Nosé-Hoover chain¹⁰⁵ (NHC) and Lowe-Andersen fluid-interface collision thermostat¹⁰⁶ (LAIFC)—yield essentially equivalent results.

a significant decrease in D_S .¹⁴⁶ This effect would be most prominent when there are no other adsorbate molecules around it; that is, at infinite dilution. As can be seen from Figure 6.8, the collision frequencies are small enough to neither change the free-energy profile nor alter the MSD (and thus D_S) when compared to simulations with a Nosé-Hoover chain¹⁰⁵ thermostat.

6.5 Simulations vs Experiments

Because the force field used in this work was carefully developed to reproduce experimental adsorption isotherms^{126,127,131} and has been shown to yield good agreement with diffusion measurements, too,¹⁰ the last section of the present chapter is meant to highlight the quality of the model (and the entire methodology of this work). More specific comparisons to experiments of properties that are central to main aims of this work will be provided in subsequent chapters where it is appropriate. Hence, this section shall provide a “general reassurance” in the methodology only.

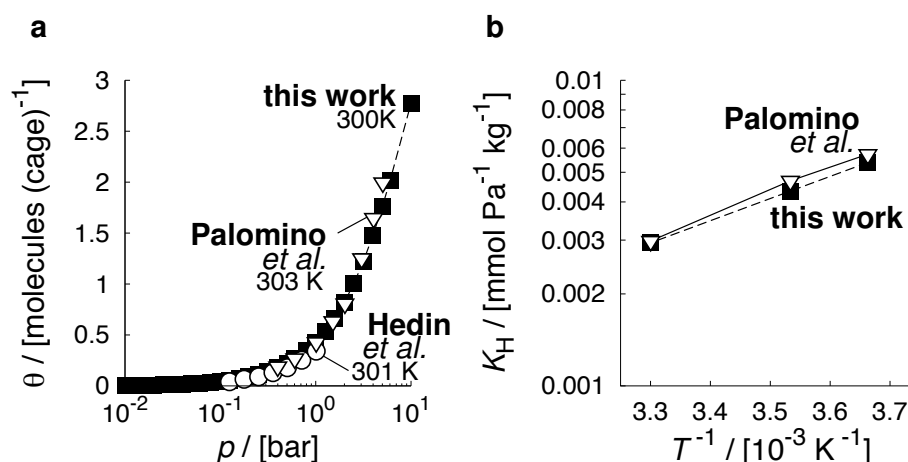


Figure 6.9: Adsorption isotherm at 300 K – 303 K (left) and Henry coefficients, K_H , over inverse temperature (right) for methane in purely siliceous LTA-type zeolites from volumetric and gravimetric measurements (Hedin *et al.*:¹⁴⁰ open circles; Palomino *et al.*:¹⁵⁸ open triangles) as well as from molecular Monte Carlo simulations (this work: filled squares). Note that statistical uncertainties of the simulation results are smaller than the symbol sizes.

6.5.1 LTA

Figure 6.9 shows experimental adsorption data for methane in siliceous LTA,³⁵ which were taken from References 140 and 158, along with molecular simulation predictions of this work. Deviations amount to at most 12 % (Reference 158) and 30 % (Reference 140) between isotherms obtained from measurements and from grand canonical Monte Carlo (Figure 6.9, left). This is a good result considering the fact that rather small perturbations in the crystal structure can easily lead to exactly this magnitude of loading discrepancy (cf., Reference 159 and Section 6.2). The deviations in the Henry coefficients (Figure 6.9, right) range between -1% and -8% , both indicating exceptional good agreement at low loadings.

Hedin *et al.*¹⁴⁰ also determined the self-diffusion coefficient of methane in LTA at 301 K and 1.013 bar ($\hat{=}$ 0.4 molecules/cage) by means of PFG NMR measurements:

- $D_S = 1.42 \cdot 10^{-10} \text{ m}^2/\text{s}$.

Note that the diffusivity is averaged over all three Cartesian coordinates and that LTA is an isotropic medium to methane diffusion such that $D_S = D_{S,x} =$

$D_{S,y} = D_{S,z}$. The molecular dynamics prediction amounts to

- $0.293 \cdot 10^{-10} \text{ m}^2/\text{s}$

at 300 K and 0.4 molecules/cage. The comparison reveals that experiment and simulation deviate by a factor of 4.8. Apart from the fact that deviations in transport coefficients (experiments vs simulations) often span several orders of magnitude,²⁰ PFG NMR measurements are known to notoriously yield inconsistent results for small hydrocarbons in siliceous LTA. Orders-of-magnitude discrepancies in diffusion coefficients are observed just by using crystallites from different synthesis batches.¹⁶⁰ Therefore, a factor of roughly five between the prediction of this work and the measurement by Hedin *et al.*¹⁴⁰ can be regarded as a positive outcome.

6.5.2 AFI

The most frequently studied zeolite in this work is the siliceous AFI structure. Because $\text{AlPO}_4\text{-5}$,⁶¹ the corresponding aluminophosphate, and SSZ-24,¹⁶¹ the siliceous AFI-type zeolite, yield comparable sorption properties of alkanes¹⁶² and because data on the latter structure are limited, experimental data with $\text{AlPO}_4\text{-5}$ are here compared with simulation results using a siliceous AFI structure whose unit cell was yet constructed on the basis of the $\text{AlPO}_4\text{-5}$ crystal structure. Experimental data of methane in $\text{AlPO}_4\text{-5}$ from References 163–167 are displayed in Figure 6.10 along with the simulation predictions of this work. Overpredictions in adsorption are observable (left) up to a factor of 2.4 at 97 K and low pressures ($4 \cdot 10^{-6}$ bar). However, this quickly levels off to negligible differences (7%–18%) from $2 \cdot 10^{-5}$ bar upwards. Importantly, inflection points are well reproduced. They usually give rise to reordering processes of the adsorbate molecules in the host structure and, hence, serve as an additional indicator of realistic modeling apart from the mere quantitative agreement.¹¹⁰ Taken together, it can be concluded that adsorption isotherms are reasonably reproduced.

The comparison of methane self-diffusion coefficients in AFI (Figure 6.10: right) shows that good agreement with the experiments is observable at the lowest temperature (97 K) only. As the temperature is raised, the discrepancies between measurements (open symbols) and predictions (filled symbols) increase to more than an order of magnitude. Note here that the statistical accuracy of the simulation is very high because the error bars, plotted along with the simulation data, are much smaller than the symbol sizes. The experimental error, on the other hand, is rather large with an estimated value of 50% as given in Reference 167 for the diffusivities at 155 K. Such large uncertainties do however not explain a more than ten-fold deviation at 300 K.

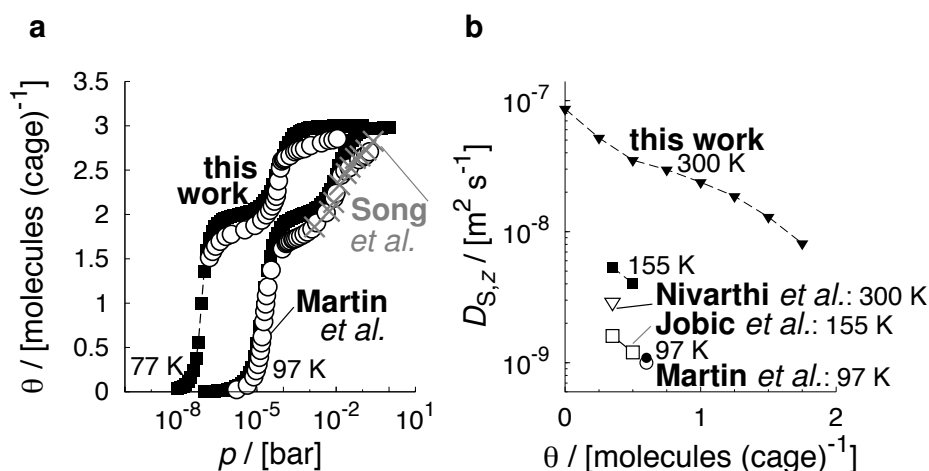


Figure 6.10: Adsorption isotherms at 77 K and 97 K (left) as well as self-diffusion coefficients over loading at various temperatures (right) for methane from measurements in $\text{AlPO}_4\text{-5}$ (Martin *et al.*:^{163,164} open circles; Song *et al.*:¹⁶⁵ crosses; Nivarthi *et al.*:¹⁶⁶ open triangle; Jobic *et al.*:¹⁶⁷ open squares) and from molecular simulations in silicious AFI (this work: filled symbols), respectively.

It can only be speculated about the reasons why the discrepancy increases with temperature. A probable explanation is that differences in $\text{AlPO}_4\text{-5}$ crystallites cause the large discrepancies in the diffusivities, as was also suggested by Jobic *et al.*¹⁶⁷ For example, different $\text{AlPO}_4\text{-5}$ batches could have had different degrees of lattice defects which formed internal transport resistances⁴ in addition to the intrinsic diffusion barriers caused by the perfect nanopore.¹¹⁰ This is quite probable because some zeolitic materials,¹⁶⁸ just as $\text{AlPO}_4\text{-5}$,¹⁶⁹ are sensitive against storage under non-dry conditions. The different degree of (hypothetical) defects may have been pure coincidence, but it is also possible that there is a relationship between intrinsic diffusion barriers, transport resistances by lattice defects and temperature. While the hypothesis is scientifically appealing, its investigation is beyond the scope of this work.

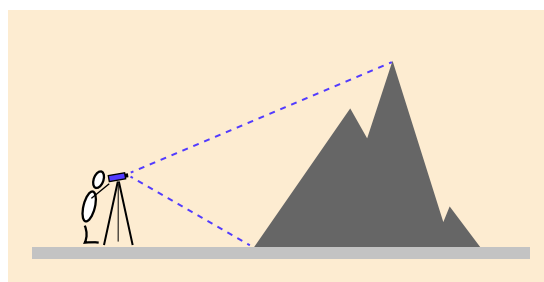
Finally, it is concluded that the methodology chosen for this work describes the systems of interest well enough but it is subject to the limitation of implementing highly ideal zeolite crystals. Therefore, the methodology, in the present form, does not capture nonideality effects such as lattice defects and pore blockage. It is however envisioned that a quantitative assessment of defects (type, number, and location) should be possible with only a few

assumptions. Validation could then be made (and improvements tested) by trial and error in the same spirit as the work by García-Pérez *et al.*¹⁷⁰ who have determined the most probable aluminum distribution within a zeolite unit cell on the basis of a reverse engineering approach.

7

Quantification of Surface Barriers

The mere comparison of transport barriers in the bulk zeolite space (regularly distributed diffusion barriers) with those barriers impeding the transport in the boundary layer between gas phase and zeolite space (surface barriers) is of little interest (Figure 7.1 bottom). This is



because the *effect* that the barrier difference *exerts* on transport/exchange of matter between the two “major phases” (gas and zeolite) represents the main concern of the present work. To arrive at a quantitative assessment of this effect consider in the following a tracer-exchange experiment (or more generally an instationary uptake/release process of guest molecules with a concentration independent diffusivity, as depicted at the top of Figure 7.1) in a zeolite with one-dimensional pores (AFI in the following). Assume that the surface barrier is larger than the diffusion barrier(s) so that the (maximal) tracer flux through the surface is smaller than the (maximal) flux(es) prevailing at the locations of the diffusion barrier top(s) ($j_{\text{surf}}^{\ddagger} < j_{\text{zeol}}^{\ddagger}$). The exchange progress can be calculated on the basis of a simple continuum model, which is described in detail in Appendix C. In all brevity, the spatial set-up (slab model) resembles the repetitive, well-ordered structure of an (ideal) single crystal. The thermodynamic input parameters reflect the adsorption strength of guest molecules in the the host structure and the remaining input parameters quantify the transport behavior (equilibrium fluxes of tagged molecules). Numerical integration yields concentration profiles and, thus, uptake/release curves, rating the exchange progress.

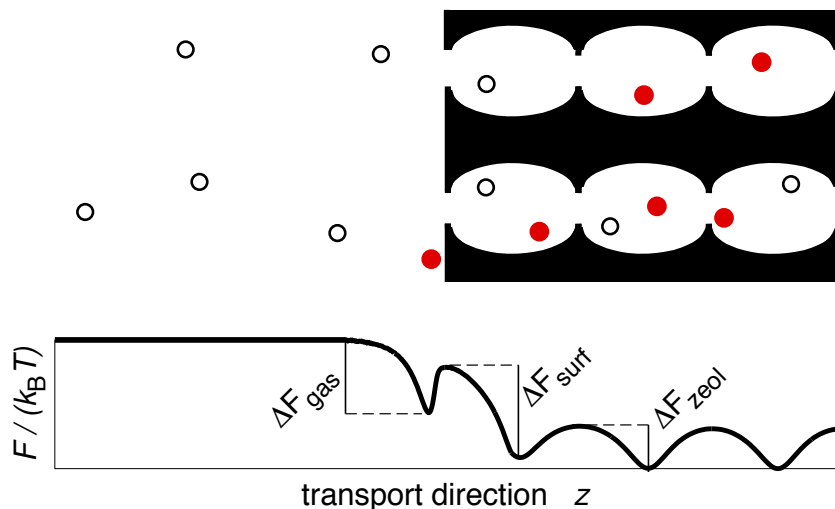


Figure 7.1: Tracer-exchange in one-dimensional pores (top) and corresponding free-energy profile as experienced by tagged molecules along the transport direction (bottom).

The input parameters were deduced from molecular simulations using the Dubbeldam force field.^{126,127} Therefore, the here presented tracer-exchange continuum calculations (TECC) are closely connected to existing chemical systems, thus, transcending the status of physical “toy” models.

Tracer-exchange curves obtained from the continuum calculations are in the following regarded as “raw measurement data” (circles in Figure 7.2), to which two different analytical solutions of the exchange curves are fitted. The first one, Equation 3.4, is often employed to evaluate tracer-exchange (or in general uptake/release) curves under the assumption of negligible surface barriers. The solution provides a single fit parameter: the effective diffusion coefficient, $D_{S,\text{eff}}$. Note that subscript “S” reiterates that, strictly speaking, a tracer-exchange (TE) and thus self-diffusion process is considered. Figure 7.2 shows a typical example, propane-tracer uptake in a small AFI crystal of thickness $\delta = 26$ nm. Large differences between TE continuum calculation and best-fitting analytical solution that neglects surface barriers are observable (dashed-dotted line). The inset highlights the parameter space; that is, the averaged relative sample standard deviation, σ_{rel} , of Equation 3.4 from the TE data in dependence of the parameter ($D_{S,\text{eff}}$) chosen. Manual inspection of the parameter space ensured most probably, if not certainly, the identification of the global minimum. The averaged relative sample standard

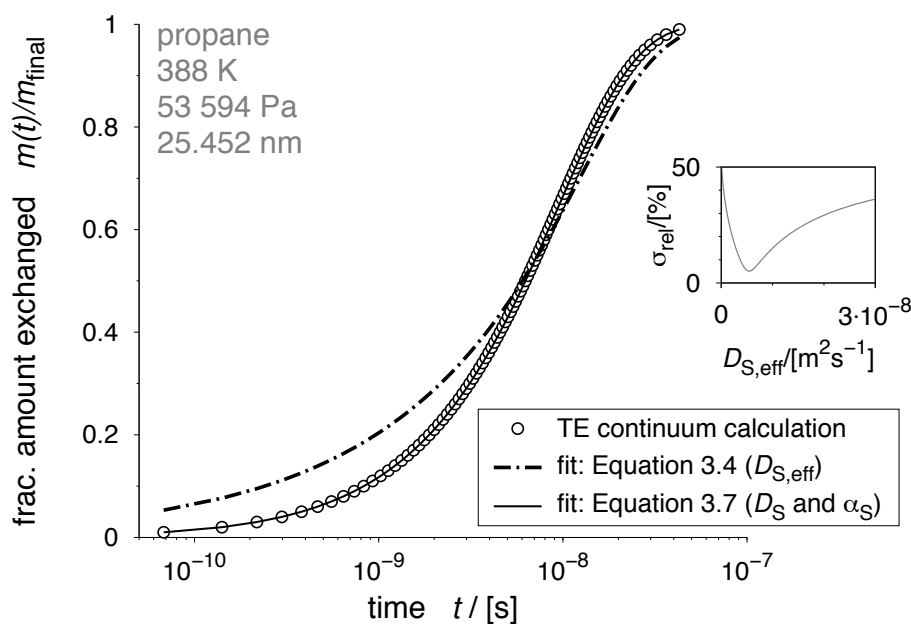


Figure 7.2: Fractional amount of tracer exchanged, $m(t)/m_{\text{final}}$, as a function of time, t , (i.e., tracer-exchange curve) for propane in an AFI zeolite ($T = 388$ K, $p = 53\,594$ Pa, $\delta = 25.452$ nm). Inset: Parameter space of Equation 3.4.

deviations was calculated by:

$$\sigma_{\text{rel}}(D_{\text{S,eff}}) \equiv \sqrt{\frac{1}{N_{\text{samp}}} \cdot \sum_{i=1}^{N_{\text{samp}}} [m(D_{\text{S,eff}}, t_i) - m^{\text{TECC}}(t_i)]^2 / m_{\text{final}}}, \quad (7.1)$$

where $m(D_{\text{S,eff}}, t_i)$ denotes the mass exchanged at time t_i as calculated with the analytical solution using $D_{\text{S,eff}}$, $m^{\text{TECC}}(t_i)$ is the corresponding mass exchanged as obtained from the tracer-exchange continuum calculation, m_{final} the mass exchanged after long time ($\rightarrow \infty$), and N_{samp} the number of sampling points (i.e., time instances), which usually equaled 20.

If, on the contrary, the slow surface transport is accounted for by an appropriate boundary condition in the mathematical description (Equation 3.5), the corresponding best fitting analytical solution (Equation 3.7) perfectly matches the tracer-exchange continuum calculation (solid lines in Figure 7.2). Two parameters are fitted here: the self-diffusion coefficient D_{S} and the tracer surface permeability α_{S} .

If the continuum calculation is repeated with the same input parameters

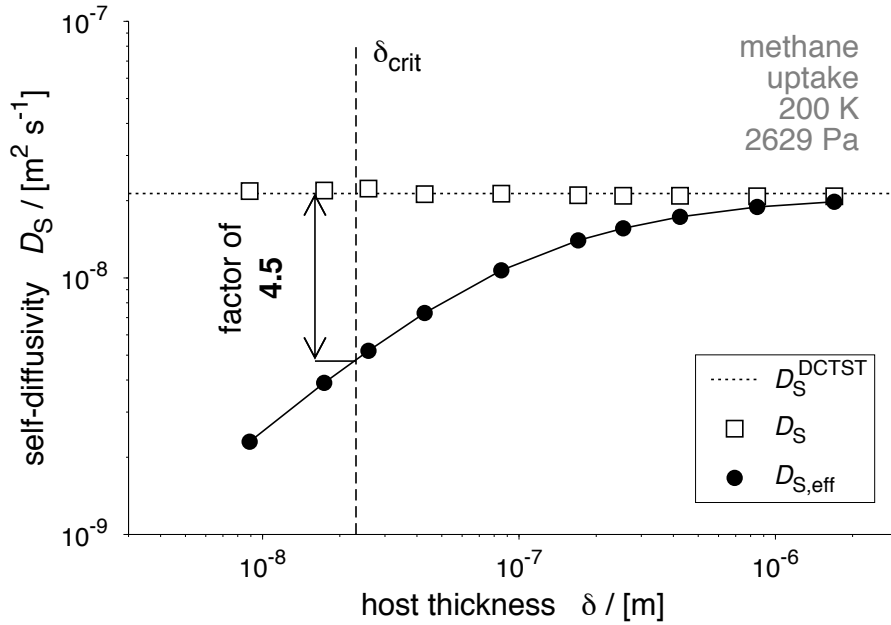


Figure 7.3: Self-diffusion coefficients, D_S , over host thickness obtained from fitting two different analytical solutions ($D_{S,\text{eff}}$: Equation 3.4; D_S : Equation 3.7) to tracer-exchange uptake curves from numerical continuum calculations (cf., Appendix C) along with the self-diffusion coefficient prediction by dynamically corrected transition state theory; methane tracer uptake in AFI, $T = 200$ K, $p = 2629$ Pa.

except for the crystal size which is varied from one calculation to another and if both analytical solutions are fitted in each case, then the fitted diffusivities can be plotted over crystal size δ . As can be seen from Figure 7.3, the effective diffusivity, $D_{S,\text{eff}}$, increases with crystal size (dots). By contrast, the diffusivity obtained with the second analytical solution, D_S , remains constant over δ (squares) and equals the theoretical estimate by dynamically corrected transition state theory (D_S^{DCTST} : dotted line). Therefore, the difference between the effective and the true diffusion coefficient can be used as a measure for surface barriers because it rates the incorporation of an error due to the inadequate use of the no surface-barrier boundary condition.

The main message of Figure 7.3 is that there exists a certain crystal size or thickness for which surface barriers are insignificant because $D_{S,\text{eff}}$ and D_S are similar for this δ and all larger ones. To calculate an estimate of this thickness, δ_{crit} , on the basis of the input parameters to the continuum calcu-

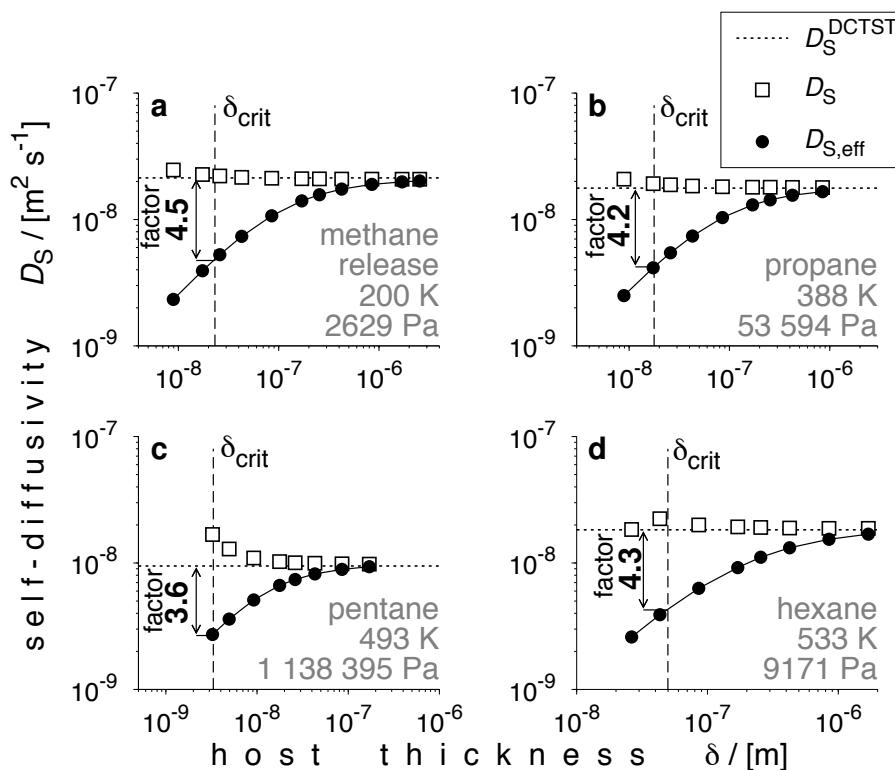


Figure 7.4: Increase of $D_{S,\text{eff}}$ with host thickness for various fluid types. Note that the exchange proceeds through a boundary layer consisting of a single region (1-step) and that the deviations between D_S and D_S^{DCTST} will be elucidated in more detail in Chapter 10.

lations from molecular simulations, a simple criterion is introduced:^{113,114}

$$\delta_{\text{crit}} = 2 \cdot l_{\text{cage}} \cdot \frac{j_{\text{zeol}}^{\ddagger}}{j_{\text{surf}}^{\ddagger}}, \quad (7.2)$$

where l_{cage} denotes the cage, intersection, or main adsorption site separation, respectively (i.e., characteristic length of a single diffusion event in the repetitive crystal structure). Figures 7.3 and 7.4 highlight that the effective self-diffusivity is always smaller than D_S by a factor of 3.6 to 4.5, provided that a crystal of δ_{crit} thickness is considered. Recalling that the relative uncertainty associated with measurements of guest diffusion in zeolites often lies in the range of these factors leads to the conclusion that the criterion is very well suited for the aims of this work. This is because surface barriers will have a considerable effect on the outcome of diffusion measurements

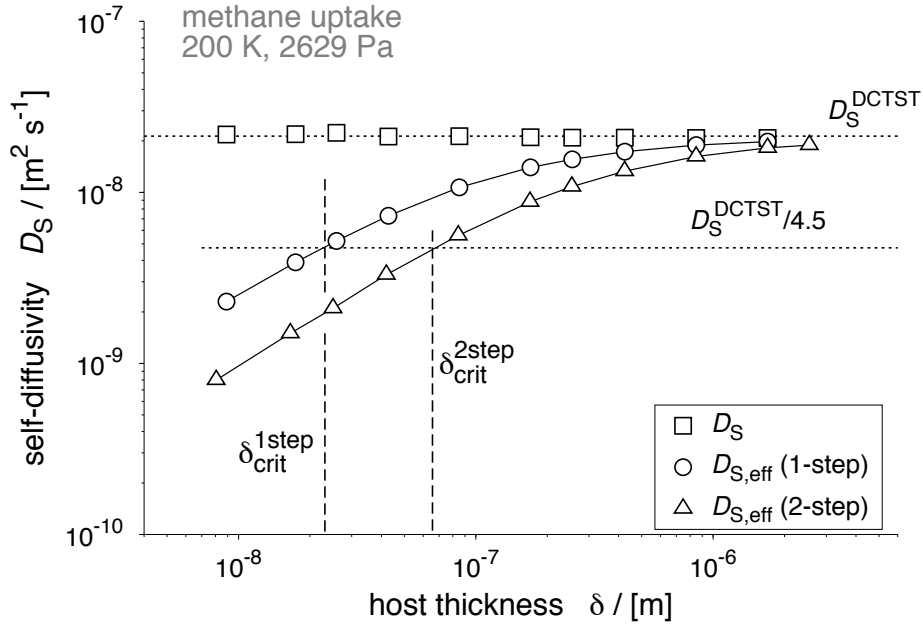


Figure 7.5: Increase of $D_{S,\text{eff}}$ with host thickness for the 1-step exchange mechanism where the boundary layer between gas phase and solid host consists of a single region (zeolite margin only) and for the 2-step exchange mechanism where a second boundary layer (surface adsorption layer) is present. Both critical thicknesses, $\delta_{\text{crit}}^{\text{1step}}$ and $\delta_{\text{crit}}^{\text{2step}}$, identify the situation where the effective diffusivity deviates from the true diffusivity by a factor of 4.5 in the present case of methane tracer uptake in AFI at 200 K and 2629 Pa.

only if crystals of thickness δ_{crit} or smaller are employed. For larger crystals, the effect of surface barriers on the diffusion coefficient measured is hardly distinguishable from the measurement uncertainty.

Note that the critical (crystal) thickness can be regarded as the inverse approach to “correlating surface permeability with intracrystalline diffusivity”⁵ (i.e., α_S/D_S). Because $j_{\text{zeol}}^{\ddagger} \propto D_S$ and $j_{\text{surf}}^{\ddagger} \propto \alpha_S$ one obtains:

$$\delta_{\text{crit}} \propto \frac{j_{\text{zeol}}^{\ddagger}}{j_{\text{surf}}^{\ddagger}} \propto \left(\frac{\alpha_S}{D_S} \right)^{-1}. \quad (7.3)$$

The interface between gas and zeolite space consists in fact of two regions as Figure 7.1 suggests. For this reason, the critical host thickness must account for this. The extension of the continuum calculation to contain a second boundary layer (slab) is straightforward (Appendix C) so that the corresponding 2-step (because two boundary regions) tracer-exchange curves

can be easily calculated, the two analytical solutions again fitted and the resulting diffusivities plotted over host size/thickness (Figure 7.5). A similar, yet shifted dependency of the 2-step $D_{S,\text{eff}}$ over δ is appreciable when compared to the 1-step $D_{S,\text{eff}}$. The corresponding critical thickness, $\delta_{\text{crit}}^{\text{2step}}$, can be calculated in analogy to two parallel resistances in electrical engineering via:

$$\delta_{\text{crit}}^{\text{2step}} = 2 \cdot l_{\text{cage}} \cdot \frac{j_{\text{zeol}}^{\ddagger}}{\left[1/j_{\text{surf}}^{\ddagger} + 1/j_{\text{gas}}^{\ddagger}\right]^{-1}}, \quad (7.4)$$

where $j_{\text{gas}}^{\ddagger}$ denotes the equilibrium flux through the dividing surface between gas phase and second boundary region (surface adsorption layer); that is, at the location where the free-energy profile attains a constant value along the transport direction (cf., Figure 7.1 bottom). Note that—unless differently indicated—the critical host thickness will refer to the 2-step exchange mechanism in subsequent chapters. Finally, the critical thickness criterion applies “exactly” to zeolite crystals with one-dimensional, unconnected channels and to membranes and sheets of any pore connectivity only. However, it is in the remainder assumed that the criterion will also provide a good first estimate of the critical host size of crystals with more complicated pore systems (e.g., silicalite/MFI) provided that the transport direction with the smallest intracrystalline diffusion resistance(s)/barrier(s) is considered.

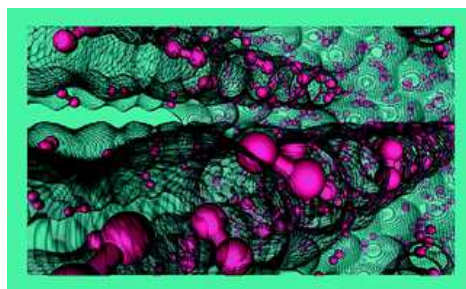
Part IV

Results

8

In-Depth Analysis of Interface Dynamics

With the aid of molecular simulation techniques (molecular dynamics, grand canonical Monte Carlo, and reactive flux simulations), the influence of the external surface on the equilibrium permeation of methane and ethane into and out of an AFI-type zeolite crystal has been studied at various pressures and 300 K. Extended dynamically corrected transition state



theory, which has been proven to describe the transport of tracers in periodic crystals correctly, has been applied to surface problems. The results suggest that the molecules follow paths that are close to the pore wall both in the interior and also at the crystal surface. Moreover, the recrossing rate at the surface turns out to be nonnegligible, yet, in contrast to the intracrystalline recrossing rate, remains almost constant over loading, thus, providing indication to diffusive barrier crossing at the crystal surface. The critical crystal thickness, beyond which surface effects can be certainly neglected, is computed on the basis of flux densities, where differently prepared crystal surfaces gave rise to comparable surface flux densities. However, the fact that the interface between gas and solid consists of two subregions measurably decreases the transport through the crystal surface region at low loadings and, thus, low pressures. Entrance/exit effects, in the present cases, are yet negligible from a diffusion measurement point of view because the critical thicknesses do not reach the sizes of crystals employed in experiments.

8.1 Introduction

Nanoporous materials, such as zeolites, metal–organic frameworks (MOFs), and carbon nanotubes (CNTs), represent a very important class of solid materials. In some cases, they have already made a significant industrial impact (zeolites). In other cases, their peculiar properties make them a promising candidate for novel applications (MOFs and CNTs). Using the example of zeolites, which have a long research history, one can grasp to what extent nanoporous materials can be potentially used. Starting with rather simple adsorption for gas separation (N_2 – O_2 separation), over ion-exchange processes (water softening), to heterogeneously catalyzed reactions (cracking of alkanes), only the most well-known applications of zeolites are listed. However, they may even be used for microelectronics and medical diagnosis⁵¹ and have the potential to serve as permanent medical material to be implanted into human bodies.²¹ The latter two applications crucially depend on a very good understanding of adsorption and diffusion of condensed matter into and out of the zeolite crystals.

Although zeolites have been the focus of innumerable works addressing adsorption, transport, and reaction issues of adsorbed matter, there is still considerable confusion even about the simpler processes of adsorption and transport inside the micropores. Consider for example diffusion: although it seems that, by now, fluid diffusion in the pores of zeolite crystals is understood quite well (e.g., see References 110,116,117 and references therein) there is still a lack of understanding why and for which adsorbent–adsorbate systems so-called surface effects have a crucial impact on the permeation into and out of the crystals. These effects are speculated to be one of the most prominent reasons to why diffusion coefficients obtained from macroscopic methods (e.g., uptake experiments) and microscopic methods (e.g., PFG NMR and quasi-elastic neutron scattering) sometimes deviate considerably for one and the same system.^{1,2} Recent works of Kärger and co-workers using the interference microscopy (IFM) technique indicate that there are systems which exhibit strong surface effects while other systems are entirely controlled by slow intracrystalline diffusion.^{142,171} The IFM technique makes use of the refractive index of the zeolite + adsorbate system which directly correlates to the prevailing loading inside the zeolite crystal,¹⁴² so that two-dimensional concentration profiles can be measured transiently. In spite of the relatively high spatial resolution of the concentration profiles ($\approx 0.5 \times 0.5 \mu\text{m}^2$), it is difficult to trace the reasons why surface barriers occur for a given adsorbent–adsorbate system on the basis of IFM. Owing to their detailed insights simulations can help finding those reasons and, in the

best case, provide a mechanism, hence, complementing the experimental observations made; for example, why no surface barriers are observed by means of IFM or why they are very large.

Several molecular simulation studies were conducted that investigated the effect of external surfaces on the adsorption and desorption of fluids.^{8,9,172–176} On the basis of molecular dynamics (MD) simulations, Schüring *et al.*¹⁷⁵ observed that, for neopentane-like systems, the condition of single-file diffusion leads to an accelerated surface exchange rate but to a slower intracrystalline exchange. Gulín-González *et al.*⁹ performed MD tracer-exchange experiments of a small heavy Lennard–Jones fluid leaving an $\text{AlPO}_4\text{-5}$ crystal. The authors suggested that large potential energy differences between the intracrystalline and intercrystalline space caused the tracer-exchange profiles along the pores of small crystals to be flat, thus, indicating a large surface transport resistance.⁹ Because the profiles became more curved as the crystal size increased, the influence of the surface transport leveled off with increasing crystal size. Arya *et al.*¹⁷² studied methane permeation through an $\text{AlPO}_4\text{-5}$ crystal using dual-control volume grand canonical MD (DCV-GCMD) simulations and equilibrium MD simulations. They showed that the effect of external surface barriers diminished as temperature and loading increased. On the basis of a simple activated transport model, they furthermore showed that the surface effect was more pronounced for large molecules, that is, when the ratio of molecule size to pore size approached unity. Newsome and Sholl^{8,176} confirmed these general observations for various fluids through a silicalite crystal and proposed their own method that uses quantities that can be readily accessed from equilibrium MD simulations for predictively assessing the importance of surface effects. Ahunbay *et al.*¹⁷³ performed DCV-GCMD simulations of methane through a silicalite crystal and they observed a coupling between entrance and exit surface resistances, when methane permeated from one gas reservoir (control volume 1) through the crystal to another gas reservoir at the opposite side of the crystal (control volume 2). When the resistances were computed by separate simulations, that is, one control volume was located inside the bulk gas phase and the other one inside the zeolite, it turned out that the resistance to adsorption was stronger than that to desorption.¹⁷³ It should be noted here that Arya *et al.*¹⁷⁷ showed that DCV-GCMD simulations can severely suffer from technical issues such as not adding streaming velocities on newly inserted molecules and choosing a low ratio of stochastic to deterministic steps.

Some of the works mentioned above computed equilibrium fluxes at the external crystal surface. These were either computed by counting the molecules passing a predefined plane that separates gas phase and zeolite space,

or the fluxes were computed on the basis of adsorption/desorption rates via free/potential-energy profiles. In either case, a phenomenon was usually disregarded that has been shown to be of great significance to self-diffusion of gas molecules inside the bulk zeolite: the so-called recrossing events.^{109,110,116,117} Recrossing events stem from viewing the self-diffusion of adsorbates in zeolites as a random walk on a lattice. A molecule can jump from one adsorption site to an adjacent one at a rate that is determined by two factors: the free-energy barrier that impedes the jump and the likelihood that a jump attempt is eventually successful. The second factor, which is, in most cases, a function of zeolite loading, is mainly influenced by these recrossing events which decrease the probability of successful jumps. The theory that comprises the underlying physics is known as “dynamically corrected transition state theory” (DCTST). Therefore, the present chapter uses DCTST in order to compute equilibrium transport rates of methane and ethane inside the micropores and at the external surface of an all-silica AFI-type zeolite crystal to eventually assess the importance of surface effects on the permeation of adsorbates into and out of the crystal.

The remainder of this chapter is structured as follows. In Section 8.2, the methodology specifically applied in this chapter will be described. Apart from modeling details (Subsection 8.2.1 and 8.2.2), the main ideas behind extended dynamically corrected transition state theory will be presented (Subsection 8.2.3). The simulation results will subsequently be reviewed and discussed (Section 8.3). Section 8.5 concludes the results from a broader point of view, whereas Section 8.6 provides supplementary data.

8.2 Methodology

8.2.1 Zeolite Description and Simulation Box

The zeolite under investigation is a purely siliceous AFI-type which exhibits parallel pores without interconnections. As experienced by methane molecules, the pores are slightly corrugated. Narrower regions with a diameter of approximately 7.3 Å (called windows in the following) are followed by wider regions of a diameter of ≈ 10 Å (called cages), as seen in Figure 8.1. The windows are formed by a ring of 12 oxygen atoms where two O-atoms are connected through one and the same silicon atom. A single unit cell consists of 96 oxygen and 48 silicon atoms, and its dimensions are 23.774 Å, 13.726 Å, and 8.484 Å in x , y , and z direction, respectively. The original crystal structure, as taken from Reference 61, was converted from monoclinic to orthorhombic for computational efficiency and thus accommodates

four cages in total.

The crystals were aligned in the (0 0 1) direction (Cartesian z direction). The simulation box included two unit cells in x , three in y , and four in the z direction which were centered in the simulation box. In addition, fractional unit cells that were cleaved perpendicular to z were “glued” on the last unit cells in the z direction. Two conceptually different truncations were chosen for one and the same simulation box:

1. On the negative z side of the zeolite plate, the window O-atoms formed the outmost zeolite atoms.
2. On the positive z side, those six oxygen atoms that form the center of the cages concluded the crystal.

This methodology permitted studying the role of the truncation plane systematically.

As can be seen in Figure 8.1 (bottom), the crystal accommodated ten full cages. The length of the zeolite space in the z direction, as measured by the position of the outmost oxygen atoms on either side, was 44.4 Å; the length of the gas phase was 50 Å. The simulation box consisted thus roughly of 50 % zeolite volume and 50 % gas volume. Periodic boundary conditions were used in all directions, creating an infinite repetition (in the z direction) of infinitely large (in x and y) zeolite plates and gas chambers. At this point, care should be taken in calling such systems zeolite membranes. This is because zeolite membrane, in the conventional sense of the term, usually relates to composites of a nonzeolitic support layer and a polycrystalline zeolite film (intergrown grains) that may be covered by an amorphous silica layer, depending on the postsynthesis treatment.^{178,179} In this context, it is worth mentioning that Caro and Noack¹¹ have reviewed recent developments and progress of such zeolite membranes. However, note that the term “zeolite membrane” refers in the present work to the perfect, single-crystal zeolite film of such composite membranes, if not indicated differently.

There is still a lack of knowledge with respect to the molecular structure of the surface of zeolite crystals. For example, cleavage of the zeolite structure will introduce silanol groups (chemical saturation of the external surface) which will have a different structure as compared to the cleaved surfaces considered in this work. This lack of molecular information renders a direct comparison with experimental data difficult. However, in order to gain some insights into the role of the surface, the above-described methodology (two different truncation planes) may be considered worthwhile. Nonetheless, it should be mentioned that Thompho *et al.*¹²⁴ introduced a potential for such silanol groups on a silicalite-1 surface and that future studies should take into account the surface saturation. Another important point with respect

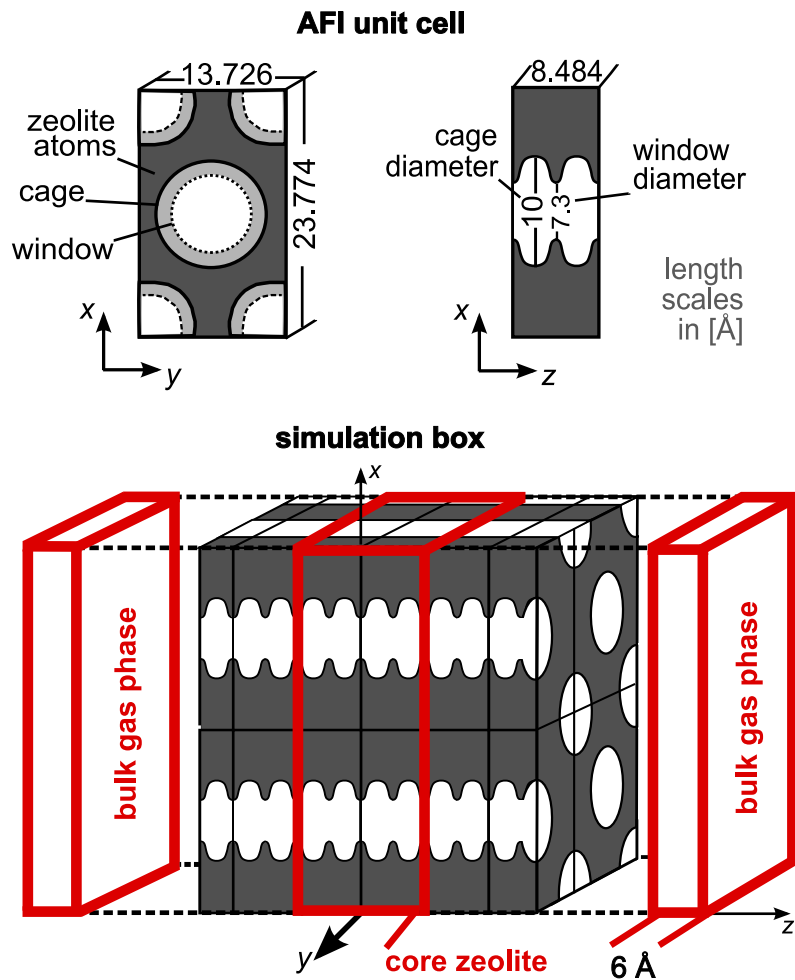


Figure 8.1: Top: sketch of the AFI unit cell—two different projections. Dark gray areas correspond to areas/volumes occupied by zeolite atoms, being thus inaccessible for adsorbate molecules of the size of a methane molecule or larger. White areas indicate accessible volumes to adsorbates and light gray rings in the x - y projection indicate the varying pore diameter along z . Note that the original monoclinic structure was converted to an orthorhombic unit cell. Bottom: simulation box (cut along x - z plane at $y = 0$ Å). Ten entire cages are accommodated in each pore of the crystal. The windows of the AFI structure form the entrance to molecules coming from the left-hand gas phase ($z < 0$); the cages conclude the crystal on the right-hand side ($z > 0$). The thick (red) lines indicate the volumes of bulk gas phase and core zeolite, that is, where the gas concentration and the zeolite loading were sampled.

to studying a realistic crystal are lattice defects¹⁸⁰ and crystal intergrowth,⁴⁰ all of which are not considered in this study but which are very likely to be found in real zeolite crystals. From another point of view, this underlines the complementary relationship between experiments and simulations. As soon as there will be experimental data of the systems under investigation, those influences may be estimated from the comparison between simulation data using highly idealized crystals and experimental results where nonidealities certainly occur.

8.2.2 Simulation Details

Molecular dynamics (MD) simulations in the NVT ensemble were performed in the present chapter whereby the crystal structure was held rigid for reasons of computational efficiency and structural concerns.¹⁴⁶ The Lowe–Andersen thermostat for interface-fluid collisions¹⁰⁶ (LA IFC) was used in order to maintain the temperature during the production phase. This thermostat mimics the energy exchange between vibrating pore atoms and adsorbate molecules correctly for carbon nanotubes.¹⁰⁶ As for zeolites, there are no parameters available. Therefore, the collision frequencies were estimated from published carbon nanotube (CNT) simulations.¹⁰⁷ The frequencies do, in fact, not vary much for methane in CNTs whose radii are of similar size as the mean AFI pore radius.¹⁵⁷ Note that, due to the corrugation of the AFI pore wall, the region to be thermalized (on basis of $r_{\text{cutoff}}^{\text{LAIFC}}$) was not a cylindrical shell, as was the case for the smooth CNTs. Rather explicit adsorbate–zeolite atom distances were determined for testing, if an adsorbate was in thermalizing distance to a zeolite atom, and the Verlet lists of the energy and force calculation helped speeding up this search.

Tests in a periodic AFI crystal revealed that, at zero loading, perturbing the chosen frequencies by a factor of 2 yielded identical self-diffusivities. The collision frequency was set to $\Gamma = 10^{11} \text{ s}^{-1}$ (equal thermalization in all directions) and the cutoff radius was set to 3.6 Å. A final comparison between the LA IFC thermostat and the Nosé–Hoover chain thermostat¹⁰⁵ in a periodic AFI crystal (cf., Figure 6.8) shows that both the free-energy profile along the diffusion direction z and the mean-squared displacement (MSD) do not differ. Finally, all simulations were performed at a temperature of 300 K.

Methane and ethane were modeled as CH_i beads of united atoms. The force field of Dubbeldam *et al.*^{126,127} was used for adsorbate–adsorbate and adsorbate–zeolite interactions. This force field was specifically developed to reproduce adsorption isotherms of alkanes in zeolites accurately. In addition, Beerdsen and Smit¹⁸¹ showed that this force field even yields a good descrip-

tion of the loading dependence of the methane self-diffusion coefficient in MFI.

Newton's equations of motion were integrated numerically using the velocity-Verlet algorithm and a time step of 1.0 fs for methane and 0.5 fs for ethane simulations, respectively. A Monte Carlo initialization phase of several thousand translational and rotational moves (the latter only for ethane) as well as a velocity-scaling MD phase (≈ 100 ps) with final equilibrium NVE-MD phase (≈ 1 ps) preceded the production runs.

8.2.3 Extended Dynamically Corrected Transition State Theory

Several publications showed that the self-diffusion of molecules adsorbed in zeolite materials can be accurately computed by the approach of extended dynamically corrected transition state theory^{109,110,116,117} (extended DCTST). As the self-diffusion coefficient, D_S , is, in general, a function of loading for a given adsorbate-zeolite system at a given temperature, extended DCTST provides a valuable means to discuss the loading dependence of D_S on the basis of those two factors that comprise the theory:

1. Free-energy contribution (static property). Usually, one of the Cartesian directions is identified as the transport coordinate (historically: reaction coordinate), q , that measures the progress of a jump event from one cage, q_A , through the window (i.e., transition state \ddagger), q^\ddagger , toward the target cage, q_B ; note that $q \equiv z$ in the following. Free-energy profiles along the transport coordinate, $F(q)$, are calculated from residence histograms of a tagged adsorbate molecule, as obtained from the simulations. Finally, the relative conditional probability, $P(q^\ddagger)|_{q(0) < q^\ddagger}$, to find the molecule on top of the barrier (i.e., in the window region) provided that it has been located in cage A before the hop attempt [i.e., $q(0) < q^\ddagger$] can be computed according to:

$$P(q^\ddagger)|_{q(0) < q^\ddagger} = \frac{\exp[-\beta F(q^\ddagger)]}{\int_{q^\ddagger} \exp[-\beta F(q)] dq}, \quad (8.1)$$

where the integration limits highlight that cage A is defined by the encompassing transition states \ddagger and \ddagger (cf., Section 4.4).

2. Flux through dividing surface (dynamic property). The idealized TST flux through the dividing surface at q^\ddagger is approximated by kinetic gas

theory so that the jump frequency from A to B, $k_{A \rightarrow B}^{\text{TST}}$, reads:

$$k_{A \rightarrow B}^{\text{TST}} = \sqrt{\frac{k_{\text{B}}T}{2\pi m}} \cdot P(q^\ddagger) \Big|_{q(0) < q^\ddagger}. \quad (8.2)$$

k_{B} is Boltzmann's constant, T the absolute temperature, and m the mass of the bead(s), or atom(s) involved in the transport coordinate (in this chapter: center-of-mass of entire molecule). Spurious crossings are accounted for by computing the reactive flux correlation function^{110–112} (RFCF), $\kappa(t)$:

$$\kappa(t) = \frac{\left\langle \dot{q}(0) \cdot \text{H}[q(t) - q^\ddagger] \cdot \widehat{\delta}[q(0) - q^\ddagger] \right\rangle}{\left\langle 0.5 \cdot |\dot{q}(0)| \cdot \widehat{\delta}[q(0) - q^\ddagger] \right\rangle} \quad (8.3)$$

where $q(0)$ and $\dot{q}(0)$ denote the initial position and velocity of the molecule, respectively. H is the Heaviside function [$\text{H}(x) = 1$ for $x \geq 0$ and $\text{H}(x) = 0$ otherwise] and $\widehat{\delta}(x)$ the Dirac delta function [$\widehat{\delta} = \infty$ for $x = 0$ and $\widehat{\delta} = 0$ otherwise]. Starting configurations for the RFCFs were generated using an MD-based approach (BOLAS¹²² and EPS¹²³). Otherwise, the procedure for the RFCF simulations is the same as in Reference 110. The plateau of the transient RFCF, κ , yields the (velocity-wise averaged) fraction of hop attempts from the barrier toward target cage B. It is referred to as the transmission coefficient or dynamical correction factor and may attain values between zero and unity only.

The methodology described above is also known as the Bennett–Chandler approach.^{111,112} It has often been used in order to understand diffusion in nanopores at the limit of infinite dilution; see, for example, the numerous references in Reference 110. The key to extending DCTST to diffusion at finite loadings is the computation of effective hopping rates of a single tagged molecule. Surrounding adsorbate molecules are viewed as an additional external field to the tagged molecule, and naturally fluctuating cage occupancies are crucial to the hopping rate computed.¹¹⁶ In fact, this viewpoint is similar to what Chandler¹¹² anticipated for the isomerization of *n*-butane: the rate constant would strongly depend on the solvent density that exerts an external field to *n*-butane.

The self-diffusion coefficient, D_{S} , can be calculated on basis of DCTST by:^{109,110}

$$D_{\text{S}} = \frac{1}{2d} \cdot \kappa \cdot k_{A \rightarrow B}^{\text{TST}} \cdot l_{\text{cage}}^2, \quad (8.4)$$

where d denotes the dimensionality of the pore system (here: $d = 1$) and l_{cage} the separation of hopping sites in the zeolite structure (here: $l_{\text{cage}} = 4.242 \text{ \AA}$).

Transition state theory has also been used to characterize equilibrium transport at crystal surfaces.^{9,182} However, the dynamic correction (spurious crossings) in such crystal surface transport situations have so-far been neglected.

Critical Crystal Thickness

In order to assess the relative importance of surface transport effects, Arya *et al.* pointed out that any such assessment “must include an estimate of the critical crystal dimension beyond which the barrier resistance becomes insignificant”.¹⁷² They, therefore, introduced a critical ratio of the two lengths involved, that is, of the pore length to the length of the pore exit region, and, on the basis of a simple activated transport model, provided a good estimate for this ratio. In a similar manner, and also using a simplified equilibrium model, Newsome and Sholl^{8,176} defined a critical crystal thickness, δ_{crit} . Using the example of adsorption, the model of the authors finally reduced to the following equation:¹⁷⁶

$$\frac{R_{\text{ads}}}{R_{\text{intra}}} \approx \frac{D_{\text{C}}(c_{\text{feed}})}{\alpha \delta} \frac{c_{\text{feed}}}{p_{\text{feed}}}, \quad (8.5)$$

where R_{ads} and R_{intra} denote the adsorption resistance and intracrystalline transport resistance, respectively, D_{C} is the corrected diffusivity, α the surface permeability rating the surface transport, δ the crystal thickness, and c_{feed} is the concentration inside the zeolite in equilibrium with p_{feed} , the latter of which being the gas-phase pressure outside the crystal. Note that Newsome and Sholl defined α as the derivative of the flux density with respect to pressure, $\alpha \equiv dj/dp$.⁸

This work exploits the computation of DCTST fluxes for a relative assessment of surface transport effects. The molar flux density in terms of DCTST is given by:

$$j_{\text{A} \rightarrow \text{B}} = \kappa \cdot \sqrt{\frac{k_{\text{B}}T}{2\pi m}} \cdot c(q^{\ddagger}). \quad (8.6)$$

The computation of concentration profiles, $c(q)$, takes place in parallel to the computation of residence histograms. The two quantities and the free-energy profile stand in a direct relationship $\{P(q) \propto c(q) \propto \exp[-\beta F(q)]\}$. Note that the simulations of this work showed that computing TST fluxes (i.e., Equation 8.6 and setting $\kappa = 1$) is exactly equivalent to computing one-way fluxes.⁸ This indicates that the temperature distributions along the transport coordinate were homogeneous enough to apply kinetic gas theory for estimating the ideal flux through the dividing surfaces.

Because a transport resistance is inversely proportional to the corresponding flux, the definition of a critical crystal thickness used in the present work can, in analogy to the work by Newsome and Sholl,⁸ be interpreted as equating the transport resistance at the external surface (or rather in the boundary layer between gas and zeolite) with the intracrystalline transport resistance:

$$\delta_{\text{crit}} = 2 \cdot l_{\text{cage}} \cdot \frac{j_{\text{zeol}}^{\ddagger}}{\left[1/j_{\text{surf}}^{\ddagger} + 1/j_{\text{gas}}^{\ddagger}\right]^{-1}}. \quad (8.7)$$

In essence, this length is the minimal crystal dimension in tracer-exchange experiments for which the surface transport resistance can, in a good approximation, be neglected in the evaluation model, considering the usually encountered high experimental measurement uncertainties (cf., Chapter 7).

Most previous studies viewed the transport through the boundary layer as a single-step process. That is, a molecule that is initially located in the last zeolite cage hops out onto the external surface and is then considered to have left the zeolite. Equation 8.7 highlights however that a two-step boundary permeation process forms the basis of the critical crystal thickness of this work. That is, this work considers also the slow hopping from the external surface adsorption layer to the gas phase. Therefore, a single-step critical thickness, $\delta_{\text{crit}}^{\text{1step}}$, neglecting the second step is calculated along with the two-step δ_{crit} from Equation 8.7 to rate the importance of the second step:

$$\delta_{\text{crit}}^{\text{1step}} = 2 \cdot l_{\text{cage}} \cdot \frac{j_{\text{zeol}}^{\ddagger}}{j_{\text{surf}}^{\ddagger}}. \quad (8.8)$$

8.3 Simulation Results

During the MD simulations the core-zeolite loading and the bulk gas-phase concentration were monitored. Core and bulk, in this context, means that it was sampled inside volumes where effects originating from the crystal surfaces can be certainly neglected (zeolite loading: the $2 \times 3 \times 2$ innermost unit cells of the simulation box; gas-phase concentration: volumes at either end of the simulation box with a width of 6 Å in z direction). The data from these MD simulations that explicitly include a zeolite *and* a gas space agree very well with adsorption isotherms obtained from grand canonical Monte Carlo (GCMC) simulations in a periodic AFI crystal that were performed with the same potential parameters (Figure 8.2). Only in the limit of very large pressures ($p \rightarrow 1000$ bar) do the results start to deviate which is due most likely to the formation of a liquid film on the external surface that does affect the bulk gas-phase concentration. The procedure is thus thermodynamically sound up to several hundred bar. However, it must be pointed out that the potential used is one of the most critical issues in molecular simulation studies. In Figure 8.2, previously published adsorption isotherms simulated by Maris *et al.*¹⁸³ are plotted for comparison. Although the isotherms of this work and the ones determined by Maris *et al.* are qualitatively similar for ethane, the saturation loadings for ethane differ, and the methane isotherms have even different evolutions. Because the potential of Maris *et al.*¹⁸³ was not specifically developed for adsorption in an AFI-type zeolite but Dubbeldam *et al.*¹²⁷ also included an isotherm of methane in AlPO₄-5 when determining their potential parameter set,¹²⁷ it is believed that the potential used in this work may be considered appropriate. Note that in the following all results are based on *NVT*-MD simulations, and the GCMC simulations served only as a consistency check.

8.3.1 Free-Energy Profiles

In Figure 8.3, free-energy profiles (left) of single tagged methane (top) and ethane molecules (bottom) in the periphery of the external crystal surface are presented for various total particle numbers inserted into the simulation box. Additionally, the mean potential energy, βU , as experienced by a single molecule, is plotted next to the F profiles on the right-hand side. At low loadings the free energy in the gas phase is higher than inside the zeolite the difference of which is larger for ethane than for methane. This free-energy behavior is a consequence of adsorption because the attractive van der Waals interaction between adsorbates and adsorbent render the probability to find

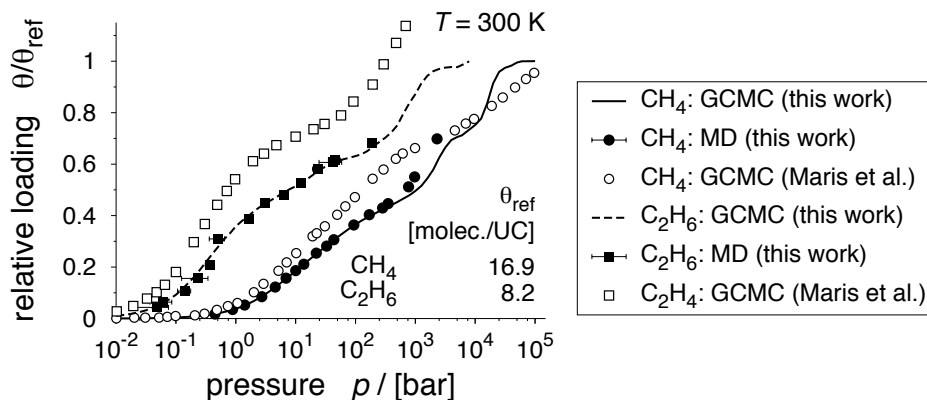


Figure 8.2: Adsorption isotherms for methane and ethane in an all-silica AFI-type zeolite at 300 K. The lines are results obtained from conventional grand canonical Monte Carlo simulations in a periodic AFI crystal. The filled squares and filled circles are results from MD simulations where a gas phase is brought into contact with a thin AFI crystal. In the case of MD simulations, the gas pressure was estimated using the gas-phase concentration and the Peng–Robinson equation of state. In the case of GCMC simulations, the same equation of state was used in order to compute the fugacity, which is necessary for the acceptance rules of insertion and deletion trials. The open symbols are results from Maris *et al.*¹⁸³ who used a different force field.

a molecule inside the zeolite higher than in the gas phase. With increasing loading, θ , and thus pressure, the relative average free-energy level inside the pores increases and, beyond a loading of 5.2 and 4.8 for CH_4 and C_2H_6 , respectively, turns out to be larger than the free energy in the gas phase.

Two-dimensional free-energy landscapes (Figure 8.4) show that the external surfaces of both truncations exhibit no holes that might allow adsorbate molecules to enter previously not accessible zeolite space. This would pose a problem to the simple one-dimensional projection of the free-energy landscape. The one-dimensional free energy to really enter the zeolite pores would be underestimated in those regions where molecules can be found in both the pore volume and newly accessible cavities. In the worst case it would then change the transition state location and thus maybe lower the free-energy barrier. Moreover, the two-dimensional free-energy landscapes confirm the conjecture made in the beginning of the section that a liquid film is forming on the external surface when the pressure is raised. This is indicated by a second layer condensing onto the external surface [yellow stripe at around -27 \AA to -28 \AA for $\theta = 9.3 \text{ molecules (unit cell)}^{-1}$]. The

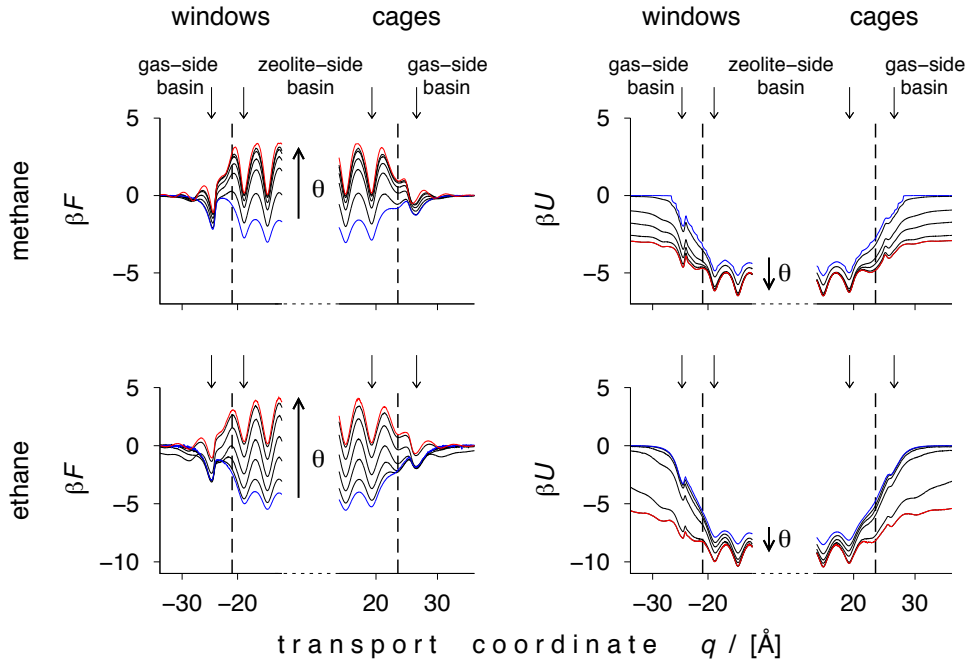


Figure 8.3: Normalized free energy, $\beta F = F/(k_B T)$ (left), and mean potential energy of a single tagged molecule, βU (right), as functions of transport coordinate, q , displayed for the end regions of the crystal. The center of the simulation box is located at $q = z = 0$. The thick dotted lines indicate the positions of the outmost O -atoms on either side of the crystal (window-wise and cage-wise truncation). The profiles were computed for methane (top) and ethane (bottom) in an all-silica AFI crystal at 300 K and various total molecule numbers, N . The resulting average loadings, θ , were 0.6, 4.3, 6.1, 6.8, 7.3, 7.6, as well as 9.3 molecules per unit cell and 0.5, 2.5, 3.7, 4.3, 4.97, 5.05, as well as 5.6 molecules per unit cell for methane and ethane, respectively.

film forms however at such high pressures that are most likely not relevant to practical applications for the present systems. For this reason, the last three state points of methane in Figure 8.2 are not considered anymore in the further analysis. Note that when longer alkanes were to be considered the liquid film might yet form at pressures that are, in fact, relevant to practical situations. A larger gas-phase volume at the ends of the simulation box would then be necessary in order to prevent the film of reaching the volumes where the bulk gas-phase concentration is to be sampled and, thus,

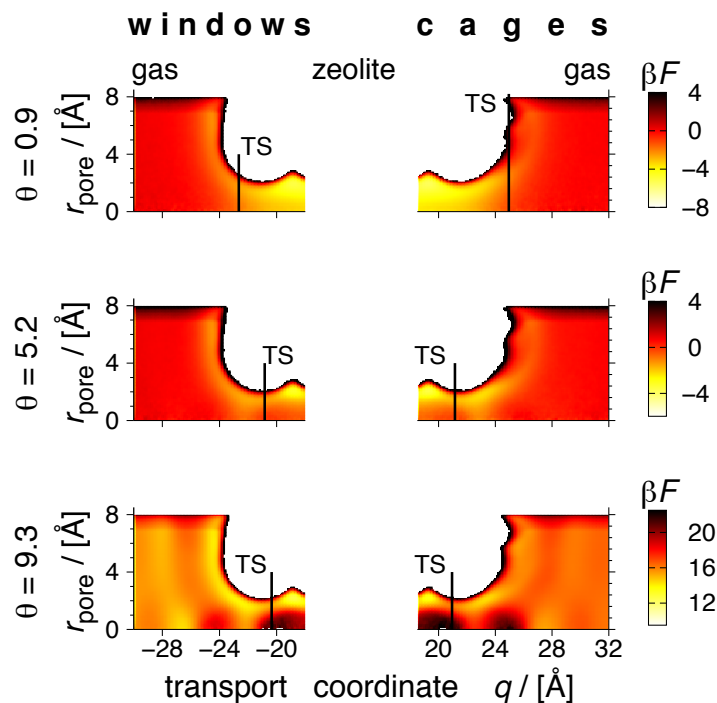


Figure 8.4: Free-energy landscape, βF , projected onto the plane of the transport coordinate, q , and the radius from the pore center, r_{pore} , around the pore mouth of the crystal (CH_4 in all-silica AFI-type crystal at 300 K). Top down: loading, θ , increases from 0.9, over 5.2, to 9.3 molecules per unit cell. Left: window-wise truncation of the crystal; right: cage-wise truncation. Note that the lower βF at $6.5 \text{ \AA} \leq r_{\text{pore}} \leq 8 \text{ \AA}$ are caused by the diminishing sampling volumes because the radii of adjacent pores start to overlap. Dark areas indicate regions where it is rather unlikely to find the tagged molecule whereas yellow represents areas where the molecule is very likely to be found. The color box range is chosen such that white areas were never visited by a molecule. The location of the respective transition state/bottleneck (TS) is indicated by a vertical line in each plot.

of distorting the isotherm.

The F barrier for entering the zeolite through a window-wise truncated surface is, at low loading, comparable to the intracrystalline barrier for both CH_4 and C_2H_6 . As loading increases, the surface barriers to adsorption are getting slightly larger than the intracrystalline barriers. This phenomenon

conversely occurs for the corresponding desorption barriers of methane and ethane attempting to leave the zeolite through a window. Here, the surface barriers are larger than the intracrystalline barriers at low loadings, θ , and they are smaller at high θ . Furthermore, as θ increases the transition state (TS) is slightly shifting from a position close to the gas-side basin toward the expected entropic barrier location (i.e., position of the outmost window of the crystal), as seen in Figure 8.4 as well as Supplementary Figure 8.12. As for the cage-wise truncation, these observations are similar, particularly at high loadings. However, the adsorption–desorption barrier difference at low loading is much more pronounced. Also, the TS location remains initially rather constant and then drops sharply at a loading between 3 and 4 molecules per unit cell. The TS locations in the bulk zeolite remain, as expected, stable in all cases. Moreover, the locations of the adsorption and desorption basins remain unchanged over loading, and are identical for both adsorbate types.

The potential-energy profiles in Figure 8.3 reveal that, in addition to an entropic component, the intracrystalline diffusion is also limited by an energetic barrier. As for the surfaces, the steep descent of the potential energy from gas-phase to zeolite crystal indicates very large energetic barriers to the molecules attempting to leave the crystal on either side. Particularly at low loadings, it is energetically very unfavorable for the molecules to leave the crystal in order to stick at the external surface, where they experience the attractive van der Waals interaction with the zeolite atoms from one side only. This energetic effect is that strong, that it shifts the TS location from the expected window location more toward the gas phase. Yet, when compared to the free-energy barriers, the potential-energy desorption barriers are larger. There is thus an entropically more favorable situation at the external surface than in the first zeolite cage. Inside the zeolite, the adsorbates can only move along the z direction. Adsorbed on the external surface, the molecules have effectively gained one additional dimension to move (x and y direction on the external surface, as compared to z only inside the pores), which has also been indicated by Arya *et al.*¹⁷² The entropic gain for methane and ethane are comparable. The energetic drop of ethane is however larger, because C_2H_6 is modeled as two beads that, in terms of ε , are comparable to the single methane bead. In any case, the entropic effect becomes more pronounced as loading increases, as evidenced by the larger adsorption barriers at high pressures.

The two-dimensional free-energy landscapes indicate the general path that the molecules take to enter and leave the crystal, respectively. When coming from the zeolite space on the window-wise truncated side of the crys-

tal, they stick in the outmost cage of the crystal and then desorb by creeping around the outer O -atoms to eventually reach the external surface. This is evidenced by the yellow region in the outmost cage and the following yellow bended tail (yellow $\hat{=}$ high likelihood to find the molecule). As for the cage-wise truncated side, this process is similar. However, the creeping-around is less evident at low loadings. This is because the end regions consist of open pore cages providing less external surface to stick on such that the molecules are partially on the external surface but also in the half end cage. Elevating the pressure results finally again in a distinct “creeping path”. In the bulk zeolite, the molecules also take a hopping path that is located close to the pore walls; compare Supplementary Figure 8.11.

Note finally that the free-energy and the potential-energy profiles of methane at very low loadings agree well with potential of mean force and average potential-energy profiles published by Arya *et al.*¹⁷²

8.3.2 Transmission Coefficient

Reactive flux correlation functions (RFCFs) of methane in a periodic AFI crystal and at the crystal ends are shown in Figures 8.5 and 8.6. The overall RFCF is comprised of two contributions:

1. Those trajectories that start with a velocity of the tagged molecule on the barrier that points toward the target cage/free-energy basin, $\kappa^+(t)$.
2. Those that start with a reverse velocity, $\kappa^-(t)$.

The overall RFCF is the sum of the two contributions:¹⁸⁴

$$\kappa(t) = \kappa^+(t) + \kappa^-(t). \quad (8.9)$$

In the case of a periodic crystal, the overall RFCF decays exponentially with time, as do the two separate contributions (Figure 8.5). The decay time, for a given loading, is thereby the same for all three functions. Furthermore, the decay time increases with loading, giving rise to retardation of the barrier crossing because of the interaction between the tagged molecule and surrounding molecules. Interestingly, the plateau value of both the positive and negative contribution decrease almost equally in magnitude when loading increases.

The situation is quite different at the crystal surface (Figure 8.6). There are two to three time frames observable for the decay of the RFCFs. A short decay time comparable to the intracrystalline decay time occurs always for the positive contribution of those tagged molecules that aim to enter the zeolite (κ_{ads}^+) and the negative contribution of those trying to desorb. A long

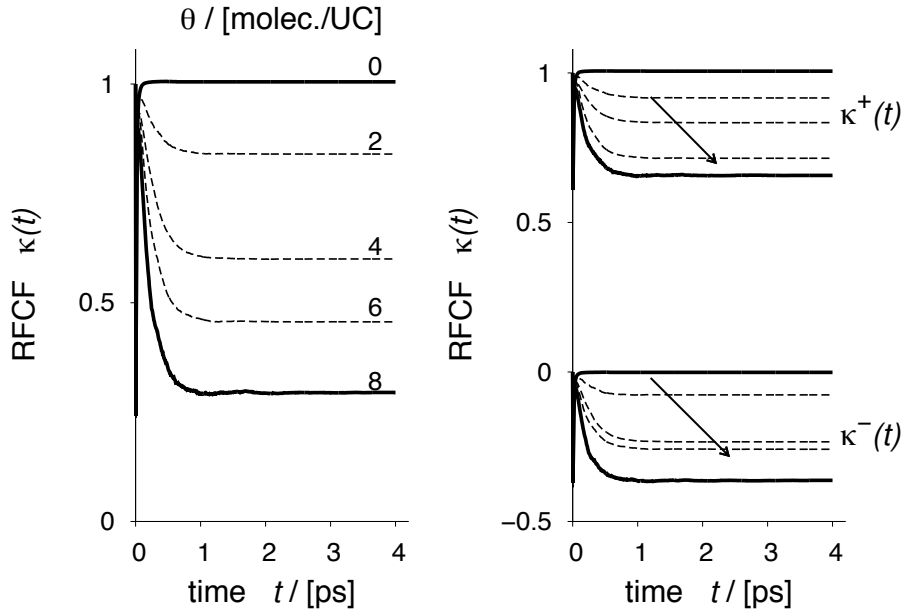


Figure 8.5: Overall reactive flux correlation function, $\kappa(t)$ (left), as well as its positive, $\kappa^+(t)$, and negative contribution, $\kappa^-(t)$ (right), for methane in a periodic AFI crystal at 300 K and various loadings: zero loading (0 molec./UC), 2, 4, 6, and 8 molecules per unit cell. Arrows (right) indicate the change of $\kappa^+(t)$ and $\kappa^-(t)$ with increasing loading.

decay time occurs for the other two cases (positive contribution to desorb and negative contribution to adsorb, respectively). In addition to these two time frames, there is a third decay time that is observable for κ_{ads}^+ and κ_{des}^- at the cage-wise truncated crystal side and low loadings only, as seen in Figure 8.6. In those cases, there are two plateaus for κ_{ads}^+ and κ_{des}^- . Irrespective of the different decay mechanisms, the overall RFCFs of adsorption and desorption are identical for a given crystal side and loading.

The different decay times have their origin most likely in the asymmetry of the barriers and the different length scales for reaching state A and B, respectively. Evidence to this is provided by time-resolved phase-space plots of the entire swarm of RFCF shoots from the barrier, shown in Figure 8.7 for CH_4 at the cage-wise truncated surface at a loading of 0.88 molecules/UC. Each plot is a “snapshot” that represents the probability of finding the tagged molecule, after some time t , at some point in q , when it had initially a velocity of $\dot{q}(0)$. The first plot at nonzero time (0.1 ps) shows the typical evolution of the diagrams when the barriers are symmetric and the crossing process

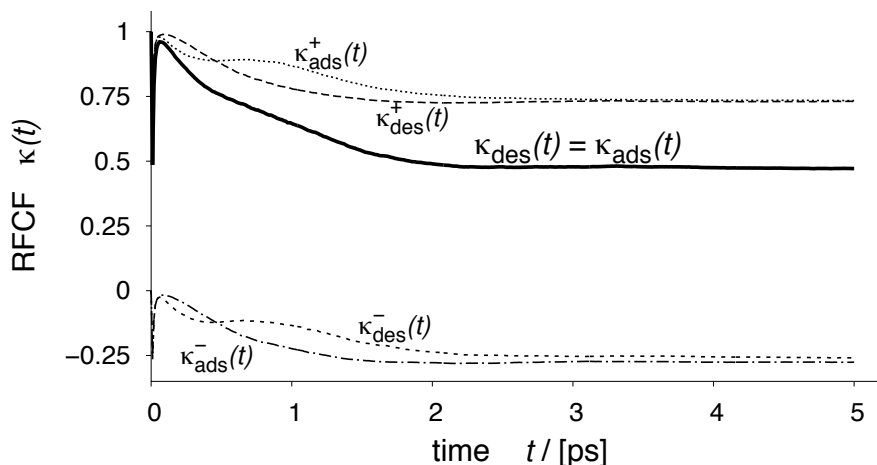


Figure 8.6: Overall reactive flux correlation function (RFCF), $\kappa(t) = \kappa_{\text{des}}(t) = \kappa_{\text{ads}}(t)$, as well as the respective positive, $\kappa_{\text{des/ads}}^+(t)$, and negative contribution, $\kappa_{\text{des/ads}}^-(t)$, for methane attempting to leave (subscript des) and enter (ads) the AFI crystal at the cage-wise truncated surface at an average loading of 0.6 molecules per unit cell (300 K).

nondiffusive (for example, intracrystalline barrier crossings of methane in AFI). The sequences, in those cases, indicate ballistic motion (i.e., $q(t) = \dot{q}(0) \cdot t$) such that the entire distribution sequence appears as a clockwise rotation around $[q = 0, \dot{q}(0) = 0]$ up to the point where the trajectories reach their initially aimed state. In the present case, however, the trajectories evolve differently (Figure 8.7, $t = 0.4$ ps).

1. The first trajectories with initially positive velocities, that is, those that aimed to desorb, have reached the crystal surface whereas all those trajectories that aimed to adsorb are still under way because of the different length scales of the adsorption and desorption states, as measured from the barrier.
2. The center of the “distribution pendulum” (red strip) has shifted so that a much larger fraction of the desorbing-aiming trajectories has been sucked into the zeolite than the initially adsorbing-aiming having redirect toward the crystal surface. This is probably because of the attractive van der Waals potential.
3. The large area of yellow color indicates a very broad distribution. As 0.4 ps is a rather short time to observe this “smearing” of the distribution, it can be concluded that the barrier crossing at the surface is

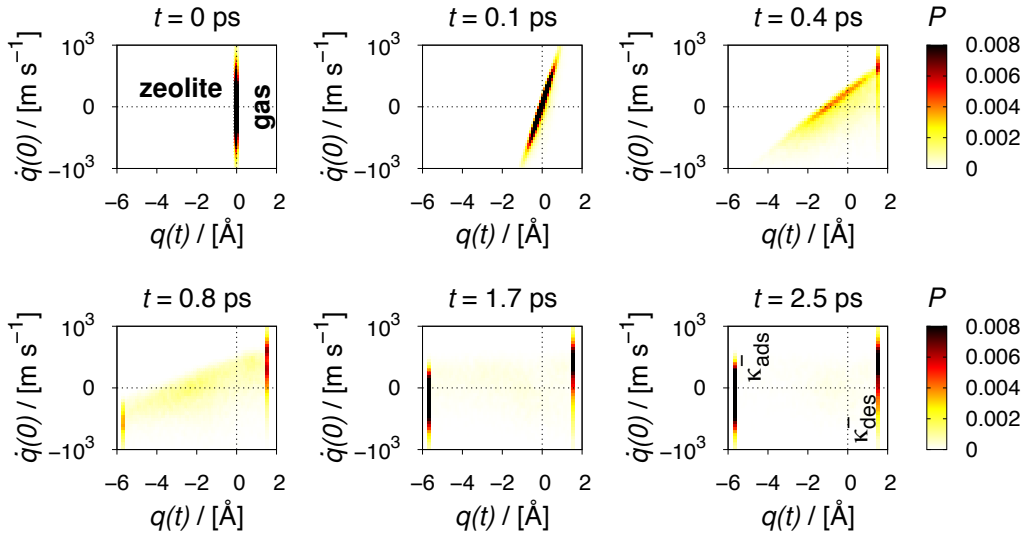


Figure 8.7: Time resolved phase-space plots, $P(q(t), \dot{q}(0))$, of trajectories starting from the adsorption/desorption barrier; methane at the cage-wise truncated crystal surface [300 K, $\theta = 0.88$ molecules (unit cell) $^{-1}$]. Note that q was shifted such to find the transition state at $q = 0$.

quite diffusive.⁹¹

From the following plots, $t > 0.4$ ps, it can be seen that the desorption state is “filled up” quite continuously over time with trajectories for which $\dot{q}(0) > 0$ which confirms that $\kappa_{\text{des}}^+(t)$ decays continuously. The negative contribution to the desorption attempts exhibits a plateau between 0.4 ps and 0.8 ps which may be due to the fact that some molecules attempted to adsorb [negative $\dot{q}(0)$], hit on the concluding half cage of the crystal such to be immediately reflected and quickly reach the desorbing state, as evidenced by the slight yellow strip for $q > 0$ and $\dot{q}(0) < 0$ at $t = 0.4$ and 0.8 ps. The time for this plateau to be reached (0.4 ps) supports this conjecture, because the mean traveled distance based on this time and an average absolute velocity in z direction of $3.15 \text{ \AA}/\text{ps}$ from kinetic gas theory yields a value (1.3 \AA) that is similar to the distance of the desorption state from the barrier (1.85 \AA). Between 0.4 ps and 0.8 ps, none of the remaining adsorption-aiming trajectories have been reflected but they are smoothly sucked in by the attractive zeolite potential. Also, the first trajectories, mostly with high initial momentum ($< -500 \text{ m/s}$), have reached the adsorption state within this time. In the time between 0.8 ps and 2.5 ps there is again a considerable fraction of trajectories recrossing that initially aimed to adsorb. The intermediate

plateau and the subsequent long second decay time of $\kappa_{\text{des}}^-(t)$ come thus from the somewhat lengthy way of the molecules into the interior of the crystal where they reside for some time, and then partially travel back toward the surface.

The transmission coefficients, κ , are identified as the plateau values of the overall RFCFs. They are displayed in Figure 8.8 and 8.9 as functions of core-zeolite loading. As for the intracrystalline case, the transmission coefficients of both adsorbates are very similar (Figure 8.8). Starting from around unity at infinite dilution, the transmission coefficient decreases only slightly, but for loadings beyond 1 molecule per unit cell, it decreases almost linearly. There is however a somewhat sharp drop at $\theta = 4$ for ethane such that it rather remains constant at subsequent loadings. As a consistency check, correlation factors, f^{FPT} , on the basis of mean first-passage times,¹⁸⁵ \bar{t}^{FPT} , were computed for methane in a periodic AFI crystal at three loadings [$\theta = 0, 2$, and 4 molecules (unit cell)⁻¹; asterisks in Figure 8.8] by:

$$f^{\text{FPT}} = \frac{0.5}{\bar{t}^{\text{FPT}} \cdot k_{\text{A} \rightarrow \text{B}}^{\text{TST}}}, \quad (8.10)$$

where $k_{\text{A} \rightarrow \text{B}}^{\text{TST}}$ is the TST hopping frequency, as computed from free-energy profiles. Note that the factor 0.5 in Equation 8.10 stems from considering a one-dimensional lattice where a molecule that starts from a given lattice site, say B, may hop to either the left, A, or right, C, neighboring lattice site with each 50% probability. The RFCF method and the first-passage time approach yield obviously equivalent results.

The transmission coefficients at the surfaces behave quite differently when compared to the loading dependence of the intracrystalline κ s. They neither start from around unity, nor do they depend much on loading. However, recrossing is a symmetric phenomenon (i.e., $\kappa_{\text{ads}} = \kappa_{\text{des}}$) for a given loading at one and the same surface. Although the data scatter, a trend is observable for methane at the window-wise truncated side: linearly decreasing from 0.63 ($\theta = 0.3$) to 0.43 ($\theta = 4$), afterwards constant. As for the cage-wise truncation, a similar trend is observable, here from 0.53 to 0.33. Interestingly, κ seems to be constant for ethane at low loadings, yielding for both truncations a value of around 0.45. Beyond 4 molecules per unit cell, the transmission coefficient drops sharply and increases then again. This together with additional correlation plots (Supplementary Figures 8.15 and 8.16) further supports the earlier statement of much more diffusive barrier crossing at the crystal surface, as compared to intracrystalline barrier crossing.

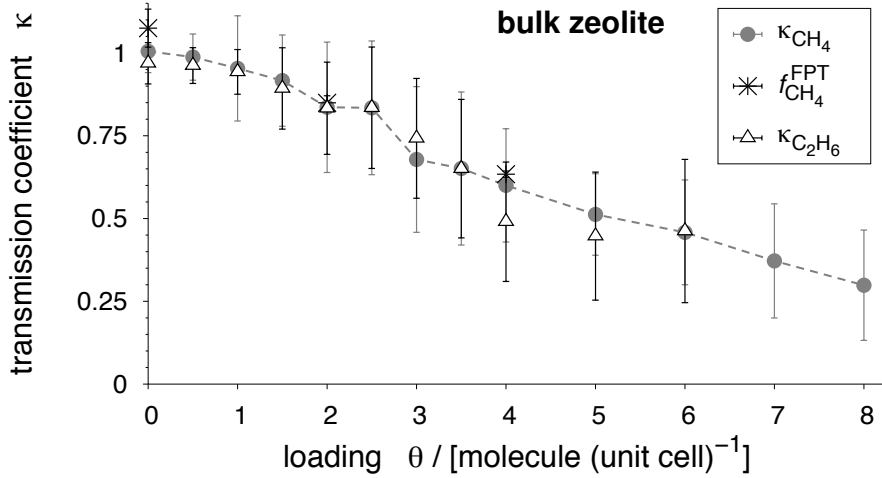


Figure 8.8: Transmission coefficient, κ , as a function of loading, θ , for methane and ethane in a periodic AFI crystal (bulk zeolite) at 300 K. The asterisks are correlation factors, f^{FPT} , that are based on TST hopping rates, $k_{A \rightarrow B}^{\text{TST}}$, and mean first-passage times, \bar{t}^{FPT} [$\theta = 0, 2, \text{ and } 4$ molecules (unit cell)⁻¹].

8.3.3 Critical Crystal Thickness

On the basis of the concentration profiles and the RFCF data, critical crystal thicknesses, δ_{crit} and $\delta_{\text{crit}}^{\text{1step}}$, were calculated, where interpolation and extrapolation was necessary in regard on the transmission coefficients because those were explicitly determined for ethane at four state points only:

- Window truncation: $\kappa = 0.45$ for $\theta \leq 3.2$ molecules/UC; $\kappa = 0.3$ otherwise.
- Cage truncation: $\kappa = 0.45$ for $\theta \leq 3.2$ molecules/UC; $\kappa = 0.25$ otherwise.

The results are plotted in Figure 8.10 as functions of zeolite loading. To facilitate interpretation of the data, recall that the critical crystal thickness gives the minimal crystal size up to which the slow transport in the gas–solid boundary layer has a strong influence on the overall transport. This surface-barriers effect is, hence, important for crystals of size δ_{crit} and below, because it decreases the effective diffusion coefficient dramatically (cf., Chapter 7), but it is negligible for all crystals that are larger than δ_{crit} .

The influence of the way the external surface was realized [window truncation (dots in Figure 8.10) vs cage truncation (triangles)] has hardly an influence which confirms earlier findings.¹⁷² Over the loading regimes studied,

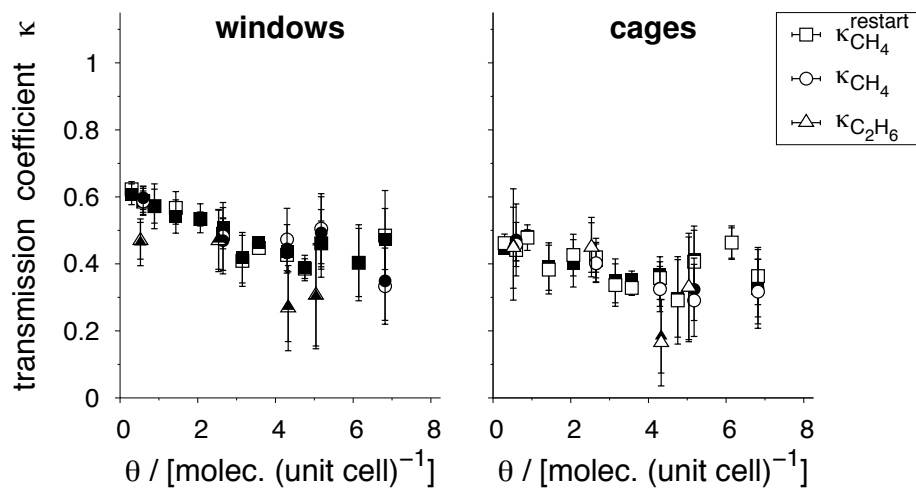


Figure 8.9: Transmission coefficient, κ , as a function of loading, θ , for methane and ethane hopping at the window-wise truncated AFI crystal surface (left) and at the cage-wise truncated surface (right), respectively; 300 K. Two κ s were computed for one and the same state point and truncation plane: the small filled symbols are the transmission coefficients of molecules to desorb (i.e., positive transport coordinate points toward the gas space), and the larger open symbols κ s for adsorption (i.e., transport coordinate points into the zeolite space). The two values agree very well with one another. The circles and triangles refer to RFCF simulation results in which an entirely new initial configuration was computed as starting point for the EPS starting-configuration sampling. The squares refer to simulation results where the initial configuration for EPS was taken from the final MD configuration of the histogram sampling (superscript “restart”).

δ_{crit} decreases from around 10 nm and 80 nm for CH_4 and C_2H_6 , respectively, to 0.8 nm, the size of the AFI unit cell in transport direction. Diminishing surface barriers with increasing loading (and thus increasing pressure) were also observed by Arya *et al.*¹⁷² for methane diffusing through an $\text{AlPO}_4\text{-5}$ crystal and by Newsome and Sholl^{8,176} for methane, ethane, and tetrafluoromethane through a silicalite crystal. Comparing the critical thickness on the basis of the two-step boundary-passing mechanism (symbols in Figure 8.10) with $\delta_{\text{crit}}^{\text{1step}}$ (solid line) leads to the conclusion that the second step has a measurable impact on the overall surface-barrier effect at low loadings only. At high pressures and, thus, loadings, the two critical thicknesses are identical.

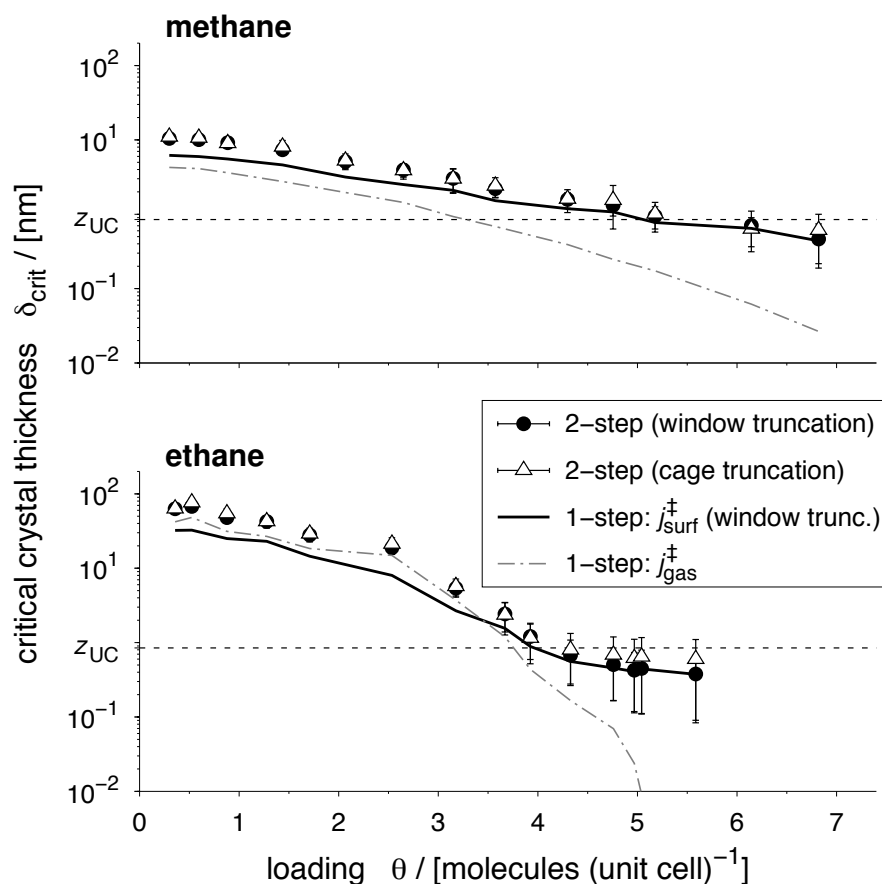


Figure 8.10: Critical crystal thickness, δ_{crit} , as a function of core-zeolite loading, θ , for methane (top) and ethane (bottom). The symbols represent the two-step critical crystal thickness according to Equation 8.7 for the two crystal truncations studied. The lines are one-step critical crystal thicknesses according to Equation 8.8, where the dash-dotted lines are obtained from substituting $j_{\text{surf}}^{\ddagger}$ with $j_{\text{gas}}^{\ddagger}$ in the equation. The dotted horizontal lines highlight the size of the AFI unit cell in z direction, which may be considered the natural lower limit of the surface-barrier effect to have an impact because of Equations 8.7 and 8.8 and the fact that $z_{\text{UC}} = 2 \cdot l_{\text{cage}}$.

Along with these critical crystal thicknesses, another one-step thicknesses was computed (dash-dotted line) that is based on the gas flux, $j_{\text{gas}}^{\ddagger}$, instead of the surface flux, $j_{\text{surf}}^{\ddagger}$. As can be seen from Figure 8.10, the two one-step critical thicknesses are similar enough to permit rough predictions of the

two-step thickness by using j_{gas}^\ddagger twice:

$$\delta_{\text{crit}} \approx 2 \cdot l_{\text{cage}} \cdot \frac{j_{\text{zeol}}^\ddagger}{\left[1/j_{\text{gas}}^\ddagger + 1/j_{\text{gas}}^\ddagger\right]^{-1}} = 2 \cdot l_{\text{cage}} \cdot \frac{j_{\text{zeol}}^\ddagger}{j_{\text{gas}}^\ddagger/2}. \quad (8.11)$$

8.4 Discussion

The AFI crystal surfaces investigated here were chemically not saturated. It is, however, certain that silanol or other terminating groups form during the synthesis of real zeolite crystals. In this context, Thompho *et al.*¹²⁴ provided indications for a five times slower surface transport when silanol groups are introduced in comparison to the transport of chemically nontreated surfaces. Combining this realization with the the predictability of the critical crystal thickness on the basis of the gas flux only, it can be concluded that there are at least three different factors influencing surface barriers: (1) adsorption, (2) idealized surface structure, and (3) chemical composition of the surface. This view on the different retarding effects may possibly be used for tailoring the external surface such that it fits the design purposes of adsorbers and heterogeneous reactors. Imagine, for example, a multicomponent stream within a given chemical process line. At a certain point, the stream comprises two components both of which may enter the micropores of a given zeolite crystal rather facile on a size basis. Because of different chemical properties, however, the surface can be tuned such that it forms chemical barriers to one component that is unwanted in the interior of the micropores. In the context of molecular path control¹⁸⁶ which may be seen as a “degree of freedom to membrane design purposes”, the surface tailoring described above provides a new and independent “design degree of freedom”.

Another interesting conclusion can be drawn with respect to the transferability of the results of equilibrium permeation to gradient-driven permeation. Because the transport coefficients of self-diffusion and collective diffusion become very similar at very low pressures (\rightarrow infinite dilution) and as the results of this chapter indicate that surface effects are, for the present cases, important only at low loadings/pressures, the critical crystal thickness computed will approximately also be valid in the case of gradient-driven permeation. Newsome and Sholl^{8,176} have thereby provided evidence to this conjecture, and have proposed a method that uses equilibrium one-way fluxes and transport diffusivities in order to assess critical crystal thickness for variable driving forces. So, for a quick estimation of the influence of surface effects on the basis of at least the simplest possible factor, the gas-phase flux, one

merely needs to compute an adsorption isotherm with simultaneous computation of histogram data inside the periodic crystal. By means of reweighting methods, as proposed for example by Schüring *et al.*,¹¹⁵ and with the aid of the method introduced by Newsome and Sholl,^{8,176} the influence of surface effects can be rapidly estimated at various state points (T) and for various driving forces (Δp).

Finally, it has to be mentioned that none of the critical crystal thicknesses computed here are in the size range of zeolite crystals that are usually employed in measurements ($\gg 1 \mu\text{m}$). Even considering additional chemical barriers¹²⁴ would at maximum (i.e., ethane at low loadings) lead to a critical crystal thickness of 400 nm only. For this reason, surface barriers resulting from the ideal crystal structure cannot be considered a significant source of error in measurements for diffusion coefficient determination; at least, for the here studied systems and conditions.

8.5 Conclusions

The present chapter has, from a technological point of view, assessed the significance of surface transport resistances of technically relevant adsorbates and, owing to the detailed analysis of the molecular simulation performed, pictorial insights into the permeation processes have been achieved. From a scientific point of view, this chapter represents the expansion of applying extended dynamically corrected transition state theory to equilibrium transport of tracers at gas–solid interfaces.

8.6 Supplementary Data

8.6.1 Transition State Locations and Free-Energy Landscapes

The location of the transition state (TS), that is, the bottleneck to the hopping process, of small hydrophobic adsorbate molecules inside *bulk* zeolites are usually known a priori, because the barriers are mostly entropic in nature and thus follow directly from the crystal structure. Also, the transition states remain usually at the same position when loading increases, as evidenced by Figure 8.11 as well as References 146 and 10. The location of the free-energy basins, where the hopping molecule spends much time in, does not change either. As for the surface hopping studied here, the situation is different. Although the location of the free-energy basin for both sides (gas-space and zeolite-space side) remain stable for one and the same crystal side (window-wise vs cage-wise truncation), the location of the transition states, that is,

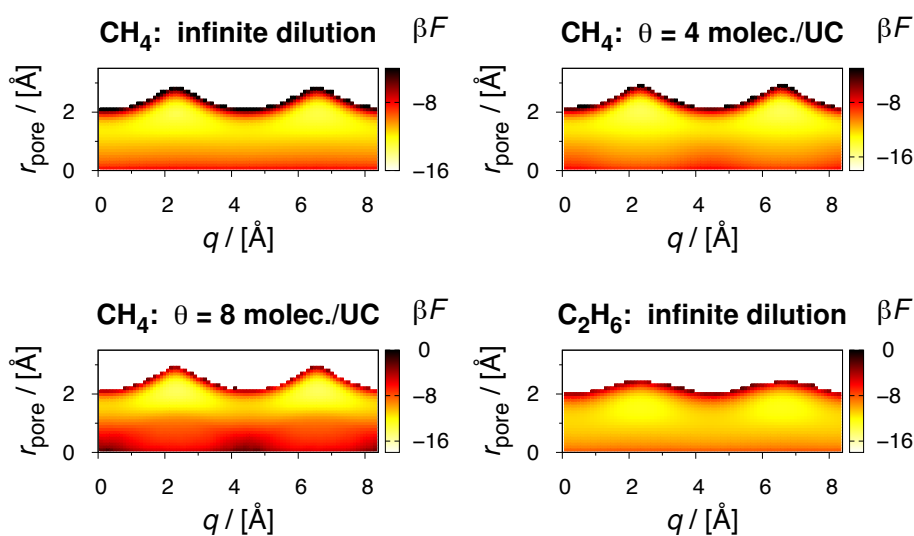


Figure 8.11: Two-dimensional free-energy landscapes, $\beta F(q, r_{\text{pore}})$, of methane and ethane inside a periodic AFI crystal (300 K, various loadings). The radius, r_{pore} , is the distance of the tagged molecule from the pore center. The color box range is chosen such that white areas indicate regions that were never visited by the molecules. The F landscapes show that ethane “feels” a less corrugated wall than methane because it is bulkier than methane.

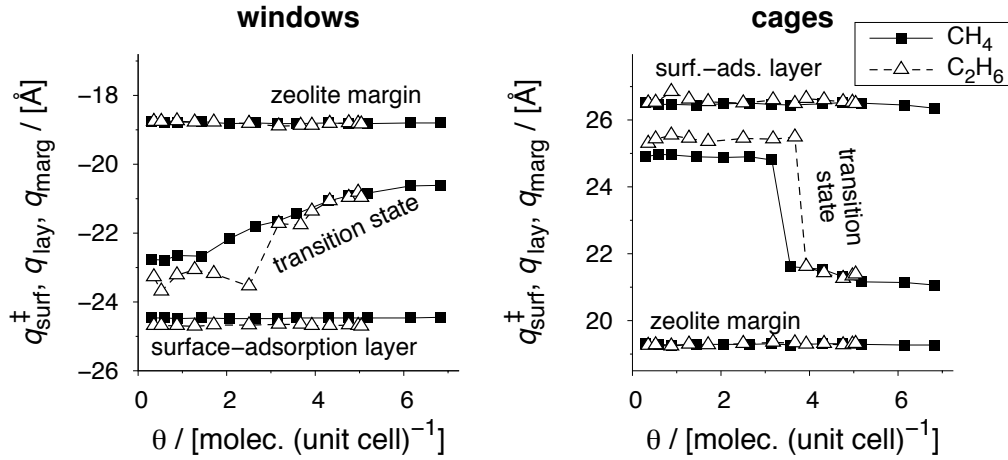


Figure 8.12: Location of the transition state at the surface, $q_{\text{surf}}^{\ddagger}$, of the gas-side basin in the surface adsorption layer, q_{lay} , and of the zeolite-side basin in the solid margin, q_{marg} , as functions of loading, θ , for methane and ethane at 300 K and both AFI crystal surfaces: window-wise truncation (left) and cage-wise truncation (right).

where the free energy reaches its local maximum in the vicinity of the outmost crystal atoms, changes with increasing number of molecules inserted into the simulation box, as seen in Figure 8.12. Initially, the TS is located outwards with respect to the anticipated barrier location (i.e., the position of the outmost window atoms). The reason is, most likely, that fluid molecules that try to desorb must overcome a huge potential-energy barrier, particularly at low loadings, θ . As this influence is very strong, the location of the potential-energy barrier determines the location of the free-energy barrier at low θ . In contrast to the smooth F profiles, the U profiles are sharply peaked, when θ is low. By inserting more and more molecules into the simulation box, a gentle but definite inward shift of the TS is observable. Because the TS is finally located at the anticipated entropic barrier for moderate and high pressures and, thus, loadings, there seem to be two mechanisms that compete with each other:

1. The energetic drag exerted by the attractive zeolite potential. At low loadings, this influence is so strong that a molecule aiming to hop from the outmost cage onto the external surface and having surpassed the position of the window atoms of the surface does not experience this intuitive entropic bottleneck as the true bottleneck.
2. The zeolite structure. The anticipated entropic barrier becomes dom-

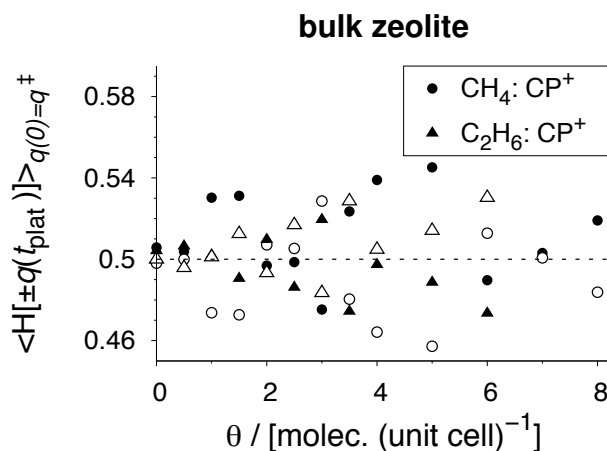


Figure 8.13: Committor probability of the forward shoot (CP⁺, filled symbols), $\langle H[q(t_{\text{plat}})] \rangle_{q(0)=q^\ddagger}$, as a function of loading, θ , for methane and ethane in a periodic AFI crystal (300 K). The committor probability (CP⁻) of the corresponding backward shoot, $\langle H[-q(t_{\text{plat}})] \rangle_{q(0)=q^\ddagger}$, is plotted with open symbols.

inating when the pores and the external surface are crowded; that is, at high loadings.

The gentle shift is observable for the window-wise truncated crystal *only*. As for the cage-wise truncation, there is a “first order transition” of the barrier location. In contrast to the window-wise truncated side, where U -barrier and the F -barrier location were quite close to each other and, thus, has led to the gentle, “smeared” transition of the TS location, the large separation between the maximum in the U profile and F profile leads to a sharp transition. That is, at some given loading one of the two mechanisms described above is entirely dominating the bottleneck location.

The usual path of hopping molecules that are confined in the bulk zeolite is close to the pore walls, as evidenced by the two-dimensional free-energy landscapes in Figure 8.11. The molecules do, hence, not adsorb/desorb “straight” from/into the gas phase but, first, stick to the external surface before proceeding further to either the gas phase or the interior of the pores. When considering the situation at low loading, where the TS at the surface is shifted outwardly, a molecule that tries to desorb thus creeps around the pore mouth and, although it has already made its way well around the concluding oxygen atoms of the pore mouth, it is rather dragged back inside the pore, because, from there, the molecule feels the attractive potential energy

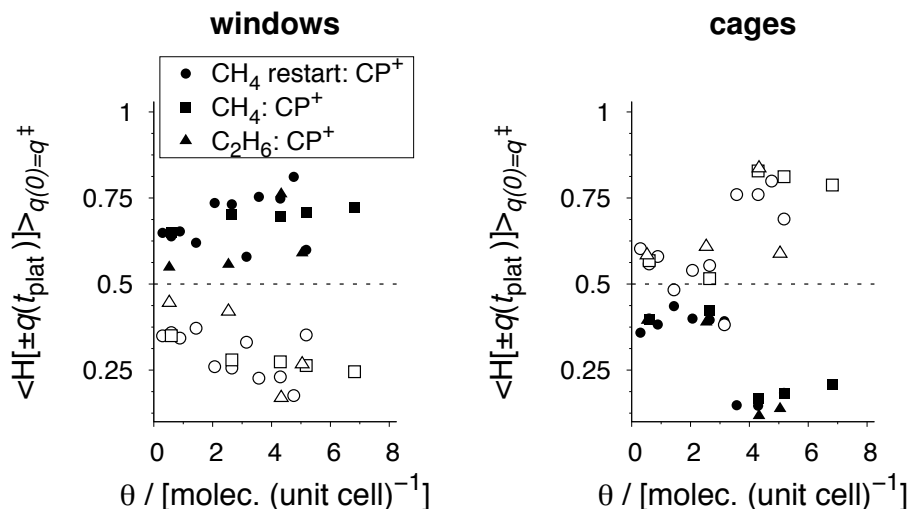


Figure 8.14: Committor probability of the forward shoot (CP⁺, filled symbols), $\langle H[q(t_{\text{plat}})] \rangle_{q(0)=q^\ddagger}$, as a function of loading, θ , for methane and ethane at the window-wise truncated crystal surface (left) and for the cage-wise truncation (right); 300 K. The committor probability (CP⁻) of the corresponding backward shoot, $\langle H[-q(t_{\text{plat}})] \rangle_{q(0)=q^\ddagger}$, is plotted with open symbols.

still very much in comparison to what lies in front of its desorption path (i.e., on the way toward the external surface).

8.6.2 Committor Probability and Correlation Plots of RF simulations

In Figures 8.13 and 8.14, the committor probabilities (CPs) obtained from reactive flux (RF) simulations in the bulk zeolite (i.e., intracrystalline hopping) and at the crystal surface (i.e., adsorption/desorption) are plotted. CP gives the “absolute” fraction (i.e., not correlated to the initial momentum) of those trajectories that were initiated at the transition state $[q(0) = q^\ddagger]$ and eventually equilibrate either in the product basin, $\langle H[q(t^{\text{plat}})] \rangle_{q(0)=q^\ddagger}$, or in the reactant basin, $\langle H[-q(t^{\text{plat}})] \rangle_{q(0)=q^\ddagger}$; compare also References 187 and 188. In the intracrystalline case, the two CPs are as expected equal because of the symmetry of the barriers (Figure 8.13). Furthermore, the values are always close to 0.5, indicating that $\approx 100\%$ of the trajectories have equilibrated in either basin within the maximum trajectory time.

Neither of the surface committor probabilities, that is, for hopping into

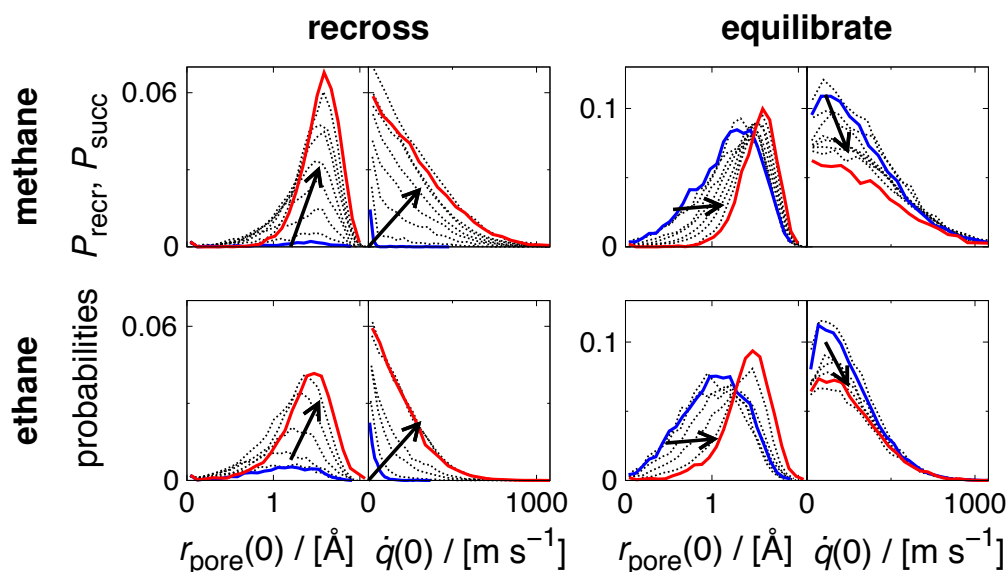


Figure 8.15: Correlation plots obtained from RF simulations in a periodic AFI crystal for methane (top) and ethane (bottom). The four diagrams on the left correspond to trajectories that have failed to equilibrate in the target cage, the four diagrams on the right correspond, thus, to the successfully equilibrated ones. $r_{\text{pore}}(0)$ denotes the distance of the tagged particle away from the pore center at the beginning of the RF trajectory, and $\dot{q}(0)$ its initial velocity in z direction. Arrows indicate the evolution of the distributions as loading, θ , increases; $\theta = 0-8$ molecules (unit cell) $^{-1}$ for methane and $\theta = 0-6$ for ethane with $\Delta\theta = 1$ molecule (unit cell) $^{-1}$.

and out of the zeolite, respectively, are 0.5 (Figure 8.14). The sum of the two CPs at a given crystal surface is, however, always close to unity, again giving rise to $\approx 100\%$ of the shoots to have finished in either free-energy basin within the maximum trajectory time chosen. The CP of the adsorption process is always larger than the CP of the corresponding desorption process. Furthermore, adsorption CP rather increases with loading for the window-wise truncated side, whereas it is initially constant and then jumps abruptly to a larger value between 3 and 4 molecules per unit cell at the cage-wise truncated crystal surface. The trend of the CPs and the location shift of the transition states seem to be correlated. This correlation, together with the seemingly constant κ at high loadings, gave the motivation to conduct additional simulations: RF simulations of methane adsorbing/desorbing at the window-wise truncated crystal side at low loading [$\theta = 0.9$ molecules (unit

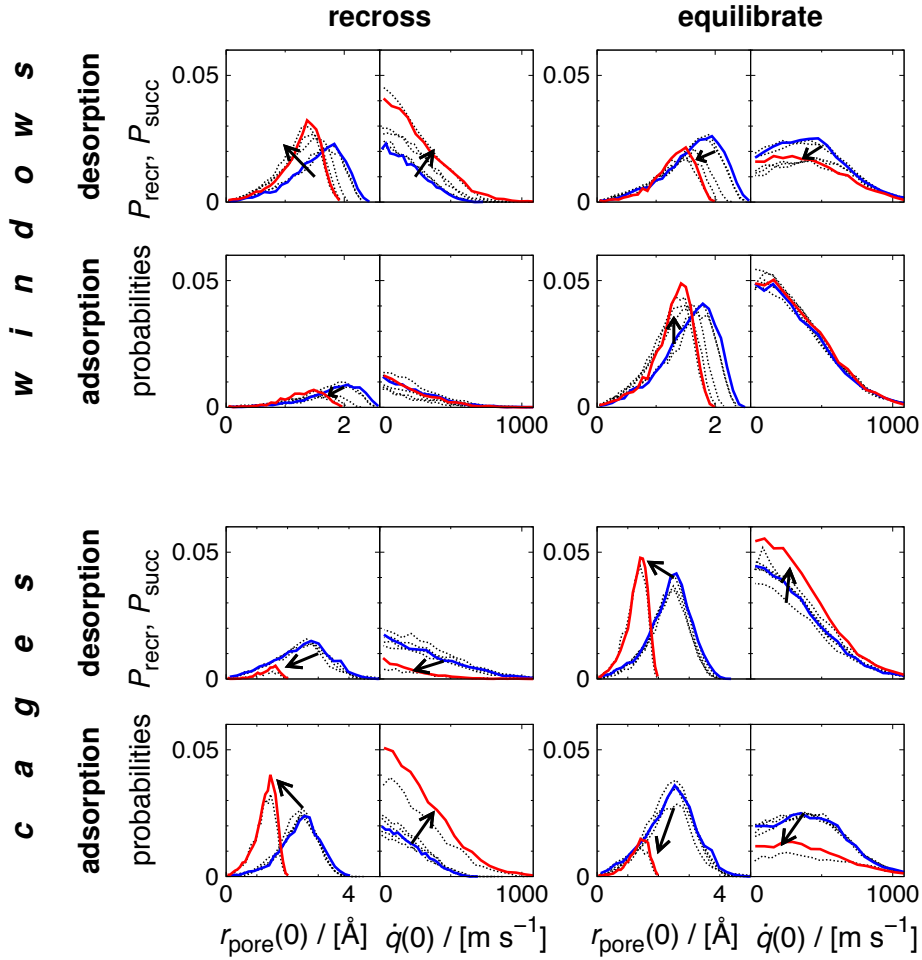


Figure 8.16: Correlation plots obtained from RF simulations initialized at the AFI crystal surface; analogously to Figure 8.15 but for methane only; 300 K, $\theta = 0.6, 0.9, 1.4, 2.1, 2.7, 4.3,$ and 5.2 molecules (unit cell) $^{-1}$. The thick blue lines and the thick red lines indicate data from the lowest loading (0.6) and at the highest loading (5.2), respectively.

cell) $^{-1}$]. This time, starting configurations were yet harvested in the window region instead of the location of the barrier. In the context of dynamically corrected transition state, that procedure is legitimate, because it is sufficient to identify the transition state in the *vicinity* of the barrier; κ will then not only account for recrossing, but also be the exact correction to this error source. It turns out that the transmission coefficient is 0.44 which is very close to the average at high loadings, where the transition state [i.e., the

maximum of $\beta F(q)$ is, in fact, found at the location of the window atoms. This further supports the conjecture that the barrier crossing is diffusive at the surface, and, moreover, shows that the extent of diffusive crossings is independent on loading when choosing the last crystal atoms as barrier location.

Distributions of the correlation between success/failure to reach the aimed cage and the tagged particle's initial distance from the pore center as well as its momentum on top of the barrier indicate three main points for the bulk-zeolite barrier crossing (cf., Figure 8.15):

1. Those trajectories that recross start predominantly farther apart from the pore axis.
2. At high loadings, the initial configuration does not have any influence on the success of the hopping attempt, that is, whether the trajectory equilibrates in the target cage or not, because there are hardly any initial configurations found close to the pore center.
3. Trajectories with initially low momentum of the tagged molecule have a chance to recross at low loadings only, whereas this continuously shifts to also high-initial-momentum trajectories, as the zeolite becomes more crowded.

At high loadings, the success of a shoot is therefore strongly dependent on the interactions with molecules that have resided in those two cages between which the tagged molecule is initially found. These observations hold for both adsorbate types.

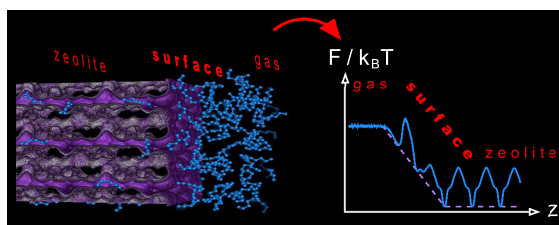
The same kind of correlation plots for the surface-barrier crossing do not reveal any indications of what the success of a jump depends on (Figure 8.16). Nevertheless, they are (1) consistent with the two-dimensional free-energy landscapes and the shift of the transition state in that starting configurations are found at smaller radii when loading is high because of the inward-shift of the transition state where the molecules are then more confined, and they (2) reflect again the diffusive character of the barrier-crossing process at the surface.

9

The Nature of Surface Barriers

Shedding light on the nature of surface barriers of nanoporous materials, molecular simulations (Monte Carlo, reactive flux) have been employed to investigate the tracer-exchange characteristics of hydrocarbons in defect-free

single-crystal zeolite membranes. The concept of a critical membrane thickness as a quantitative measure of surface barriers has been earlier shown to be appropriate and advantageous. Here, this critical membrane thickness is therefore exploited systematically to screen technologically important systems for their sensitivity toward surface barriers. As a result, nanopore smoothness, framework density, and thermodynamic state of the fluid phase have been identified as the most important influencing variables of surface barriers. Despite the ideal character of the adsorbent, the simulation results support experimental findings on both MOF Zn(tbip) and zeolite $\text{AlPO}_4\text{-LTA}$, where large numbers of blocked pore entrances caused exceptionally strong surface barriers. However, complementary density functional theory calculations suggest that the blockages may in fact be traceable to surface relaxation effects and, hence, not to nonidealities such as foreign matter deposition and severe lattice defects. Most significantly, this chapter predicts that the idealized crystal structure without any defects and surface relaxations will already be a critical aspect of experimental analysis and process design in many cases of the upcoming class of extremely thin and highly oriented nanoporous membranes.



9.1 Introduction

The current prospect of increasing usage of fossil fuels in conjunction with the ongoing research on carbon dioxide sequestration excites interest in processes employing nanoporous materials as catalyst or separation medium to open alternative routes to existing technologies. Carbon nanotubes (CNTs), metal–organic frameworks (MOFs), and zeolites represent the foremost candidates to be incorporated in such applications.^{4,13,46,48,189,190} An integral part of the process design will be the role of transport of the guest molecules into, through and out of the nanopores.^{4,5,8,11,113,190}

Recent progress in the synthesis of zeolite membranes¹¹ paves the way for ultrathin films which may be used on a support layer as molecular sieve membranes with low internal transport resistance. In such cases, however, the issue of surface barriers arises, that is, transport resistances located in the boundary layer between intracrystalline space and fluid phase. These barriers may dominate the overall transport for very thin membranes (or crystals).^{8,113,172} In this context, two aspects are important:

1. Approximately, up to which membrane thickness or crystal size, respectively, will the influence of surface barriers be noticeable?
2. What do those barriers depend on? And, what triggers them?

To address the above questions, the influences of molecule type and chain length of normal hydrocarbons (C1–C6) as well as the temperature, and the impact of the nanopore structure on surface barriers in all-silica zeolites of topologies AFI, LTL, and MFI are investigated in this chapter. State-of-the-art molecular simulation approaches are employed on ideal systems, and the previously proposed criterion of a critical membrane thickness,¹¹³ δ_{crit} , serves as a quantitative measure of surface barriers.

9.2 Methodology

Most of the methodology is equivalent to the one described in Chapter 8. Therefore, this section focuses on the zeolite structures studied and briefly reiterates the concept of a critical membrane thickness as an assessment of surface barriers^{113,172} (question one from the Introduction of this chapter). In short, however, the framework of dynamically corrected transition state theory was employed where Monte Carlo simulations in the NVT ensemble (NVT -MC) provided residence histograms of the guest molecules [$P(q)$], and reactive flux simulations yielded transmission coefficients (κ) of the elementary transport processes identified. On this basis, molar fluxes at the barriers

considered were computed. More simulation details and evidence that the methodologies of the previous chapter and of this chapter yield equal results are provided in the Supplementary Subsection 9.6.1.

9.2.1 Zeolites

Two zeolite structures featuring one-dimensional pore systems (AFI, LTL) and a structure with a three-dimensional pore network (MFI) were studied whereby all zeolites were purely siliceous (SiO_2). The major difference between the AFI and the LTL structure is the larger cage-to-window ratio of the latter. Within the categorization of Reference 41, all three types of nanopores and diffusion behaviors are hence investigated: channel-type (AFI), cage-type (LTL), and intersecting channel-type (MFI). The crystal structures were taken from References 61,63,64 and, if necessary, converted to purely siliceous structures.¹⁵⁹ The AFI and LTL unit cells accommodate in total four and two cages, respectively, whereas four intersections of straight (y direction) and zigzag ($x-z$) channels are found in a single MFI unit cell (Figure 9.1). The zeolite atoms were kept fixed at their crystallographic positions because framework flexibility in the sense of a dynamic effect (e.g., breathing window) does not have any significant influence on adsorption and diffusion in zeolites.¹⁴⁶ However, diffusion coefficients may be quite sensitive to subtle differences in the time-averaged crystal structure in consequence of a flexible zeolite lattice^{156,159,191} for which reason the rigid-lattice assumption is justified.¹⁴⁶

As in the previous chapters, the zeolite crystal slabs consisted of full unit cells and fractional, concluding unit cells at the outer surface, and the slabs were centered in the simulation box. In each case two different external surfaces were investigated. The AFI and LTL pores were cut such to let the pore windows (left) and cages (right) terminate the pores, which run along the z direction (Figure 9.1, top and center). As for MFI, the single-crystal membrane was aligned along the straight channels (y direction), because the flux is maximal in this direction.^{8,46} The MFI unit cells were cut at fractional coordinates of 0.125 and 0.73. This yielded a left surface that exhibits tighter canyons for guest molecules to enter the zeolite in comparison to the right surface which is rather flat, giving quite direct access to the straight channels (Figure 9.1, bottom).

Free-energy profiles are plotted along with the respective pore structure in Figure 9.1. They indicate that adsorbate molecules “feel” the internal channel structure being not affected by the presence of the external surface. Therefore, the computation of a single representative flux ($j_{\text{zeol}}^{\ddagger}$) between the

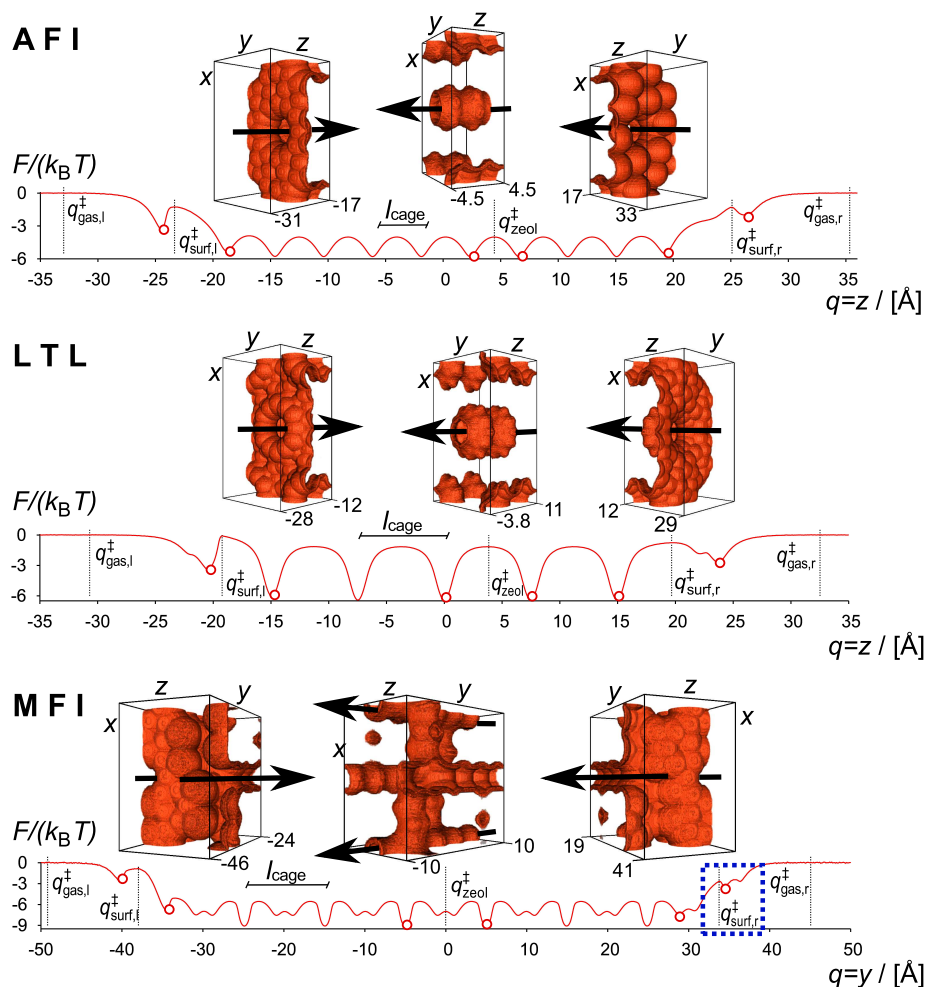


Figure 9.1: Zeolites investigated: AFI (top), LTL (center), MFI (bottom). Free-energy profiles of methane in all three zeolites are plotted along with representations of the repetitive pore structures (center) and the two external surfaces which mark the left and right-hand borders of the single crystal slabs. The dividing surfaces for flux computation are identified as vertical lines. The free-energy wells, left and right from the barriers, are highlighted by open circles. Those mark the end points for reactive flux simulations. l_{cage} is the length of a single diffusion event inside the crystal. Black arrows indicate the direction along which the membranes were aligned.

innermost adsorption sites/cages, that is, through the dividing surface $q_{\text{zeol}}^{\ddagger}$, as indicated in Figure 9.1, is justified for the bulk zeolite fluxes. The environment inside the cage or intersection next to the surface, that is, where

the flux $j_{\text{surf}}^{\ddagger}$ prevails, is slightly different from the innermost cages; particularly for the side toward the pore mouth. Thus, on a microscopic scale, the single-crystal membrane is composed of two types of regions, each with its characteristic flux:

1. The innermost cages/intersections which are assembled to an N_{slabs} -long array of consecutive slabs, making up the largest part of the membrane; compare also Figure C.1 in Appendix C. The equilibrium flux $j_{\text{zeol}}^{\ddagger}$ establishes between two adjacent “cage” slabs.
2. The cages/intersections next to the pore mouth (referred to as zeolite margin in the remainder) where $j_{\text{surf}}^{\ddagger}$ establishes between this first slab and the external surface adsorption layer.

Because the boundary layer between bulk zeolite space and gas phase comprises in fact a second region in addition to the zeolite margin, a third flux, $j_{\text{gas}}^{\ddagger}$, rates the transport of tracer molecules from this gas-side located boundary layer region (external surface adsorption layer), to the gas phase; compare also Figure 9.1.

9.2.2 Assessment of Surface Barriers

In the following, a short review is given of how surface barriers were assessed in the present work, which directly addresses to—and, thus, answers—question 1 from the Introduction. A direct comparison of the transport barriers in the intracrystalline space with the one at the surface is not meaningful because what really matters in the context of surface barriers is the effect that the barrier difference has. Therefore, one should start by asking “What process or application is considered?”, and, *subsequently*, “How does the presence of surface barriers manifest itself in this process/application?”.

Here, a tracer-exchange process forms the basis of all further considerations. That is, instationary transport of labeled molecules between an adsorbed (zeolite) phase and a pure fluid (e.g., gas) phase in thermodynamic equilibrium. The process can be described with conventional analytical solutions of Fick’s diffusion equations using, however, different boundary conditions. Given that the transport of molecules at the surface (or, rather, through the entire boundary layer) is slow compared to the intracrystalline transport, analytical solutions with and without an explicit description of the slow surface transport yield similar concentration profiles, only if the host dimension (here: membrane thickness) is very large. As the membrane thickness decreases, the agreement between the two solutions worsens, giving rise to a critical point (thickness) where the discrepancies cannot be tolerated

anymore. To define “tolerable” in this context consider that uncertainties of guest diffusion coefficients in zeolites determined by experimental means usually amount to factors between 2 and 5 (compare, for example, Figure 3 in Reference 139). Therefore, transport data (here: tracer exchange) can be fitted to both analytical solutions to yield diffusion coefficients, where the one from the simple solution without explicit description of slow boundary layer transport will be smaller than the true diffusion coefficient. The crucial point to realize is now that this deviation in diffusivities is only important, if it approaches (or even exceeds) the experimental uncertainty, thus, defining a critical thickness “beyond which the barrier resistance becomes insignificant”.¹⁷² Chapter 7 has shown that this critical thickness can be reliably predicted on the basis of DCTST flux ratios because the deviations in diffusivities lie always between of 3 and 5; that is, within the range of experimental certainty.

As a last important point to mention, the incidence that the boundary layer actually comprises two regions, the zeolite margin and the surface adsorption layer, is taken care of in the analysis by computing two critical thicknesses. The first one neglects the surface adsorption layer, representing an often made approximation for assessing surface transport resistances^{8,176,189} and surface permeabilities.^{9,113} The corresponding critical thickness, $\delta_{\text{crit}}^{\text{1step}}$, is given by (compare also Chapter 7):

$$\delta_{\text{crit}}^{\text{1step}} = 2 \cdot l_{\text{cage}} \cdot \frac{j_{\text{zeol}}^{\ddagger}}{j_{\text{surf}}^{\ddagger}}. \quad (9.1)$$

Taking both boundary layer subregions into account the critical thickness, δ_{crit} , is calculated by:

$$\delta_{\text{crit}} = 2 \cdot l_{\text{cage}} \cdot \frac{j_{\text{zeol}}^{\ddagger}}{\left[1/j_{\text{surf}}^{\ddagger} + 1/j_{\text{gas}}^{\ddagger}\right]^{-1}}, \quad (9.2)$$

where, in the above equations, l_{cage} denotes the separation of *intracrystalline* sites (cages, intersections), and $j_{\text{zeol}}^{\ddagger}$, $j_{\text{surf}}^{\ddagger}$, and $j_{\text{gas}}^{\ddagger}$ the fluxes at the dividing surfaces separating two intracrystalline sites (subscript “zeol”), the zeolite margin and the surface adsorption layer (“surf”), and the surface adsorption layer and the gas phase (“gas”), respectively. The computation of and systematic comparison between both critical thicknesses facilitates a quantitative assessment of how significant the boundary layer substructure indeed is.

9.3 Results

On the basis of the simulation results, the second question from the Introduction of this chapter will be now addressed to, that is, what surface barriers depend on. Note that the temperatures in the simulations were set to $T = 1.05 \cdot T_{\text{crit}}$, with T_{crit} the guest molecule's critical temperature,¹⁹² to ensure similar corresponding states for the investigation of chain length and pore structure influence. The force field developed by Dubbeldam *et al.*¹²⁷ and extended by Liu *et al.*¹³¹ was used with some minor differences (cf., Section 6.1).

9.3.1 One-Dimensional Pores

The critical membrane thicknesses of *n*-alkanes and *n*-alkenes adsorbed in all-silica AFI single-crystal membranes decrease with increasing pressure (symbols in Figure 9.2). Surface barriers will therefore have a profound impact on the overall tracer-exchange process for a wider range of membrane thicknesses at low pressures as compared to high *p*. This observation is consistent with previous results¹¹³ and underlines that this behavior is quite general, irrespective of the guest molecule, the nature of the external crystal surface, and the host material as such (Figures 9.3 and 9.4).

A common trend can be observed in Figure 9.2. As the thermodynamical critical point at $p^* = 1$ is approached, the magnitude of the critical thickness, δ_{crit} , becomes comparable to the size of the unit cell. Surface barriers do thus not matter for any membrane width, as long as the fluid phase is near-critical. On the other extreme, the trend of δ_{crit} signifies that the more the fluid phase behaves like an ideal gas (left-hand side), the stronger will be the impact of surface barriers. Inserting a single molecule into the simulation box ($p^* \rightarrow 0$) maximizes therefore the critical membrane thickness for a given host–guest system (left end of abscissa). The value of δ_{crit} obtained at the smallest finite pressure for a given fluid is already close to this maximum. It thus starts decreasing significantly when the isotherm *increases* distinctly (Supplementary Figure 9.9).

At equal reduced pressures, a trend of increasing δ_{crit} with molecule chain length is appreciable, with the exception that methane exceeds the values of ethane, ethene, and propene at infinite dilution. The type of molecule (alkane vs alkene) does not reveal any trend. Therefore, one might state that the molecule type has a weaker impact than the chain length. Considering the error bars and the moderate spread of the critical thicknesses at equal pressures leads to the conclusion that even the hydrocarbon chain length

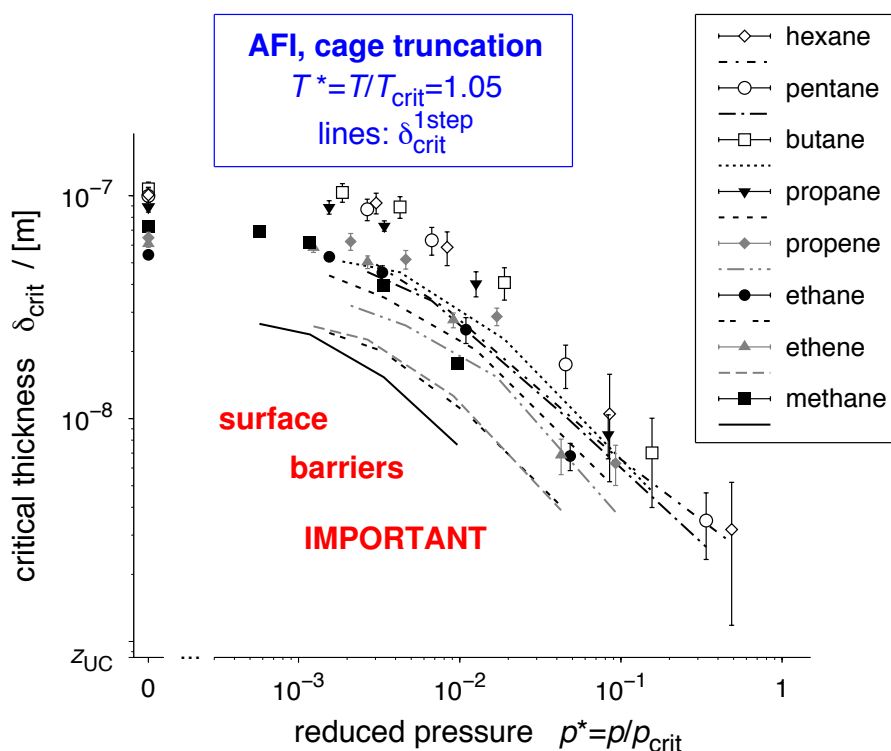


Figure 9.2: Critical membrane thickness, δ_{crit} , as a function of reduced pressure, $p^* = p/p_{\text{crit}}$, for different n -alkanes (C1–C6) and n -alkenes (C1–C2) adsorbed in all-silica AFI-type zeolites (membranes were truncated at the position of the cage atoms). Note that (i) while the symbols represent results accounting for the fact that the boundary layer consists of two subregions, the lines are approximations because the second boundary layer passing step (surface adsorption layer \rightarrow gas phase) is here neglected, (ii) zero pressure corresponds to the limit where a single fluid molecule is found in the simulation box, and (iii) the lower range of the ordinate was set to the thickness of the AFI unit cell, z_{UC} .

has a rather small influence and levels off, the longer the chain becomes. Finally, the nature of the surface (cage vs window-wise truncated membrane side) does not have any influence on the critical AFI thickness at all (cf., Supplementary Figure 9.13).

Comparing the 2-step δ_{crit} (symbols in Figure 9.2) with corresponding $\delta_{\text{crit}}^{\text{1step}}$ (lines) emphasizes the importance of the boundary layer microstructure. At low pressures, the two critical thicknesses deviate by factors of 2–2.3 for

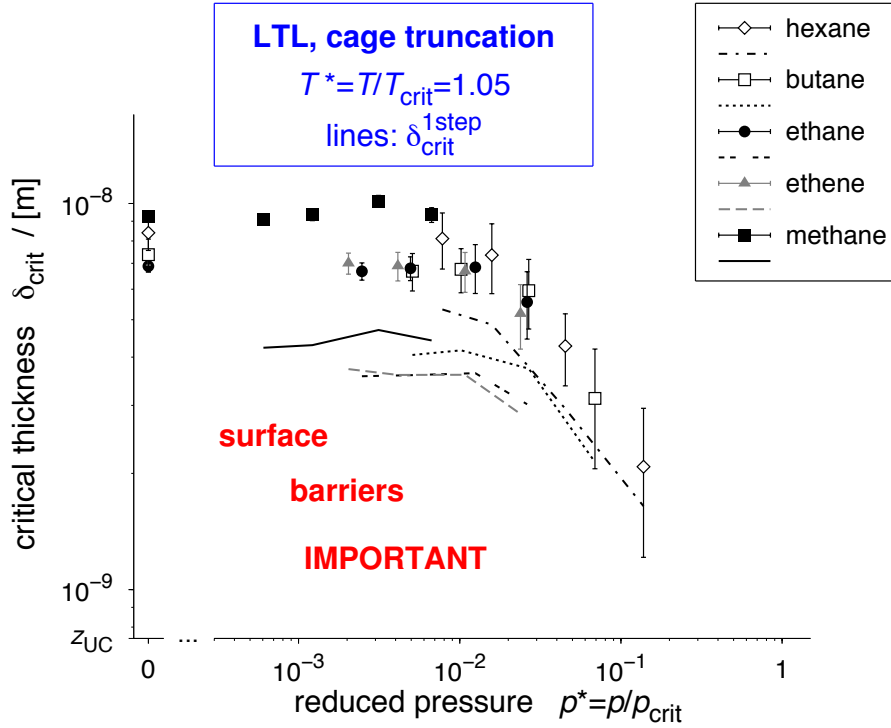


Figure 9.3: Critical membrane thickness, δ_{crit} , vs reduced pressure, $p^* = p/p_{crit}$, for LTL (cf., Figure 9.2).

the different guest species, which indicates that the two fluxes, j_{surf}^\ddagger and j_{gas}^\ddagger , are of similar magnitude. As can be seen from the data of the longer chain molecules, the importance of the second step vanishes however when the fluid state approaches thermodynamic criticality because symbols and lines collapse. This is clear indication of the gas flux being much larger than the flux at the surface and, thus, of the associated transport resistance to vanish ($1/j_{gas}^\ddagger$ term in the denominator of Equation 9.2).

As for LTL, similar trends can be observed as for AFI with respect to the influences of chain length and boundary layer microstructure (Figure 9.3). However, the LTL surface itself seems to have some influence on the critical thickness in contrast to AFI (cf., Supplementary Figure 9.14). The two most striking facts about the LTL results are that the critical thicknesses are roughly one order of magnitude smaller than the AFI values and they are therefore close to the theoretical lower limit of the membrane size (z_{UC}) for most pressures. At this point, it is instructive to turn the attention

back to the free-energy profiles of Figure 9.1. These profiles, obtained from simulations with a single methane molecule, give a good impression of how far δ_{crit} will be apart from this lower membrane limit. If the free energy of the barrier at the external surface, $F(q_{\text{surf}}^{\ddagger}) = F_{\text{surf}}^{\ddagger}$, is similar to the one within the (repetitive) intracrystalline space (i.e., $F_{\text{surf}}^{\ddagger} \sim F_{\text{zeol}}^{\ddagger}$), δ_{crit} will be close to the lower limit. This is true for LTL but not for AFI where $F_{\text{zeol}}^{\ddagger}$ is markedly smaller than $F_{\text{surf}}^{\ddagger}$. It is intuitive altogether that relatively large intracrystalline diffusion barriers render the associated surface barriers less significant.

9.3.2 Intersecting Channels

Figure 9.4 summarizes the results obtained with the MFI-type membranes. Because the MFI slabs were aligned along the maximal flux direction,⁸ the worst case for the surface barriers is probed. Investigating MFI membranes along the x or z coordinate will result in smaller critical membrane thicknesses. Large error bars in the butane and hexane data at the right boundary layer (Figure 9.4b) are observed because vanishing entrance barriers have led to overly sensitive transmission coefficients (cf., Figure 9.1, blue rectangle). A twofold increase in reactive flux trajectories from 5000 to 10 000 did not improve the statistical accuracy, as to be expected from theoretical considerations.⁹¹

The guest molecule chain length has again little influence on the critical thickness and the boundary layer microstructure (symbols vs lines in Figure 9.4) a measurable impact at low pressures only. Similar to LTL, the membrane surface has some influence, which is in agreement with the findings by García-Pérez *et al.*¹⁹³ who investigated ethane–propane adsorption on silicalite-1 surfaces. The authors observed that the surface excess adsorption was dependent on where the crystal was truncated. As can be seen from Figure 9.1 (bottom), canyons form the entrance to the MFI pore network on either side of the crystal slab. The left-hand canyons are however evidently tighter, providing indication for an increasing steric hindrance to pore entrance at the left boundary layer as the molecule chain grows so that the critical thickness in Figure 9.4a are larger than in Figure 9.4b. The most remarkable outcome of the MFI results is that the critical thicknesses reach values of ultrathin zeolite films (> 100 nm) that have already been successfully grown on support materials.^{13,46,48} This illustrates the potential importance of surface barriers to reliable design of hydrocarbon separation by future membrane processes.

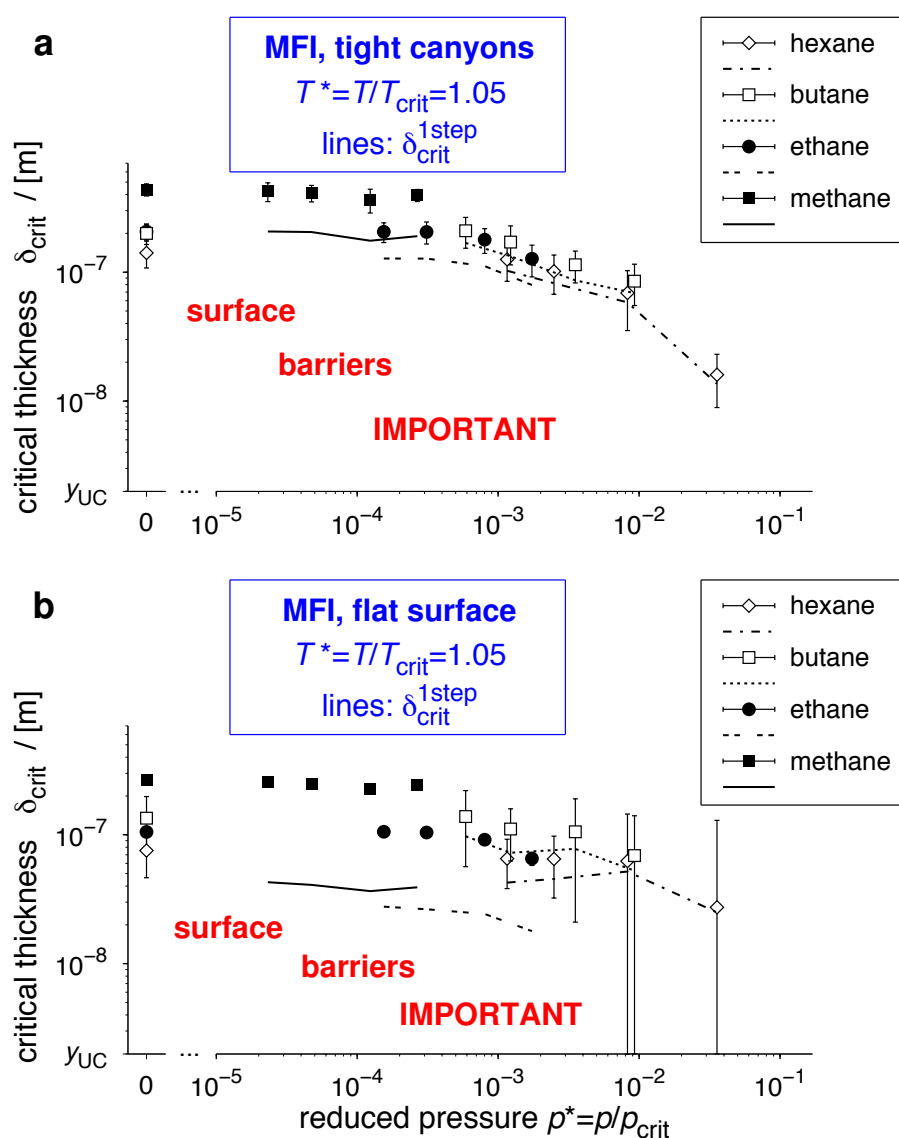


Figure 9.4: Critical membrane thickness, δ_{crit} , vs reduced pressure, $p^* = p/p_{\text{crit}}$, for MFI (cf., Figures 9.2 and 9.3). a) "Tight-canyon" surface (Figure 9.1, bottom left); b) flat surface (Figure 9.1, bottom right).

9.3.3 Temperature

Considering the example of the hydrocarbon–AFI systems, the influence of temperature on surface barriers was investigated on the basis of the 1-step critical thickness, $\delta_{\text{crit}}^{\text{1step}}$. This is because the quite constant factor of 2 sep-

arating δ_{crit} and $\delta_{\text{crit}}^{\text{1step}}$ of these systems will very likely cancel out exactly in the relative consideration pursued below. Furthermore, note that the temperature effect was investigated in the zero-pressure regime only to probe the case of maximal impact of surface barriers and that the ratio of transmission coefficients ($\kappa_{\text{zeol}}/\kappa_{\text{surf}}$) was assumed to remain constant with varying temperature (compare also Supplementary Table 9.1).

Defining $T_{\text{ref}} \equiv 1.05 \cdot T_{\text{crit}}$, the ratio of the critical membrane thickness at any temperature relative to the one at the reference temperature (i.e., the enhancement) reduces to:

$$\frac{\delta_{\text{crit}}^{\text{1step}}(T)}{\delta_{\text{crit}}^{\text{1step}}(T_{\text{ref}})} = \frac{P_{\text{zeol}}^{\ddagger}(T)/P_{\text{surf}}^{\ddagger}(T)}{P_{\text{zeol}}^{\ddagger}(T_{\text{ref}})/P_{\text{surf}}^{\ddagger}(T_{\text{ref}})} = \frac{\exp\left\{\beta[F_{\text{surf}}^{\ddagger}(T) - F_{\text{zeol}}^{\ddagger}(T)]\right\}}{\exp\left\{\beta_{\text{ref}}[F_{\text{surf}}^{\ddagger}(T_{\text{ref}}) - F_{\text{zeol}}^{\ddagger}(T_{\text{ref}})]\right\}}, \quad (9.3)$$

with P_i^{\ddagger} denoting the residence probability at the barrier (\ddagger) i . Instead of correlating this enhancement directly with the corresponding temperature variation (i.e., T/T_{ref}), the abscissa in Figure 9.5, which depicts the results, is the square root of a dimensionless coefficient X . This coefficient is defined as:

$$X \equiv \exp\left[\frac{a \cdot n + \Delta H_{\text{ads},0}}{R} \cdot \left(\frac{1}{T} - \frac{1}{T_{\text{ref}}}\right)\right], \quad (9.4)$$

where R denotes the universal gas constant and a and $\Delta H_{\text{ads},0}$ are parameters that describe the linear relationship between molecular chain length, n , and heat of adsorption, ΔH_{ads} . From the definition of X follows that it effectively represents the enhancement of the Henry coefficient induced by temperature reduction¹⁹⁴ [i.e., $K_{\text{H}}(T)/K_{\text{H}}(T_{\text{ref}})$] while simultaneously accounting for stronger adsorption of larger molecules;¹²⁷ more details are given in Supplementary Subsection 9.6.5.

The critical membrane thickness increases with \sqrt{X} , as seen in Figure 9.5. Because \sqrt{X} increases with decreasing temperature for a given molecule (e.g., methane), surface barriers get stronger as the temperature drops. Strikingly, the enhancement of the critical membrane thickness follows more or less exactly the square root of the enhancement of the Henry coefficient (dashed line). As will be explained below, this square root correlation is caused by the functional relationship of the (free) energy and its associated residence probability in conjunction with a mean-field theory⁹⁶ based argument.

The dimensionless Henry coefficient can be written as:

$$K_{\text{H}} = \frac{\langle c_{\text{zeol}} \rangle}{\langle c_{\text{gas}} \rangle}, \quad (9.5)$$

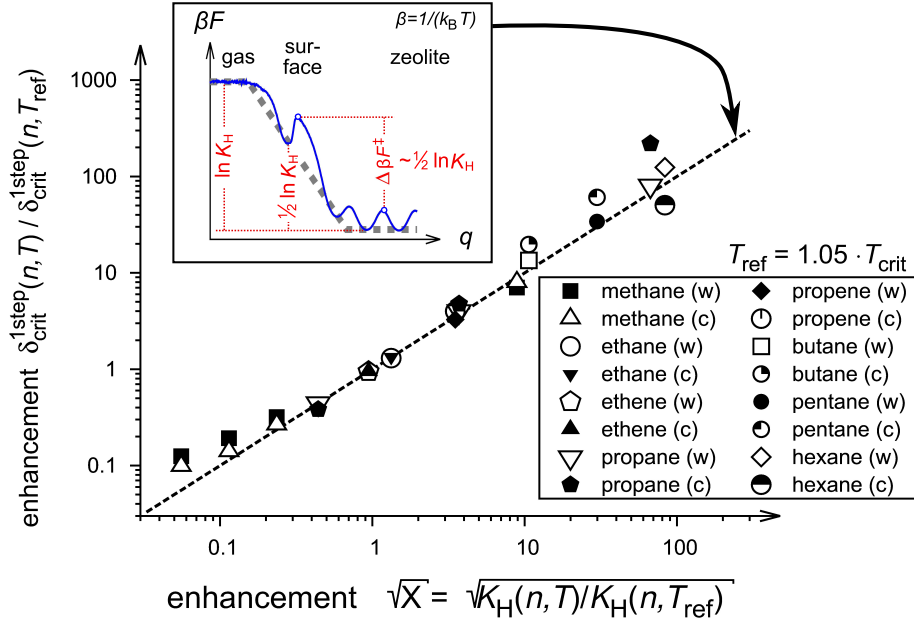


Figure 9.5: Enhancement of the approximate 1-step critical membrane thickness relative to T_{ref} with square root of dimensionless coefficient X (= change in Henry coefficient induced by temperature variation away from T_{ref}). The straight line depicts the case of one-to-one correspondence. Whereas (c) indicates results obtained with the cage-wise truncated surface, (w) refers to the window-wise truncated surface. Insert: Representative free-energy profile (blue solid line) providing an explanatory approach to the square root dependence [thick dashed line: rough approximation to $F(q)$].

where $\langle c_{\text{zeol}} \rangle$ and $\langle c_{\text{gas}} \rangle$ are the average concentrations in the adsorbed (zeolite) phase and in the bulk gas, respectively. Residence probabilities, P , are directly proportional to concentrations. The average concentration in the zeolite, $\langle c_{\text{zeol}} \rangle$, can be approximated with the probability at the intracrystalline free-energy well (P_{zeol}) because, there, the molecules spend most time. The functional relationship between free energy and residence probability is given by $\beta F = -\ln P + \text{const}$. Hence, the difference between free energy in the gas and inside the zeolite is $\beta(F_{\text{gas}} - F_{\text{zeol}}) \sim \ln K_H$ (left-hand side of insert in Figure 9.5). Neglecting any structural details of the zeolite membrane and thus details of the free-energy profile (solid blue line in the insert), and interpolating between gas and zeolite space linearly (thick dotted line in insert), the decisive free-energy difference $\Delta\beta F^\ddagger$ is approximately $1/2 \cdot \ln K_H$ which translates to a square root dependence for the critical membrane length

($\delta_{\text{crit}}^{\text{1step}} \propto \exp \Delta\beta F^\ddagger \sim K_{\text{H}}^{1/2}$). Obviously, these arguments hold only if the intracrystalline barrier is comparable to the barrier at the surface just in front of the pore mouth, that is, the barrier experienced by gas molecules trying to enter from the bulk gas.

9.4 Discussion

Concerning the adsorbent, two main conclusions can be drawn:

1. The importance of surface barriers increases with the smoothness of the nanopore, as the comparison between AFI and LTL suggests. This is supported by the work of Newsome and Sholl¹⁸⁹ who have investigated carbon nanotubes (extremely smooth) revealing very strong surface barriers, and by a current study by Combariza and Sastre.¹⁹¹ The latter authors found virtually no surface barriers for methane uptake in a siliceous LTA slab ($\delta_{\text{crit}} \sim 1$ unit cell), the structure of which exhibits very large intracrystalline barriers (very corrugated pore wall).
2. Comparing the impact of surface barriers on the basis of the critical thickness at zero pressure and the estimate given by Combariza and Sastre,¹⁹¹ a distinct trend is observable, which follows the order MFI > AFI > LTL > LTA and which mirrors the order of decreasing host density (MFI: 18 Si-atoms/[1000 Å³]; AFI: 17.3; LTL: 16.3; LTA: 14.4). In fact, this provides an additional indication of the importance of the rough mean field between bulk gas and zeolite space on surface barriers, as has been discussed in the previous section.

Interestingly enough, both conclusions can, at least from a conceptual view, be exploited in regard of rational process design to decrease surface barriers by choosing less smooth pores in highly porous hosts. Indeed, this route is—probably unintentionally—pursued at present when it comes to the novel group of metal–organic frameworks with ever record-breaking porosity.¹⁹⁵ Provided such structures remain mechanically stable under process conditions, this work foreshadows that surface barriers will be of little concern in any application where these promising materials may be implemented in the future.

Although both the molecule type (alkane vs alkene) and the chain length have very little impact on the strength of surface barriers, an interesting conclusion can be drawn regarding the mobile species. The bulk fluid state of the here studied hydrocarbons was gaseous. As has been shown earlier in this chapter, the more the critical pressure is approached, the more the impact of surface barriers decreases because the fluxes and thus the transport

resistances in the boundary layer and in the zeolite become equal. Moreover, the link between surface barriers and Henry's law provides further indication that the thermodynamic state of the fluid plays an important role for surface barriers. In this context, it is interesting that Webb III and Grest¹⁷⁴ studied liquid hexadecane entering into and traveling through a silicalite zeolite by molecular dynamics where the fluid bulk phase was liquid. The authors did not observe significant surface barriers for this system because the entering mechanism of the long molecule was mainly determined by the subsurface pore structure.¹⁷⁴ Together with the results of this chapter, it can be concluded that surface barriers, as triggered by ideal structures, are expected to be significant for gases in contact with quite thin zeolite layers only (thickness $\lesssim 100$ unit cells), but not for liquids and supercritical fluids.

An important implication follows from the here presented results for such an industrially relevant process as benzene alkylation. Hansen *et al.*²⁰ investigated the reaction-diffusion behavior of benzene alkylation over single H-ZSM-5 particles on the basis of a multiscale simulation approach. Because diffusion limitation was very important,²⁰ the question arises whether or not surface barriers would have had a significant impact on the transport limitation and, hence, on the apparent reaction rate. Benzene and ethylbenzene exhibited very small diffusion coefficients (three magnitudes below the smallest D_S of any system investigated in the previous section). Therefore, it seems unlikely that surface barriers would have been important for the transport limitation of these bulky molecules. By contrast, ethene transport might potentially have been affected by surface barriers because of quite large diffusivities (10^{-8} m²/s) and small crystal sizes (down to 0.1 μm). However, Hansen *et al.*²⁰ clearly showed that the reaction-diffusion system was hardly sensitive to orders-of-magnitude changes in the diffusion coefficient and thus transport rate of ethene. Therefore, it is concluded that the surface barriers reported here would not have influenced the apparent reaction rates and thus effectiveness factors of benzene alkylation as determined by Hansen *et al.*²⁰

The gained insights confirm current experimental breakthroughs by the group around Kärger and Chmelik on MOF Zn(tbip),^{4,5} a nanoporous material with a one-dimensional pore system. Combining experimental microscopy methods with statistical modeling, the group thoroughly studied the transport characteristics of guest molecules in single Zn(tbip) crystals.^{4,5} The diffusion coefficients of *n*-alkanes in that MOF were extremely small—in most cases more than two magnitudes below the here probed ones. This was very likely due to the exceptionally narrow windows that connected adjacent cages which, thus, formed large intracrystalline diffusion barriers.⁴ Most important, however, the authors reported large surface barriers whose primary nature

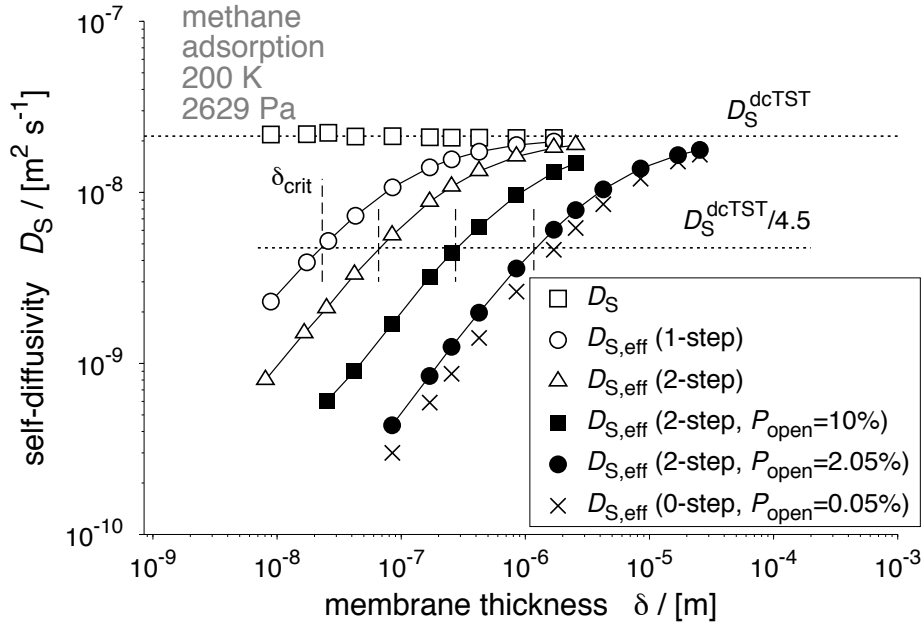


Figure 9.6: Increase of $D_{S,\text{eff}}$ with host thickness for the 1-step exchange mechanism where the boundary layer between gas phase and solid host consists of a single region (zeolite margin only) and for the 2-step exchange mechanism where a second boundary layer (surface adsorption layer) is present (analogous to Figure 7.5); methane tracer uptake in AFI at 200 K and 2629 Pa. Three further cases are included, the first two of which reflect the situation when the surface flux is scaled down by a factor P_{open} to mimic a fraction of $1 - P_{\text{open}}$ blocked pore entrances and where $\delta_{\text{crit}} = 2 \cdot l_{\text{cage}} \cdot j_{\text{zeol}}^{\ddagger} / \{1/[1/j_{\text{gas}}^{\ddagger} + 1/(P_{\text{open}} \cdot j_{\text{surf}}^{\ddagger})]\}$ holds. The third case is similar, yet with the difference that the characteristics of the boundary layer region were neglected ($j_{\text{gas}}^{\ddagger} = j_{\text{surf}}^{\ddagger} = j_{\text{zeol}}^{\ddagger}$ labeled “0-step”) and the slow transport at the surface therefore only due to blocked pore entrances.

was identified as blocked pore entrances (99.95 %) and internal lattice defects, causing the extremely slow uptake. Because of the large intracrystalline barriers and the large crystal size ($> 10 \mu\text{m}$), this work, by contrast, would have predicted no significant influence of surface barriers. Viewed from a different angle, the ideal crystal structures (no defects) and highly ideal surfaces (all channels open) from this study cannot be the reason for the surface barriers from the experimental works which clearly supports the findings of Kärger’s and Chmelik’s group. The reasoning is supported by a subsequent study by the same group that focused on propene transport into an aluminumphos-

phate of LTA type (AlPO₄-LTA).¹³⁹ The authors concluded that the number of blocked pore entrances at the crystal's surface was again extractable from the direct correlation between D_T and α (here: one in 1000–10 000 was open). This points at the fact that the measurement techniques (IFM and IRM) are well suited for surface defect detection of cage-type nanopores^{4,139} and other guest–host systems with exceptionally small intracrystalline diffusivities.^{171,196} But it is questionable whether the methods can go beyond this limitation. That is, assessing relative impacts of surface barriers caused by the ideal crystal and, thus, surface structure as probed here (referred to as “intrinsic surface barriers”) plus departure from ideality (called “defect barrier” in the following). To illustrate that the combined occurrence of both surface barrier types could lead to 40-fold overprediction of the number estimate of blocked entrances the following paragraph turns back to the starting point of how surface barriers are assessed in this work (Figure 9.6).

Chapter 7 has shown that the effective diffusion coefficient that neglects the influence of surface barriers increases with membrane thickness or, more generally, host size. That gave rise to the introduction of a critical thickness where the influence of the surface-barriers effect becomes indistinguishable to the experimental accuracy of diffusion measurements. The microstructure of the boundary layer has, in this context, been shown to be important because the 2-step δ_{crit} is considerably larger than $\delta_{\text{crit}}^{\text{1step}}$ (compare circles and triangles in Figure 9.6). If the tracer-exchange continuum calculations that provided the data for Figure 9.6 are repeated (cf., Chapter 7 and Appendix C) but by scaling down the flux at the surface (j_{surf}^\ddagger) so as to mimic a well defined fraction ($1 - P_{\text{open}}$) of blocked pore entrances ($\rightarrow P_{\text{open}} \cdot j_{\text{surf}}^\ddagger$), the critical thickness decreases further (filled squares: $P_{\text{open}} = 0.1$; filled circles: $P_{\text{open}} = 0.0205$). On the other hand, consider that the entire boundary layer behaved like the bulk zeolite space in regard on the transport characteristics (i.e., $j_{\text{gas}}^\ddagger = j_{\text{surf}}^\ddagger = j_{\text{zeol}}^\ddagger$), which, crucially, is assumed in the evaluation of the experimental works,^{4,5,139} and assume that the fraction of blocked entrances was $P_{\text{open}} = 5 \cdot 10^{-4}$ (“0-step, P_{open} 0.05 %” in Figure 9.6). In that case, the resulting critical thickness is comparable to the “true” situation where intrinsic and defect barriers occur simultaneously (“2-step, P_{open} 2.05 %” in Figure 9.6), hence, yielding an estimate of the blockage number that is approximately 40 times too large. The presented considerations tacitly assume that the unconnected AFI channels are, in fact, connected and that the exchange between channels is very facile (cf., Reference 5). While these facts make the above discussion quite theoretical, remember that MFI exhibited even stronger intrinsic surface barriers, for which reason the same discussion should apply to that structure, which allows for exchange between parallel

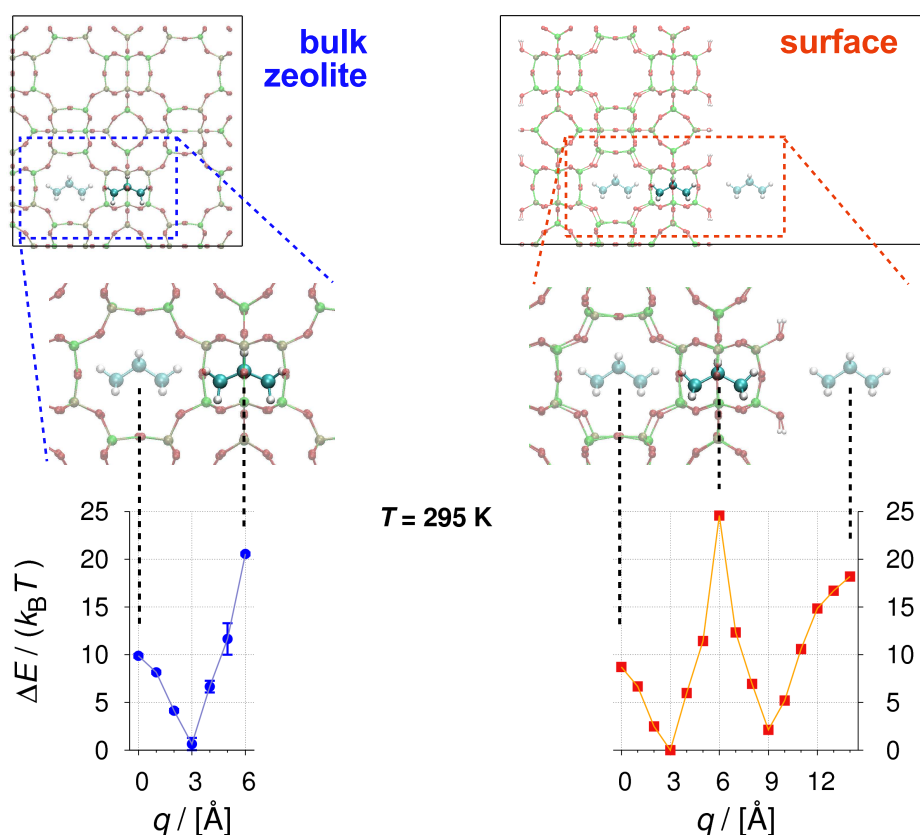


Figure 9.7: Relative energy, ΔE , along transport coordinate, q , for propane in bulk AlPO_4 -LTA (left) and at a corresponding hydroxylated surface (right) obtained from density functional theory calculations that account for dispersive interactions, too. Because two slightly different propane input structures were relaxed in the case of bulk zeolite calculations, two different energies were obtained whose spread is displayed by error bars. Details of the DFT calculations are provided in Supplementary Subsection 9.6.1.

running channels.

An interesting idea to overcome the limitation of the experimental techniques, that is, an idea to also measure intrinsic surface barriers, follows directly from the here unraveled importance of the mean field: decrease T to go to thermodynamic conditions of strong adsorption. This should enhance the importance of intrinsic surface barriers and, consequently, permit the determination of surface permeabilities corresponding to the ideal crystal structure.

The preceding paragraphs have crystallized that the numerous—and very much appreciated—works by the group around Kärger and Chmelik in the quest after the nature of surface barriers *always* came to the conclusion that the effect encountered in their studies must be due to blocked pore entrances.^{4,5,139,171,196} To put to test the conjecture made by the authors¹³⁹ that the nature was in fact true blockage by either foreign matter deposition or severe lattice defects, nonempirical density functional theory (DFT) calculations of propane in bulk AlPO_4 -LTA and at a hydroxylated surface of this zeolite material have been performed. The results are depicted in Figure 9.7, from which a rough self-diffusivity estimate (at infinite dilution) was calculated by $D_S^{\text{TST}} = \sqrt{k_B T / (2\pi m)} \cdot \exp[-(\Delta E/T - \Delta S)/k_B] \cdot l_{\text{cage}}$, where the energy difference was taken from the here reported data (window – cage center; not: window – minimum), the entropy difference estimated on the basis of methane in siliceous LTA (cf., Figure 6.6), and recrossings neglected ($\kappa = 1$). The value, $4 \cdot 10^{-15} \text{ m}^2/\text{s}$, compares surprisingly well with the transport diffusion coefficient at a loading of 2 molecules per cage determined by interference microscopy¹³⁹ ($1.3 \cdot 10^{-15} \text{ m}^2/\text{s}$). Because the true entropic barrier is likely higher and $\kappa < 1$, the true match between experiments and combined DFT–classical simulations is expected to be even better. Similar arguments and approximations should hold for the surface permeability so that the same $-\Delta S$ is encountered at the marginal cage. This, together with the assumption of $\kappa_{\text{surf}}/\kappa_{\text{zeol}} \approx 0.5$ (cf., Supplementary Subsection 9.6.3), results in an approximate correlation between the two coefficients of $\alpha_S^{\text{DCTST}} \cdot l_{\text{cage}}/D_S^{\text{DCTST}} = 0.5 \cdot \exp[-(\Delta E_{\text{surf}} - \Delta E_{\text{zeol}})/(k_B T)] = 0.0037$ on the basis of the data from Figure 9.7. This is a most remarkable result because this figure suggests that the estimate of blocked pore entrances given by Hibbe *et al.*¹³⁹ could have been too high by a factor of ≈ 269 . This would increase the fraction of open entrances from one in 1000–10 000 to one in 4–40! In other words, if more detailed investigations confirm the here presented approximative assessment the hypothesis of true pore blockage “rather than (...) the presence of a more or less uniform surface layer with a substantially reduced permeability”¹³⁹ will be refuted.

Three points should be mentioned to underline that the here presented indications are in fact strong. First, the excellent agreement between the measured propane diffusivity and the estimate of this work validate the approximative assessment. Second, this work has crystallized the high sensitivity of the diffusion coefficient against very subtle window area perturbations and that the sensitivity increases overproportionately with decreasing diffusivity (compare Figure 6.7). Therefore, the surface permeability was expected to be similarly sensitive to only small changes in the window area, too, to

the conjecture of which the just presented DFT results provide evidence. And third, the direct transferability from propene, for which the transport coefficient ratio and thus the estimate of P_{open} in the case of $\text{AlPO}_4\text{-LTA}$ was determined in the experiments, to propane studied here leaves room for uncertainties and doubts. These are, however, eradicated by the work of Kärger's and Chmelik's group on MOF $\text{Zn}(\text{tbip})$ because the $\alpha\text{-}D$ ratios perfectly remained constant in that study,¹³⁹ irrespective of the guest species, loading, and temperature. The incidence that the ratio slightly varied from crystal to crystal finally suggests that the two mechanisms (pore blockage and substantial permeability reduction by the perfectly intact but relaxed crystal surface) occurred in parallel and gave rise to similarly strong transport resistances. Clearly, the true nature of surface barriers remains an exciting scientific quest, even after the here presented efforts.

9.5 Conclusions

To sum up the questions raised in the Introduction of this chapter will be answered.

1. The impact of surface barriers can be well assessed by a critical crystal length beyond which the influence can be assumed insignificant.¹⁷²
2. The barriers strongly depend on the nanopore type and on the thermodynamic state of the surrounding fluid phase, and
3. they are triggered by the ideal crystal structure and by highly ideal surfaces in the here performed simulations.

These insights forecasts that surface barriers will be of importance in many cases of the evolving generation of ultrathin, highly oriented and well intergrown zeolite films^{13,46,48} because the idealized surface alone will retard the overall transport significantly—be it in the analysis of uptake, permeation, or tracer-exchange experiments for transport parameter determination or in the design of membrane reactors. The present chapter has furthermore unraveled that

1. surface barriers can in fact have different reasons and thus natures (intrinsic vs defects), where the mean-field difference between adsorbed and gas phase is a first very important factor to the here probed intrinsic barriers.
2. the different mechanisms can possibly occur simultaneously, thus, rendering defect number estimates very approximative, and

3. the surface structure and chemistry seems to have a much more important influence than usually anticipated, as complementary DFT calculations revealed.

9.6 Supplementary Data

9.6.1 Methodology Details

Molecular Simulations

In contrast to the previous chapter, residence histograms and concentration profiles along the transport coordinates were sampled by *NVT* Monte Carlo simulations instead of *NVT* molecular dynamics. This has the advantage that thermostat issues do not play any role⁸ because homogeneous temperature distributions are rigorously imposed via the acceptance rules that contain the temperature. Two other differences to the methodology of the previous chapter are (1) *NVT* MC simulations generated starting configurations to the reactive flux (RF) simulations¹¹⁰ and *NVE* instead of *NVT* molecular dynamics were used for computing the RF trajectories, which was recommended in Reference 110. Furthermore, a specific bead defined the position of the tagged chain molecule along the transport coordinate instead of its center of mass. In this context, it is important to stress that the mass of that bead instead of the mass of the entire molecule must be inserted into the formula for calculating the ideal kinetic gas theory estimate of the flux/velocity (square root term in Equation 4.55). Both procedures yield same results as the example of a single ethane molecule diffusing in a periodic AFI crystal highlights. Despite obvious differences in free-energy barriers and transmission coefficients, as seen in Figure 9.8, these differences equal out exactly when calculating the DCTST diffusivity:

- $D_S^{\text{DCTST}} = \kappa \cdot D_S^{\text{TST}} = 0.97 \cdot 4.63 \cdot 10^{-8} \text{ m}^2/\text{s} = 4.49 \cdot 10^{-8} \text{ m}^2/\text{s}$ (COM).
- $D_S^{\text{DCTST}} = \kappa \cdot D_S^{\text{TST}} = 0.62 \cdot 7.35 \cdot 10^{-8} \text{ m}^2/\text{s} = 4.56 \cdot 10^{-8} \text{ m}^2/\text{s}$ (bead).

The transmission coefficients for hopping from the external surface toward the gas phase (κ_{gas}) were assumed to equal unity in all cases. This is a good approximation, as will be evidenced in Subsection 10.6.2 on the example of methane hopping away from the external AFI surface adsorption layer at different temperatures.

Electronic Structure Calculations

Density functional theory calculations of propane in bulk $\text{AlPO}_4\text{-LTA}$ and at a hydroxylated surface of this zeolite material have been performed. The projected augmented-wave method was used as implemented in the Vienna *ab initio* simulation package.^{197,198} Dispersive interactions were accounted for by the nonlocal exchange-correlation functional in the van der Waals

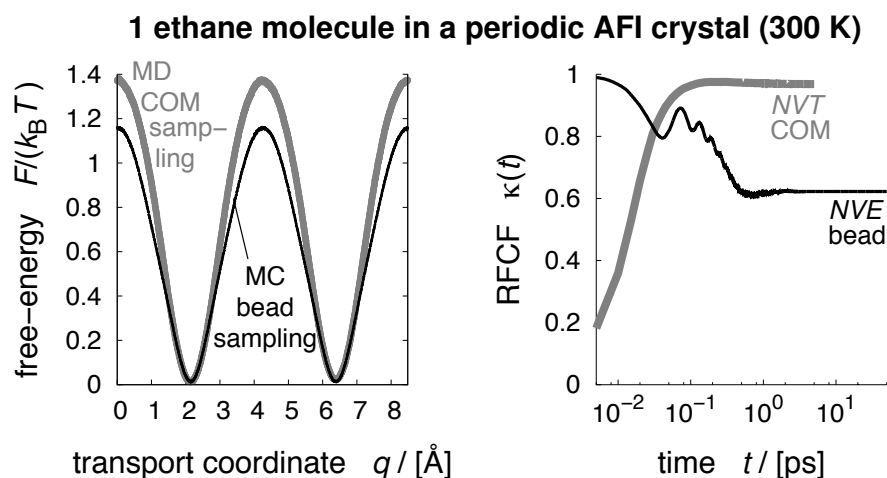


Figure 9.8: Free-energy profiles, $F/(k_B T)$ vs q , (left) and reactive flux correlation function (RFCF), $\kappa(t)$, (right) of a single ethane molecule diffusing in a periodic AFI crystal at 300 K. The thick gray lines represent results where the center-of-mass (COM) defined the position of the molecule, whereas thin black lines used one of the two identical beads of ethane as a measure of the hopping process. Furthermore, the COM histograms were obtained from MD simulations with the LA IFC thermostat while *NVT* MC was used for the bead-sampling histograms and the RFCF were determined with *NVT* MD (thick gray line) and *NVE* MD (thin black line), respectively. The initial $\kappa(t)$ increase in the case of the “*NVT* COM” procedure stems from the starting configurations being located in a small region around the transition state rather than exactly at the barrier position as in the “*NVE* bead” case.

density functional (vdW-DF) formulation.¹⁹⁹ An energy cutoff of 250 eV for the plane-wave basis and the convergence criterion of 10^{-5} eV for the self-consistent solution of the Kohn–Sham equations have been used. Due to the large supercell, the Brillouin zone has been sampled at the gamma point only. For the surface calculations, a vacuum layer of 25 Å has been introduced to avoid spurious interaction between supercell images.

9.6.2 Isotherms and Heats of Adsorption

The adsorption isotherms of the hydrocarbon–zeolite systems, as obtained from GCMC simulations, are provided in Figure 9.9.

In Figure 9.10, the isosteric heats of adsorption obtained at zero loading in AFI are plotted over chain length of the molecule for two temperatures:

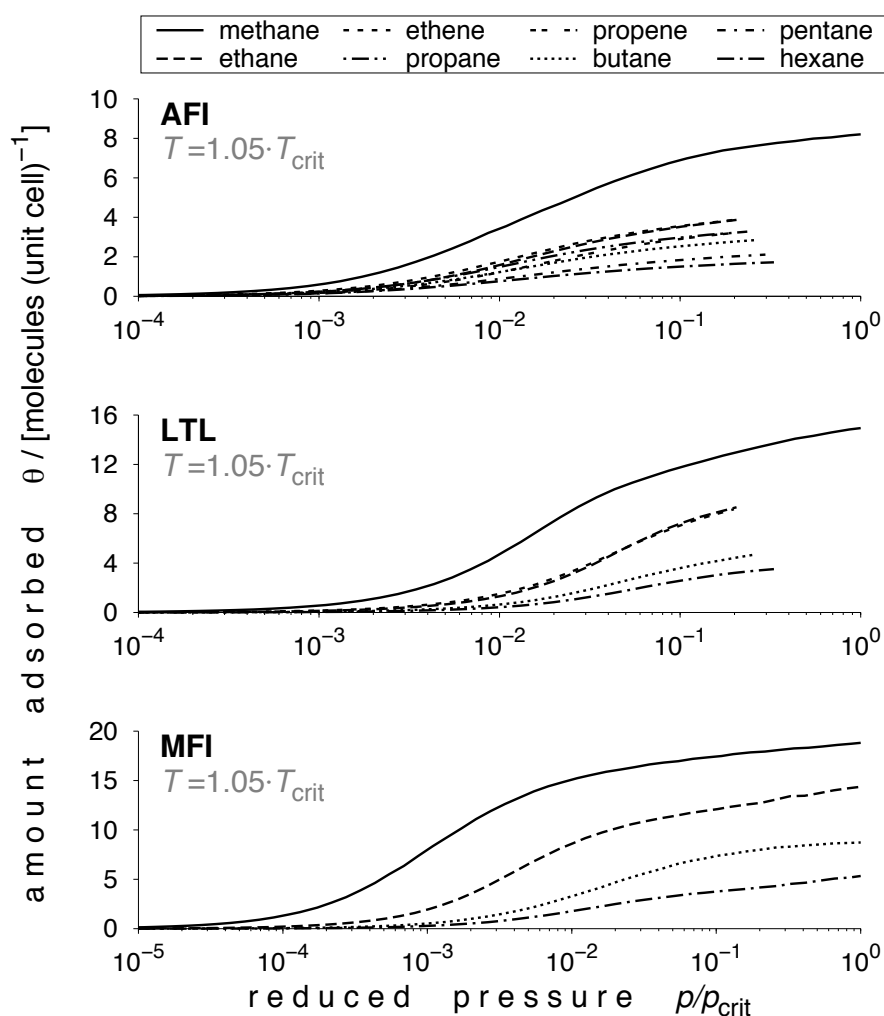


Figure 9.9: Isotherms of various linear hydrocarbons from GCMC simulations in fully periodic zeolites (no surface) of type AFI (top), LTL (center), and MFI (bottom). The temperature was set to $1.05 \cdot T_{\text{crit}}$, where the hydrocarbons' critical temperatures T_{crit} were taken from Reference 192.

300 K and $1.05 \cdot T_{\text{crit}}$. Despite the fact that for hexane, for example, $1.05 \cdot T_{\text{crit}}$ is 233 K larger than 300 K (almost a factor of 2), the temperature has no evident influence on $-\Delta H_{\text{ads}}$. Also, the data of the n -alkanes and n -alkenes lie on a common trend line. Therefore, following linear function describes the dependence of the molecule's chain length on the heat of adsorption very well:

$$-\Delta H_{\text{ads}} = 7.21 \text{ kJ/mol} \cdot n + 7.21 \text{ kJ/mol}. \quad (9.6)$$

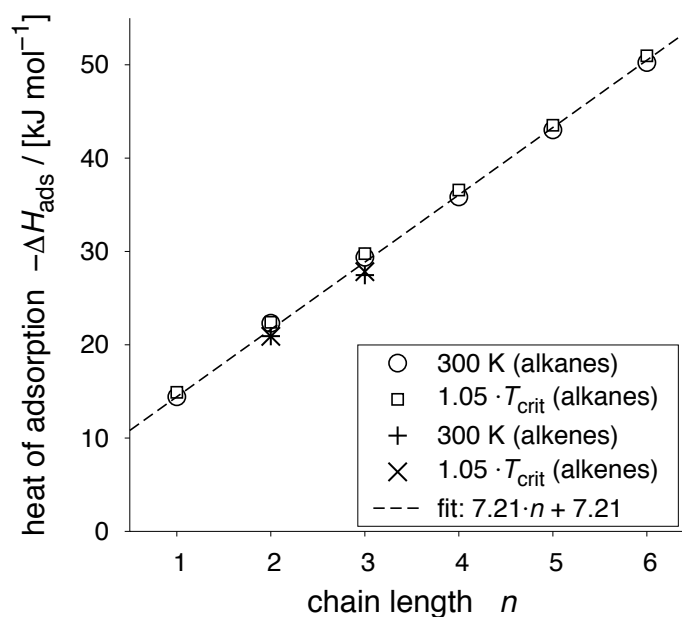


Figure 9.10: Isosteric heat of adsorption, $-\Delta H_{\text{ads}}$, at infinite dilution as a function of hydrocarbon chain length, n .

As in the previous chapter, the bulk fluid concentration and the core zeolite loading were sampled during the simulation of guest molecules that are in contact with a single-crystal zeolite membranes. The agreement of the thus determined isotherms is excellent with data from GCMC simulations, as can be seen in Figure 9.11.

Except for the zero-pressure/zero-loading limit where a single fluid molecule was put into the entire simulation box, the finite-pressure simulations were performed with 10, 20, 50 and 100 molecules, respectively. The pressure was calculated on the basis of the mean bulk gas concentration and the Peng–Robinson equation of state.

9.6.3 Transmission Coefficients

In Figure 9.12, the transmission coefficients in the boundary layers, κ_{surf} , of the three different zeolite membranes are plotted over loading, θ . Linear relationships between κ_{surf} and θ are observable in all cases. This was exploited to calculate the coefficients at zero loading (and thus zero pressure), compare fitted lines in Figure 9.12.

The transmission coefficient ratio (surface to bulk zeolite) remains con-

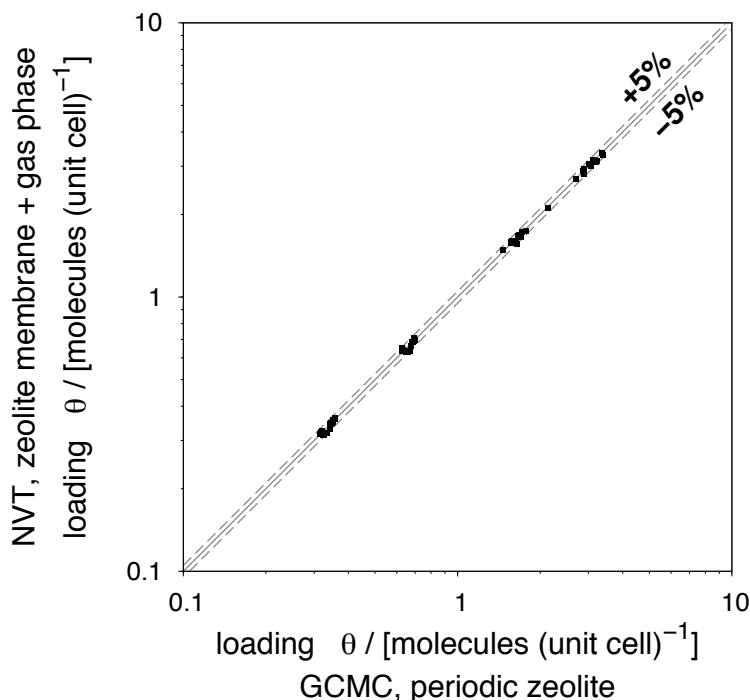


Figure 9.11: Parity plot of loading, θ , at equal T and p obtained from GCMC simulations with a fully periodic zeolite structure (no surface present; abscissa) and from NVT MC simulations using a single-crystal zeolite membrane (with surface and thus explicit gas-phase; ordinate), respectively. Results are from all guest–host systems studied in the present chapter. The lines indicate the region of $\pm 5\%$ deviation.

stant with temperature, as can be seen from the examples given in Table 9.1. This justifies the simplified calculation of the change in (1-step) critical membrane thickness with temperature by just using the ratio of the respective histogram ratios:

$$\frac{\delta_{\text{crit}}^{\text{1step}}(T)}{\delta_{\text{crit}}^{\text{1step}}(T_{\text{ref}})} = \frac{P_{\text{zeol}}^{\ddagger}(T)/P_{\text{surf}}^{\ddagger}(T)}{P_{\text{zeol}}^{\ddagger}(T_{\text{ref}})/P_{\text{surf}}^{\ddagger}(T_{\text{ref}})}. \quad (9.7)$$

In fact, the κ ratios do not vary much with neither temperature nor guest molecule type and surface nature.

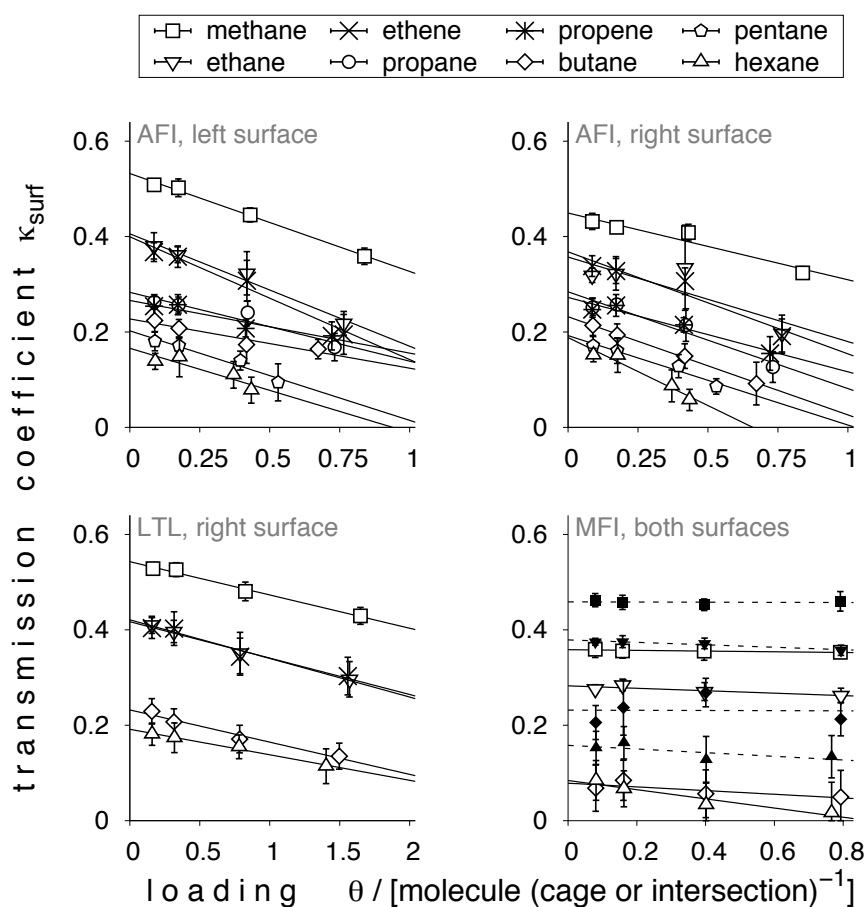


Figure 9.12: Transmission coefficients in zeolite boundary layer, κ_{surf} , vs average loading, θ : AFI window truncation (top, left), AFI cage truncation (top, right), LTL cage truncation (bottom, left), MFI left and right surface (bottom, right).

9.6.4 Critical Membrane Thickness—Remaining Surfaces

In Figure 9.13, critical membrane thicknesses obtained with the left, window-wise truncated AFI surface are displayed. Differences between Figures 9.2 and 9.13 are hardly detectable, justifying the conclusion that the surface structure does not significantly influence the transport in the AFI boundary layer.

The LTL results obtained with the window-wise truncated surface (Figure 9.14) are not too different from the corresponding results of the cage-wise

Table 9.1: Transmission coefficients for hopping between sites inside the bulk zeolite structure (subscript “zeol”) and between zeolite margin and surface adsorption layer (“surf”) as well as their ratios for different hydrocarbons at different surfaces and temperatures. Errors of κ are given as subscripts and the asterisk indicates a case where no free-energy barrier was appreciable.

	T	κ_{zeol}	$\kappa_{\text{surf,l}}$	$\kappa_{\text{surf,r}}$	$\frac{\kappa_{\text{surf,l}}}{\kappa_{\text{zeol}}}$	$\frac{\kappa_{\text{surf,r}}}{\kappa_{\text{zeol}}}$
	[K]	[-]	[-]	[-]	[-]	[-]
methane	200	1.005 _{0.014}	0.528 _{0.021}	0.463 _{0.026}	0.525	0.461
	300	1.005 _{0.064}	0.602 _{0.026}	0.456 _{0.028}	0.599	0.454
ethane	300	0.623 _{0.037}	0.378 _{0.027}	0.305 _{0.029}	0.607	0.490
	321	0.624 _{0.018}	0.383 _{0.035}	0.329 _{0.029}	0.614	0.527
hexane	300	0.280 _{0.020}	0.142 _{0.036}	—*	0.507	—*
	533	0.305 _{0.019}	0.153 _{0.028}	0.171 _{0.028}	0.502	0.561

truncated surface either (Figure 9.3). Only, the “window” results are shifted up, roughly by a factor of two, which indicates that surface barriers in LTL are sensitive to the surface nature, in contrast to AFI. It, however, has to be pointed out that the results for LTL at the window-wise truncated membrane side are subject to an approximation, as discussed below.

The approximation made was that transmission coefficients at the left LTL surface were, for a given molecule and state point, assumed to be equal to the one calculated at the right boundary ($\kappa_{\text{surf,l}} = \kappa_{\text{surf,r}}$). The problem was the quite exceptional surface structure, as seen in Figure 9.1. The simple reaction coordinate (Cartesian z direction) did not describe the process of a guest molecule leaving the pore correctly. To explain this consider Figure 9.15, where a two-dimensional free-energy landscape along with the corresponding 1D profile is shown for methane found in the vicinity of the left LTL pore mouth.

The dividing surface between crystal exterior (external surface plus gas region) and interior is located at $q_{\text{surf}}^{\ddagger} = -19.2 \text{ \AA}$. The Cartesian reaction coordinate adequately describes a hop progress of the molecule from the barrier into the pore interior (first cage at $q_{\text{B}} = -14.9 \text{ \AA}$) because, between \ddagger and B, there exist only one single region with respect to r_{pore} where residence is possible. This is yet not true for the opposite side. If a molecule attempts to move from \ddagger along the minimum free-energy path toward A it

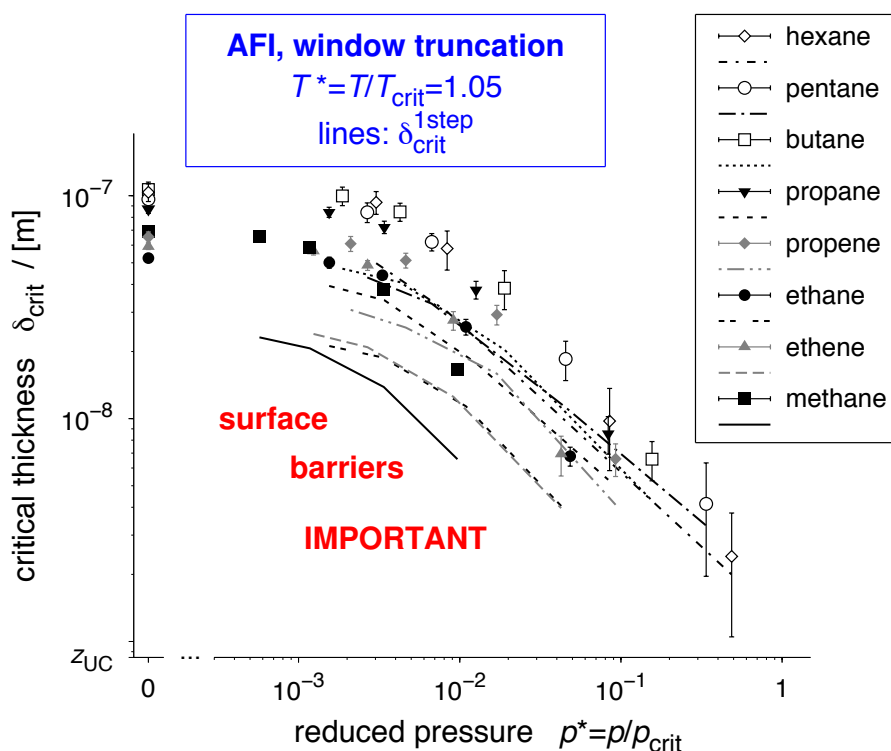


Figure 9.13: Critical membrane thickness, δ_{crit} , as a function of reduced pressure, $p^* = p/p_{\text{crit}}$, for different n -alkanes (C1-C6) and n -alkenes (C1-C2) adsorbed in all-silica AFI-type zeolites (membranes were truncated at the position of the window atoms). Note that (i) while the symbols represent results accounting for the fact that the boundary layer consists of two subregions, the lines are approximations because the second boundary layer passing step (surface adsorption layer \rightarrow gas phase) is here neglected, (ii) zero pressure corresponds to the limit where a single fluid molecule is found in the simulation box, and (iii) the lower range of the ordinate was set to the thickness of the AFI unit cell, z_{UC} .

has to first cross $q_A = -20.4 \text{ \AA}$ once at A^* ($r_{\text{pore}} \leq 3 \text{ \AA}$) to finally equilibrate in $[q_A, r_{\text{pore}} \sim 8 \text{ \AA}]$, being the true “stable state” for the “backward reaction” (out-of-crystal jump). So, two separate regions of possible residence exist between A and \ddagger . A reactive flux shoot from q_{surf}^\ddagger that aims to the external surface will therefore be stopped premature, if hop success is measured by the Cartesian reaction coordinate only and, thus, without any additional order parameter. But this procedure is implemented in the simulation package

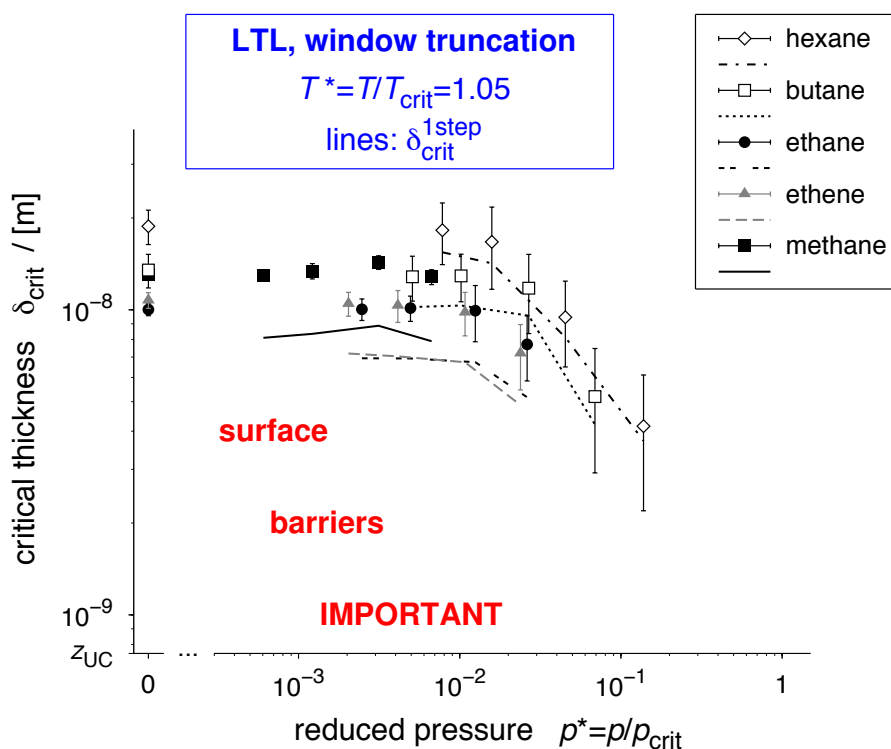


Figure 9.14: Critical membrane thickness, δ_{crit} , vs reduced pressure, $p^* = p/p_{crit}$, for LTL (cf., Figure 9.13). The transmission coefficients at the left surface were approximated by those determined at the right surface. This is, $\kappa_{surf,l} = \kappa_{surf,r}$.

used.

9.6.5 Temperature and Chain-Length Dependence of Henry Coefficient

In Subsection 9.3.3, a coefficient, X , is used to correlate the change in critical membrane length with change in temperature, taking simultaneously into account the chain length of the molecules which, of course, exhibit different adsorption strengths. Here, it is shown how this coefficient was obtained and that it equals the change in Henry coefficient, K_H , with varying temperature, T , and chain length, n .

The starting point is the temperature dependence of the Henry coefficient

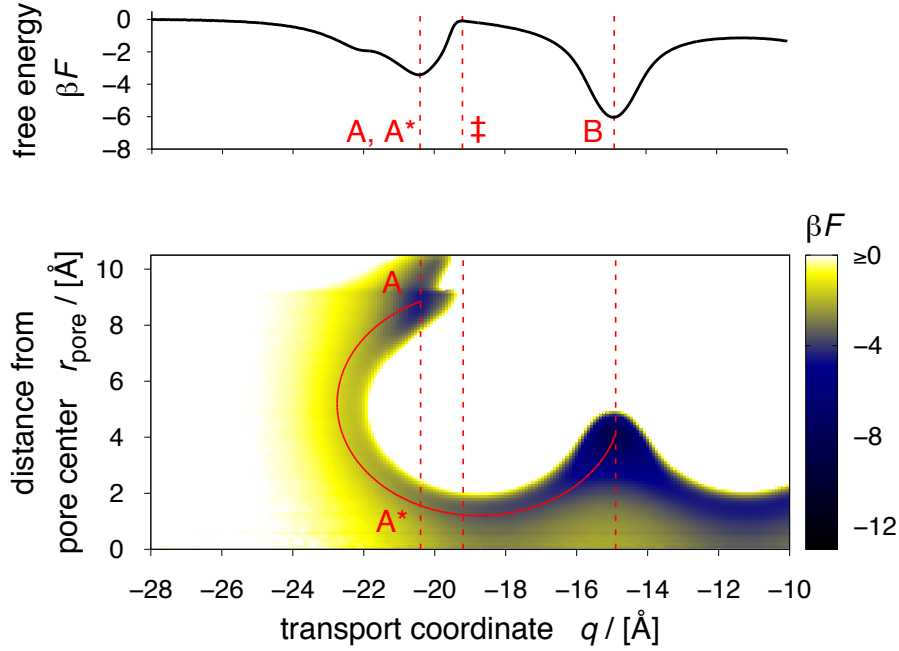


Figure 9.15: Top: one-dimensional free-energy profile, $\beta F(q)$; bottom: two-dimensional free-energy landscape, $\beta F(q, r_{\text{pore}})$; methane around the window-wise truncated LTL surface (1 molecule, 200 K).

for a given gas molecule (see, for example, Reference 194):

$$\ln K_{\text{H}}(T) = -\frac{\Delta H_{\text{ads}}}{R} \cdot \frac{1}{T} - \text{const.}, \quad (9.8)$$

where ΔH_{ads} denotes the isosteric heat of adsorption which is usually negative, R is the universal gas constant and T the temperature. The heat of adsorption can be expressed in terms of the molecule's chain length, n , as has been shown in Supplementary Subsection 9.6.2:

$$-\Delta H_{\text{ads}}(n) = a \cdot n + \Delta H_{\text{ads},0}. \quad (9.9)$$

a and $\Delta H_{\text{ads},0}$ are fitting parameters to the linear function, as determined earlier. Because the heat of adsorption does not change with temperature (Figure 9.10), Equation 9.9 can be inserted into Equation 9.8 and rearranged to:

$$K_{\text{H}}(n, T) = \exp \left[\frac{a \cdot n + \Delta H_{\text{ads},0}}{R} \cdot \frac{1}{T} - \text{const.} \right]. \quad (9.10)$$

Defining T_{ref} as an (arbitrary) reference temperature, the ratio of the Henry coefficient at any temperature to its reference value at T_{ref} follows:

$$\frac{K_{\text{H}}(n, T)}{K_{\text{H}}(n, T_{\text{ref}})} = \exp \left[\frac{a \cdot n + \Delta H_{\text{ads},0}}{R} \cdot \left(\frac{1}{T} - \frac{1}{T_{\text{ref}}} \right) \right] = X. \quad (9.11)$$

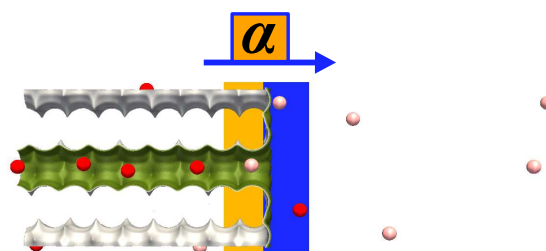
Hence, the coefficient X represents the analytical change in Henry coefficient with varying temperature by accounting for the length of the molecule, at the same time.

10

Predicting Surface Permeabilities

The regular nanoporous structure make zeolite membranes attractive candidates for separating molecules on the basis of differences in transport rates (diffusion). Because improvements in synthesis have led to membranes as thin as several

hundred nanometers by now, the slow transport in the boundary layer separating bulk gas and core of the nanoporous membrane is becoming increasingly important. Therefore, the predictability of the coefficient quantifying this local process, the surface permeability α_S , is investigated by means of a two-scale simulation approach. Methane tracer-release from the one-dimensional nanopores of an AFI-type zeolite is employed. Besides a pitfall in determining α_S on the basis of tracer exchange, importantly, an accurate prediction of the surface permeability is presented using readily available information from molecular simulations. Moreover, it is shown that the prediction is strongly influenced by the degree of detail with which the boundary region is modeled. It turns out that not accounting for the fact that molecules aiming to escape the host structure must indeed overcome two boundary regions yields too large a permeability by a factor of 1.7–3.3, depending on the temperature. Finally, the results of this chapter have far-reaching implications for the design of future membrane applications.



10.1 Introduction

Molecular exchange between a gas reservoir and a nanoporous crystalline solid (e.g., a zeolite membrane or crystal) represents a key design process in applications, such as adsorption, molecular-sieving, catalysis, and ion-exchange. Over the last few decades, a good understanding has been developed with regard to the role²⁰ and dependence^{4,5,10,41,106,146} of guest diffusion in such regular host structures, that is, the transport mechanism of molecules inside the nanopores far away from the interface to the fluid phase.^{200,201} For example, gas diffusion in zeolites is known to be an activated process^{4,5,10,146} where molecules need to overcome a series of regularly distributed internal diffusion barriers which arise from nanopore shape in the unit cell alone.⁴¹ Many phenomena, including the loading dependence of the self-diffusion coefficient, can be explained by the variation of such (free) energy barriers. In this context, molecular simulations have been proven to be invaluable,^{10,146,159} owing to improved agreement with experiments.^{90,181,202} Despite these accomplishments, there are still unresolved problems,²⁰³ many of which are related to the boundary layer separating the gas-phase region from the core zeolite space.

While cases exist in which the boundary layer may accelerate molecular exchange between the reservoir and the porous host,^{204,205} it usually slows down the transport rate close to the surface,^{4,5,113,114,171,206} leading to the name of this phenomenon: surface barriers. Exciting insights into their nature have been unraveled only recently.^{4,5,114} Microscopy experiments⁴ in conjunction with mesoscopic modeling⁵ evidenced that exceptionally few accessible pore entrances together with a large number of lattice defects (i.e., vast crystal nonidealities as depicted in Figure 10.1 on the left) formed extremely high surface barriers on very large MOF Zn(tbip) crystals (labeled “defect barriers” here). On the other hand, Zimmermann *et al.*¹¹⁴ have recently shown with the aid of molecular simulations that perfect single-crystal zeolite membranes (i.e., highly ideal crystal and surface structure) can also possess strong barriers at the external surface, as long as thin membranes ($\lesssim 100$ unit cells) are being considered. The origin of these barriers lay in the difference of the mean field experienced by the guest molecules in gas and adsorbed phase (Figure 10.1 right), for which reason they are labeled intrinsic barriers in the following. Therefore, a unique source of surface barriers does obviously not exist, emphasizing the necessity of a consequent discrimination between different effects.

Despite the improvement of understanding surface barriers, an assessment of the coefficient quantifying the rate of transport in the boundary

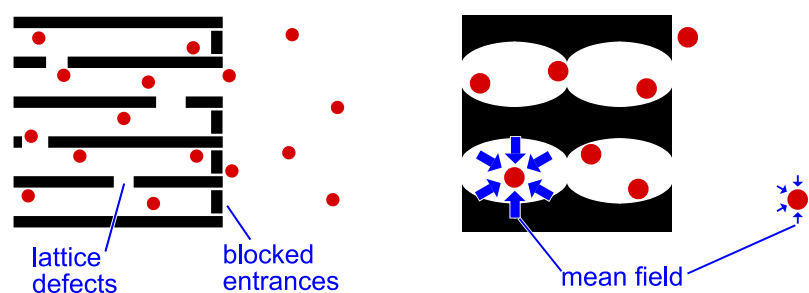


Figure 10.1: Surface barriers can have different reasons. Blocked pore entrances together with lattice defects (left) and mean-field differences (right) “felt” by molecules in adsorbed and gas space, respectively, can both render the rate of transport at the solid–gas interface extremely small.

layer, the surface permeability α_S , is so far possible to a satisfactory degree for the defect barriers only. In numerous case studies, Kärger, Chmelik, and co-workers^{3,4,168,171,206} successfully measured the surface permeabilities of gas molecules in large crystals. However, the consistent prediction of this coefficient for intrinsic surface barriers via information from molecular simulations is a challenging task to date.^{9,113,191,207} This chapter therefore highlights a pitfall that might have been overlooked so far and, most importantly, provides a satisfying prediction of the surface permeability over those conditions that are currently of practical interest.

10.2 Methodology

The focus of the present chapter lies on the conceptually simplest case of molecular exchange—tracer exchange—where macroscopic concentration gradients are absent and the exchange involves differently “colored” molecules rather than different species (Figure 10.2a). Because tracer exchange situations directly relate to self-diffusion, all diffusion coefficients presented here are self-diffusivities (D_S).

Several steps are necessary for molecules to be exchanged between the zeolite space and the gas-phase region, as illustrated by the trajectory of a single molecule in Figure 10.2a:

1. A molecule needs to traverse the nanopore to eventually reach the outermost cage, which is referred to as the zeolite margin in the remainder. This intracrystalline diffusion is impeded by successive barriers originating from the repetitive crystal structure (internal diffusion barriers,

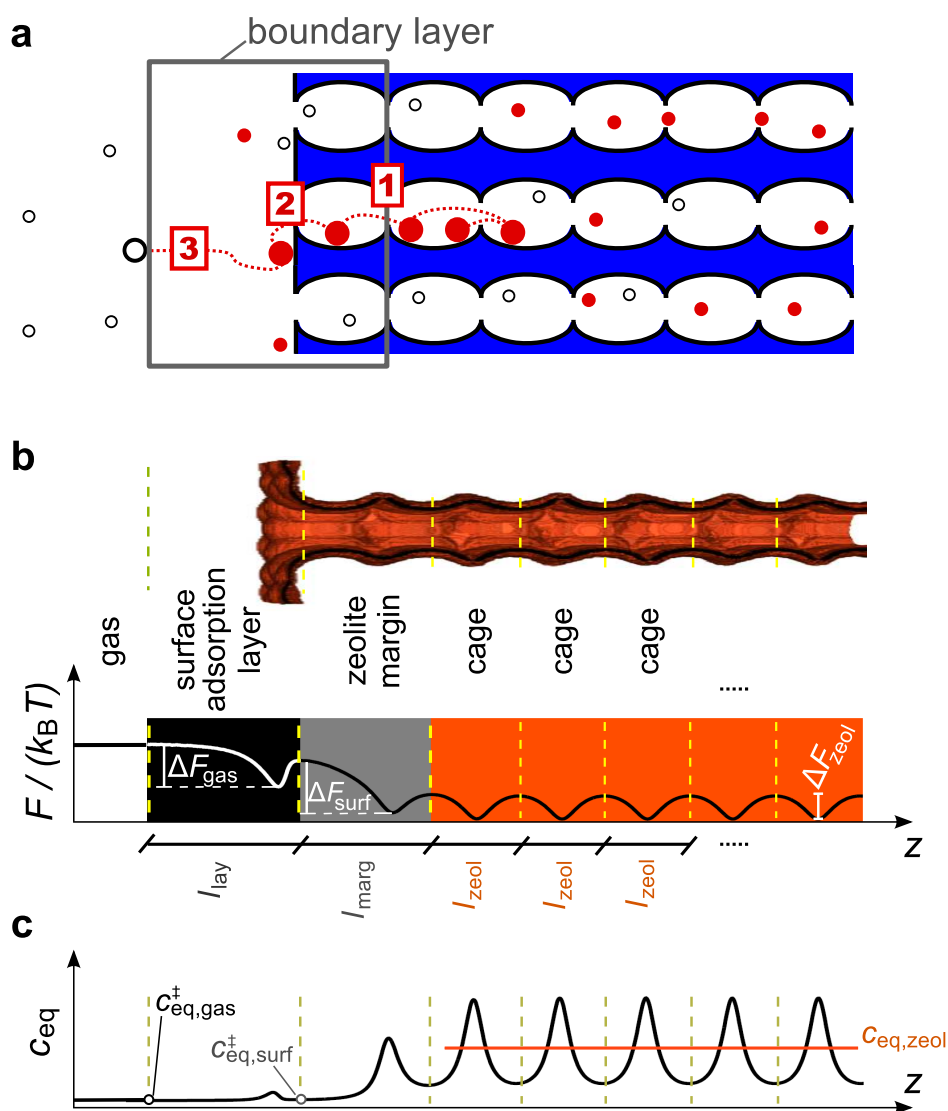


Figure 10.2: (a) Exchange of a tracer molecule involves three steps: (1) Diffusion to reach the outermost cage (zeolite margin). (2) Jumping out of the pore structure to reach the external surface adsorption layer. (3) Finally, leaving this layer to disappear in the gas phase. (b) Channel and surface structure of the here studied AFI-type zeolite together with a representative free-energy profile, $F/(k_B T)$, along the exchange direction, z . (c) Equilibrium concentration profile, c_{eq} , corresponding to (b); note that $c_{\text{eq}}(z) = \exp[-F(z)/(k_B T)] \cdot \text{const}$ and that l_{zeol} equals l_{cage} .

ΔF_{zeol} , as seen at the end of the orange region of Figure 10.2b).

2. The molecule must then get out of the pore and reside on the external surface adsorption layer. This process is controlled by a first boundary barrier, ΔF_{surf} (gray region in Figure 10.2b).
3. Finally, to truly desorb from the solid and thus to lose the color, the molecule must overcome a second boundary barrier, ΔF_{gas} , that separates the surface adsorption layer from the gas-phase region, as evidenced by Figure 10.2b (black region).

Step 1 is mathematically described by the standard Fickian diffusion equations. Steps 2 and 3 are usually modeled with a surface evaporation boundary condition,⁹² yielding a relationship between the current net flux of tracer molecules at the boundary, $j_{\text{surf}}(t)$, the surface permeability, and the driving force:

$$j_{\text{surf}}(t) = \alpha_{\text{S}} \cdot [c_{\text{surf}}(t) - c_{\text{surf}}(t \rightarrow \infty)], \quad (10.1)$$

where c denotes concentration of tracer (i.e., colored) molecules and $c_{\text{surf}}(t \rightarrow \infty) = 0$ in the present case because complete exchange is considered.⁹² At this point, a first problem arises because, obviously, two different processes (steps 2 and 3) need to be described with a single coefficient (α_{S}), which represents one of the main tasks of the present chapter. However, the release in the first part of the analysis is considered to proceed via a one-step mechanism in which molecules are assumed to be exchanged when they have performed step 2 in Figure 10.2a. This is instructive because the approximation has been made often in the past but it is not free of problems, as mentioned earlier. Moreover, the resulting one-step surface permeability prediction helps in fact rationalizing the final two-step permeability.

The example of methane desorbing from siliceous AFI-type zeolite membranes will be employed, the structure⁶¹ of which exhibits one-dimensional channels (Figure 10.2b). The methodologies underlying Chapters 7 and 9 is used, which comprises two stages, each involving a different maximum length scale: (i) molecular-detailed simulations, where AFI membranes of ≈ 5 nm thickness are used (cf., Chapter 9), and (ii) continuum calculations to reach membranes of up to several micrometer width (cf., Chapter 7 and Appendix C). In the first stage, methane is modeled as a united atom¹²⁶ and the AFI membrane concludes with the pore windows. This stage yields free-energy and concentration profiles (Figure 10.2), from which the input data to the second stage are extracted, notably, equilibrium transport rates between the different compartments (zeolite cages, margin, surface adsorption layer) as well as their equilibrium concentrations and widths. In the second stage, the material balances are solved numerically on the basis of the data obtained

from the molecular simulations. These calculations provide transient concentration profiles (Figure 10.3a). Integral tracer-release curves, $1 - m(t)/m(0)$, are then determined (Figure 10.3b), describing the progress of exchanging “colored” molecules (red circles in Figure 10.2a) for “uncolored” molecules (open circles). Such exchange curves are commonly encountered in diffusion-experiment analysis,²⁰⁸ and they can be envisioned in an integral modeling approach to pressure swing adsorption.⁵³

The release curves are fitted to the analytical solution⁹² of Fick’s laws under consideration of the evaporation boundary condition (Equation 10.1):

$$1 - \frac{m(t)}{m(0)} = 1 - \sum_{i=1}^{\infty} \frac{2L^2 \exp[-\gamma_i^2 D_S t / (\delta/2)^2]}{\gamma_i^2 (\gamma_i^2 + L^2 + L)}, \quad (10.2)$$

with $L = (\delta/2)\alpha_S/D_S$, δ the membrane thickness, and γ_i are the positive roots of $\gamma \tan \gamma = L$. The thus obtained transport coefficients are plotted in Figure 10.3c,d for increasing membrane thickness and a single state point (T , p). Note again that these results are obtained from one-step release calculations.

The here presented two-stage simulation strategy features two distinct advantages. First, simulations with membrane thicknesses up to the micrometer range become feasible, which would not be possible with conventional equilibrium molecular dynamics (MD),⁹ let alone nonequilibrium MD^{124,125} employing thick zeolite membranes. Second, the condition of tracer exchange avoids the possibility that the surface permeability is process dependent, that is, whether molecule release or uptake is being investigated (cf., Supplementary Subsection 10.6.1 and Reference 206). Therefore, the present chapter can mainly focus on the concentration dependence of the permeability which is indeed speculated to be the reason why α varies for uptake and release in nonequilibrium conditions.²⁰⁶

10.3 Results

10.3.1 One-Step Release Mechanism

It might seem trivial to match the surface permeability from the continuum calculation with predictions based solely on information from the first stage (molecular simulations). Figure 10.3 shows however that both D_S and α_S are dependent on the membrane thickness for a given state point. Theoretically, the parameters must not vary with membrane thickness. When the continuum simulations are repeated by setting the zeolite margin width

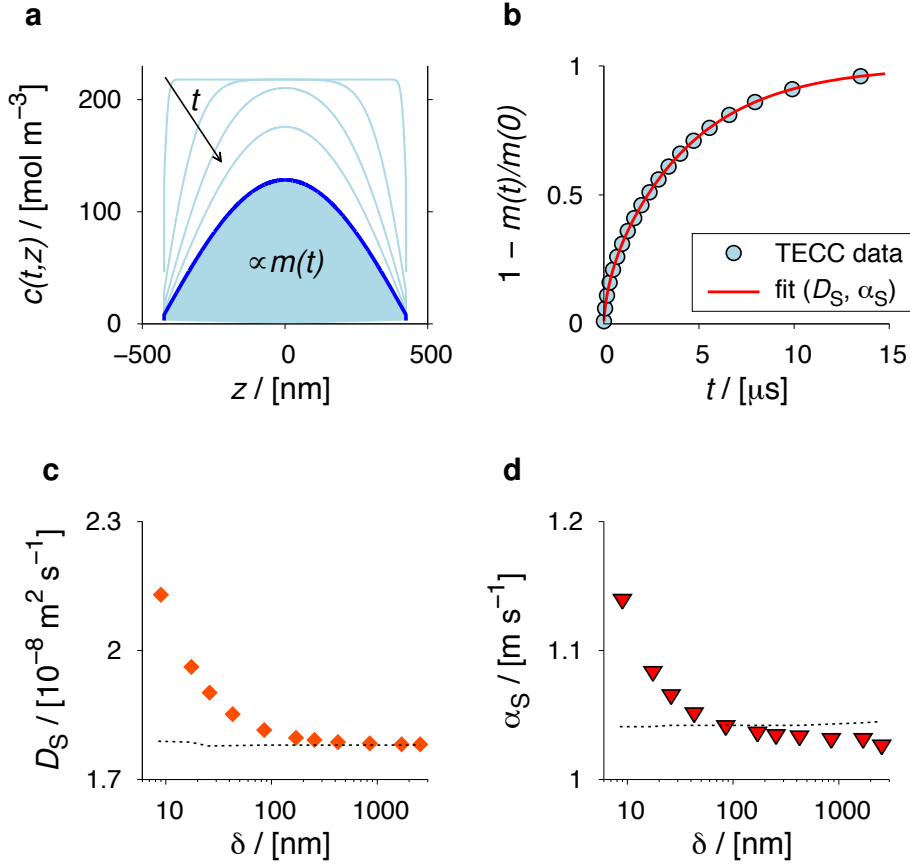


Figure 10.3: Concentration profiles (a) obtained from a tracer-exchange continuum calculation (TECC) via the one-step release mechanism ($\delta = 848 \text{ nm}$) yield the tracer-exchange curve (b). The fitted self-diffusion coefficients (c) and tracer-exchange surface permeabilities (d) depend on the membrane thickness, δ . ($T = 181 \text{ K}$, $p = 1202 \text{ Pa}$).

equal to the cage separation ($l_{\text{marg}} = l_{\text{zeol}}$) and also equating the equilibrium concentration in the margin with the one of the bulk-zeolite space ($c_{\text{eq,marg}} = c_{\text{eq,zeol}}$), the horizontal dashed lines in Figure 10.3c,d are obtained, where the diffusivity equals the prediction by dynamically corrected transition state theory.^{109,110,113,116} With these assumptions, the transport coefficients do not change with thickness, hence, illustrating an important point. The dependence of the transport coefficients on the membrane thickness is brought about by subtle differences of the properties of the zeolite margin from the properties of the inner cages. The maximal deviation of D_S and α_S amounts to 20% and 10%, respectively. This underlines the ne-

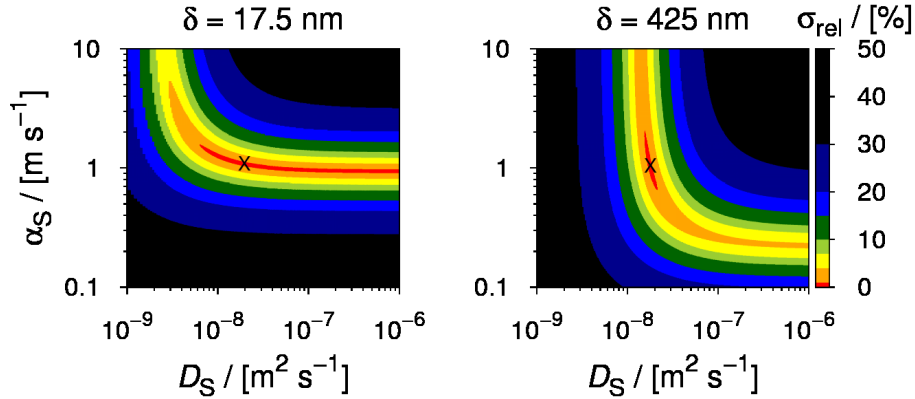


Figure 10.4: Parameter space of Equation 3.7 for two different membrane thicknesses: 17.5 nm (left) and 425 nm (right); methane in AFI at 181 K and 1202 Pa.

cessity for an improved analytical integral solution of the diffusion process incorporating varying margin width and equilibrium concentration into the boundary condition.

The effect, however, can so far not have had any immediate implication to membranes that are currently producible because their thicknesses¹³ are yet more than a magnitude apart from the region where it becomes significant. Although it might come into play in the future, because improvements in membrane synthesis adumbrate constantly decreasing thicknesses,^{11,209} the effect seems weak. A comparison between Figure 10.3 and Figure 7.3 reveals that the fitted self-diffusivity from Chapter 7 remains constant despite similar conditions (methane exchange in AFI at 181 K and 200 K as well as 1202 Pa and 2629 Pa, respectively). The reason lies in the parameter space associated with Equation 3.7, which is displayed in Figure 10.4 for two different membrane thicknesses at otherwise equal conditions. The optimum parameter pair is well localized in the case of thick membranes; compare “x” in plot on the right-hand side of Figure 10.4. But this behavior cannot be confirmed for thin membranes because the optimum parameter region resembles a shallow canyon, stretching parallel to the D_S axis over several orders of magnitude at more or less constant α_S (red stripe in Figure 10.4, left). As a consequence, increasing D_S by a factor of, say, 10 has hardly an influence on the reproducibility of the tracer-exchange continuum calculation data (i.e., σ_{rel} hardly changes), which underlines the weak nature of the effect. This, in turn, means that the true optimum in D_S can be easily missed in the case of thin membranes, if the corresponding grid spacing (ΔD_S) was

too coarse. That was true for the generation of Figure 7.3.

The practically relevant membrane width range is several hundred nanometers and onward,^{11,13} for which both transport coefficients show asymptotic values (Figure 10.3c,d). This means that the determination of the surface permeability would involve an entire set of continuum calculations to identify when α_S becomes constant or, alternatively, a long simulation with a very thick membrane. Instead, one wants to skip this stage altogether and calculate α_S directly based on data of the first (molecular level) stage. In this context, three different models were tested. Figure 10.5 summarizes the results, where different symbols represent predictions by different models and the line represents the target surface permeabilities obtained from tracer-exchange continuum calculations with very thick membranes.

The first model (crosses in Figure 10.5) was suggested by Kärger and co-workers^{4,5} and assumes that the surface permeability is proportional to the diffusion coefficient:

$$\alpha_S = 0.5 \cdot \frac{D_S}{l_{\text{zeol}}}. \quad (10.3)$$

While the surface permeabilities obtained from tracer-exchange calculations increase with loading (line), the model predicts a declining trend of α_S because the corresponding diffusion coefficients decrease with loading. Hence, the model of Kärger and co-workers^{4,5} is not applicable for the here studied systems. As it was validated against diffusion experiments probing defect barriers, the qualitative discrepancy emphasizes again the imperative of discriminating between different surface-barrier sources. As a consequence, different local transport coefficients are naturally obtained depending on the relative significance of the two different influences (intrinsic vs defect barriers).

Gulín-González *et al.*⁹ suggested that a correlation between the two transport coefficients should be corrected by inclusion of an additional *potential-energy* barrier. This is because a molecule experiences a higher barrier, ΔU_{surf} , when hopping out from the marginal cage onto the external surface in comparison to the internal diffusion barriers, ΔU_{zeol} :

$$\alpha_S = \exp\left(-\frac{\Delta\Delta U}{k_B T}\right) \cdot \frac{D_S}{l_{\text{zeol}}}, \quad (10.4)$$

with $\Delta\Delta U = \Delta U_{\text{surf}} - \Delta U_{\text{zeol}}$. However, this model does not lead to satisfactory qualitative results either (triangles in Figure 10.5). What changes the trend of the permeability prediction over loading is the consideration of higher free-energy barriers:

$$\alpha_S = \exp\left(-\frac{\Delta\Delta F}{k_B T}\right) \cdot \frac{D_S}{l_{\text{zeol}}}, \quad (10.5)$$

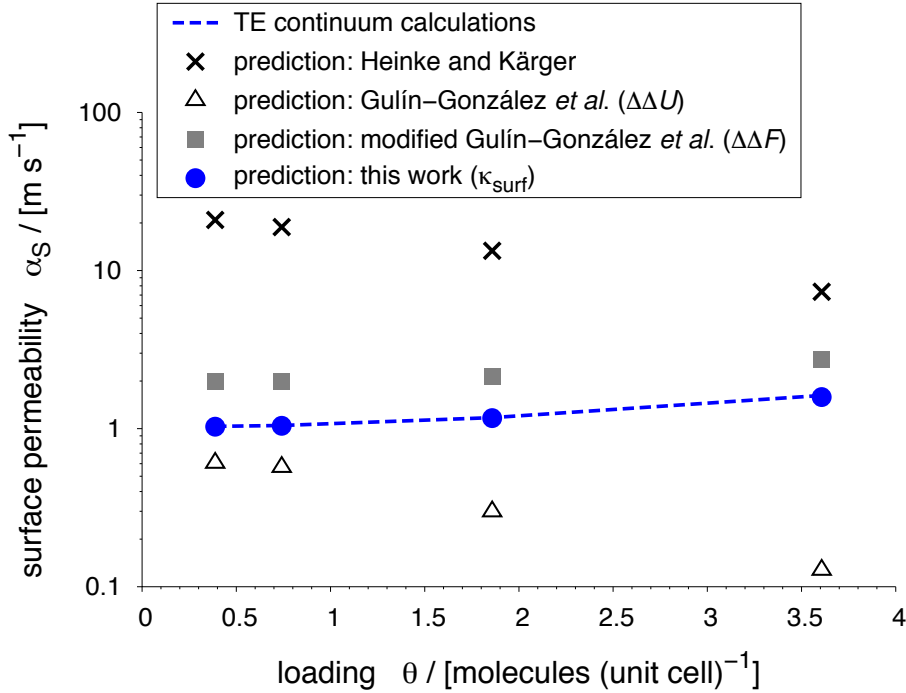


Figure 10.5: Surface permeability as a function of loading ($T = 181$ K), obtained from the two-stage simulation approach (line) used in the present chapter to mimic tracer-exchange experiments. Permeability predictions using information from the first, the molecular, simulation stage only are presented as symbols, where different models are tested. Note, first, that the main difference between the modified estimate by Gulín-González *et al.*⁹ and the here proposed prediction lies in κ_{surf} because of the earlier mentioned relationship of free energy and concentration and, second, the molecules are assumed being exchanged when they arrive on the external surface adsorption layer (one-step desorption mechanism).

labeled modified Gulín-González *et al.* in Figure 10.5 (squares). Still, a discrepancy is observed that is due mainly to the transmission coefficient,^{91,112–114} κ_{surf} , the significance of which is discussed shortly. The accurate prediction of α_S (blue circles in Figure 10.5) follows:

$$\alpha_S^{\text{1step}} = \bar{v} \cdot \kappa_{\text{surf}} \cdot \frac{c_{\text{eq,surf}}^\ddagger}{c_{\text{eq,zeol}}}, \quad (10.6)$$

where $\bar{v} = \sqrt{k_B T / (2\pi m)}$ is the average velocity of the methane molecule in

a single direction on the basis of kinetic gas theory, $c_{\text{eq,surf}}^\ddagger$ is the equilibrium concentration of molecules at the location of the surface barrier and $c_{\text{eq,zeol}}$ the average guest concentration inside the bulk-zeolite structure (\propto loading). The additional subscript “eq” facilitates discriminability between concentrations obtained from equilibrium c profiles (i.e., time-invariant, as seen in Figure 10.2c) and transient concentrations which do change with time (Figure 10.3a).

The surface-permeability prediction proposed by this work is in fact the equivalent to the self-diffusion coefficient estimate in the framework of dynamically corrected transition state theory (DCTST). To realize this, consider the DCTST self-diffusivity:^{109,110,116}

$$D_S^{\text{DCTST}} = \bar{v} \cdot \kappa_{\text{zeol}} \cdot \frac{\exp[-F(z_{\text{zeol}}^\ddagger)/k_B T]}{\int_{\text{cage}} \exp[-F(z)/k_B T] dz} \cdot l_{\text{zeol}}^2. \quad (10.7)$$

The equivalency of the terms $\bar{v} \cdot \kappa_i$ in Equations 10.6 and 10.7 is obvious. Recalling that $c_{\text{eq}} \propto \exp[-F/(k_B T)]$ leads directly to the correspondence of the integral in the denominator divided by l_{zeol} and $c_{\text{eq,zeol}}$, except for a factor which, however, is the same one between the two nominators and, thus, cancels out exactly.

The role of the transmission coefficient is an important finding. For predicting the permeability, it is usually neglected that not 100% of the molecules having arrived on top of the barrier between zeolite margin and surface adsorption layer will in fact end up on the external surface. The error introduced by assuming $\kappa_{\text{surf}} = 1$ amounts to a factor of 1.7–2.8 (cf., Supplementary Subsection 10.6.2), which clearly manifests a profound quantitative impact on the final permeability estimate. Furthermore, it is pointed out that κ_{surf} may not simply be set to κ_{zeol} and that incorporating κ_{surf} into the modified model by Gulín-González *et al.* still suffers from small deviations from the tracer-exchange data because κ_{zeol} is dragged along in D_S . Finally, note also that α_S is a system property that depends on the combination of guest molecule and host structure as well as on the properties of the surface and its immediate vicinity.²⁰⁶

10.3.2 Two-Step Release Mechanism

The investigation of the one-step surface permeability has shed light on the peculiarities encountered when one aims at predicting α_S . Now, the second exchange step is considered too, that is, a molecule must also leave the surface adsorption layer for the gas phase to be considered truly exchanged. Again,

the “target” $\alpha_S^{2\text{step}}$ are determined from tracer-exchange calculations with thick membranes, with the difference that the surface adsorption layer is added in the continuum calculations. As seen from the excellent agreement between the thus obtained data (lines in Figure 10.6) and direct molecular-simulation predictions (large blue symbols), the two-step surface permeability is found to be given by:

$$\alpha_S^{2\text{step}} = \frac{\bar{v}}{\frac{1}{\kappa_{\text{gas}} c_{\text{eq,gas}}^\ddagger} + \frac{1}{\kappa_{\text{surf}} c_{\text{eq,surf}}^\ddagger}}, \quad (10.8)$$

where $c_{\text{eq,gas}}^\ddagger$ is the equilibrium concentration of molecules on the barrier between external surface adsorption layer and gas-phase region and κ_{gas} represents its corresponding transmission coefficient; note that $c_{\text{eq,gas}}^\ddagger = c_{\text{eq,gas}}$ (Figure 10.2c). The total surface permeability hence follows the behavior of parallel resistances in electricity theory, that is, $\alpha_S^{2\text{step}} = 1/(1/\alpha_S^{\text{gas}} + 1/\alpha_S^{1\text{step}})$, when one defines $\alpha_S^{\text{gas}} \equiv \bar{v} \cdot \kappa_{\text{gas}} \cdot c_{\text{eq,gas}}^\ddagger / c_{\text{eq,zeol}}$.

The only alternative two-step permeability prediction model that has been found is due to Schüring *et al.*²⁰⁷ (small gray symbols in Figure 10.6):

$$\alpha_S = \bar{v} \cdot \frac{P_{\text{enter}}}{\tilde{K}}. \quad (10.9)$$

\tilde{K} denotes the ratio of the average concentrations in the zeolite margin and the bulk gas^{191,207} and P_{enter} represents the fraction of molecules that enter the zeolite of all molecules hitting on the surface in total.¹⁸² While the model captures the qualitative trend of increasing α_S with loading, it does not predict the permeability quantitatively in a satisfactory manner. Deviations from the tracer-exchange calculations range between 2.3 and 3.2, remaining significant even in the case when the transmission coefficients (κ_{surf} and κ_{gas}) are incorporated into the model (1.6–2.7). At this point, it is important to reiterate that the tracer-exchange surface permeabilities for release and uptake are equivalent (Supplementary Subsection 10.6.1).

10.4 Discussion

A comparison between surface permeabilities obtained from the simplistic one-step and the more realistic two-step mechanism reveals that the external surface adsorption layer substantially retards the desorption from the membrane ($\alpha_S^{2\text{step}} \ll \alpha_S^{1\text{step}}$). The effect becomes the stronger the lower the temperature gets and amounts to a factor of ($\alpha_S^{1\text{step}}/\alpha_S^{2\text{step}}$) 1.7, 2.8, and 3.3 for

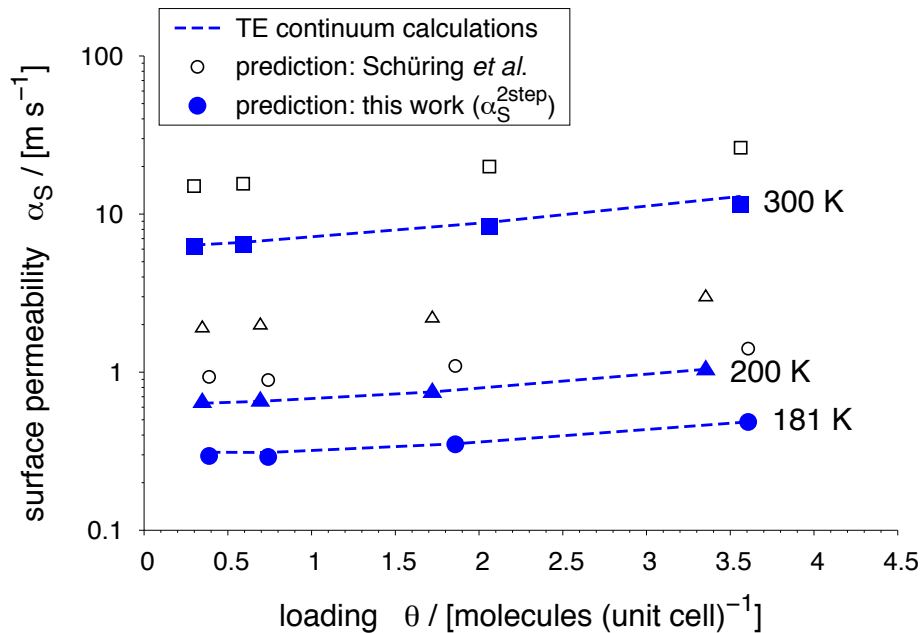


Figure 10.6: Surface permeability vs loading for the case that tracer release included the desorption from the external surface adsorption layer (two-step release process). Results for various temperatures are shown, where the lines reflect data from the two-stage simulation approach mimicking tracer-exchange experiments and the symbols are predictions on the basis of readily available information from the first, the molecular, simulation stage only. Whereas the filled symbols represent surface permeability predictions of this work, the small open symbols are predictions due to Schüring *et al.*²⁰⁷

$T = 300, 200,$ and 181 K, respectively. The comparison clearly underlines that the detailed structure of the membrane boundary layer is exceptionally important to obtain accurate permeability estimates. As the accuracy is validated against tracer-exchange *simulations* rather than *experiments*, this fact deserves some final remarks.

The influence of the here reported intrinsic surface barriers on the permeability likely vanishes for the giant crystals⁷⁵ employed in microscopy experiments.⁴ This is because the measurements are subject to spatial resolution limitations of around $0.5 \mu\text{m}$ (interference microscopy) and larger (infrared microscopy). The resolution, consequently, prohibits the detection of intrinsic surface barriers because the effect of the intrinsic barriers level off at this length scale.^{113,114} Nevertheless, the question arises to which extent

possible defects would play a role, given that those were to occur in ultrathin membranes and, thus, together with intrinsic barriers.²¹⁰ To provide at least a rough answer to this question, a rule of thumb assessment is performed in the following.

The rating compares the different effects by computing the associated permeabilities and by defining a reference value, which corresponds to the limiting case of diffusion-controlled transport ($\alpha_S \propto D_S$). Subsequent introduction of impact factors permits a quantitative assessment of the different effects' relative importance because the strength of a certain effect scales directly with the associated surface permeability (Supplementary Subsection 10.6.3 for more details). It turns out that the impact of intrinsic surface barriers varies between 1.5 (almost pure diffusion control observed for high θ and T) to 70 (low θ and T). An upper bound for the defect-barrier impact was determined to be ≈ 2000 . The simultaneous occurrence of intrinsic barriers and defects leads to a total surface-barrier impact factor of 2000–40 000. Clearly, when both effects appear together, the defects exert a stronger influence on the surface barriers than the intrinsic barriers because of the exceptionally large number of closed entrances. However, such a high fraction (99.95%) as observed by Hibbe *et al.*⁴ for MOF Zn(tbip) is unlikely to occur for the broad AFI pore entrances too (Supplementary Subsection 10.6.3). Furthermore, efficient and effective applications implementing ultrathin membranes (e.g., gas separation, heterogeneous catalysis) usually require high accessibility of guest molecules to the zeolite pores, pointing at improvements of corresponding postsynthesis treatment of the membranes in question.

10.5 Conclusions

Apart from highlighting the need for new integral diffusion solutions, the present chapter provides an accurate prediction of the local transport coefficient that prevails at gas–solid interfaces: the surface permeability. This coefficient does not follow the behavior of the associated diffusion coefficient and can be very small, especially at low temperature and loading. In this respect, realizing that latest improvements in synthesis enable the production of ultrathin and highly oriented zeolite films¹¹ enhances the significance of the here reported slow boundary layer transport. This is because the importance of surface barriers scales inversely with membrane width.¹¹⁴ As a final consequence, simple design protocols, such as membrane selectivity formulas on the mere basis of adsorption data and diffusion coefficients, are becoming

increasingly inappropriate for the new generation of ultrathin membranes, calling for development of more accurate design models.

10.6 Supplementary Data

10.6.1 Comparison Tracer Release and Uptake

Additional tracer-exchange simulations at 181 K were performed, where the labeled molecules were entering the zeolite membrane (tracer uptake or adsorption) instead of leaving it (tracer release or desorption). The results correlate exactly with those from the release simulations (Figure 10.7). Therefore, it is concluded that neither α_S nor D_S is process-dependent (adsorption vs desorption) in the here studied cases.

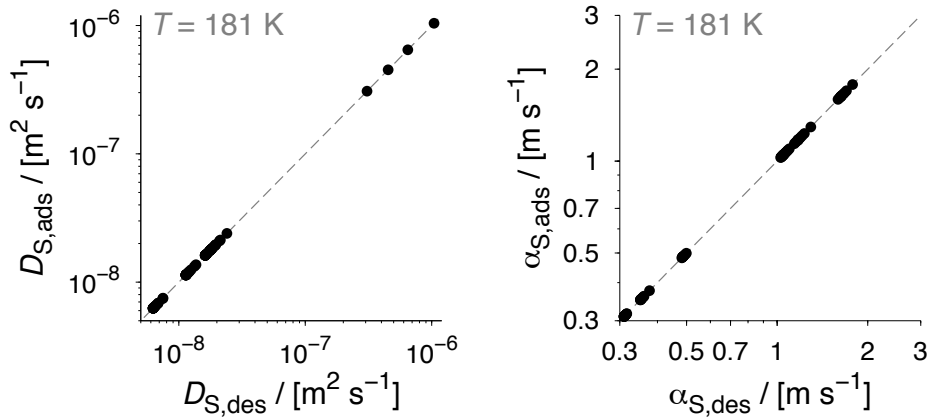


Figure 10.7: Parity plots of self-diffusivities (left) and surface permeabilities (right) obtained from tracer-exchange continuum calculations at 181 K where the tracer was leaving (x -axis) and entering (y -axis) the AFI membrane, respectively. Data correspond to all state points/loadings and all membrane thicknesses investigated at 181 K.

10.6.2 Transmission Coefficients in the Boundary Layer

Figure 10.8 shows that the transmission coefficient obtained at the free-energy barrier separating zeolite margin and surface adsorption layer, κ_{surf} , varies between 0.36 and 0.59, depending on the loading and temperature. Because the one-step surface permeability prediction of the present work scales directly with κ_{surf} (Equation 10.6) the error introduced by rigorously neglecting any recrossings at the surface (i.e., setting $\kappa_{surf} = 1$ and thus yielding

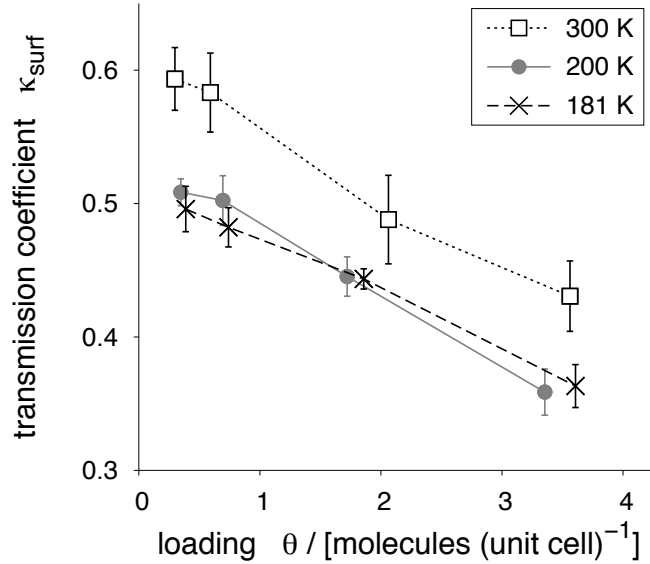


Figure 10.8: Transmission coefficients obtained at the dividing surface between zeolite margin and surface adsorption layer; all state points (T , p).

$\tilde{\alpha}_{\text{S}}^{\text{1step}} = \bar{v} \cdot c_{\text{eq,surf}}^{\ddagger} / c_{\text{eq,zeol}}$ amounts to $\tilde{\alpha}_{\text{S}}^{\text{1step}} / \alpha_{\text{S}}^{\text{1step}} = 1 / \kappa_{\text{surf}} = 1.7\text{--}2.8$.

Figure 10.9 depicts on the left side the transmission coefficient obtained at the location separating the surface adsorption layer and the bulk gas phase, κ_{gas} , which generally equals unity except for the two highest zeolite loadings studied at 300 K. This is understandable because transmission coefficients are known to largely depend on the current number of molecules found at the site to which the tagged molecule is aiming.^{110,113} In this context, the free-energy well of the surface adsorption layer (\square in Figure 10.10) for 300 K and 3.6 molecules per unit cell is as deep as the wells representing adsorption in the innermost zeolite cages (\triangle in Figure 10.10). This, in turn, is indicative of equal concentrations due to the exponential relationship between F and c mentioned earlier. On the other hand, the free-energy difference of the two different wells is larger than $1 k_{\text{B}}T$ for the other state points shown. That translates into a (minimum) factor of 2.7 between the respective concentrations and, thus, highlights a considerably smaller number of molecules in the surface adsorption layer than inside the zeolite. The profile at the bottom provides, furthermore, evidence to the fact that the gas-phase can, by no means, be considered diluted anymore if T and θ are high. A methane molecule that is starting from the edge between gas region and surface ad-

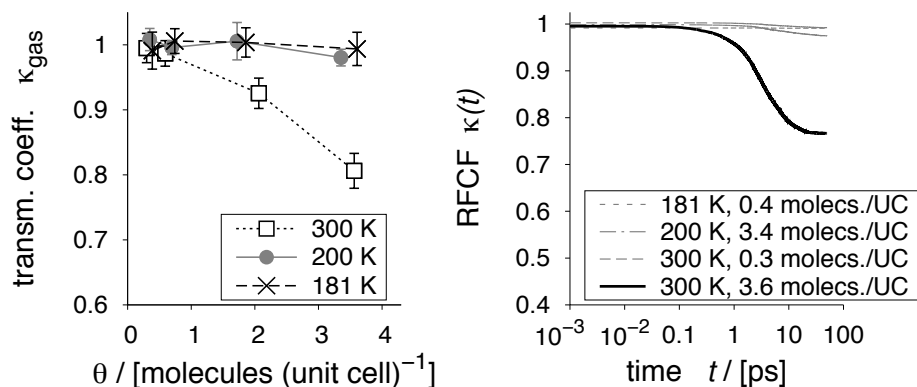


Figure 10.9: Transmission coefficients (left) of hopping away from the dividing surface between surface adsorption layer and gas phase [all state points (T, θ)], which were determined on the basis of the plateau of the respective transient reactive flux correlation functions (four examples shown on the right).

sorption layer (\times in Figure 10.10) and traveling to either side [surface layer (\square) or gas phase (\circ)] will therefore encounter a non-negligible number of molecules on an average when compared to the other state points where molecular encounters are scarce. It is simply getting crowded left and right from the molecule. The more encounters with other molecules occur, the larger is the probability that the tagged molecule is bounced back to the region from where it came and, thus, the smaller will be κ_{gas} . This provides the rational behind the occurrence of a decreasing κ_{gas} observed at elevated T and θ only.

As a last important point, the reactive flux correlation functions (Figure 10.9, right) did not show any significant long-term decline. Such a trend might have been expected from the fact that the barrier (\times in Figure 10.10) and the left-hand end point (\circ in Figure 10.10) are connected by a flat free-energy line.

10.6.3 Impact Factors of Permeability Influences

The present section explains the computation of impact factors, f_{imp} , to quantitatively assess different sources to surface barriers, which is grounded on the calculation of different surface permeabilities.

To start rating the relative impacts of the barrier sources (defects vs intrinsic vs intrinsic+defects), the reference permeability value, $\alpha_{\text{S,ref}}$, is defined

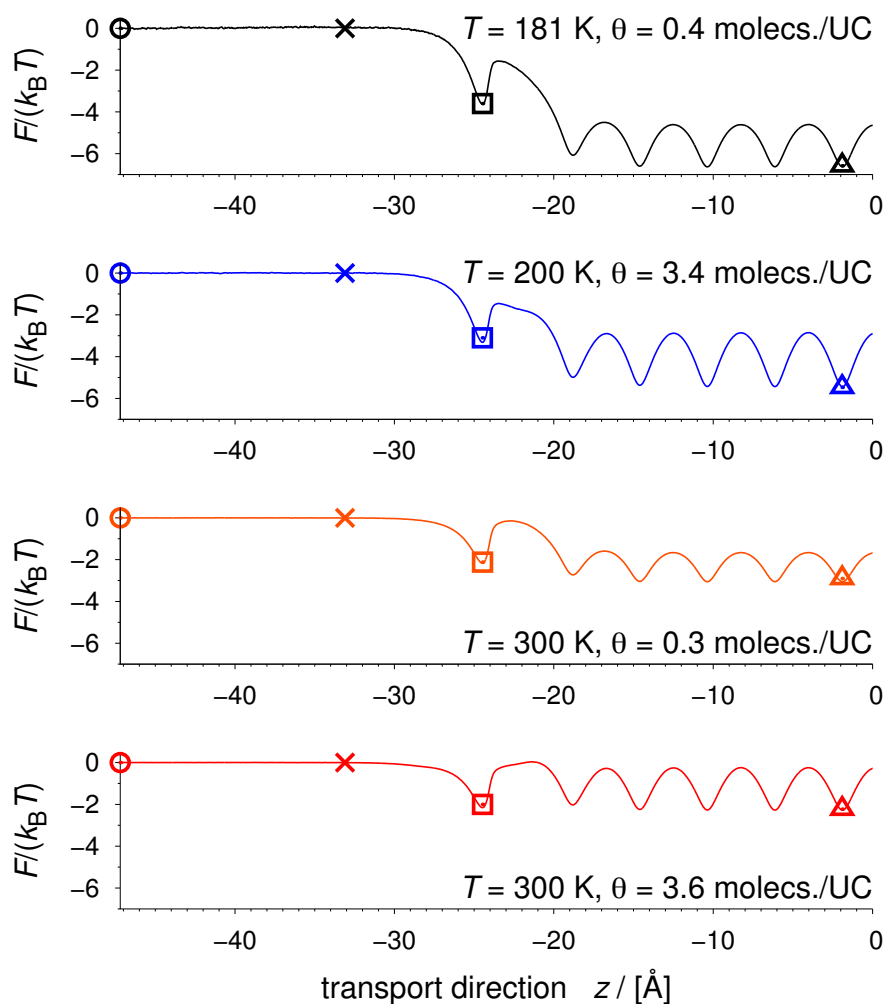


Figure 10.10: Free-energy profiles of methane at different temperatures and loadings. Symbols highlight the positions of free-energy wells corresponding to the location of a representative zeolite cage (\triangle) and the surface adsorption layer (\square), as well as the position of the dividing surface between surface adsorption layer and gas phase (\times) and the left-hand end point of the RFCF for κ_{gas} computation (\odot).

as the value obtained with the prediction model by Heinke and Kärger:⁵

$$\alpha_{\text{S,ref}} = 0.5 \cdot D_{\text{S}}/l_{\text{zeol}}. \quad (10.10)$$

Second, the defect-barrier influence can be directly accounted for by down-

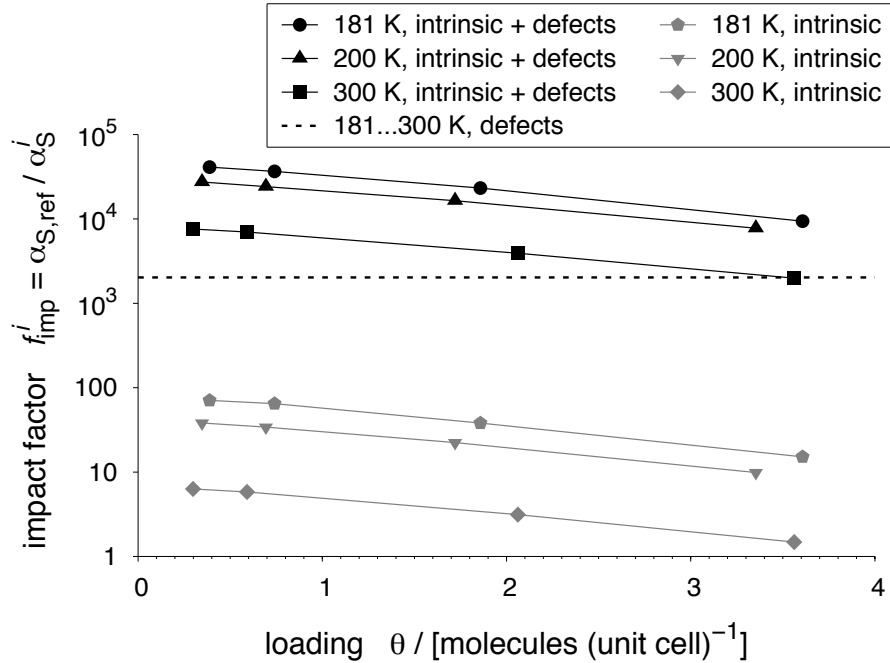


Figure 10.11: Impact factors, f_{imp}^i , of different surface-barrier sources i (intrinsic, defects) and their possible combination (intrinsic + defects) as functions of loading, θ , and for different temperatures, T .

scaling of the reference by the expected fraction of open entrances, P_{open} :

$$\alpha_{\text{S}}^{\text{def}} = P_{\text{open}} \cdot \alpha_{\text{S,ref}}. \quad (10.11)$$

In doing so, it is tacitly assumed that numerous lattice defects *inside* the structure permits rapid guest exchange between adjacent channels that are ideally not connected. This is the limiting case of $P_y \rightarrow 1$ in Heinke's original formula.⁵ Furthermore, one in 2025 pore openings is assumed to be permeable only, as was estimated by Hibbe *et al.*⁴ for MOF Zn(tbip). The number is very likely too large because the MOF pores possess extremely small windows (4.5 Å) which are much more sensitive to small distortions in comparison to the rather large AFI pore windows (7.3 Å). Therefore, the MOF entrances are blocked far more easily and the estimate represents an upper bound for the defect-barrier influence in AFI. Third, the influence of intrinsic barriers

is, of course, rated via the two-step permeability prediction (Equation 10.8):

$$\alpha_S^{\text{intrin}} = \alpha_S^{\text{2step}} \quad (10.12)$$

$$= \frac{\bar{v}/c_{\text{eq,zeol}}}{1/(\kappa_{\text{gas}}c_{\text{eq,gas}}^\ddagger) + 1/(\kappa_{\text{surf}}c_{\text{eq,surf}}^\ddagger)}. \quad (10.13)$$

Fourth, the coupled impact of both barrier sources is also grounded on Equation 10.8, differing, however, in a down-scaled α_S^{1step} by $P_{\text{open}} = 1/2025$:

$$\alpha_S^{\text{intrin+def}} = \frac{1}{1/\alpha_S^{\text{gas}} + 1/(P_{\text{open}} \cdot \alpha_S^{\text{1step}})}. \quad (10.14)$$

Finally, the ratio of the reference value to an individual surface permeability rates the impact of the effect i associated with this permeability, thus, yielding:

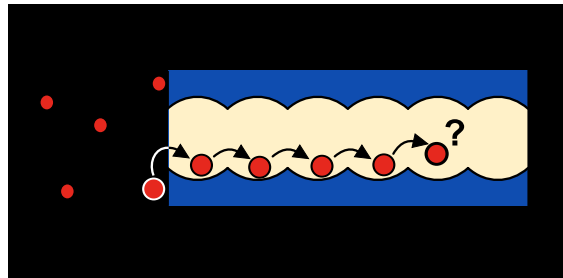
$$f_{\text{imp}}^i \equiv \alpha_{S,\text{ref}}/\alpha_S^i. \quad (10.15)$$

The results are displayed in Figure 10.11. For your guidance, an impact factor of unity represents the case when surface barriers are absent. Hence, there is no slowing-down of the overall tracer exchange, and, consequently, the process is essentially diffusion controlled. In contrast, a high impact factor indicates that surface barriers may potentially control the transport, depending, however, on the crystal size or membrane thickness.¹¹⁴

11

Transport into Nanosheets

Ultrathin porous materials, such as zeolite nanosheets, are prominent candidates for performing catalysis, drug supply, and separation processes in a highly efficient manner due to exceptionally short transport paths. Predictive design of such processes requires the application of diffu-



sion equations, which were derived for macroscopic, homogeneous surroundings to nanoscale, nanostructured host systems. Therefore, different analytical solutions of Fick's diffusion equations are tested for their applicability to methane transport into two different zeolite nanosheets (AFI, LTA) under instationary conditions. Transient molecular dynamics simulations provide hereby concentration profiles and uptake curves to which the different solutions are fitted. Two central conclusions are deduced by comparing the fitted transport coefficients. First, the transport can be described correctly only if concentration profiles are used and the transport through the gas–solid interface is explicitly accounted for by the surface permeability. Second and most importantly, a size limitation to applying the diffusion equations to nanoscale objects is unraveled in the present chapter. This is because transport diffusion coefficients, D_T , and surface permeabilities, α , of methane in AFI become dependent on nanosheet thickness. Deviations can amount to factors of 2.9 and 1.4 for D_T and α , respectively, when, in the worst case, results from the thinnest AFI nanosheet are compared with data from the

thickest sheet. A molecular explanation of the size limitation is presented, which is based on memory effects of entering molecules and therefore only observable for smooth pores such as AFI and carbon nanotubes. Hence, the present work provides important tools to accurately predict and intuitively understand transport of guest molecules into porous host structures, a fact that will become the more valuable the more tiny nanotechnological objects get.

11.1 Introduction

Fueled by recent synthesis breakthroughs,¹⁴ nanoscale objects, such as nanosheets,^{14,16,21,211,212} nanoflakes,²¹³ and nanotubes,⁶⁹ have attracted the attention of many scientists and engineers in the past decade. Two main factors captivated the interest. On the one hand, the materials forming nanoobjects serve as catalysts,¹⁴ drug supply systems,²¹ adsorbents,¹⁶ energy storage media,^{211,212} thermoelectric elements,²¹³ and gas sensing devices,⁶⁹ thus, opening abundant application possibilities. On the other hand, fabricating the material as small as possible is critical to almost any of the processes to be performed as efficiently as possible. This is because molecular transport of guest species, reactants/products,^{14,20} drugs,²¹ dyes,¹⁶ ions,^{211,212} and gas molecules,⁶⁹ into or through the solid turns out to be a crucial, if not the rate-limiting step^{20,69} of many of the above processes. Reducing the dimensions of the porous host structure and thereby the diffusion path of the guest species is therefore the most direct means to increase apparent reaction rates,^{14,20} decrease detection⁶⁹ and recharge²¹² times, and, thus, optimize the process efficiency.²¹¹

Transport into porous materials^{4,139,171} is usually described by Fick's laws:⁹⁵

$$j(z) = -D_T \cdot \frac{dc(z)}{dz}, \quad (11.1)$$

$$\frac{\partial c(t, z)}{\partial t} = D_T \cdot \frac{\partial^2 c(t, z)}{\partial z^2}. \quad (11.2)$$

These well-known equations connect the transport flux, j , with the driving force, $-dc(z)/dz$, via the transport diffusion coefficient, D_T , state how concentration fluctuations decay with time, t , and are strictly speaking valid for constant diffusivities only. While special transport problems might require suitable extensions and adaptations, for example, Maxwell–Stefan formulation for multicomponent diffusion⁹⁰ and extra adsorption terms for strongly

interacting guest–host systems,¹³⁶ single-component transport of hydrocarbons into zeolites is well described by Fick’s laws.^{139,171} However, because these equations were derived under specific assumptions⁹² and applied to rather large crystals^{4,139,171} two critical issues appear for novel nanoscale host structures.

The first one is a consequence of the host materials’ periodic structure, where the focus lies on zeolites in the following. The discrete subunits that build up the host crystal (i.e., cages of the unit cell) contrast a main assumption upon which the diffusion equations were derived:⁹² a structureless, homogeneous continuum. However, as long as the host structure is large, ideally consisting of an infinite number of cages, previous efforts, by means of simulations⁹⁰ and experiments,^{4,139,171} have shown that the conventional equations are well applicable to describe guest molecule transport. But what happens when the size of the material leaves the macro- and microscale to reach just some nanometers? Are the diffusion equations still valid and reliable at this small scale?

Second, the role of the interface between gas space and bulk host interior is often assumed to be negligible. In this respect, cases have been identified where the interface exhibited very similar^{4,139} transport characteristics as the bulk host structure, influenced only by the number of blocked pore entrances.¹³⁹ However, Zimmermann *et al.*²¹⁴ have recently shown that this is not generally true. The transport coefficient at the interface, the so-called surface permeability, α , varied in a distinctly different manner with loading in that study compared to the diffusivity.²¹⁴ So, in which cases does the surface permeability correlate with the diffusion coefficient?⁵ And, is this relevant to processes implementing nanosheets or ultrathin membranes?¹³

Given the problems outlined, here the validity of Fick’s diffusion equations and their existing analytical solutions is tested to guide future process design improvements in nanotechnology. For this purpose, the dynamics of methane transport into initially empty zeolite nanosheets was studied until saturation was reached. Transient molecular dynamics simulations¹²⁴ were employed, and three factors represent the main aspects investigated in this chapter: (1) type of analytical solution of diffusion equations (local vs integral), (2) role of boundary conditions (surface-barrier effects), and (3) influence of sheet thickness (“nano effect”). Two zeolite types were investigated: an AFI-type zeolite (Figure 11.1a) with smooth one-dimensional channels, and an LTA zeolite that possesses bulky cages connected via narrow pore windows (Figure 11.1c). The respective external surfaces, which were in both cases obtained by cutting a periodic structure behind the location of the diffusion windows, are depicted in Figure 11.1b,d.

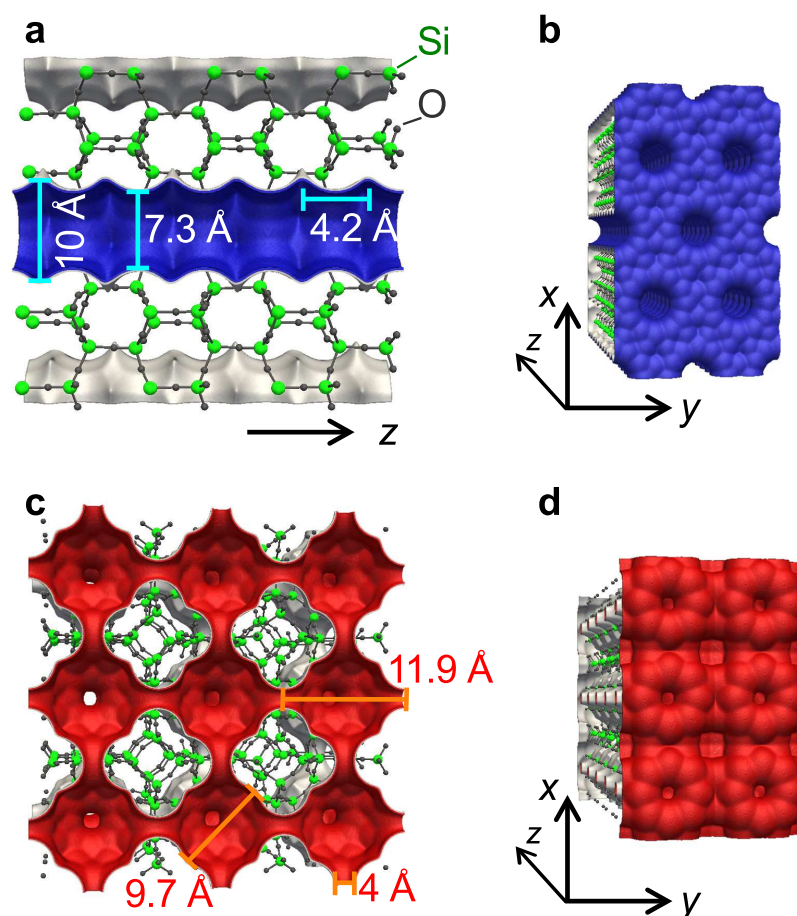


Figure 11.1: Representations of zeolite nanosheets investigated and their external surface: AFU (a, b) and LTA (c, d).

11.2 Methodology

Transient molecular dynamics (TrMD), which is also referred to as nonequilibrium molecular dynamics (NEMD),¹²⁴ represents a subtype of conventional equilibrium molecular dynamics (EMD).²¹⁵ Both simulation methods determine the evolution of a many-molecule system via numerical solution of Newton's equations of motion.⁹¹ The difference lies in the fact that TrMD allows for a varying number of molecules, N , in the simulation box whereas N is strictly constant in EMD. Variation of the number of molecules is achieved by executing conventional MD integration steps and grand-canonical Monte Carlo (GCMC) trials in an alternating manner, as depicted in Figure 4.5 of

Chapter 4 (top). Importantly, all molecules are subject to MD irrespective of their positions (Figure 4.5, bottom). However, molecules are restricted to be inserted into and deleted from a specific region of the simulation box via GCMC: the control volume (CV). GCMC trials mimic therefore exchange with a hypothetical, infinite gas reservoir, whose chemical potential, μ_{res} , is identical to the one imposed on the control volume, μ_{CV} . Thus, the control volume is automatically replenished with molecules once too many have left the CV to maintain μ_{CV} . Molecules outside the CV may now enter the zeolite that was initially empty.

The gradual filling of the nanosheet with methane molecules is monitored in two ways during a TrMD simulation. First, concentration profiles, $c(t_i, z_k)$, are determined across the sheet (i.e., along z) at successive times t_i , where the spacing between neighboring data points (e.g., z_k and z_{k+1}) reflects the nanostructured nature of the zeolite (i.e., $\Delta z = l_{\text{cage}}$). This approach to track the sheet filling will be referred to as *local* in the remainder. Second, an uptake curve,^{114,208,214} $m(t_i)$, is calculated on the basis of the concentration profiles, which describes the increase of the total mass adsorbed inside the nanosheet as a function of time. Because an uptake curve is, by definition, spatially not resolved, it is referred to as an *integral* approach to monitor the transport process. Such integral solutions of the diffusion equations are important because they are central functions in both diffusion experiment evaluation²⁰⁸ and process design.^{53,114} More details on the simulations¹²⁴ and an in-depth discussion about the models used^{35,61,126,146,159} are provided in Sections 4.5, 4.6, 6.5, and Supplementary Subsections 11.5.1 and 11.5.2. It is, at this point, important to emphasize that molecular simulations are the methods of choice for this study. There is presently no measurement technique that has both the necessary spatial and temporal resolution to directly monitor local molecular uptake inside porous nanosheets and thus being capable of checking the validity of Fick's diffusion equations for guest transport into nanoscale host materials. Furthermore, the here employed computationally demanding nonequilibrium methodology¹²⁴ and a similar approach¹⁹¹ have so far been used to assess surface transport resistances only. Hence, the crucial difference to previous works^{124,191} is the simultaneous occurrence of surface and (varying) intracrystalline transport resistances.

Figure 11.2 shows typical concentration profiles (a) and an uptake curve (b), both obtained from TrMD simulations of methane entering a $\delta = 10.2$ nm thick AFI sheet (dots connected with lines). The temperature was 300 K and the chemical potential in the control volume corresponded to 10 bar of gas-phase pressure. The concentration profiles and the uptake curve from TrMD were used in the analysis to fit analytical solutions of the diffusion equations

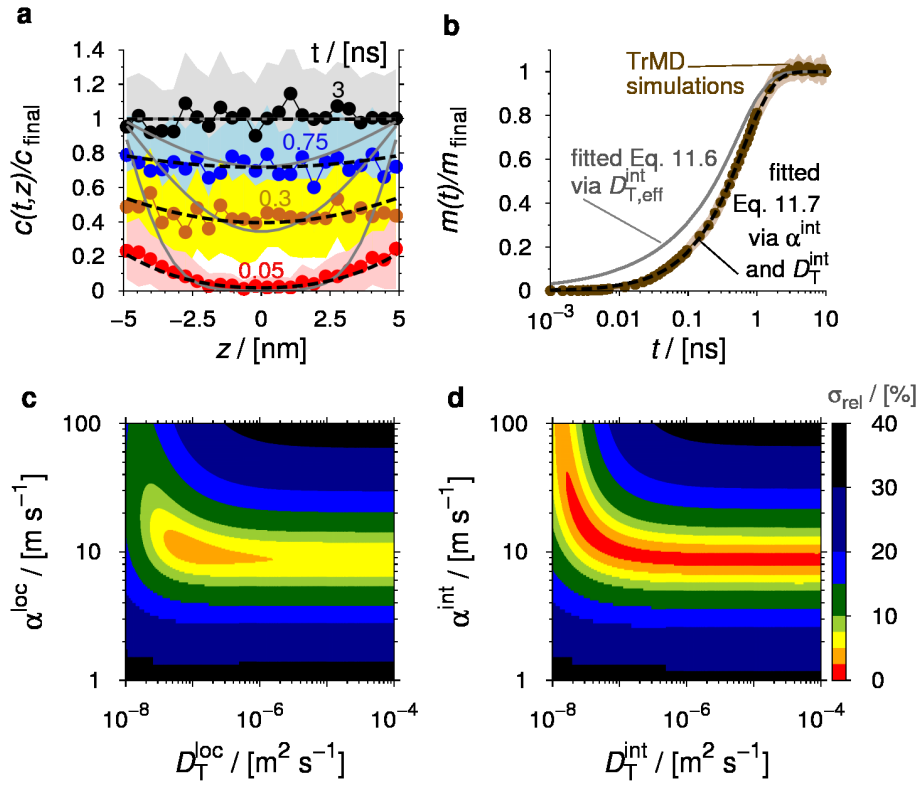


Figure 11.2: Relative concentration profiles, $c(t, z)/c_{\text{final}}$, and the resulting uptake curve, $m(t)/m_{\text{final}}$, from transient MD (dots connected with solid lines in a and b) for methane entering a 10.2 nm AFI nanosheet at 300 K. Acceptable noise was achieved by performing 40 independent transient MD runs over which the profiles were averaged. Therefore, colored domains indicate the statistical spread. Gray solid lines in (a) represent the best fit of Equation 11.4 by variation of $D_{\text{T,eff}}^{\text{loc}}$ to the TrMD data, whereas dashed lines correspond to results of fitting c profiles via α^{loc} and $D_{\text{T}}^{\text{loc}}$ (Equation 11.5). Likewise, the gray line in (b) is the result of fitting the uptake curve via $D_{\text{T,eff}}^{\text{int}}$ to the TrMD curve (Equation 11.6), and the dashed line is the best fit of Equation 11.7 by variation of α^{int} and $D_{\text{T}}^{\text{int}}$. The parameter spaces, $\sigma_{\text{rel}}(D_{\text{T}}, \alpha)$, for the solutions with surface permeability are highlighted at the bottom (c, d). They depict the agreement between TrMD data and analytical solutions of the diffusion equations in dependence of parameters D_{T} and α . Red and orange areas indicate good agreement, whereas black and blue correspond to large deviations.

provided by Crank⁹² for a plane sheet. Two analytical solutions were investigated per approach (i.e., local via c profiles and integral via uptake curves) which differed in their boundary conditions. The first one assumes that the transport at the gas–solid interface proceeds so fast that the final equilibrium concentration, c_{final} , is attained instantaneously at the sheet boundaries. In that case, a single parameter, the effective transport diffusion coefficient, $D_{\text{T,eff}}$, describes the entire process. The second boundary condition models finite transport through the gas–solid boundary layer by introducing a second transport parameter in addition to the transport diffusivity, D_{T} : the surface permeability α . It links the instantaneous guest flux, $j(t, \pm\delta/2)$, at time t across the boundary layers at $z = \pm\delta/2$ (right and left sheet surfaces) with the driving concentration difference via:

$$j(t, \pm\delta/2) = \alpha \cdot [c(t, \pm\delta/2) - c_{\text{final}}]. \quad (11.3)$$

Four analytical solutions were hence investigated here.⁹²

Concentration profiles derived by neglecting surface barriers at the sheet entrances represent the first type of analytical solutions investigated:

$$\frac{c(t, z)}{c_{\text{final}}} = 1 - \frac{4}{\pi} \sum_{i=0}^{\infty} \frac{(-1)^i}{2i+1} \cdot \exp \left[-D_{\text{T,eff}}^{\text{loc}} (2i+1)^2 \pi^2 t / \delta^2 \right] \cdot \cos \frac{(2i+1)\pi z}{\delta}, \quad (11.4)$$

where δ is the thickness of the nanosheet. Superscripts of transport coefficients indicate in the following the solution type to which the coefficients were fitted (concentration profiles: “loc” for local; uptake curves: “int” for integral). Furthermore, subscript “eff” signifies cases in which the diffusion coefficients capture in effect both transport resistance types: diffusion barriers caused by the repetitive zeolite structure^{41,110} and surface barriers at the gas–zeolite boundary layer.^{113,114,214}

Concentration profiles (superscript “loc”) derived with the surface-barrier boundary condition by introduction of α are the second type of solutions:

$$\frac{c(t, z)}{c_{\text{final}}} = 1 - \sum_{i=1}^{\infty} \frac{2L \cdot \exp \left[-\gamma_i^2 D_{\text{T}}^{\text{loc}} t / (\delta/2)^2 \right]}{(\gamma_i^2 + L^2 + L) \cos \gamma_i} \cdot \cos [\gamma_i z / (\delta/2)]. \quad (11.5)$$

Here, γ_i is the i -th positive root of $\gamma \tan \gamma = L$ with $L = (\delta/2)\alpha^{\text{loc}}/D_{\text{T}}^{\text{loc}}$, where superscript “loc” of γ and L in Equation 11.5 was omitted for reasons of clarity.

Uptake curves (superscript “int”) derived by neglecting surface barriers at the sheet entrances (subscript “eff”) represent the third analytical solution

type:

$$\frac{m(t)}{m_{\text{final}}} = 1 - \sum_{i=0}^{\infty} \frac{8 \cdot \exp \left[- D_{\text{T,eff}}^{\text{int}} (2i+1)^2 \pi^2 t / \delta^2 \right]}{(2i+1)^2 \pi^2}, \quad (11.6)$$

where m_{final} denotes the final mass after saturation of the nanosheet with guest molecules.

Finally, uptake curves (superscript “int”) derived with the surface-barrier boundary condition are the fourth type of solutions:

$$\frac{m(t)}{m_{\text{final}}} = 1 - \sum_{i=1}^{\infty} \frac{2L^2 \cdot \exp \left[- \gamma_i^2 D_{\text{T}}^{\text{int}} t / (\delta/2)^2 \right]}{\gamma_i^2 (\gamma_i^2 + L^2 + L)}, \quad (11.7)$$

where again γ_i is the i -th positive root of $\gamma \tan \gamma = L$, here, however, with $L = (\delta/2) \alpha^{\text{int}} / D_{\text{T}}^{\text{int}}$.

The results of fitting the four different analytical solutions have been included in Figure 11.2a,b for the given example. Figure 11.2c,d highlight the parameter spaces of the analytical solutions with the surface-barrier boundary condition. That is, the averaged relative sample standard deviation, σ_{rel} in [%], in dependence of transport coefficients D_{T} and α . The averaged relative sample standard deviation is hereby defined as:

$$\begin{aligned} & \sigma_{\text{rel}}(D_{\text{T}}^{\text{loc}}, \alpha^{\text{loc}}) / [\%] \\ & \equiv 100 \sqrt{\frac{1}{N_t N_z} \cdot \sum_{i=1}^{N_t} \sum_{k=1}^{N_z} [c(D_{\text{T}}^{\text{loc}}, \alpha^{\text{loc}}, t_i, z_k) - \bar{c}(t_i, z_k)]^2 / c_{\text{final}}}, \quad (11.8) \end{aligned}$$

where N_t and N_z denote, respectively, the (discrete) number of time instances and the number of points in the concentration profiles and $c(D_{\text{T}}^{\text{loc}}, \alpha^{\text{loc}}, t_i, z_k)$ the concentration value from the analytical solution (here: Equation 11.5) at time t_i and position z_k . Note that the corresponding concentration from TrMD is an average $[\bar{c}(t_i, z_k)]$ because 40 independent TrMD simulations were required to yield profiles with acceptable noise. The definition of σ_{rel} for uptake-curve fitting is similar, with the difference that one does not need to average over N_z spatial points:

$$\sigma_{\text{rel}}(D_{\text{T}}^{\text{int}}, \alpha^{\text{int}}) / [\%] \equiv 100 \sqrt{\frac{1}{N_t} \cdot \sum_{i=1}^{N_t} [m(D_{\text{T}}^{\text{int}}, \alpha^{\text{int}}, t_i) - \bar{m}(t_i)]^2 / m_{\text{final}}}. \quad (11.9)$$

11.3 Results

Figure 11.2 shows that the analytical solutions of the diffusion equations that are based exclusively on the effective diffusivity (gray solid lines in Figure 11.2a,b) cannot accurately reproduce neither the concentration profiles nor the uptake curve from transient MD. That is particularly evident at early stages and the outermost region of the c profiles. The shortcoming of describing the TrMD data is quantitatively reflected in an increasing effective diffusivity with sheet thickness, δ , as seen in Table 11.1, because diffusion coefficients must theoretically not depend on primary geometrical parameters. An increasing diffusivity is observable for both solution types, local and integral, and for both zeolites, AFI and LTA. Because it is well-known that adsorbate diffusion coefficients in zeolites can exhibit strong concentration dependencies,^{90,146} methane transport diffusivities have been determined using conventional EMD and GCMC simulations in periodic crystals (Supplementary Subsection 11.5.3). The transport diffusivities were averaged over the concentration range relevant to the TrMD simulations (\bar{D}_T) and amounted to $755 \cdot 10^{-10} \text{ m}^2/\text{s}$ and $9.2 \cdot 10^{-10} \text{ m}^2/\text{s}$ for AFI and LTA, respectively. The effective diffusion coefficients $D_{T,\text{eff}}^{\text{loc}}$ and $D_{T,\text{eff}}^{\text{int}}$ in Table 11.1 asymptotically approach the concentration-averaged values from EMD with increasing sheet thickness, where the effective LTA diffusivities converge faster than the diffusivities from AFI. Therefore, it is concluded that the quality of describing guest transport on the basis of diffusion coefficients alone, that is, by neglecting the influence of surface barriers altogether, worsens the smaller the host dimension becomes and the larger the average guest diffusivity.

Those two analytical solutions that account for possible surface barriers through the surface permeability α yield excellent agreement with the simulation data (dashed lines in Figure 11.2a,b). In fact, the concentration profiles' shape and evolution, very flat lines that gradually shift toward the equilibrium value, are already clear indicators of strong surface barriers,⁵ and they resemble profiles obtained from interference microscopy (IFM) experiments on giant crystals.^{4,139} The difference to the experiments lies in the complementary nature of the barrier types probed. While IFM measurements detect blocked pore entrances and therefore departure from the ideal crystal surface,^{4,5,139} the present work probes surface barriers that are inherent to the crystal structure.²¹⁴ Importantly, both methods for assessing surface barriers have their drawbacks. IFM measurements alone cannot provide the reason to pore blockage (e.g., foreign matter, lattice dislocations, surface reconstruction/relaxation) and the results of this work usually provide only a lower bound to surface barriers because of the highly idealized nature of the

Table 11.1: Effective transport diffusion coefficients, $D_{T,\text{eff}}$, from fitting Equations 11.6 and 11.4 to data from transient molecular dynamics (TrMD) simulations. Transport diffusivities derived from conventional equilibrium molecular dynamics and grand-canonical Monte Carlo simulations averaged over the concentration ranges relevant to the TrMD simulations amounted to $\bar{D}_T = 755 \cdot 10^{-10} \text{ m}^2/\text{s}$ [AFI, $T = 300 \text{ K}$, $p(\mu_{\text{CV}}) = 10 \text{ bar}$] and $9.2 \cdot 10^{-10} \text{ m}^2/\text{s}$ [LTA, $T = 750 \text{ K}$, $p(\mu_{\text{CV}}) = 100 \text{ bar}$]. Note that elevated temperature and pressure were required for TrMD simulations of CH_4 in LTA for the reasons given in Supplementary Section 11.5.1.

	δ [nm]	$D_{T,\text{eff}}^{\text{int}}$ [$10^{-10}\text{m}^2/\text{s}$]	σ_{rel} [%]	$D_{T,\text{eff}}^{\text{loc}}$ [$10^{-10}\text{m}^2/\text{s}$]	σ_{rel} [%]
AFI	2.6	38	6.6	43	16
	5.1	73	5.5	78	16
	10.2	124	4.7	137	16
	20.4	175	4.3	189	16
	40.7	263	3.9	284	14
LTA	4.8	1.29	9.4	1.40	11
	11.9	3.08	8.2	2.88	13
	26.1	4.94	5.2	4.61	11

structures employed.

Despite the good agreement between both analytical solutions using the surface-barrier boundary conditions and TrMD simulation data, the corresponding fitted transport coefficients reveal two peculiarities (Table 11.2). First, diffusion coefficients determined by the integral solution deviate strongly from the EMD concentration-averaged value, \bar{D}_T , but, interestingly, in different manners for the two zeolites. In contrast to AFI, for which the fitted values (D_T^{int}) are smaller than \bar{D}_T by a factor of 2 on the average, fitted LTA diffusivities are, on average, 1000 times larger than \bar{D}_T . Note that D_T^{int} obtained from the thinnest AFI sheet is considered as an outsider for reasons given below (second peculiarity). However, using concentration profiles to describe the transport (D_T^{loc}) yields a good match between TrMD and EMD data. This implies that accurate modeling of guest transport into nanoscale host materials is achieved only by spatially resolved analytical solutions of the diffusion equations. The argument is all the more valid because there are similar indications from the surface permeability.

Table 11.2: Transport diffusion coefficients, D_T , and surface permeabilities, α , from fitting Equations 11.7 and 11.5 to data from transient molecular dynamics (TrMD) simulations; compare also data from EMD and MC simulations: $\bar{D}_T = 755 \cdot 10^{-10} \text{ m}^2/\text{s}$ and $\bar{\alpha}_S = 7.6 \text{ m/s}$ [AFI, $T = 300 \text{ K}$, $p(\mu_{CV}) = 10 \text{ bar}$] as well as $9.2 \cdot 10^{-10} \text{ m}^2/\text{s}$ and 0.383 m/s [LTA, $T = 750 \text{ K}$, $p(\mu_{CV}) = 100 \text{ bar}$]. Note that fitting Equation 11.5 via a concentration-dependent transport diffusivity gives mean values, \bar{D}_T^{loc} , that compare well with the here presented concentration independent diffusivities D_T^{loc} (cf., Supplementary Subsection 11.5.5).

	δ	α^{int}	D_T^{int}	σ_{rel}	α^{loc}	D_T^{loc}	σ_{rel}
	[nm]	[m/s]	[$10^{-10} \text{ m}^2/\text{s}$]	[%]	[m/s]	[$10^{-10} \text{ m}^2/\text{s}$]	[%]
AFI	2.6	10.8	15200	2.6	11.0	2319	3.9
	5.1	13.6	328	1.9	11.1	1065	3.9
	10.2	15.5	313	0.9	10.5	835	3.6
	20.4	13.7	375	0.4	8.8	868	3.3
	40.7	11.4	490	0.4	7.8	798	3.4
LTA	4.8	0.200	8850	4.1	0.262	6.5	5.1
	11.9	0.198	21900	2.2	0.294	10.5	4.3
	26.1	0.210	18.1	0.8	0.340	8.9	3.6

Only recently, Zimmermann *et al.*²¹⁴ have provided an accurate prediction of the surface permeability, α_S , which applies to tracer-exchange and, thus, self-diffusion situations, hence, subscript ‘‘S’’. Using the data from Reference 214 for AFI and calculating fresh tracer-exchange surface permeabilities for methane in LTA (Supplementary Subsection 11.5.4), concentration-averaged values, $\bar{\alpha}_S$, are obtained of 7.6 and 0.383 m/s, being in good agreement with the values from fitting concentration profiles (α^{loc} in Table 11.2). However, surface permeabilities from fitting uptake curves (α^{int}) tend to over- and underrate the equilibrium simulation prediction $\bar{\alpha}_S$ by average factors of 1.8 and 1.9 for AFI and LTA, respectively, which is regarded as further evidence of the inappropriateness of using uptake curves.

Finally, the parameter spaces are also indicative of the problem because a well-localized minimum of $\sigma_{\text{rel}}(D_T^{\text{loc}}, \alpha^{\text{loc}})$ is observed for c profile fitting (orange region in Figure 11.2c). By contrast, the optimum parameter region of the integral solution is very flat and L-shaped, indeed stretching along the axis of both parameters as a red stripe in Figure 11.2d (note the several

orders of magnitude displayed for D_T^{int}). Therefore, if one were to use integral analytical solutions of the diffusion equations to analyze guest transport data^{208,214} in nanoscale host objects by applying automatic optimization algorithms, the present work gives clear evidence that care must be taken because such algorithms are prone to oscillations in flat parameter spaces.

The deficiency of uptake curves to accurately describe the transport progress into nanoscale objects may be grounded on the statistical noise of the TrMD data. Reference 214 and Chapter 10 have shown that diffusivities and surface permeabilities are generally extractable from tracer-exchange uptake curves, when the data exhibit virtually no statistical noise. The analysis of the TrMD simulations was indicative of decreasing noise with increasing sheet thickness. For this reason, it seems reasonable that once the noise has fallen below a certain threshold it is possible that the transport coefficients obtained from uptake-curve and concentration-profile fitting, respectively, will agree with one another. This, however, would be observable above a “threshold” thickness only, which had apparently not been reached yet in the present cases.

Focusing in the remainder on the spatially resolved surface-barrier model for the reasons given above, the second peculiarity deduced from the fitted transport data lies in the following. AFI diffusion coefficients, D_T^{loc} , and surface permeabilities, α^{loc} , distinctly decrease with increasing sheet thickness. They slowly approach the (concentration-wise averaged) values from EMD simulations, where the deviation between the thinnest sheet and EMD values amount to factors of 3 and 1.5 for D_T^{loc} and α^{loc} , respectively. The diffusivity deviations are in fact so strong that, except for the thickest nanosheet, all D_T^{loc} exceed the maximum D_T from EMD in the concentration range of interest. Clearly, the concentration dependence of the diffusion coefficient itself cannot be the reason for the deviations.

The trend of decreasing D_T^{loc} and α^{loc} is entirely absent for LTA. However, a similar decrease of the methane tracer diffusion coefficient with AFI sheet thickness has been observed in Reference 214 (cf., Chapter 10). In that case, the decrease could be attributed to the influence of lower methane adsorption in the gas–solid interface region as compared to the adsorption in the bulk solid space.^{193,214} For the present chapter, the adsorption influence was yet circumvented by excluding the interface region (external surface adsorption layer and outermost zeolite cage) from the concentration profiles that were fitted to the analytical solutions (cf., Figure 4.6 in Chapter 4). Therefore, the origin of the here reported decreasing diffusion coefficients in AFI must have other reasons. It is hypothesized that this is indeed owing to the exceptionally thin host structure in conjunction with the shape of the pores.

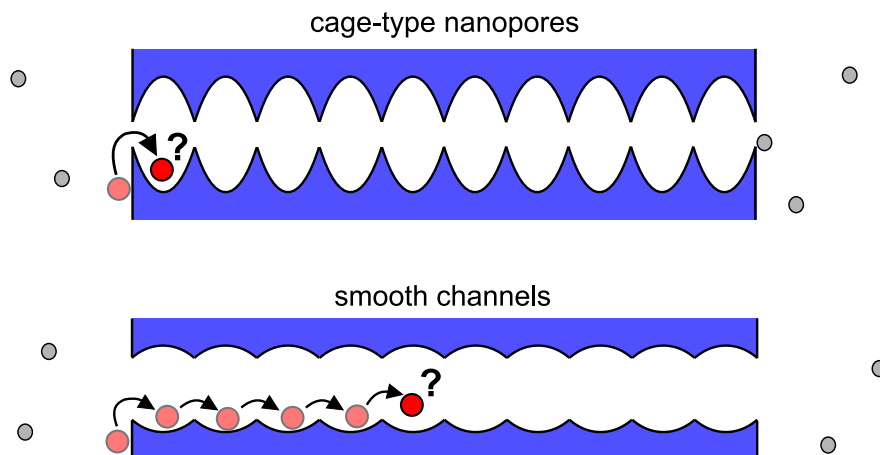


Figure 11.3: Molecule (red circle) loses its memory immediately provided it enters a cage-type zeolite pore (top). If the pores are however rather smooth (bottom), the molecule will have a high likelihood to perform a series of multijumps over several cages until it “forgets” where it came from.

To understand the mechanism behind the hypothesis consider a single molecule entering an empty nanopore (Figure 11.3). That situation is encountered at early stages in TrMD simulations. In the case of LTA, a molecule that has just entered the first cage (Figure 11.3 top) will immediately lose its memory where it came from because of high entropic diffusion barriers.⁴¹ The quick loss of memory is a prerequisite for applying random-walk theory on the length scale of a single zeolite cage. The smooth AFI pore shape (Figure 11.3 bottom), on the contrary, does not cause as large diffusion barriers between adjacent cages as in LTA. Because of the low barriers, which range around $1 k_B T$,^{110,146} the molecule is unlikely to equilibrate in the first cage and jumps immediately into the next cage and even further to undertake a cascade of jumps. As a result of these multijumps,¹¹⁰ the diffusivities at low loadings are higher than the corresponding free-energy barrier estimates. This phenomenon, called kinetic jump correlations,^{110,118} implies that while random walk theory is not applicable on the length scale of a *single cage* it just takes the molecule more time and, therefore, a longer distance to lose its memory where it came from.²¹⁶ Absence of any systematic deviation of the mean-squared displacement (MSD) from ideal self-diffusion behavior,¹⁴⁶ that is, $MSD \propto t$, serves yet as strong evidence of the existence of an underlying Markovian chain on *some* length scale. Obviously, the smallest sheet thicknesses used in the TrMD simulations are just within this randomization length scale because the first molecules entering the sheet at low concentra-

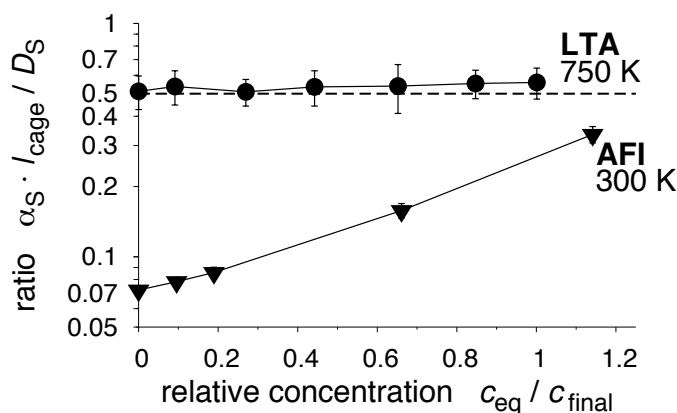


Figure 11.4: Ratio of methane tracer surface permeability,²¹⁴ α_S , to diffusivity, D_S , normalized by distance l_{cage} and plotted as a function of relative concentration, c_{eq}/c_{final} , for the two zeolite materials studied. Note that the subscript “eq” signifies that the data and thus the concentration dependence was obtained from equilibrium molecular simulations and not from TrMD simulations.

tions do not have enough time to lose their memory. This gives rise to faster filling and, thus, larger diffusivities with decreasing sheet size. The similar though more subtle trend for the surface permeability, α^{loc} , is attributable to exactly the same reason. Crucially, this “nano effect” manifests a size limitation to describing guest transport into porous materials with Fick’s laws in such a sense that the transport coefficients depend on the geometrical parameters of the host.

As mentioned earlier, interference¹³⁹ and infrared^{4,139} microscopy measurements have unraveled that the transport diffusivity and the surface permeability of hydrocarbons follow the same concentration dependence in the case of the metal–organic framework Zn(tbip) and zeolite $AlPO_4$ -LTA. However, Zimmermann *et al.*²¹⁴ have recently shown that this correlation⁵ between the two transport coefficients is not unique. While the tracer-exchange surface permeability, α_S , of methane in AFI increased with concentration, the self-diffusivity decreased.²¹⁴ Here, the permeability-to-diffusivity ratio can be directly compared over concentration for AFI and LTA using the data from equilibrium molecular simulations (cf., Supplementary Subsection 11.5.4). As seen from Figure 11.4, α_S correlates with D_S for LTA but not for AFI, in the latter case of which the permeability is markedly smaller than the diffusivity but increases with concentration. The correlation might lead

to the impression that surface barriers are not important to methane transport into LTA nanosheets¹¹⁴ because α_S and D_S are alike. However, recall that increasing the thickness of the LTA nanosheet by a factor of 5.4 yields a 3.3 times larger effective transport diffusivity (Table 11.1), which is still only half of the true transport diffusivity D_T^{loc} . Hence, accurate modeling of molecular transport into nanosheets always needs to employ the surface-barrier boundary condition, which is due only to the exceptional small thickness of the host material.

11.4 Conclusions

Three central consequences follow from the results of this chapter to predictive process design where guest transport into nanoobjects plays a critical role. First, the imperative has been emphasized to model transport with spatially resolved models (c profiles) that are grounded on an explicit description of the transport in the boundary layer between sheet and bulk fluid phase (α), irrespective of the guest–host match.^{114,159} Second, the present chapter has indicated that rapid equilibrium simulations can be used to predict both the diffusion coefficient⁹⁰ and the surface permeability,²¹⁴ provided that the sheet thicknesses are larger than 100 nm or guest diffusivities lower than $\approx 10^{-8}$ m²/s. Rare event techniques¹²³ and histogram reweighting methods¹¹⁵ may in this context be used to push the prediction range even further to cases of extremely high diffusion and surface barriers. This may ultimately permit automated,²¹⁷ high throughput, *in-silico* screening studies⁶ to account also for (surface) transport influences. However, it needs to be pointed out that *single*-component transport has been investigated only. Most applications^{16,21,69,211,212} have yet to deal with a mixture of various guest species. It will, hence, be necessary to test the applicability and predictability of the surface permeability in *multi*component situations, too. Incorporation into the Maxwell–Stefan formulation^{20,90} seems to be a valuable starting point. In the opinion of the author, this represents one of the future key challenges in diffusion theory in order to meet the needs of nanotechnology from a process design perspective. Third, a limitation to applying Fick’s laws to nanoscale objects has been detected which is due to the combination of their exceptional size and memory effects of the diffusing guest molecules. Owing to the crucial role of nanopore shape, this phenomenon is expected to be even stronger in carbon nanotubes compared to the here studied AFI-type zeolite. This would, for example, imply that predictive design of future gas-sensing devices⁶⁹ needs to account for CNT-length dependent diffusion coefficients, in the context of which transient molecular dynamics¹²⁴ will be a useful com-

plementary design tool.

Finally, a quote shall be given from David Chandler's seminal 1987 text-book on statistical mechanics, in which he, probably in anticipation of such circumstances as indicated by the results of methane in AFI-type nanosheets, noted:⁹⁶

Of course, it is impossible for equations like $\partial C/\partial t = D\nabla^2 C$ to be correct for all time or spatial variations. The error in the equation is due to the inadequacies of Fick's law.*

* C represents here the time-correlation function of fluctuations in the instantaneous density rather than the (normalized) concentration.

11.5 Supplementary Data

11.5.1 Methodology Details

Nanosheets were created by placing $N_{\text{UC},x} \times N_{\text{UC},y} \times N_{\text{UC},z}$ unit cells in the box center (AFI: 2×2 in x and y as well as 3, 6, 12, 24, and 48 along z coordinate for enabling increasing nanosheet thickness; LTA: 3×3 in x and y as well as 6, 12, and 24 in z). In addition, a layer of half a unit cell was added along z in case of AFI. In contrast to x and y , void space was added along z in order for a gas space to establish. Because periodic boundary conditions were used in all directions, the set-up resembled an infinitely repeating sequence of nanosheets and gas space along z , which extended infinitely in x and y . Both surfaces, AFI and LTA, concluded with the respective window rings so that the entropic diffusion bottlenecks formed the entrances to the pore structures in both cases.

Room temperature (300 K) was imposed in the AFI simulations, whereas T was set to 750 K in case of LTA. Preliminary tests using conventional equilibrium molecular dynamics (EMD) at room temperature clearly showed that methane diffusivities are exceptionally small in LTA ($\approx 2 \cdot 10^{-11} \text{ m}^2/\text{s}$). The low temperature would have prohibited long enough transient MD simulations of methane at room temperature with increasing nanosheet thickness. In fact, the simulations at 750 K employing the thickest LTA sheet were already such time-consuming that a single run took, on an average, 88 days on a state-of-the-art Intel quad-core cluster!* Noting that the diffusivities at 750 K amounted to roughly $6 \cdot 10^{-10} \text{ m}^2/\text{s}$ leads to an increase in the diffusion coefficient by a factor of 30. Taking the opposite point of view, a single TrMD simulation would, in first order approximation, have taken $30 \cdot 88 \text{ days} = 2640 \text{ days}$ at room temperature, obviously being infeasible. Furthermore, it has to be reiterated that 40 independent simulation runs were performed in order for the concentration profiles and uptake curves to show little noise and thus providing statistically significant data (cf., Figure 11.2a and b). This sums up to remarkable $40 \cdot 88 \text{ days} = 3520 \text{ days} \approx 10 \text{ years}$ of single-core cluster time necessary for the most demanding system in fact studied in this chapter (thickest LTA sheet).

The pressure imposed on the control volume was 10 bar and 100 bar for

*The cluster was purchased from COMPTRONIC GmbH, Germany, and is based on SuperMicro-Barebone systems. Each node has two quad-core CPUs (Intel XEON Harpertown E5430 and XEON Nehalem X5550), where each core has a performance of 2.66 GHz. The RAM ranges between 16 and 24 gigabyte per node and, thus, 2 to 3 gigabyte per core. Operating system is SuSE SLES 11.

AFI and LTA, respectively. The saturation concentration at the end of the TrMD simulations agreed perfectly with the adsorption isotherms obtained from conventional grand-canonical Monte Carlo simulations and amounted to $c_{\text{final}} = 1872 \text{ mol/m}^3$ and 994 mol/m^3 for AFI and LTA, respectively. The corresponding loadings were 0.78 and 1 molecule per cage, indicating that the higher pressure in LTA simulations compared to AFI runs was necessary to ensure comparable adsorption conditions.

In regard on the concentration-profile sampling, it has to be stressed that the data points representing the outermost cages on either side of the sheet were ignored (cf., X's in Figure 4.6, Chapter 4). By this, the influence could be circumvented that lower adsorption in the nanosheet boundary region exerts on transport coefficients (cf., Chapter 10 and Reference 214). The low-adsorption effect causes decreasing tracer-exchange diffusion coefficient, D_S , and surface permeability, α_S , with increasing sheet thickness, δ . Therefore, it can be concluded that the decrease of both D_T and α as observed in the present chapter for AFI is very likely due to memory effects only.

An order- n scheme⁹¹ was adopted for sampling of transient concentration profiles, $c(t, z)$. This has been proven to be very helpful because the short time uptake behavior is decisive for accurate determination of the surface permeability, the observation of which was also made during the analysis of tracer-exchange results (Chapter 10 and Reference 214) but not explicitly mentioned. The thinner the membrane or sheet was, the more important were data at early uptake stages. In a conventional scheme, where constant sampling frequencies were used to save concentration profiles (i.e., linear in time), short time intervals would have been necessary for a reliable determination of α . This, however, would have led to an extremely high number of total sampling points. Obviously not being efficient from a memory point of view, the linear sampling is neither wanted in regard of the CPU time that would be necessary to fit the resulting exceptionally large number of profiles with different diffusion models having various parameters. Therefore, concentration profiles were sampled every 100th step for the first 1000 MD steps and, after these initial 1000 steps (= 1 ps), switched over to an order- n scheme. Each order of magnitude was divided into 20 blocks, thus, yielding 20 c profiles per time magnitude.

All TrMD simulations were run until saturation was attained or longer. In two cases, this was however not possible because of an unexpected shut-down of the computer cluster: AFI simulations with the thickest sheet [$m(t)/m_{\text{sat}} = 0.85$] and LTA calculations using the intermediate sheet thickness [$m(t)/m_{\text{sat}} = 0.93$].

11.5.2 Parameter Tests

Because the control volume and thus its size as well as the number of GCMC trials performed are rather specific parameters to TrMD simulations their influence was tested on the basis of methane uptake into the smallest LTA nanosheet at 300 K and 10 bar. The frequency of switching from MD to GCMC is also an important and specific quantity. But it has been shown elsewhere for similar systems^{177,218} that every tenth MD step should be high enough a frequency to ensure steady supply to the control volume and, hence, to simulate a stable gas reservoir. In the references given, the highest frequency was every 20th MD step.

Keeping all other parameters constant, the size of the control volume (total width) was varied from $l_{CV} = 2 \cdot 1.6 \text{ nm} = 3.2 \text{ nm}$ over $2 \cdot 8 \text{ nm} = 16 \text{ nm}$ to $2 \cdot 16 \text{ nm} = 32 \text{ nm}$. To ensure the same GCMC trial rate per volume, the number of GCMC trials ($N_{\text{ins+del}}$ = insertion plus deletion) was proportionately adjusted to the control volume length; thus, $N_{\text{ins+del}} = 10, 50, \text{ and } 100$. However, the influence of the number of GCMC trials was also investigated by varying it from 10 over 20 to 50 for a constant control volume size of 3.2 nm. Note that as many insertion ($N_{\text{ins+del}}/2$) as deletion attempts ($N_{\text{ins+del}}/2$) were performed per GCMC phase.

A sequence of resulting concentration profiles is shown in Figure 11.5 for the parameter combinations studied. At any time, the profiles fall on top of one another, subject to only minor deviations in consequence of statistical fluctuations. Clearly, the parameters have no influence on the filling of the nanosheet with methane molecules in the ranges investigated. Therefore, the most efficient setup was used, that is, the smallest control volume width (3.2 nm) and the smallest number of GCMC trials (10).

11.5.3 Transport Diffusion Coefficient from EMD

To compare diffusion coefficients from transient MD simulations with diffusivities from equilibrium MD the thermodynamic correction factor, Γ , is used.²¹⁹ The factor is defined for single component adsorption under isothermal conditions by the change in the logarithm of the fugacity, $\partial \ln f$, with change in logarithm of equilibrium concentration in the adsorbed zeolite phase, $\partial \ln c_{\text{eq}}$:

$$\Gamma \equiv \left. \frac{\partial \ln f}{\partial \ln c_{\text{eq}}} \right|_T. \quad (11.10)$$

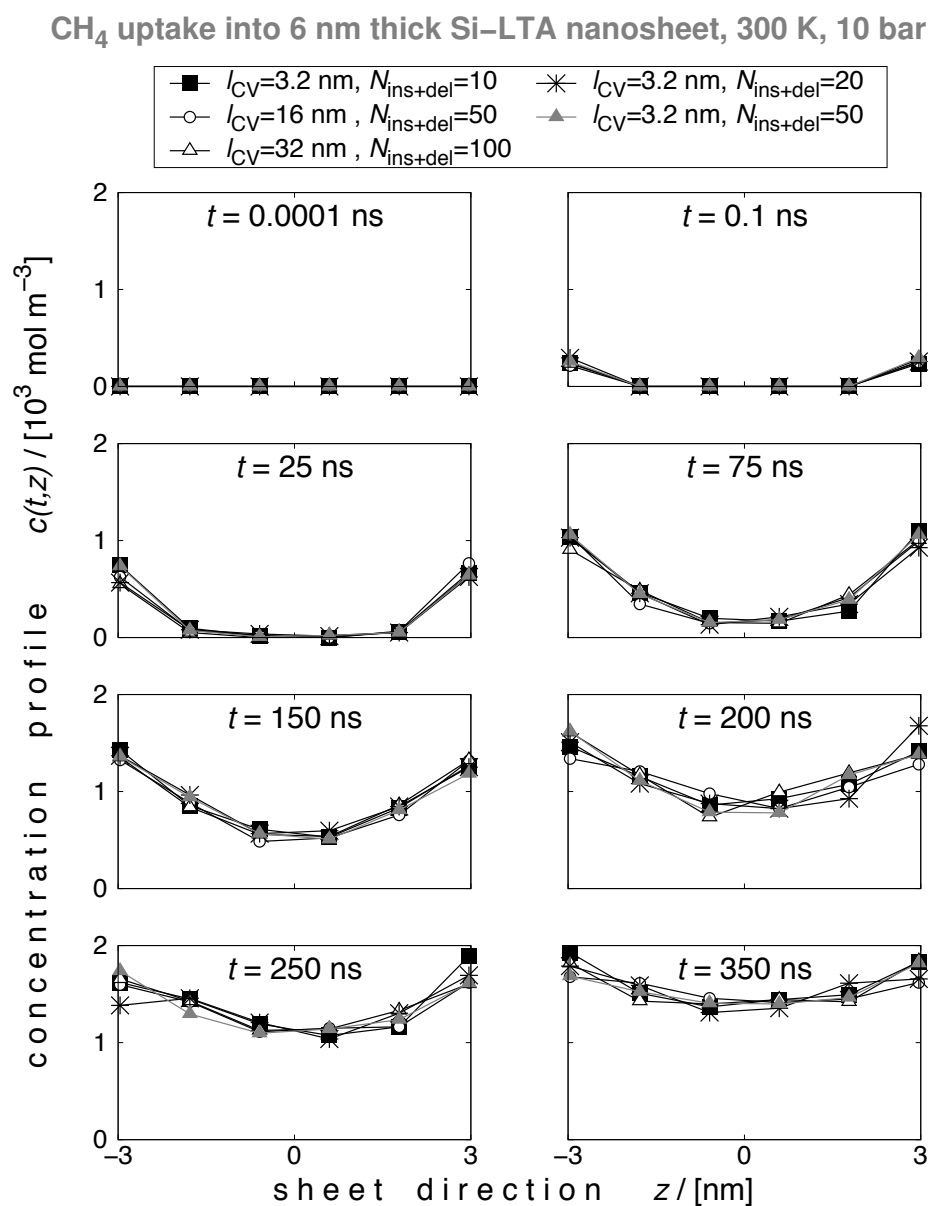


Figure 11.5: Concentration profiles of methane uptake into the smallest LTA nanosheet studied ($\delta \approx 6$ nm) at 300 K and 10 bar and for different widths of the control volume, l_{CV} , as well as different numbers of GCMC trials ($N_{ins+del}$ = insertion plus deletion) during each GCMC phase. Each profile represents an average from 15 independent simulations under same conditions.

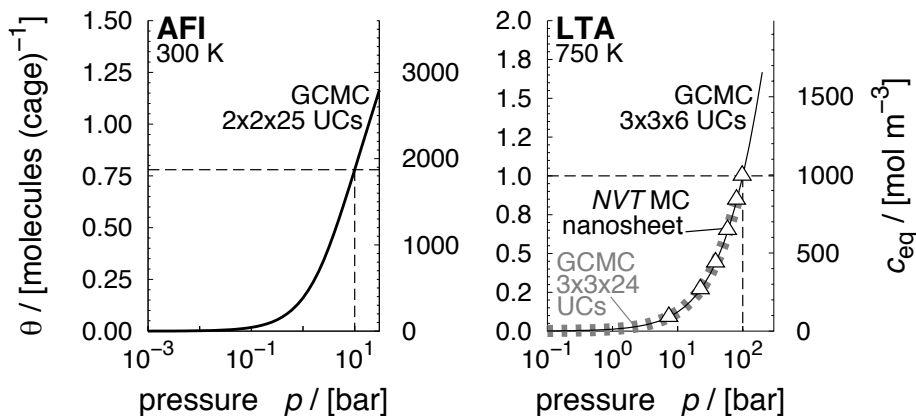


Figure 11.6: Adsorption isotherms of methane in siliceous AFI at 300 K (left) and in siliceous LTA at 750 K (right) obtained from GCMC simulations in periodic zeolite crystals (solid and dotted lines). Vertical and horizontal dashed lines highlight final equilibrium state points of the transient MD simulations. Triangles (left) are isotherm results from *NVT* MC instead of GCMC where, however, the simulation box contained an explicit gas space. In that case, the gas-phase pressure was calculated on the basis of the average gas-phase concentration via the Peng-Robinson equation of state.

The thermodynamic correction factor links the corrected diffusion coefficient, D_C , with the transport diffusion coefficient, D_T , via:¹

$$D_T(c_{\text{eq}}) = \Gamma(c_{\text{eq}}) \cdot D_C(c_{\text{eq}}), \quad (11.11)$$

where all three quantities usually depend on guest concentration, c_{eq} , in the adsorbed zeolite phase. The equation originates from deriving the diffusion equations on the basis of an energy balance where the chemical potential driving force is opposed by a friction force.¹ From a scientific point of view, it provides an ideal means to investigate diffusion phenomena because the relative significance of thermodynamic effects (Γ) and mobility effects (D_C) on the transport diffusivity can be extracted.¹ It is noteworthy that many authors in zeolite science prefer to present diffusion coefficients as functions of loading (θ), that is, in molecules per unit cell or cage, but that both quantities are directly related ($\theta \propto c_{\text{eq}}$).

The comparison of diffusion coefficients requires obviously the calculation of both corrected diffusion coefficients as well as adsorption isotherms, the latter permitting numerical determination of Γ . Therefore, adsorption

isotherms of methane in AFI at 300 K and in LTA at 750 K obtained from GCMC simulations are presented in Figure 11.6. The final equilibrium states of the transient MD simulations are indicated by dashed lines. Evidently, the two states are at comparable isotherm locations. Note that tests were performed whether or not the LTA isotherm is sensitive against changes in simulation box size. This biasing influence could be successfully ruled out, as evidenced in Figure 11.6 (right) by the comparison between solid line (small simulation box) and dotted line (large box).

Results of corrected diffusion coefficients from EMD simulations are presented in Figure 11.7. Different symbols represent data where increasing equilibrium concentration, c_{eq} , was achieved by changing the number of methane molecules while using a simulation box of (approximately) constant size. By contrast, the grey-shaded areas correspond to the opposite case where the simulation box size varies while the number of methane molecules is (roughly) the same. The corrected diffusivity in LTA (Figure 11.7, bottom) exhibits a slight adsorbate-particle number influence which, however, levels off as soon as more than 100 methane molecules are simulated. This effect can be ascribed to the thermostat and it has been also reported by Dubbeldam *et al.*¹¹⁰ The authors recommended to couple more than 100 particles to the thermostat to avoid this biasing effect.¹¹⁰ The thermostat influence is regarded to also be the reason why both the transport diffusivity and the surface permeability from TrMD in LTA increase slightly with sheet thickness ($D_{\text{T}}^{\text{loc}}$ and α^{loc} in Table 11.2). The thicker the sheet is, the higher will be the average number of molecules in the TrMD simulation at comparable uptake rates. The higher the average number of molecules, the larger the diffusion coefficient as a result of the thermostat effect. Because the surface permeability follows the same concentration behavior as the diffusivity (Figure 11.11), the same reasoning applies to α with respect to the thermostat influence.

Analytic functions were used to describe the concentration dependence of D_{C} (dashed lines in Figure 11.7) for the determination of the transport diffusion coefficient on the basis of EMD simulations. In the case of AFI, an exponential reproduced the trend best, whereas a simple linear relationship was sufficient for LTA. Also, the thermodynamic correction factors derived from the adsorption isotherm by numerical differentiation (symbols in Figure 11.8a), were fitted to analytical solutions (lines in Figure 11.8a). Here, a parabola worked best in both cases, where Γ increased monotonically in the concentration range relevant to the TrMD simulations. In Figure 11.8b,c, both diffusion coefficients from equilibrium MD simulations are plotted over relative concentration, $c_{\text{eq}}/c_{\text{final}}$: the corrected diffusion coefficient (dotted

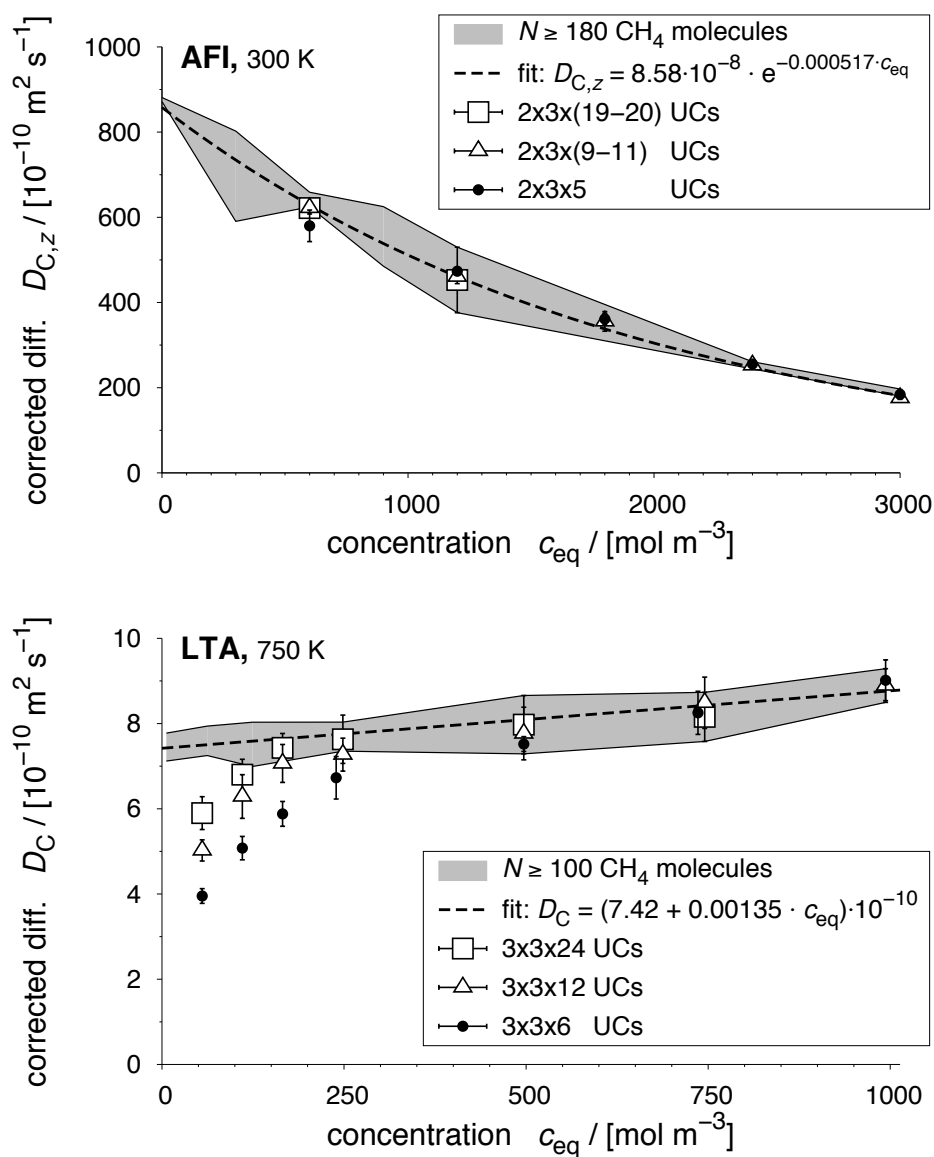


Figure 11.7: Corrected diffusion coefficients of methane in AFI at 300 K (top) and LTA at 750 K (bottom) from equilibrium molecular dynamics simulations (*NVT*). LTA is an isotropic medium to methane diffusion, that is, $D_C = D_{C,x} = D_{C,y} = D_{C,z}$. Error bars were computed via the sample variance of the results of at least five independent simulations.

lines) and the transport diffusivity (solid lines) for AFI (b) and LTA (c). The mean transport diffusion coefficients, \bar{D}_T , are hence $7.55 \cdot 10^{-8} \text{ m}^2/\text{s}$ and

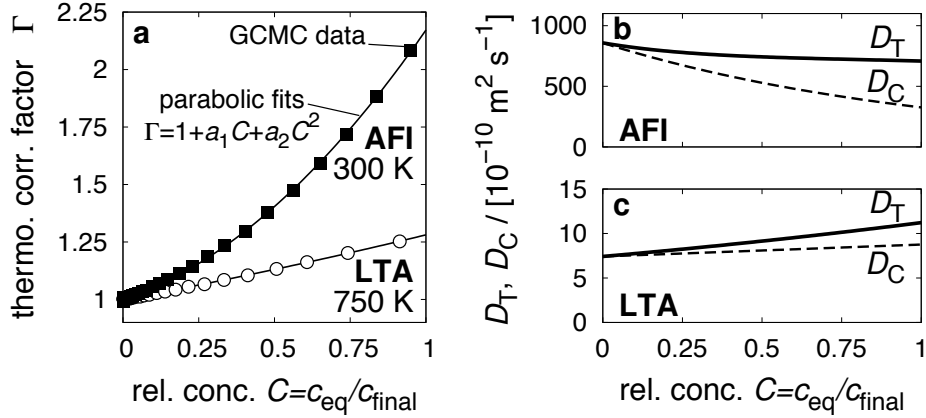


Figure 11.8: (a) Thermodynamic correction factors, Γ , as functions of relative concentration, $C = c_{\text{eq}}/c_{\text{final}}$, for methane in AFI at 300 K and in LTA at 750 K. Parabolas (lines) were fitted to the correction factors from GCMC (symbols), providing excellent agreement with following parameters: $a_1 = 0.444$ and $a_2 = 0.728$ as well as $a_1 = 0.241$ and $a_2 = 0.0396$ for AFI and LTA, respectively. (b,c) Transport, D_T , and corrected diffusion coefficients, D_C , vs relative concentration (same systems), where D_C is obtained from equilibrium MD simulations and converted to D_T with Γ via Equation 11.11.

$9.2 \cdot 10^{-10} \text{ m}^2/\text{s}$ for AFI and LTA, respectively.

11.5.4 LTA Tracer-Exchange Surface Permeability

The surface permeability, α_S , of methane under tracer-exchange conditions in LTA was determined by means of a prediction²¹⁴ that is grounded on dynamically corrected transition state theory^{109,111,112} and the assumption that the interface between gas and solid consists of two sublayers^{207,214} (cf., Figure 10.2):

$$\alpha_S = \frac{\bar{v}/c_{\text{eq,zeol}}}{1/(\kappa_{\text{gas}}c_{\text{eq,gas}}^\ddagger) + 1/(\kappa_{\text{surf}}c_{\text{eq,surf}}^\ddagger)}. \quad (11.12)$$

In that equation, \bar{v} denotes the average directed velocity of a methane molecule along the z coordinate which equals $\sqrt{k_B T/(2\pi m)}$, $c_{\text{eq,zeol}}$ the average equilibrium concentration throughout the zeolite nanosheet whereas $c_{\text{eq,gas}}^\ddagger$ and $c_{\text{eq,surf}}^\ddagger$ denote the equilibrium concentrations at the positions of the transition states for methane molecules moving between the surface adsorption layer and the gas space as well as between the surface adsorption layer and

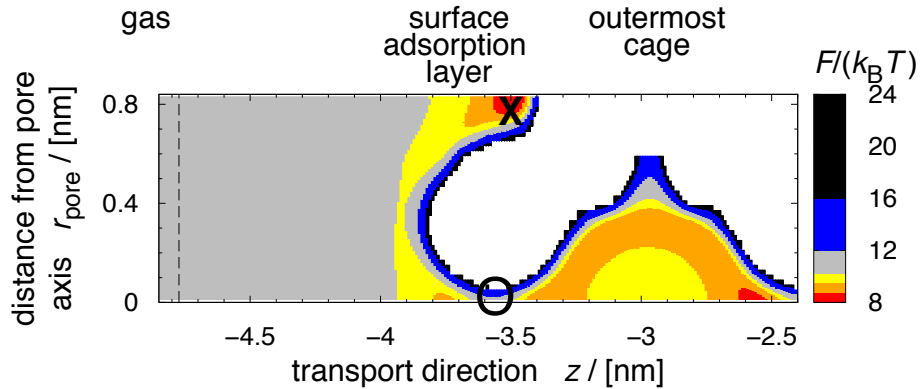


Figure 11.9: Two-dimensional free-energy landscapes, $F(z, r_{\text{pore}})/(k_{\text{B}}T)$, of methane in the interface between LTA nanosheet interior (right hand-side) and gas space (left hand-side). White areas indicate regions that were never visited by a methane molecule, black and blue regions are rarely visited regions, and red frequently visited regions. The landscapes are based on three-dimensional residence probability distributions of methane molecules in the simulation box, where it is important to underline that they were corrected for a nonlinear mapping of the Cartesian x and y coordinate. That is, $F(z, r_{\text{pore}})/k_{\text{B}}T = -\ln[N_{\text{hits}}(z, r_{\text{pore}})/r_{\text{pore}}^2]$, where $N_{\text{hits}}(z, r_{\text{pore}})$ denotes the accumulated, *not the averaged*, number of hits of having found a molecule at z and a distance r_{pore} apart from the pore axis.

the outermost zeolite cage, and κ_{gas} and κ_{surf} are the corresponding transmission coefficients for crossing the just mentioned transition states. Subscript “eq” signifies that the concentrations refer to equilibrium profiles along the simulation box obtained from standard NVT Monte Carlo simulations.

Before the results are shown, two differences to predict α_{S} via Equation 11.12 in comparison to the recent approach by Zimmermann *et al.*²¹⁴ have to be highlighted. First, the surfaces of the LTA nanosheets have regularly distributed hollows (Figure 11.1), which complicate the calculation of concentration profiles and thus evaluation of Equation 11.12. The problem becomes more tangible by considering Figure 11.9, which shows a two-dimensional free-energy landscape of methane in the interface region between gas phase and zeolite interior. Positions marked with large “O” and large “X” highlight the transition state locations for methane molecules traveling from the outermost cage to the surface adsorption layer and the location of the adsorption site in this layer, respectively. Clearly, if simple concentration profiles along z were used the low concentration at the transition state

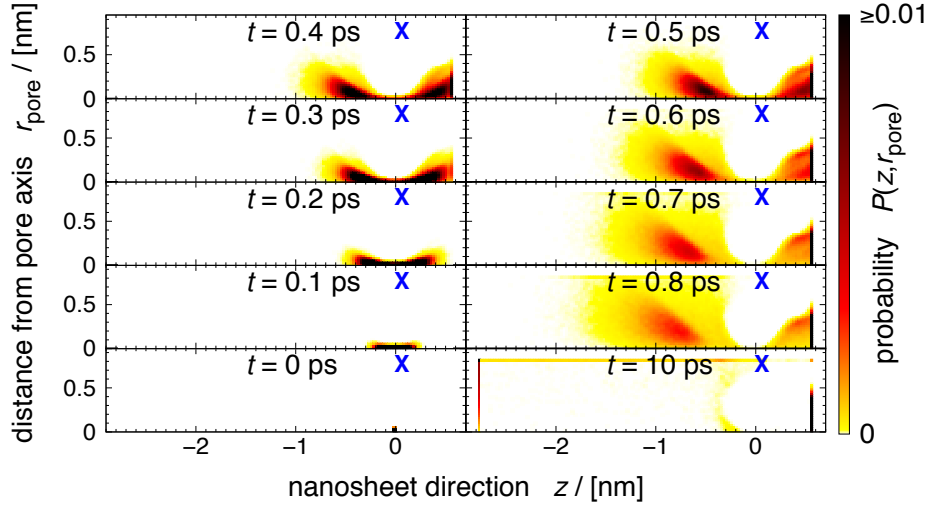


Figure 11.10: Evolution of a swarm of reactive flux trajectories leaving the surface barrier between external adsorption layer and outermost zeolite cage. The origin of the z coordinate was shifted to the location of the surface barrier in comparison to Figure 11.9, in which the barrier is found at $z = -3.57$ nm.

“O” (i.e., $c_{\text{eq,surf}}^\ddagger$) would be superimposed by the high concentration of the surface adsorption layer at “X”. That would lead to an artificial increase of the surface permeability. To avoid this bias the three-dimensional residence distributions, on which Figure 11.9 is based, were directly analyzed [i.e., the number of hits in each voxel, $N_{\text{hits}}(x, y, z)$]. Therefore, $c_{\text{eq,zeol}}$ was substituted by the number of hits averaged over all voxels that belonged to the innermost cage, $\bar{N}_{\text{hits,zeol}}$. Likewise, $c_{\text{eq,surf}}^\ddagger$ was obtained by averaging the number of hits, $\bar{N}_{\text{hits,surf}}^\ddagger$, in the plane at $z = -3.57$ nm (position of outermost zeolite atoms) with the restriction that voxels were included for averaging only if they were at most 0.15 nm apart from the pore axis along z . Finally, $c_{\text{eq,gas}}^\ddagger$ was substituted by the number of hits, $\bar{N}_{\text{hits,gas}}^\ddagger$, averaged over the separation plane between surface adsorption layer and gas phase (dashed lines in Figure 11.9). To test its validity the concentration-dependent self-diffusion coefficients was calculated based on transition state theory employing the 3D distribution analysis, which gave identical results in comparison to conventional 1D histogram analysis.

The second difference was also due to the structure of the LTA surface and concerned the transmission coefficients. The location of the surface adsorp-

tion site would have also required an additional order parameter, such as the distance from the pore axis, r_{pore} , to be used in the reactive flux (RF) simulations for determination of the transmission coefficients. This is because the final state for a methane molecule hopping either from the outermost cage onto the surface layer (κ_{surf}) or for a movement from the gas phase towards the surface layer (κ_{gas}) is not unequivocal with a simple one-dimensional transport coordinate. Despite this problem, it seems sufficient to start the RF simulations from the surface barrier (“O” in Figure 11.9) and stop a given shoot if the molecule has reached either the center plane of the outermost cage ($z = 2.95$ nm) or if it has left the simulation box at the left hand-side end at $z = 6.34$ nm. Evidence comes from probability distributions that track the temporal evolution of the entire swarm of RF trajectories,^{113,123} as displayed in Figure 11.10. Only a very small fraction of the swarm aims for the surface adsorption site, which is again marked with an “X” (blue). This fact leads finally to the vast majority of RF trajectories arriving either at the left boundary of the surface adsorption layer ($z = -2.8$ nm in Figure 11.10) or at the right boundary of the outermost cage ($z = 0.55$ nm in Figure 11.10) after 10 ps. Hence, a negligibly small number of trajectories is “caught” between the surface adsorption layer and gas phase only. It is therefore concluded that neither $\bar{N}_{\text{hits,gas}}^{\ddagger}$ nor κ_{gas} is actually needed because methane molecules on the surface barrier commit directly to either the gas phase or the zeolite interior. Hence, α_{S} is, in good approximation, predictable by:

$$\alpha_{\text{S}} = \frac{\bar{v}\kappa_{\text{surf+gas}}\bar{N}_{\text{hits,surf}}^{\ddagger}}{\bar{N}_{\text{hits,zeol}}}. \quad (11.13)$$

Here $\kappa_{\text{surf+gas}}$ is the combined transmission coefficient for methane molecules starting from the surface barrier and ending up in either the outermost zeolite cage or in the gas phase.

Finally, Figure 11.11 shows the resulting tracer-exchange surface permeability predictions (circles) of methane through the interface of the LTA nanosheet over the relative concentration, $c_{\text{eq}}/c_{\text{final}}$. In addition, a linear fit to the data points is provided, from which the mean surface permeability has been determined to 0.383 m/s. Also, a surface permeability prediction is shown that is based on a direct relationship to the self-diffusion coefficient⁵ (crosses). It is furthermore instructive to mention that the corrected diffusivity is identical to the self-diffusion coefficient in the concentration range of Figure 11.11.

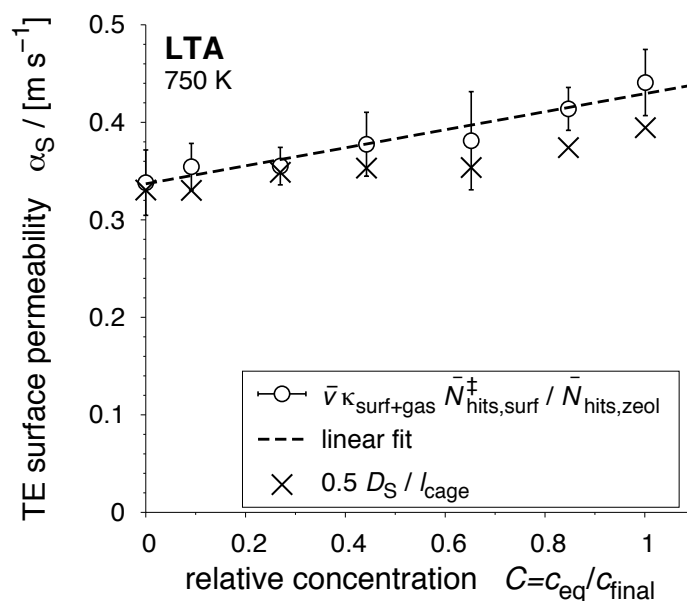


Figure 11.11: Tracer-exchange surface permeability prediction, α_S , of methane through the LTA nanosheet interface over relative zeolite concentration, c_{eq}/c_{final} , at 750 K.

11.5.5 Concentration-Dependent Corrected Diffusivity from TrMD

As mentioned in Table 11.2, the analytical solutions of the concentration profiles with the surface-barrier boundary condition have been also fitted to the transient MD data by introducing a third parameter. That parameter describes the concentration dependence of the corrected diffusion coefficient. In agreement with the EMD findings (Subsection 11.5.3), an exponential function is employed in the case of AFI:

$$D_C(c) = D_{C,0} \cdot \exp(a_3 \cdot c) \quad (11.14)$$

and a linear relationship for LTA:

$$D_C(c) = D_{C,0} + a_4 \cdot c, \quad (11.15)$$

with $D_{C,0}$ the zero-concentration diffusivity and a_3 as well as a_4 being constants. Obviously, the thermodynamic correction factor has to be inputted into the fitting approach as well. This was actually the reason to introduce analytical descriptions of Γ in Subsection 11.5.3 in the first place because

Table 11.3: Parameters ($D_{C,0}$, a_3 , a_4) describing the concentration dependencies of the transport diffusion coefficients and surface permeabilities (α) obtained from fitting Equation 11.5 to data from transient molecular dynamics (TrMD) simulations, along with the resulting average transport diffusion coefficients, \bar{D}_T^{loc} , obtained from these fits (i.e., not averages from EMD).

	δ [nm]	α [m/s]	$D_{C,0}$ [$10^{-10}\text{m}^2/\text{s}$]	a_3, a_4 [$10^{-3}\text{m}^3/\text{mol}$] [$10^{-13}\text{m}^5/(\text{s mol})$]	σ_{rel} [%]	\bar{D}_T^{loc} [$10^{-10}\text{m}^2/\text{s}$]
AFI	10.2	10.6	900	-0.475	3.6	823
	20.4	8.9	1000	-0.575	3.3	835
	40.7	7.9	920	-0.525	3.4	804
LTA	4.8	0.27	0.65	12.4	3.7	8.01
	11.9	0.29	3.75	12.9	3.3	11.82
	26.1	0.34	6.00	4.5	3.1	9.44

they are easier to handle during fitting than a discrete data set on Γ . Finally, note that the average methane concentration throughout the entire nanosheet, $\bar{c}(t_i)$, at a given instance of time was used for the determination of the “instantaneous” concentration-dependent transport diffusion coefficient, $D_T(t) = D_C[\bar{c}(t_i)] \cdot \Gamma[\bar{c}(t_i)]$, and thus for calculation of the analytical concentration profile at time instance t_i .

The results are presented in Table 11.3 along with the mean transport diffusivity resulting from the fitted functionals. The mean diffusivities and also the surface permeabilities agree very well with those from fitting of c profiles with α and a *constant* D_T . However, the fitted parameters are consistent with the one from EMD simulations in the case of AFI only. As Figure 11.12 shows, EMD data and TrMD fits fall on top of one another for AFI, whereas strong deviations for LTA are observable. The fact that the mean transport diffusivity is nonetheless consistent with the average derived in Subsection 11.5.3 leads to the conclusion that the concentration dependence of the diffusivity does not play as important a role for methane uptake into very thin LTA nanosheets as for methane uptake into AFI sheets. Furthermore, the agreement between TrMD and EMD data provides confidence in view of the validity and appropriateness of transient MD simulations, which is im-

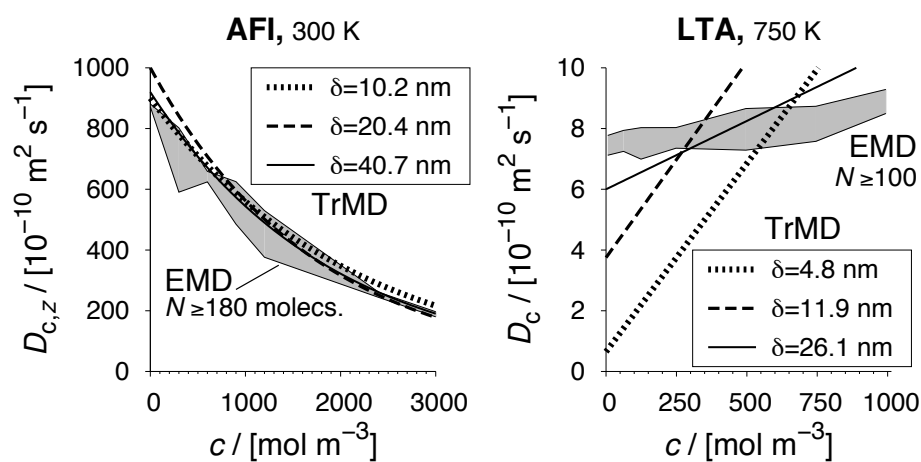


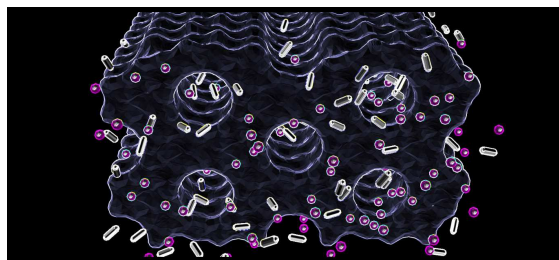
Figure 11.12: Corrected diffusion coefficients of methane in AFI at 300 K (left) and LTA at 750 K (right) from equilibrium molecular dynamics simulations (NVT) and from fitting analytical solutions of concentration profiles to data from transient molecular dynamics simulations where a concentration-dependent diffusion coefficient was used in the analytical solutions.

portant because TrMD are rarely used due to the enormous computational resource required.

12

Binary Transport

Single-component systems in equilibrium and nonequilibrium situations have been considered up to this point in the present work only. Because conventional grand-canonical Monte Carlo (GCMC) and equilibrium molecular dynamics (EMD)



are routinely employed to study multicomponent guest adsorption and diffusion in periodic nanoporous crystals,^{20,194,200} the present chapter aims at providing evidence to the transferability of transient molecular dynamics (TrMD) to reliably describe multicomponent transport into porous nanosheets. A binary mixture of methane and ethane entering an AFI-type nanosheet at 300 K serves here as a probe system.

Single-component isotherms from GCMC simulations reveal that ethane adsorbs more strongly than methane below 10 bar (Figure 12.1, left). That is due to (1) the longer molecule chain length of ethane, where (2) each bead has similar Lennard–Jones interaction parameters as the single methane bead (cf., Subsection 9.6.5). At elevated pressures, the behavior changes because of size issues. A methane molecule is roughly half the size of an ethane molecule so that methane adsorption, in terms of molecules per cage, can easily exceed ethane adsorption at these conditions. On a CH_i -bead basis, ethane adsorbs however still stronger than methane, even at high pressure. The isotherms suggest that a gas-phase pressure of 10 bar might be an interesting state point for the TrMD simulations because the two species adsorb similarly strong. However, ethane was still anticipated to exclude methane if both species competed for adsorption in the AFI pores. Therefore, mixture adsorption

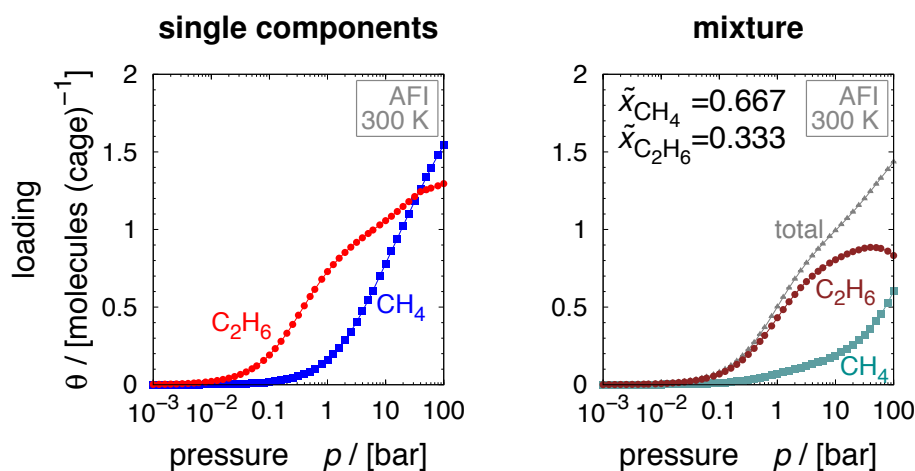


Figure 12.1: Single-component (left) and mixture (right) adsorption isotherms of methane and ethane in AFI at 300 K determined with GCMC simulations.

isotherms were calculated by GCMC (Figure 12.1, right), but not at equal gas-phase composition (i.e., $\tilde{x}_{CH_4} = \tilde{x}_{C_2H_6} = 0.5$), as is mostly done in mixture adsorption studies, but rather at an enhanced gas-phase mole fraction of methane ($\tilde{x}_{CH_4} = 0.667$) in comparison to ethane ($\tilde{x}_{C_2H_6} = 0.333$). The comparable adsorption in the single-component situation ($\theta_{CH_4} = 0.78$ molecules per unit cell and $\theta_{C_2H_6} = 1.06$ molecules per unit cell at 10 bar) has changed when both species truly compete in the mixture adsorption case. The mole fractions in the adsorbed phase amount to $\tilde{y}_{CH_4} = 0.189$ and $\tilde{y}_{C_2H_6} = 0.811$, respectively, underlining much stronger ethane adsorption even though the gas-phase composition was adjusted to enhance methane adsorption. It was yet decided to conduct TrMD simulations of the mixture at 10 bar and the 2-to-1 ratio in the gas phase because of two reasons. First, the total amount of methane adsorbed seemed large enough to expect a true multicomponent diffusion situation rather than an approximate single-component (ethane) situation. Second, the pressure was the same as in the previous chapter, where single-component transport of methane by TrMD simulations was investigated, thus, permitting direct comparison between the single-component and multicomponent results.

To get a first impression of the probable time frame to transiently fill the pores with a methane–ethane mixture, single-component EMD simulations were performed of ethane diffusing in a periodic AFI crystal. This also complemented the EMD data on methane from the previous chapter.

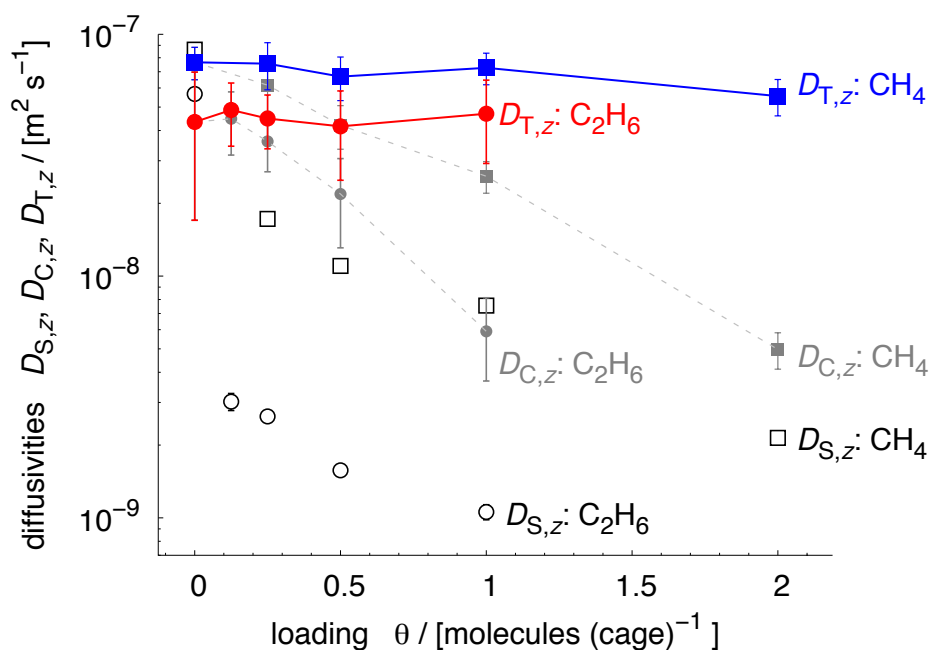


Figure 12.2: Self-diffusion, D_S , corrected diffusion, D_C , and transport diffusion coefficients, D_T , as functions of loading, θ , for methane and ethane in periodic AFI crystals at 300 K, as obtained from single-component EMD simulations. Numerical differentiation of the single-component isotherms of Figure 12.1 provided thermodynamic correction factors, Γ , which were necessary to calculate transport diffusion coefficients via $D_T = \Gamma \cdot D_C$. All diffusivities were determined for motion along z only (thus, not spatially averaged and therefore subscript “ z ”), because the one-dimensional channels of AFI run along z and the nanosheet for the TrMD simulations were hence aligned in this direction, too.

All three diffusion coefficients, that is, the self-diffusivity, D_S , the corrected diffusion coefficient, D_C , and the transport diffusivity, D_T , are plotted in Figure 12.2 for both adsorbate molecules and varying loading. Two trends are observable at finite loadings (i.e., $\theta > 0$). First, the different diffusion coefficients for the same molecule and loading increase in the order $D_S < D_C < D_T$. Second, when the same type of diffusion coefficient is compared among the two guest species at the same loading the diffusion coefficient of methane always exceeds the one of ethane. Interestingly, the difference is rather constant over loading in the case of the transport diffusivity (\approx factor of 1.6), which is the decisive diffusion coefficient to the TrMD

simulations, as the previous chapter uncovered. The factor closely resembles the ratio of the average molecular velocities on the basis of kinetic gas theory ($\bar{v}_{\text{CH}_4}/\bar{v}_{\text{C}_2\text{H}_6} = \sqrt{(1/m_{\text{CH}_4})/(1/m_{\text{C}_2\text{H}_6})} = 1.37$), which is usually found in any estimate of a single-component diffusion coefficient. Hence, the difference in transport diffusivities seems to be primarily caused by the difference in molecular masses. The important result in view of the TrMD simulations is that the time frame involved in filling an AFI nanosheet by either methane or ethane should be roughly the same because of comparable transport diffusivities. Also, the analysis of the mean-squared displacement indicated ideal diffusion behavior of both molecules so that single-file diffusion can be ruled out. This diffusion type is characterized by the fact that molecules cannot pass each other in the pores. Consequently, normal Fickian diffusion behavior should govern the filling of the nanosheet with the here considered mixture of methane and ethane, however, potentially subject to the memory effect described in the previous chapter.

The technical adoption of the simulation package to enable transient molecular dynamics simulations of mixtures was straightforward because the package, carefully built up by Jakobtorweihen,⁷⁰ already included both facilities, MD and MC, and, importantly, the treatment of mixtures in both cases. The crucial difference to the single-component TrMD lies in the fact that GCMC insertion and deletion trials into and from the control volume should reflect the gas-phase composition. This means in the here studied case that twice as many trials on methane as on ethane should be performed. The integration time step size was 1 fs.

The filling of a 6 nm thick AFI sheet with a methane–ethane mixture of 2-to-1 gas-phase composition was simulated with TrMD. Figure 12.3 shows the results: uptake curves of methane (left) and ethane (right). TrMD-specific parameters, notably, the number of MC trials, the number of MD steps, and the control volume size, were screened for their influence, as done in the single-component case (cf., Chapter 11). The most striking feature of the results is that methane fills the pores to a much higher amount than the mixture isotherm predicts; compare time span $10^{-10} - 10^{-8}$ s. In all cases, that is, irrespective of the simulation parameters, the system strives yet for the thermodynamic state predicted by the mixture GCMC isotherm, from which the saturation concentration, c_{sat} , and, thus, the normalization constant, m_{sat} , were deduced. This is reflected by the uptake curves tending to reach a value of unity after long time. However, the time that it takes the system to reach this point seems to be dependent on the TrMD-specific simulation parameters. In particular, the size of the control volume (CV) seems of significance in this respect because the largest CV investigated (640 Å) yields a final up-

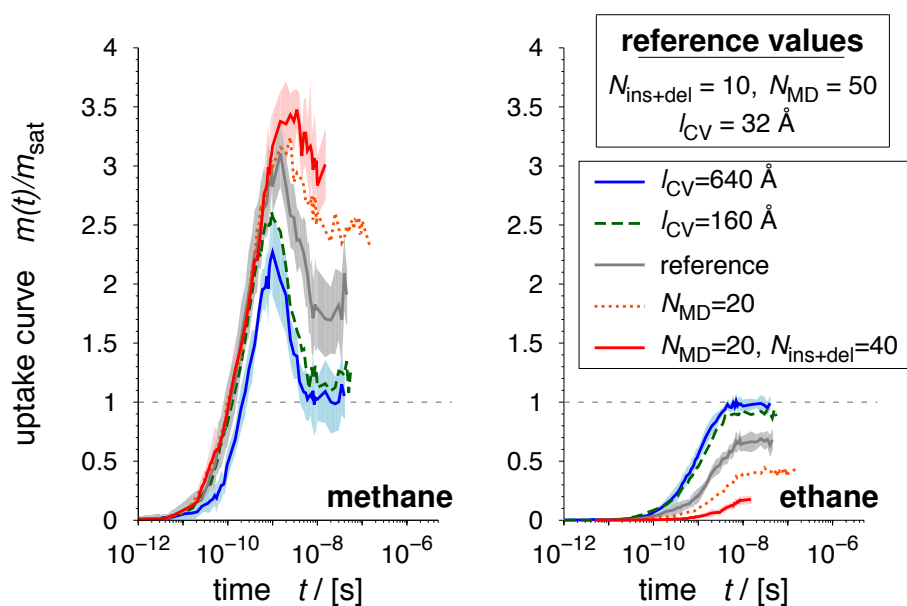


Figure 12.3: Uptake curves of methane (left) and ethane (right) into an AFI sheet of 6 nm thickness obtained from mixture-component TrMD simulations; $T = 300$ K, $p = 10$ bar, $\tilde{x}_{\text{CH}_4} = 0.667$, $\tilde{x}_{\text{C}_2\text{H}_6} = 0.333$. The TrMD specific parameters tested were, respectively, the number of insertion and deletion trials per Monte Carlo phase, $N_{\text{ins+del}}$, the number of integration steps performed per molecular dynamics phase, N_{MD} , and the size (here: width) of the control volume, l_{CV} .

take curve value of unity only. That is a most remarkable outcome because the overshoot behavior was not observed in the single-component methane TrMD simulations. In those cases, the control volume was 20 times smaller than the CV that gave here sound results from an adsorption perspective. The reason of the overshoot is likely found in the slow supply of ethane from the reservoir (control volume). This conjecture is supported by the facts that both the concentration in the gas phase and the mean velocity of ethane are smaller compared to methane, together reducing the mean flux in gas phase ($j \approx c \cdot v$). Ideally, such reservoir size effects should not have an influence on the results of neither experiments nor simulations. Because the effect levels off with increasing CV size and because this size (< 100 nm) is much smaller than any reservoir dimension usually encountered in experiments (> 1 mm) two consequences follow: (1) the effect seems to be of physical nature and, hence, not an artefact of the simulation methodology, and (2) the effect is not expected to have influenced binary transport measurements to any con-

siderable extent.

To conclude the present chapter provides the proof-of-principle that transient molecular dynamics can be extended in a straightforward manner to mixture transport cases. However, specific issues in comparison to the single-component transport problems of the preceding chapters have arisen, which call for further, more thorough investigations.

Part V
Resolution

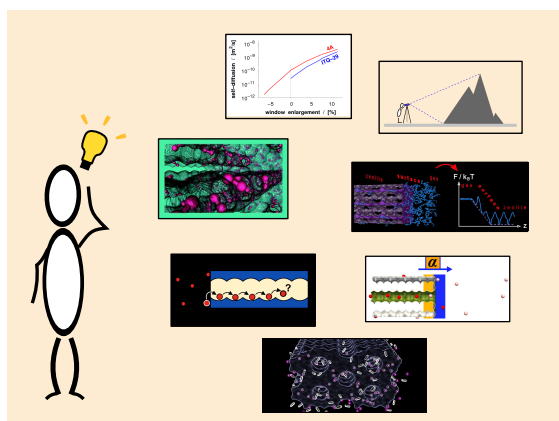
13

Summary

Before addressing to the two main questions from the Introduction and, thus, concluding from a broader perspective, this chapter first reiterates the main insights gained by the simulations performed in the present work.

The reliability of the molecular simulation methodology chosen was highlighted in Chapter 6. The chapter, furthermore, investigated the sensitivity of adsorption and diffusion of guest molecules towards subtle differences in the zeolite crystal structure that was used in the simulations. As a result, diffusivities differed by orders-of-magnitude when the smallest cross section of the pore (window area) was changed by only a few percent given that the fit between diffusing molecule and window was very tight (cage-type zeolites).

Chapter 8 presented an in-depth study of the interface dynamics of methane and ethane at different surfaces of an AFI-type zeolite crystal using equilibrium molecular dynamics and reactive flux simulations. On the basis of two-dimensional free-energy landscapes, the path of the molecules to reach the external surface was localized close to the pore wall. Most importantly, the transmission coefficient of hopping between an internal adsorption site and the external surface adsorption layer was calculated for the first time. Comparison to the transmission coefficient for hopping inside the bulk zeolite



space indicated more diffusive barrier crossing at the surface by a smaller transmission coefficient by up to a factor of ≈ 2 at the same thermodynamic conditions. In this respect, it was additionally shown that two different approaches (dynamically corrected transition state theory vs first-passage times) to determine the fraction of recrossings are equivalent.

To better understand on what the transport through the gas–zeolite interface depends a screening was conducted on the basis of equilibrium Monte Carlo and reactive flux simulations (Chapter 9). It included various normal alkanes (C1–C6) and alkenes (C1–C6) as well as three different zeolites (AFI, LTL, MFI), for which critical thicknesses were calculated. They reflected the maximal host extensions (crystal size or membrane thickness) up to which the effect of the slow transport through the boundary layer (surface-barriers effect) remains strong enough to cause large deviations in diffusion coefficients. The deviations were chosen such to be indistinguishable from experimental uncertainties (\approx factor 3–5, compare also Chapter 7). The results indicated that the surface-barriers effect was strongest at low pressures but negligible for systems close to the thermodynamic critical point. Smooth pores were identified to enhance the effect, whereas the porosity of the material constituted a decreasing influence factor. Because of these results, the mean field between gas and adsorbed phase was identified as the main source of the surface barriers encountered in the screening study. To complement the insights using highly idealized surfaces that were neither relaxed nor chemically saturated electronic structure calculations on propane in AlPO_4 -LTA and a corresponding hydroxylated and relaxed surface were conducted. While the screening study would have predicted no influence of the highly idealized surfaces in this case, the density functional theory (DFT) results were indicative of extremely slow transport through the surface in comparison to the intracrystalline transport, thus, highlighting that surface barriers inherent to ideal surfaces have in fact different sources.

Chapter 10 investigated the predictability of the local transport coefficient that rates the slow transport in the boundary layer: the surface permeability. Methane tracer exchange was used as a probe system, and a two-scale simulation approach was employed comprising a molecular detailed level and a continuum level for verification. An accurate prediction was presented, which, in particular, accounted for the diffusive surface barrier crossing mentioned earlier and the detailed structure of the boundary layer (zeolite margin and surface adsorption layer). Both effects were usually neglected in the past. But each effect represents an important quantitative factor for a reliable prediction because each of them can lead to a two-fold decrease of the surface permeability, or more, depending on the thermodynamic conditions. In this

respect, it must be added that also the surface-barriers screening study emphasized the significance of the boundary layer substructure. For example, neglecting the external surface adsorption layer for any of the hydrocarbons in contact with the AFI membrane reduced the critical membrane thickness by a factor of 2 at low pressure.

Testing the applicability of Fick's laws to well-ordered, nanometer sized host systems, instationary methane uptake into AFI- and LTA-type nanosheets was studied in Chapter 11 by computationally demanding transient molecular dynamics simulations. An in-depth analysis of different analytical solutions of the diffusion equations was performed. As a result, transport into these exceptionally small hosts could be described correctly only if spatially resolved solutions that explicitly accounted for a finite boundary layer transport rate via the surface permeability were used. Most importantly, a size limitation of the applicability of Fick's laws was unraveled, which was caused by memory effects of entering molecules in consequence of small intracrystalline diffusion barriers (smooth AFI pores). The effect leveled off with increasing AFI sheet thickness and was entirely absent in the case of LTA. In these situations, the surface-permeability prediction of Chapter 10 proved reliable also under instationary transport conditions. Furthermore, the results of the nonequilibrium simulations indicated that insights of the surface-barriers effect that were obtained via equilibrium simulation data should be transferable to instationary and, thus, nonequilibrium situations.

In Chapter 12, the proof-of-principle to apply transient molecular dynamics to multicomponent situations was provided on the example of a methane-ethane mixture entering an AFI-type nanosheet. The results indicated however that these systems might be prone to a specific issue. Methane temporarily adsorbed more than twice as strong as predicted by conventional grand-canonical Monte Carlo simulations. But all systems clearly strived to attain the expected adsorption behavior after long enough time. While the size of the control volume was identified as an influencing parameter in this respect, the effect persisted for huge control volume widths and even seemed physical because it could be traced back to the slow supply of ethane from the gas phase.

In view of the question whether surface barriers triggered by the ideal crystal structure could have caused orders-of-magnitude deviations in diffusion coefficients from different experimental techniques, the present study comes to following conclusions. It is very important to realize that different sources to the surface-barriers effect exist and that they can, crucially, occur in parallel. First, the ideal crystal structure and corresponding highly idealized surfaces that are neither relaxed nor chemically saturated represent

the first source. This type of surface barriers was thoroughly investigated in the present work and has its origin in mean-field differences between gas and adsorbed phase. Importantly, these surface barriers yielded critical host sizes that were below 1 μm . Hence, they are unlikely to have biased diffusion measurements because the crystals employed in the experiments usually exceed this size in both microscopic^{3,4,139,145} and macroscopic^{220,221} measurement techniques ($\geq 10 \mu\text{m}$). Second, relaxation and chemical saturation of the ideal surface can trigger large barriers provided that the diffusing molecule is of similar size as the smallest pore cross section (window). Density functional theory calculations of a single system indicated that these two effects can decrease the expected surface permeability by a factor of more than 200 and, thus, constitute a hitherto often underrated influence to surface barriers. Third, nonidealities, such as pore blockage by foreign matter deposition and severe lattice defects, can further increase the surface-barriers effect, where microscopy techniques seem well-suited to determine the number of blocked pore entrances.^{4,139} However, the DFT results of this work indicated that such number estimates from microscopy studies could be too large by a factor of 200 and more because of the neglected influences of surface relaxation and saturation. Therefore, this work concludes that highly ideal surfaces could have biased past diffusion measurements because of relaxation and chemical saturation of the intact surface. However, it seems most likely that the role of pore blockage and reduced intrinsic transport coefficient at the surface by relaxation and saturation played similarly important roles in a recent microscopy study.¹³⁹ Consequently, following statement by Jörg Kärger²²² from 2002 has not lost much of its validity, although 11 years have gone by since:

So far, however, any contribution raising some hope of “bridging the gap between macroscopic and NMR diffusivities” has been followed by presentations “reopening the gap...”. An eventual clarification of the problem, which may very well involve several different system-dependent answers rather than a single, unique response, may only be expected to be achieved by joint efforts and close contact between the specialists in zeolite synthesis and characterization, in diffusion measurement, and in diffusion theory.

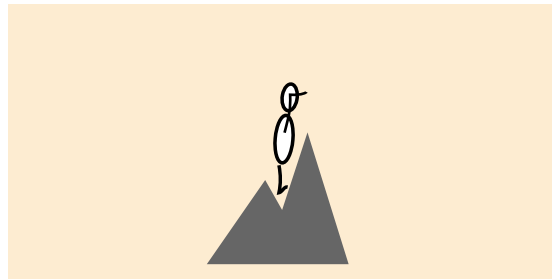
In turning to the consequences of future applications using ultrathin zeolite membranes or nanosheets, the present thesis clearly foreshadows that the gas-zeolite interface will play a pivotal role in reliable process design. This is because the highly ideal surfaces alone triggered surface barriers that led to critical membrane thicknesses of several hundred nanometers, exactly the size now achievable from a synthesis point of view.¹³ Surface relaxation

and saturation were neglected in the assessment of the critical membrane thickness. Therefore, it is here anticipated that the transport through the interface further decreases when these effects will be consequently accounted for, which will enhance the significance of surface barriers to accurate process design even more. Another phenomenon, which was highlighted in this thesis and which will likely come into play in the design of future applications employing nanoporous materials of nanometer size, is the issue that Fick's laws can break down at this small scale. It was here shown that process design of systems that are prone to this effect will have to account for diffusion coefficients and surface permeabilities that depend on nanosheet size. In this context, the author of the present thesis is convinced that the methods underlying this work will prove valuable to tackle these and similar nanotechnology specific problems because contemporary measurement techniques do yet not seem fit to accomplish these requirements.

Outlook

The results and conclusions of the present thesis provide two starting points for immediate research projects as well as a first idea of a novel measuring principle, as expounded below.

In most technological applications where a porous material and a gas or fluid phase come into contact, the fluid phase consists in fact of several components. Because the length scale of porous materials that determines the transport path of guest molecules into the host is constantly decreasing (“nanoage”) this work crystallized that two aspects will require thorough investigation in the future. First, the emerging significance of the surface permeability for an accurate description of transport into, through, and out of ultrathin zeolite films calls for a proper incorporation into a framework that treats multicomponent systems. The Maxwell–Stefan formulation⁹⁰ seems to be an ideal starting point to include mixture surface permeabilities into a continuum model. However, discrete kinetic Monte Carlo schemes²²³ might turn out to be a valuable alternative to the continuum approach. Second, the present thesis underlined the exceptional usefulness of transient molecular dynamics to verify physical laws at the nanoscale under instationary conditions, but for single-component systems only. Although the proof-of-principle was presented to extend this method to multicomponent cases a specific issue was encountered that requires further work to be fully understood. The importance of this extension is grounded on the idea that multicomponent transient molecular dynamics represents the perfect verification method for the first

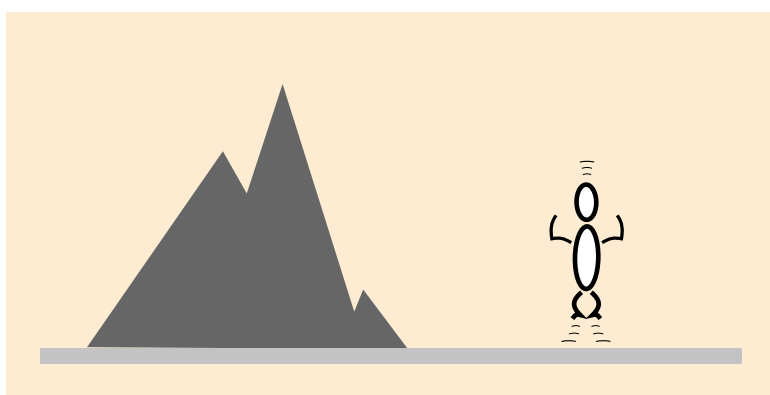


point: the incorporation of mixture surface permeabilities into a simulation approach of large length scale.

Having sparked the quest for the nature of surface barriers once again, the density functional theory (DFT) results of this work illustrated the imperative of detailed electronic structure methods to improve understanding and permit accurate predictions.²²⁴ Crucially, the results necessitate further investigation because they were analyzed in an approximative, yet rational way. Following aspects are likely the most important issues to be clarified in order to verify the consequences, at which the DFT results currently point; that is, at a high likelihood to the overestimation of defect rates.¹³⁹ First, the reduction in surface permeability relative to the diffusivity was based on differences in energy barriers only. Hence, neither differences in entropic barriers nor recrossings of molecules were considered, where this thesis emphasized the importance of the latter. These two factors are however envisioned to be determinable by classical molecular simulations using rare-event techniques,¹²³ in the case of which careful linkage of both scales (DFT and molecular level) might turn out as the bottleneck to the assessment. While this seems to be a ready-for-takeoff project an exciting possibility for predicting chemophysical properties is currently appearing that will go beyond such separate-multiscale approach: on-the-fly combination of quantum mechanics and molecular mechanics (QM/MM approaches).²²⁵ Joining such approaches with rare-event techniques should yield results of unprecedented chemical *and* statistical accuracy.

Obviously, neither the separate top-down approach usually followed in experiments nor the pure bottom-up route pursued in simulation approaches can reliably assess all influencing parameters to the slow transport through the interfaces of porous materials. The logical consequence is that any accurate assessment as to the reasons of the slow interface transport, that is, any “measurement” of all surface-barriers effects, should be carried out in a modulated way. On the one hand, electronic structure calculations in conjunction with molecular simulations could be performed to rate the influences of surface structure and chemistry and provide intrinsic transport coefficients. On the other hand, microscopy measurements would probe the combined effect of “naturally reduced” transport parameters and nonidealities such as pore blockage and, thus, yield apparent transport coefficients. These two modules are then connected by modeling and simulations at an intermediate length scale. This will not only allow the determination of the *correct* number of blocked pore entrances but this sketch will also be easily extendable to account for and rate the influence of other effects. For example, consider surface tailoring in the context of some separation process. Imagine that

the surface silanol groups would be substituted by, say, a medium-molecular-weight organic group to tune the separation characteristics in a rational but speculative way. Repeating the modulated assessment of surface barriers with this functionalized surface should enable quantitative statements about both the separation feasibility itself and the “relative” reasons to it. The fact that the two effects, surface chemistry and pore blockage, could be distinguished would possibly help improving this and similar processes even more because of certainty as to the reasons to the separation. In essence, the just presented idea of a measuring principle to surface barriers follows directly from—and thus exploits—the complementarity of experimental and theoretical approaches.



Nomenclature

A

Appendix A provides the list of symbols and abbreviations used in the present work. Note that the units represent the standard units associated with the quantities listed and that the actual units, in a figure for example, may however differ which is then explicitly highlighted. Furthermore, it was adhered to SI units with few exceptions, the most frequent of which is probably that many length and width variables and parameters are given in Ångström [Å] instead of meters [m] or nanometers [nm], where $1 \text{ \AA} \hat{=} 10^{-10} \text{ m}$.

A.1 List of Symbols

Symbol	Description	Units
a	fit parameter of relationship between heat of adsorption and hydrocarbon chain length	$\text{kg m}^2 \text{ s}^{-2} \text{ mol}^{-1}$
\mathbf{a}	unit-cell or nanosheet basis vector	–
\hat{a}	crystallographic coordinate	m
a_1	parameter of analytical description of Γ	–
a_2	parameter of analytical description of Γ	–
a_3	parameter of analytical description of $D_{C,z}$ in AFI	$\text{m}^3 \text{ mol}^{-1}$
a_4	parameter of analytical description of D_C in LTA	$\text{m}^5 \text{ mol}^{-1} \text{ s}^{-1}$
$\text{acc}(i \rightarrow j)$	acceptance probability of transition from state i to state j	–
A	some thermodynamic property	–

To be continued on next page.

Symbol	Description	Units
A	(cross-sectional) area	m^2
$\langle A \rangle$	ensemble average of property A	–
\mathbf{b}	unit-cell or nanosheet basis vector	–
\hat{b}	crystallographic coordinate	m
\mathbf{c}	unit-cell basis vector	–
c	concentration	mol m^{-3}
\hat{c}	crystallographic coordinate	m
c_{eq}	equilibrium concentration	mol m^{-3}
C	relative concentration (e.g., c/c_{final})	–
$C(\mathbf{r}, t)$	generalized correlation function	–
d	diameter	m
D	diffusion coefficient	$\text{m}^2 \text{s}^{-1}$
D_{eff}	effective diffusion coefficient (i.e., comprising both intracrystalline and surface transport resistance)	$\text{m}^2 \text{s}^{-1}$
D_{C}	corrected diffusion coefficient	$\text{m}^2 \text{s}^{-1}$
D_{S}	self-diffusion coefficient	$\text{m}^2 \text{s}^{-1}$
D_{T}	transport diffusion coefficient	$\text{m}^2 \text{s}^{-1}$
E	internal energy	$\text{kg m}^2 \text{s}^{-2}$
f	fugacity	$\text{kg m}^{-1} \text{s}^{-2}$
\mathbf{f}	force vector	–
f_{imp}^i	impact factor ($\equiv \alpha_{\text{S,ref}}/\alpha_{\text{S}}^i$)	–
f^{FPT}	first-passage time correlation factor	–
$f_{i,j,k}$	i -component of force acting on atom or bead j due to the presence of atom or bead k	kg m s^{-2}
F	free energy	$\text{kg m}^2 \text{s}^{-2}$
g	magnetic field gradient	$\text{kg m}^{-1} \text{s}^{-2} \text{A}^{-1}$
h	Planck constant ($6.626068 \cdot 10^{-34}$)	$\text{kg m}^2 \text{s}^{-1}$
\mathcal{H}	Hamiltonian	$\text{kg m}^2 \text{s}^{-2}$
$H(x)$	Heaviside function [$H(x) = 1$ if $x > 0$, $H(x) = 0$ if $x < 0$]	–
ΔH_{ads}	heat of adsorption	$\text{kg m}^2 \text{s}^{-2} \text{mol}^{-1}$

To be continued on next page.

Symbol	Description	Units
$\Delta H_{\text{ads},0}$	fit parameter of relationship between heat of adsorption and hydrocarbon chain length	$\text{kg m}^2 \text{s}^{-2} \text{mol}^{-1}$
i	index variable	–
j	molar flux	$\text{mol m}^{-2} \text{s}^{-1}$
j	index variable	–
k	transport or transition frequency	s^{-1}
k	index variable	–
$k_{j,k,\dots}^i$	constant associate with interaction type i between atoms or beads j, k, \dots	$\text{kg m}^2 \text{s}^{-2}$ kg s^{-2}
k_{B}	Boltzmann constant ($1.3806488 \cdot 10^{-23}$)	$\text{kg m}^2 \text{s}^{-2} \text{K}^{-1}$
K	kinetic energy	$\text{kg m}^2 \text{s}^{-2}$
\tilde{K}	ratio of average equilibrium concentrations in the zeolite margin to the one in the bulk gas phase	–
K_{H}	Henry coefficient	$\text{mol kg}^{-1} \text{m}^{-2} \text{s}$
l	length or width	m
l	index variable	–
L	dimensionless coefficient [$\equiv (\delta/2)\alpha/D$]	–
m	mass	kg
m	index variable	–
m_i	mass of a single atom or molecule of type i	kg
M_{\parallel}	magnetization parallel to an applied field	A m^{-1}
M_{\perp}	magnetization orthogonal to an applied field	A m^{-1}
n	index parameter	–
n	length of molecule chain	–
$n_i(t)$	dynamical variable indicating whether or not a molecule is in a certain state (here: i)	–
N	number of atoms and molecules	–

To be continued on next page.

Symbol	Description	Units
$\mathcal{N}(i)$	probability density of state i	–
N_{atoms}	number of atoms	–
N_A	Avogadro constant ($6.02214 \cdot 10^{23}$)	mol ⁻¹
N_f	number of degrees of freedom	–
N_{groups}	number of groups	–
$N_{\text{hits}}(x, y, z)$	accumulated number of instances that a molecule was found in a small voxel around position (x, y, z)	–
$N_{\text{hits}}(z, r_{\text{pore}})$	accumulated number of instances that a molecule was found in a small ring at z around the pore axis with an average radius of r_{pore}	–
$\bar{N}_{\text{hits}}(z_i \pm \Delta z)$	average number of instances that a molecule was found in bin i (i.e., within $z_i \pm \Delta z$)	–
N_i	number of steps, trials, cycles, etc. of type i	–
N_{samp}	number of samples, sampling or measurement points	–
N_{slabs}	number of slabs	–
N_{steps}	number of time steps	–
N_t	number of discrete time instances in a sampling or fitting context	–
$N_{\text{UC}, \xi}$	number of (full) unit cells aligned in the simulation box along Cartesian ξ coordinate	–
N_z	number of discrete spatial points (here: along z) in a sampling or fitting context	–
N_ν	number of members in group ν	–
o	index parameter	–
$\mathcal{O}(N^i)$	terms of order N^i or smaller	–
p	pressure	kg m ⁻¹ s ⁻²
\mathbf{p}	momentum vector	–
p^*	reduced pressure ($\equiv p/p_{\text{crit}}$)	–

To be continued on next page.

Symbol	Description	Units
\mathbf{p}^N	momentum space	–
\mathbf{p}_i^N	a point in momentum space	–
P	(residence) probability (distribution)	–
P_i^\ddagger	residence probability of a molecule to be found at barrier i [$\equiv P(q_i^\ddagger)$]	–
P_A^\ddagger	committor probability to arrive in A	–
P_{enter}	fraction of all molecules hitting on the external crystal surface that eventually enter the pore space	–
P_{open}	fraction of open pore entrances	–
P_y	relative occurrence of crystal defects, allowing a molecule to jump into a parallel, ideally not accessible channel	–
q	process, reaction, or transport coordinate	m
\dot{q}	time derivative of transport coordinate	m s ⁻¹
Q	canonical partition function	–
r	distance	m
\mathbf{r}	coordinate vector	–
\mathbf{r}^N	configuration space	–
\mathbf{r}_i^N	a point in configuration space	–
r_{cutoff}	cutoff distance for interaction calculation	m
$r_{\text{cutoff}}^{\text{LAIFC}}$	cutoff distance for LA IFC thermostat model collisions	m
$r_{i,j}$	distance between atoms or beads i and j	m
R	ideal gas constant (8.3144622)	kg m ² s ⁻² × K ⁻¹ mol ⁻¹
R_{ads}	adsorption transport resistance	m ⁻² s
R_{intra}	intracrystalline transport resistance	m ⁻² s
\mathbf{s}	space coordinate	–
S	entropy	kg m ² s ⁻² K ⁻¹

To be continued on next page.

Symbol	Description	Units
S_{switch}	parameter in continuum calculations (= 0 for tracer release; = 1 for tracer uptake)	–
t	time	s
Δt	time step size	s
t_i	discrete time point	s
t_{interval}	time interval between two PFG NMR pulses	s
t_{pulse}	length of each PFG NMR pulse	s
T	temperature	K
T^*	reduced temperature ($\equiv T/T_{\text{crit}}$)	–
$u_{j,k,\dots}^i$	interaction energy of type i between atoms or beads j, k, \dots	kg m ² s ⁻²
U	potential energy	kg m ² s ⁻²
U^i	entire sum of interaction energy type i	kg m ² s ⁻²
v	velocity	m s ⁻¹
\mathbf{v}	velocity vector	–
v_i	velocity of an atom or molecule of type i	m s ⁻¹
V	volume	m ³
w_i	Rosenbluth weight of atom i	–
W	work	kg m ² s ⁻²
W_{ros}	Rosenbluth factor	–
$\mathcal{W}_{\text{ros},A}$	normalized Rosenbluth factor for molecule type A	–
x	Cartesian x coordinate	m
\tilde{x}_i	mole fraction of species i (fluid phase)	–
X	dimensionless coefficient [$\equiv K_{\text{H}}(n, T)/K_{\text{H}}(n, T_{\text{ref}})$]	–
y	Cartesian y coordinate	m
\tilde{y}_i	mole fraction of species i (adsorbed phase)	–
z	Cartesian z coordinate	m

To be continued on next page.

Symbol	Description	Units
z_k	discrete point along Cartesian z coordinate	m
Z	configurational part of canonical partition function	–
Greek Symbols		
α	surface permeability	m s ⁻¹
$\alpha(i \rightarrow j)$	probability of performing a trial move from state i to state j	–
α_S	tracer-exchange surface permeability	m s ⁻¹
$\tilde{\alpha}_S^{\text{1step}}$	simplified one-step α_S prediction of this work ($\kappa_{\text{surf}} = 1$)	m s ⁻¹
β	reciprocal temperature [$\equiv 1/(k_B T)$]	kg ⁻¹ m ⁻² s ²
γ_i	i -th positive root of $\gamma \tan \gamma = L$	–
$\hat{\gamma}$	gyromagnetic ratio	A s kg ⁻¹
Γ	thermodynamic correction factor ($\equiv \partial \ln f / \partial \ln c _T$)	–
Γ^{LAIFC}	isotropic LA IFC collision frequency	s ⁻¹
$\Gamma_{xy}^{\text{LAIFC}}$	orthogonal LA IFC collision frequency	s ⁻¹
Γ_z^{LAIFC}	parallel LA IFC collision frequency	s ⁻¹
δ	thickness	m
δ	incremental change	–
$\hat{\delta}(x)$	Dirac delta function [$\hat{\delta}(x) = \infty$ if $x = 0$, $\hat{\delta}(x) = 0$ otherwise]	–
δ_{crit}	critical host thickness (crystal, membrane, sheet)	m
Δ	increment or difference of some variable	–
ε	Lennard–Jones well depth	kg m ² s ⁻²
η_i	i -th torsional potential constant	kg m ² s ⁻²
θ	loading or cage occupancy	molecules $\times (\text{cage})^{-1}$
θ_i	loading of species i	molecules $\times (\text{unit cell})^{-1}$

To be continued on next page.

Symbol	Description	Units
κ	transmission coefficient	–
$\kappa(t)$	reactive flux correlation function	–
$\kappa^+(t)$	positive contribution to reactive flux correlation function (i.e., molecules starting with velocity pointing toward target state or cage)	–
$\kappa^-(t)$	negative contribution to reactive flux correlation function (i.e., molecules starting with velocity pointing away from target state or cage)	–
Λ	thermal de Broglie wavelength	m
μ	chemical potential	kg m ² s ⁻² mol ⁻¹
ν	index variable	–
ξ	one of the three Cartesian coordinates x , y , or z	m
Ξ	grand-canonical partition function	–
π	3.141592653589793238	–
$\pi(i \rightarrow j)$	transition probability from state i to state j	–
ρ	(solute or tracer) density	mol m ⁻³
σ	Lennard–Jones zero-potential distance	m
σ_{rel}	averaged relative sample standard deviation	–
τ_{col}	characteristic time in addition to τ_{mol} when density and thus collisions increase	s
τ_{hop}	characteristic time for an entire molecule transition from one site to an adjacent one	s
τ_{mol}	characteristic short-term time of a molecule transition from a dividing surface to either of the neighboring sites	s
$\tilde{\phi}_{i,j,k,l}$	dihedral angle between atoms or beads i , j , k , and l	rad

To be continued on next page.

Symbol	Description	Units
$\varphi_{i,j,k}$	bond angle between atoms or beads i , j , and k	rad
χ_g	random number from a Gaussian distribution with zero mean and unit variance	–
ψ	PFG NMR spin echo attenuation	–
Ω	number of microstates in the micro-canonical ensemble	–

Superscript	Description
‡	reference to a (free) energy barrier
1step	related to transport or exchange proceeding via a single boundary layer region
2step	related to transport or exchange proceeding via both boundary layer regions
bend	reference to bond-angle bending
cut	indicates cutting a potential
def	reference to a property caused by defects and thus departure from ideality
DCTST	reference to dynamically corrected transition state theory
elec	reference to electrostatic interaction
extern	reference to external interaction contribution
FPT	reference to first-passage times approach
int	reference to an integral analytical diffusion solution
intern	reference to internal interaction contribution
intrin	reference to an intrinsic property (i.e., unbiased by nonidealities such as defects)
IG	reference to ideal gas state
loc	reference to a spatially resolved (i.e., local) analytical diffusion solution
LJ	reference to Lennard–Jones interaction

To be continued on next page.

Superscript	Description
restart	indicates a value obtained from restarting a simulation instead of generating an entirely fresh starting configuration
shift	indicates shifting of a potential
tors	reference to bond twisting (torsion)
tot	reference to the entire sum of some composite property
TECC	reference to tracer-exchange continuum calculation
TrMD	related to transient molecular dynamics
vib	reference to bond vibration

Subscript	Description
ads	related to an adsorption process (molecule enters pore space)
A → B	related to a transition from cage A to cage B
backw	related to a backward hop (i.e., $q \equiv -\xi$)
bath	related to a heat bath
box	related to the simulation box
B → A	related to a transition from cage B to cage A
cage	related to a zeolite cage or adsorption site/channel intersection within the zeolite structure
crit	indicates a critical property
CV	related to a control volume
del	reference to an MC molecule deletion move
des	related to a desorption process (molecule leaves pore space)
displ	reference to an MC molecule displacement trial move
eq	indicates an equilibrium (time-invariant) property
feed	related to the feed side of a membrane process
final	related to a final state (e.g., guest uptake into a nano-sheet)
forw	related to a forward hop (i.e., $q \equiv +\xi$)
gas	related to the bulk gas phase or to the dividing surface between gas phase and surface adsorption layer

To be continued on next page.

Subscript	Description
init	related to an initial state
ins	reference to an MC molecule insertion move
ins + del	reference to both MC insertion and deletion moves
l	reference to the left surface of a (plane) zeolite crystal or membrane
lay	related to the surface adsorption layer (region around the external surface)
marg	related to the zeolite margin (outermost cage)
MD	reference to molecular dynamics
plat	indicates a plateau value
pore	related to a pore, to the pore axis, or to a pore atom
r	reference to the right surface of a (plane) zeolite crystal or membrane
recr	reference to barrier recrossing
regr	reference to an MC molecule regrow trial move
ref	indicates a reference value
res	related to a (hypothetical, infinite) gas reservoir
rot	reference to an MC molecule rotation trial move
sat	indicates a saturation value
slab	related to a slab of a membrane or nanosheet
surf	related to the surface separating the surface adsorption layer and the zeolite margin
surf + gas	related to hopping through both subregions of the boundary layer (i.e., surface adsorption layer and zeolite margin)
succ	reference to successful barrier passing
UC	related to the unit cell
wind	related to a zeolite window
x	related to Cartesian x coordinate
y	related to Cartesian y coordinate
z	related to Cartesian z coordinate
zeol	related to the bulk zeolite space or to a property resulting from the repetitive crystal structure

To be continued on next page.

Subscript	Description
Greek Subscripts	
ξ	related to any one of the three Cartesian coordinates x , y , or z
Accents	
–	indicates an average

A.2 List of Abbreviations

Abbreviation	Meaning
8R	eight ring
CBMC	configurational-bias Monte Carlo
CCS	carbon capture and storage
CLSM	confocal laser scanning microscopy
CNT	carbon nanotube
CP	committor probability
CV	control volume
DCTST	dynamically corrected transition state theory
DCV GCMD	dual control volume grand-canonical molecular dynamics
DFT	density functional theory
EMD	equilibrium molecular dynamics
FCC	fluid catalytic cracking
FCS	fluorescence correlation spectroscopy
FPT	first-passage time
GC	grand canonical
GCMC	grand-canonical Monte Carlo
IFM	interference microscopy
IRM	infrared microscopy
IUPAC	International Union for Pure and Applied Chemistry

To be continued on next page.

Abbreviation	Meaning
IZA	International Zeolite Association
LA IFC	Lowe–Andersen fluid-interface collision
MC	Monte Carlo
MD	molecular dynamics
MOF	metal–organic framework
MS	Maxwell–Stefan
MSD	mean squared displacement
NEMD	nonequilibrium molecular dynamics
NHC	Nosé–Hoover chain
NMR	nuclear magnetic resonance
PBU	primary building unit
PFM NMR	pulsed field gradient nuclear magnetic resonance
QM/MM	quantum mechanics/molecular mechanics
RF	reactive flux
RFCF	reactive flux correlation function
SBU	secondary building unit
TrapPE	transferable potentials for phase equilibria
TrMD	transient molecular dynamics
TE	tracer exchange
TECC	tracer-exchange continuum calculation
TST	transition state theory
UA	united atom
UC	unit cell
vdW-DF	van der Waals density functional
ZLC	zero-length column

Zeolite Unit Cells

B

Appendix B provides the unit-cell definitions of all zeolite structures used in the present work. The structures were siliceous and thus converted into pure silica materials when the original structure was in fact of different composition. In such cases, it has to be stressed that no further structure optimization was performed.

B.1 AFI from Qiu *et al.*

This structure was taken from Qiu *et al.*⁶¹
Note that the original monoclinic unit cell was converted
to an orthorhombic unit cell for computational convenience;
compare also Reference 127.

$$\hat{a}_0 = 2.3774 \text{ nm} \quad \hat{b}_0 = 1.3726 \text{ nm} \quad \hat{c}_0 = 0.8484 \text{ nm}$$

Si	0.2262	0.1021	0.0780	Si	0.3358	0.2117	0.5780
Si	0.7262	0.6021	0.0780	Si	0.8358	0.7117	0.5780
Si	0.2288	0.1089	0.4500	Si	0.3311	0.2112	0.9500
Si	0.7288	0.6089	0.4500	Si	0.8312	0.7111	0.9500
O	0.2105	0.0032	0.0280	O	0.3931	0.1858	0.5280
O	0.7105	0.5032	0.0280	O	0.8931	0.6858	0.5280
O	0.2278	0.1035	0.2500	O	0.3344	0.2101	0.7500
O	0.7278	0.6035	0.2500	O	0.8344	0.7101	0.7500
O	0.1835	0.1749	0.0260	O	0.3208	0.3122	0.5260
O	0.6835	0.6749	0.0260	O	0.8208	0.8122	0.5260
O	0.2842	0.1284	0.0140	O	0.2937	0.1379	0.5140
O	0.7842	0.6284	0.0140	O	0.7937	0.6379	0.5140
Si	0.3358	0.7883	0.0780	Si	0.4380	0.8903	0.5780
Si	0.8358	0.2883	0.0780	Si	0.9379	0.3903	0.5780
Si	0.3311	0.7889	0.4500	Si	0.4400	0.8977	0.9500
Si	0.8312	0.2888	0.4500	Si	0.9400	0.3977	0.9500
O	0.3931	0.8142	0.0280	O	0.3963	0.8174	0.5280
O	0.8931	0.3141	0.0280	O	0.8963	0.3174	0.5280
O	0.3344	0.7899	0.2500	O	0.4379	0.8933	0.7500

To be continued on next page.

O	0.8344	0.2899	0.2500	O	0.9378	0.3933	0.7500
O	0.3208	0.6878	0.0260	O	0.4957	0.8627	0.5260
O	0.8208	0.1878	0.0260	O	0.9957	0.3627	0.5260
O	0.2937	0.8621	0.0140	O	0.4221	0.9905	0.5140
O	0.7937	0.3621	0.0140	O	0.9221	0.4905	0.5140
Si	0.4380	0.1096	0.0780	Si	0.2262	0.8979	0.5780
Si	0.9379	0.6097	0.0780	Si	0.7262	0.3979	0.5780
Si	0.4400	0.1023	0.4500	Si	0.2288	0.8911	0.9500
Si	0.9400	0.6023	0.4500	Si	0.7288	0.3911	0.9500
O	0.3963	0.1827	0.0280	O	0.2105	0.9968	0.5280
O	0.8963	0.6826	0.0280	O	0.7105	0.4968	0.5280
O	0.4379	0.1066	0.2500	O	0.2278	0.8965	0.7500
O	0.9378	0.6067	0.2500	O	0.7278	0.3966	0.7500
O	0.4957	0.1373	0.0260	O	0.1835	0.8251	0.5260
O	0.9957	0.6373	0.0260	O	0.6835	0.3251	0.5260
O	0.4221	0.0095	0.0140	O	0.2842	0.8716	0.5140
O	0.9221	0.5095	0.0140	O	0.7842	0.3716	0.5140
Si	0.2738	0.3979	0.0780	Si	0.1641	0.2883	0.5780
Si	0.7738	0.8979	0.0780	Si	0.6642	0.7883	0.5780
Si	0.2712	0.3911	0.4500	Si	0.1689	0.2888	0.9500
Si	0.7712	0.8911	0.4500	Si	0.6688	0.7889	0.9500
O	0.2895	0.4968	0.0280	O	0.1069	0.3141	0.5280
O	0.7895	0.9968	0.0280	O	0.6069	0.8142	0.5280
O	0.2722	0.3966	0.2500	O	0.1656	0.2899	0.7500
O	0.7722	0.8965	0.2500	O	0.6656	0.7899	0.7500
O	0.3165	0.3251	0.0260	O	0.1792	0.1878	0.5260
O	0.8165	0.8251	0.0260	O	0.6792	0.6878	0.5260
O	0.2158	0.3716	0.0140	O	0.2063	0.3621	0.5140
O	0.7158	0.8716	0.0140	O	0.7063	0.8621	0.5140
Si	0.1641	0.7117	0.0780	Si	0.0621	0.6097	0.5780
Si	0.6642	0.2117	0.0780	Si	0.5621	0.1096	0.5780
Si	0.1689	0.7111	0.4500	Si	0.0600	0.6023	0.9500
Si	0.6688	0.2112	0.4500	Si	0.5600	0.1023	0.9500
O	0.1069	0.6858	0.0280	O	0.1037	0.6826	0.5280
O	0.6069	0.1858	0.0280	O	0.6037	0.1827	0.5280
O	0.1656	0.7101	0.2500	O	0.0621	0.6067	0.7500
O	0.6656	0.2101	0.2500	O	0.5622	0.1066	0.7500
O	0.1792	0.8122	0.0260	O	0.0043	0.6373	0.5260
O	0.6792	0.3122	0.0260	O	0.5043	0.1373	0.5260
O	0.2063	0.6379	0.0140	O	0.0779	0.5095	0.5140
O	0.7063	0.1379	0.0140	O	0.5779	0.0095	0.5140
Si	0.0621	0.3903	0.0780	Si	0.2738	0.6021	0.5780
Si	0.5621	0.8903	0.0780	Si	0.7738	0.1021	0.5780
Si	0.0600	0.3977	0.4500	Si	0.2712	0.6089	0.9500
Si	0.5600	0.8977	0.4500	Si	0.7712	0.1089	0.9500
O	0.1037	0.3174	0.0280	O	0.2895	0.5032	0.5280
O	0.6037	0.8174	0.0280	O	0.7895	0.0032	0.5280
O	0.0621	0.3933	0.2500	O	0.2722	0.6035	0.7500
O	0.5622	0.8933	0.2500	O	0.7722	0.1035	0.7500
O	0.0043	0.3627	0.0260	O	0.3165	0.6749	0.5260
O	0.5043	0.8627	0.0260	O	0.8165	0.1749	0.5260
O	0.0779	0.4905	0.0140	O	0.2158	0.6284	0.5140
O	0.5779	0.9905	0.0140	O	0.7158	0.1284	0.5140

B.2 ITE from Camblor *et al.*

This structure was taken from Camblor *et al.*⁶²

$$\hat{a}_0 = 2.0622 \text{ nm} \quad \hat{b}_0 = 0.9724 \text{ nm} \quad \hat{c}_0 = 1.9623 \text{ nm}$$

Si	0.3202	0.9570	0.1701	O	0.0978	0.2516	0.0287
Si	0.3202	0.0430	0.8299	O	0.0978	0.7484	0.9713
Si	0.6798	0.9570	0.3299	O	0.9022	0.2516	0.4713
Si	0.6798	0.0430	0.6701	O	0.9022	0.7484	0.5287
Si	0.6798	0.0430	0.8299	O	0.9022	0.7484	0.9713
Si	0.6798	0.9570	0.1701	O	0.9022	0.2516	0.0287
Si	0.3202	0.0430	0.6701	O	0.0978	0.7484	0.5287
Si	0.3202	0.9570	0.3299	O	0.0978	0.2516	0.4713
Si	0.8202	0.4570	0.1701	O	0.5978	0.7516	0.0287
Si	0.8202	0.5430	0.8299	O	0.5978	0.2484	0.9713
Si	0.1798	0.4570	0.3299	O	0.4022	0.7516	0.4713
Si	0.1798	0.5430	0.6701	O	0.4022	0.2484	0.5287
Si	0.1798	0.5430	0.8299	O	0.4022	0.2484	0.9713
Si	0.1798	0.4570	0.1701	O	0.4022	0.7516	0.0287
Si	0.8202	0.5430	0.6701	O	0.5978	0.2484	0.5287
Si	0.8202	0.4570	0.3299	O	0.5978	0.7516	0.4713
Si	0.0756	0.4067	0.0561	O	0.0000	0.4105	0.0718
Si	0.0756	0.5933	0.9439	O	0.0000	0.5895	0.9282
Si	0.9244	0.4067	0.4439	O	0.0000	0.4105	0.4282
Si	0.9244	0.5933	0.5561	O	0.0000	0.5895	0.5718
Si	0.9244	0.5933	0.9439	O	0.5000	0.9105	0.0718
Si	0.9244	0.4067	0.0561	O	0.5000	0.0895	0.9282
Si	0.0756	0.5933	0.5561	O	0.5000	0.9105	0.4282
Si	0.0756	0.4067	0.4439	O	0.5000	0.0895	0.5718
Si	0.5756	0.9067	0.0561	O	0.2148	0.1587	0.0569
Si	0.5756	0.0933	0.9439	O	0.2148	0.8413	0.9431
Si	0.4244	0.9067	0.4439	O	0.7852	0.1587	0.4431
Si	0.4244	0.0933	0.5561	O	0.7852	0.8413	0.5569
Si	0.4244	0.0933	0.9439	O	0.7852	0.8413	0.9431
Si	0.4244	0.9067	0.0561	O	0.7852	0.1587	0.0569
Si	0.5756	0.0933	0.5561	O	0.2148	0.8413	0.5569
Si	0.5756	0.9067	0.4439	O	0.2148	0.1587	0.4431
Si	0.2641	0.2255	0.1121	O	0.7148	0.6587	0.0569
Si	0.2641	0.7745	0.8879	O	0.7148	0.3413	0.9431
Si	0.7359	0.2255	0.3879	O	0.2852	0.6587	0.4431
Si	0.7359	0.7745	0.6121	O	0.2852	0.3413	0.5569
Si	0.7359	0.7745	0.8879	O	0.2852	0.3413	0.9431
Si	0.7359	0.2255	0.1121	O	0.2852	0.6587	0.0569
Si	0.2641	0.7745	0.6121	O	0.7148	0.3413	0.5569
Si	0.2641	0.2255	0.3879	O	0.7148	0.6587	0.4431
Si	0.7641	0.7255	0.1121	O	0.3870	0.9372	0.1288
Si	0.7641	0.2745	0.8879	O	0.3870	0.0628	0.8712
Si	0.2359	0.7255	0.3879	O	0.6130	0.9372	0.3712
Si	0.2359	0.2745	0.6121	O	0.6130	0.0628	0.6288
Si	0.2359	0.2745	0.8879	O	0.6130	0.0628	0.8712
Si	0.2359	0.7255	0.1121	O	0.6130	0.9372	0.1288
Si	0.7641	0.2745	0.6121	O	0.3870	0.0628	0.6288
Si	0.7641	0.7255	0.3879	O	0.3870	0.9372	0.3712
Si	0.1530	0.1551	0.0036	O	0.8870	0.4372	0.1288
Si	0.1530	0.8449	0.9964	O	0.8870	0.5628	0.8712

To be continued on next page.

Si	0.8470	0.1551	0.4964	O	0.1130	0.4372	0.3712
Si	0.8470	0.8449	0.5036	O	0.1130	0.5628	0.6288
Si	0.8470	0.8449	0.9964	O	0.1130	0.5628	0.8712
Si	0.8470	0.1551	0.0036	O	0.1130	0.4372	0.1288
Si	0.1530	0.8449	0.5036	O	0.8870	0.5628	0.6288
Si	0.1530	0.1551	0.4964	O	0.8870	0.4372	0.3712
Si	0.6530	0.6551	0.0036	O	0.2913	0.1093	0.1625
Si	0.6530	0.3449	0.9964	O	0.2913	0.8907	0.8375
Si	0.3470	0.6551	0.4964	O	0.7087	0.1093	0.3375
Si	0.3470	0.3449	0.5036	O	0.7087	0.8907	0.6625
Si	0.3470	0.3449	0.9964	O	0.7087	0.8907	0.8375
Si	0.3470	0.6551	0.0036	O	0.7087	0.1093	0.1625
Si	0.6530	0.3449	0.5036	O	0.2913	0.8907	0.6625
Si	0.6530	0.6551	0.4964	O	0.2913	0.1093	0.3375
O	0.3427	0.9419	0.2500	O	0.7913	0.6093	0.1625
O	0.3427	0.0581	0.7500	O	0.7913	0.3907	0.8375
O	0.6573	0.9419	0.2500	O	0.2087	0.6093	0.3375
O	0.6573	0.0581	0.7500	O	0.2087	0.3907	0.6625
O	0.8427	0.4419	0.2500	O	0.2087	0.3907	0.8375
O	0.8427	0.5581	0.7500	O	0.2087	0.6093	0.1625
O	0.1573	0.4419	0.2500	O	0.7913	0.3907	0.6625
O	0.1573	0.5581	0.7500	O	0.7913	0.6093	0.3375
O	0.2675	0.8515	0.1491	O	0.3275	0.2871	0.0695
O	0.2675	0.1485	0.8509	O	0.3275	0.7129	0.9305
O	0.7325	0.8515	0.3509	O	0.6725	0.2871	0.4305
O	0.7325	0.1485	0.6491	O	0.6725	0.7129	0.5695
O	0.7325	0.1485	0.8509	O	0.6725	0.7129	0.9305
O	0.7325	0.8515	0.1491	O	0.6725	0.2871	0.0695
O	0.2675	0.1485	0.6491	O	0.3275	0.7129	0.5695
O	0.2675	0.8515	0.3509	O	0.3275	0.2871	0.4305
O	0.7675	0.3515	0.1491	O	0.8275	0.7871	0.0695
O	0.7675	0.6485	0.8509	O	0.8275	0.2129	0.9305
O	0.2325	0.3515	0.3509	O	0.1725	0.7871	0.4305
O	0.2325	0.6485	0.6491	O	0.1725	0.2129	0.5695
O	0.2325	0.6485	0.8509	O	0.1725	0.2129	0.9305
O	0.2325	0.3515	0.1491	O	0.1725	0.7871	0.0695
O	0.7675	0.6485	0.6491	O	0.8275	0.2129	0.5695
O	0.7675	0.3515	0.3509	O	0.8275	0.7871	0.4305
O	0.0996	0.5000	0.0000	O	0.1308	0.0000	0.0000
O	0.9004	0.5000	0.5000	O	0.8692	0.0000	0.5000
O	0.9004	0.5000	0.0000	O	0.8692	0.0000	0.0000
O	0.0996	0.5000	0.5000	O	0.1308	0.0000	0.5000
O	0.5996	0.0000	0.0000	O	0.6308	0.5000	0.0000
O	0.4004	0.0000	0.5000	O	0.3692	0.5000	0.5000
O	0.4004	0.0000	0.0000	O	0.3692	0.5000	0.0000
O	0.5996	0.0000	0.5000	O	0.6308	0.5000	0.5000

B.3 ITE from IZA

This structure was taken from Baerlocher and McCusker²²

$$\hat{a}_0 = 2.0753 \text{ nm} \quad \hat{b}_0 = 0.9804 \text{ nm} \quad \hat{c}_0 = 2.0009 \text{ nm}$$

O	0.2614	0.8673	0.1438	O	0.8270	0.7763	0.0588
O	0.2614	0.1327	0.8562	O	0.8270	0.2237	0.9412
O	0.7386	0.8673	0.3562	O	0.1730	0.7763	0.4412
O	0.7386	0.1327	0.6438	O	0.1730	0.2237	0.5588
O	0.7386	0.1327	0.8562	O	0.1730	0.2237	0.9412
O	0.7386	0.8673	0.1438	O	0.1730	0.7763	0.0588
O	0.2614	0.1327	0.6438	O	0.8270	0.2237	0.5588
O	0.2614	0.8673	0.3562	O	0.8270	0.7763	0.4412
O	0.7614	0.3673	0.1438	O	0.2118	0.1581	0.0637
O	0.7614	0.6327	0.8562	O	0.2118	0.8419	0.9363
O	0.2386	0.3673	0.3562	O	0.7882	0.1581	0.4363
O	0.2386	0.6327	0.6438	O	0.7882	0.8419	0.5637
O	0.2386	0.6327	0.8562	O	0.7882	0.8419	0.9363
O	0.2386	0.3673	0.1438	O	0.7882	0.1581	0.0637
O	0.7614	0.6327	0.6438	O	0.2118	0.8419	0.5637
O	0.7614	0.3673	0.3562	O	0.2118	0.1581	0.4363
O	0.3314	0.9350	0.2500	O	0.7118	0.6581	0.0637
O	0.3314	0.0650	0.7500	O	0.7118	0.3419	0.9363
O	0.6686	0.9350	0.2500	O	0.2882	0.6581	0.4363
O	0.6686	0.0650	0.7500	O	0.2882	0.3419	0.5637
O	0.8314	0.4350	0.2500	O	0.2882	0.3419	0.9363
O	0.8314	0.5650	0.7500	O	0.2882	0.6581	0.0637
O	0.1686	0.4350	0.2500	O	0.7118	0.3419	0.5637
O	0.1686	0.5650	0.7500	O	0.7118	0.6581	0.4363
O	0.2941	0.1262	0.1640	O	0.1278	0.0000	0.0000
O	0.2941	0.8738	0.8360	O	0.8722	0.0000	0.5000
O	0.7059	0.1262	0.3360	O	0.8722	0.0000	0.0000
O	0.7059	0.8738	0.6640	O	0.1278	0.0000	0.5000
O	0.7059	0.8738	0.8360	O	0.6278	0.5000	0.0000
O	0.7059	0.1262	0.1640	O	0.3722	0.5000	0.5000
O	0.2941	0.8738	0.6640	O	0.3722	0.5000	0.0000
O	0.2941	0.1262	0.3360	O	0.6278	0.5000	0.5000
O	0.7941	0.6262	0.1640	Si	0.3175	0.9685	0.1717
O	0.7941	0.3738	0.8360	Si	0.3175	0.0315	0.8283
O	0.2059	0.6262	0.3360	Si	0.6825	0.9685	0.3283
O	0.2059	0.3738	0.6640	Si	0.6825	0.0315	0.6717
O	0.2059	0.3738	0.8360	Si	0.6825	0.0315	0.8283
O	0.2059	0.6262	0.1640	Si	0.6825	0.9685	0.1717
O	0.7941	0.3738	0.6640	Si	0.3175	0.0315	0.6717
O	0.7941	0.6262	0.3360	Si	0.3175	0.9685	0.3283
O	0.3833	0.9457	0.1288	Si	0.8175	0.4685	0.1717
O	0.3833	0.0543	0.8712	Si	0.8175	0.5315	0.8283
O	0.6167	0.9457	0.3712	Si	0.1825	0.4685	0.3283
O	0.6167	0.0543	0.6288	Si	0.1825	0.5315	0.6717
O	0.6167	0.0543	0.8712	Si	0.1825	0.5315	0.8283
O	0.6167	0.9457	0.1288	Si	0.1825	0.4685	0.1717
O	0.3833	0.0543	0.6288	Si	0.8175	0.5315	0.6717
O	0.3833	0.9457	0.3712	Si	0.8175	0.4685	0.3283
O	0.8833	0.4457	0.1288	Si	0.0767	0.4032	0.0620
O	0.8833	0.5543	0.8712	Si	0.0767	0.5968	0.9380

To be continued on next page.

O	0.1167	0.4457	0.3712	Si	0.9233	0.4032	0.4380
O	0.1167	0.5543	0.6288	Si	0.9233	0.5968	0.5620
O	0.1167	0.5543	0.8712	Si	0.9233	0.5968	0.9380
O	0.1167	0.4457	0.1288	Si	0.9233	0.4032	0.0620
O	0.8833	0.5543	0.6288	Si	0.0767	0.5968	0.5620
O	0.8833	0.4457	0.3712	Si	0.0767	0.4032	0.4380
O	0.0987	0.5000	0.0000	Si	0.5767	0.9032	0.0620
O	0.9013	0.5000	0.5000	Si	0.5767	0.0968	0.9380
O	0.9013	0.5000	0.0000	Si	0.4233	0.9032	0.4380
O	0.0987	0.5000	0.5000	Si	0.4233	0.0968	0.5620
O	0.5987	0.0000	0.0000	Si	0.4233	0.0968	0.9380
O	0.4013	0.0000	0.5000	Si	0.4233	0.9032	0.0620
O	0.4013	0.0000	0.0000	Si	0.5767	0.0968	0.5620
O	0.5987	0.0000	0.5000	Si	0.5767	0.9032	0.4380
O	0.0000	0.4222	0.0758	Si	0.2677	0.2322	0.1076
O	0.0000	0.5778	0.9242	Si	0.2677	0.7678	0.8924
O	0.0000	0.4222	0.4242	Si	0.7323	0.2322	0.3924
O	0.0000	0.5778	0.5758	Si	0.7323	0.7678	0.6076
O	0.5000	0.9222	0.0758	Si	0.7323	0.7678	0.8924
O	0.5000	0.0778	0.9242	Si	0.7323	0.2322	0.1076
O	0.5000	0.9222	0.4242	Si	0.2677	0.7678	0.6076
O	0.5000	0.0778	0.5758	Si	0.2677	0.2322	0.3924
O	0.0920	0.2447	0.0436	Si	0.7677	0.7322	0.1076
O	0.0920	0.7553	0.9564	Si	0.7677	0.2678	0.8924
O	0.9080	0.2447	0.4564	Si	0.2323	0.7322	0.3924
O	0.9080	0.7553	0.5436	Si	0.2323	0.2678	0.6076
O	0.9080	0.7553	0.9564	Si	0.2323	0.2678	0.8924
O	0.9080	0.2447	0.0436	Si	0.2323	0.7322	0.1076
O	0.0920	0.7553	0.5436	Si	0.7677	0.2678	0.6076
O	0.0920	0.2447	0.4564	Si	0.7677	0.7322	0.3924
O	0.5920	0.7447	0.0436	Si	0.1512	0.1565	0.0121
O	0.5920	0.2553	0.9564	Si	0.1512	0.8435	0.9879
O	0.4080	0.7447	0.4564	Si	0.8488	0.1565	0.4879
O	0.4080	0.2553	0.5436	Si	0.8488	0.8435	0.5121
O	0.4080	0.2553	0.9564	Si	0.8488	0.8435	0.9879
O	0.4080	0.7447	0.0436	Si	0.8488	0.1565	0.0121
O	0.5920	0.2553	0.5436	Si	0.1512	0.8435	0.5121
O	0.5920	0.7447	0.4564	Si	0.1512	0.1565	0.4879
O	0.3270	0.2763	0.0588	Si	0.6512	0.6565	0.0121
O	0.3270	0.7237	0.9412	Si	0.6512	0.3435	0.9879
O	0.6730	0.2763	0.4412	Si	0.3488	0.6565	0.4879
O	0.6730	0.7237	0.5588	Si	0.3488	0.3435	0.5121
O	0.6730	0.7237	0.9412	Si	0.3488	0.3435	0.9879
O	0.6730	0.2763	0.0588	Si	0.3488	0.6565	0.0121
O	0.3270	0.7237	0.5588	Si	0.6512	0.3435	0.5121
O	0.3270	0.2763	0.4412	Si	0.6512	0.6565	0.4879

B.4 LTA from Corma *et al.*

This structure was taken from Corma *et al.*³⁵

$$\hat{a}_0 = 1.1867 \text{ nm} \quad \hat{b}_0 = 1.1867 \text{ nm} \quad \hat{c}_0 = 1.1867 \text{ nm}$$

O	0.0000	0.2179	0.5000	O	0.0000	0.2939	0.2939
O	0.0000	0.5000	0.2179	O	0.0000	0.7061	0.2939
O	0.0000	0.5000	0.7821	O	0.0000	0.2939	0.7061
O	0.5000	0.2179	0.0000	O	0.2939	0.2939	0.0000
O	0.7821	0.0000	0.5000	O	0.7061	0.2939	0.0000
O	0.2179	0.0000	0.5000	O	0.7061	0.0000	0.2939
O	0.5000	0.0000	0.2179	O	0.2939	0.0000	0.2939
O	0.2179	0.5000	0.0000	O	0.7061	0.7061	0.0000
O	0.7821	0.5000	0.0000	O	0.2939	0.0000	0.7061
O	0.5000	0.0000	0.7821	O	0.7061	0.0000	0.7061
O	0.0000	0.7821	0.5000	O	0.2939	0.7061	0.0000
O	0.5000	0.7821	0.0000	O	0.0000	0.7061	0.7061
O	0.1098	0.1098	0.3429	Si	0.0000	0.1847	0.3683
O	0.1098	0.6571	0.1098	Si	0.0000	0.6317	0.1847
O	0.1098	0.3429	0.8902	Si	0.0000	0.3683	0.8153
O	0.3429	0.1098	0.8902	Si	0.3683	0.1847	0.0000
O	0.6571	0.1098	0.1098	Si	0.6317	0.1847	0.0000
O	0.8902	0.1098	0.3429	Si	0.8153	0.0000	0.3683
O	0.1098	0.8902	0.3429	Si	0.1847	0.0000	0.3683
O	0.3429	0.1098	0.1098	Si	0.3683	0.0000	0.1847
O	0.1098	0.3429	0.1098	Si	0.1847	0.3683	0.0000
O	0.8902	0.6571	0.1098	Si	0.8153	0.6317	0.0000
O	0.3429	0.8902	0.8902	Si	0.3683	0.0000	0.8153
O	0.8902	0.3429	0.8902	Si	0.1847	0.0000	0.3683
O	0.6571	0.8902	0.1098	Si	0.8153	0.3683	0.0000
O	0.6571	0.1098	0.8902	Si	0.6317	0.0000	0.1847
O	0.1098	0.6571	0.8902	Si	0.1847	0.6317	0.0000
O	0.1098	0.8902	0.6571	Si	0.0000	0.8153	0.6317
O	0.8902	0.1098	0.6571	Si	0.0000	0.1847	0.6317
O	0.8902	0.8902	0.3429	Si	0.0000	0.8153	0.3683
O	0.1098	0.1098	0.6571	Si	0.1847	0.0000	0.6317
O	0.8902	0.8902	0.6571	Si	0.8153	0.0000	0.6317
O	0.3429	0.8902	0.1098	Si	0.3683	0.8153	0.0000
O	0.6571	0.8902	0.8902	Si	0.6317	0.8153	0.0000
O	0.8902	0.3429	0.1098	Si	0.0000	0.3683	0.1847
O	0.8902	0.6571	0.8902	Si	0.0000	0.6317	0.8153

B.5 LTA from IZA

This structure was taken from Baerlocher and McCusker²²

$$\hat{a}_0 = 1.1919 \text{ nm} \quad \hat{b}_0 = 1.1919 \text{ nm} \quad \hat{c}_0 = 1.1919 \text{ nm}$$

O	0.0000	0.2122	0.5000	O	0.0000	0.2967	0.2967
O	0.0000	0.5000	0.2122	O	0.0000	0.7033	0.2967
O	0.0000	0.5000	0.7878	O	0.0000	0.2967	0.7033
O	0.5000	0.2122	0.0000	O	0.2967	0.2967	0.0000
O	0.7878	0.0000	0.5000	O	0.7033	0.2967	0.0000
O	0.2122	0.0000	0.5000	O	0.7033	0.0000	0.2967
O	0.5000	0.0000	0.2122	O	0.2967	0.0000	0.2967
O	0.2122	0.5000	0.0000	O	0.7033	0.7033	0.0000
O	0.7878	0.5000	0.0000	O	0.2967	0.0000	0.7033
O	0.5000	0.0000	0.7878	O	0.7033	0.0000	0.7033
O	0.0000	0.7878	0.5000	O	0.2967	0.7033	0.0000
O	0.5000	0.7878	0.0000	O	0.0000	0.7033	0.7033
O	0.1103	0.1103	0.3384	Si	0.0000	0.1823	0.3684
O	0.1103	0.6616	0.1103	Si	0.0000	0.6316	0.1823
O	0.1103	0.3384	0.8897	Si	0.0000	0.3684	0.8177
O	0.3384	0.1103	0.8897	Si	0.3684	0.1823	0.0000
O	0.6616	0.1103	0.1103	Si	0.6316	0.1823	0.0000
O	0.8897	0.1103	0.3384	Si	0.8177	0.0000	0.3684
O	0.1103	0.8897	0.3384	Si	0.1823	0.0000	0.3684
O	0.3384	0.1103	0.1103	Si	0.3684	0.0000	0.1823
O	0.1103	0.3384	0.1103	Si	0.1823	0.3684	0.0000
O	0.8897	0.6616	0.1103	Si	0.8177	0.6316	0.0000
O	0.3384	0.8897	0.8897	Si	0.3684	0.0000	0.8177
O	0.8897	0.3384	0.8897	Si	0.8177	0.3684	0.0000
O	0.6616	0.8897	0.1103	Si	0.6316	0.0000	0.1823
O	0.6616	0.1103	0.8897	Si	0.6316	0.0000	0.8177
O	0.1103	0.6616	0.8897	Si	0.1823	0.6316	0.0000
O	0.1103	0.8897	0.6616	Si	0.0000	0.8177	0.6316
O	0.8897	0.1103	0.6616	Si	0.0000	0.1823	0.6316
O	0.8897	0.8897	0.3384	Si	0.0000	0.8177	0.3684
O	0.1103	0.1103	0.6616	Si	0.1823	0.0000	0.6316
O	0.8897	0.8897	0.6616	Si	0.8177	0.0000	0.6316
O	0.3384	0.8897	0.1103	Si	0.3684	0.8177	0.0000
O	0.6616	0.8897	0.8897	Si	0.6316	0.8177	0.0000
O	0.8897	0.3384	0.1103	Si	0.0000	0.3684	0.1823
O	0.8897	0.6616	0.8897	Si	0.0000	0.6316	0.8177

B.6 LTA from Pluth and Smith

This structure was taken from Pluth and Smith³⁶

$$\hat{a}_0 = 2.4555 \text{ nm} \quad \hat{b}_0 = 2.4555 \text{ nm} \quad \hat{c}_0 = 2.4555 \text{ nm}$$

Si	0.0000	0.0932	0.1850	Si	0.5000	0.0932	0.6850
Si	0.0000	0.1872	0.0904	Si	0.5000	0.1872	0.5904
O	0.0000	0.1137	0.2466	O	0.5000	0.1137	0.7466
O	0.0000	0.1446	0.1459	O	0.5000	0.1446	0.6459
O	0.0538	0.0587	0.1715	O	0.5538	0.0587	0.6715
Si	0.0000	0.9068	0.1850	Si	0.5000	0.9068	0.6850
Si	0.0000	0.8128	0.0904	Si	0.5000	0.8128	0.5904
O	0.0000	0.8863	0.2466	O	0.5000	0.8863	0.7466
O	0.0000	0.8554	0.1459	O	0.5000	0.8554	0.6459
O	0.9462	0.9414	0.1715	O	0.4462	0.9414	0.6715
Si	0.0000	0.0932	0.8150	Si	0.5000	0.0932	0.3150
Si	0.0000	0.1872	0.9096	Si	0.5000	0.1872	0.4096
O	0.0000	0.1137	0.7534	O	0.5000	0.1137	0.2534
O	0.0000	0.1446	0.8541	O	0.5000	0.1446	0.3541
O	0.9462	0.0587	0.8285	O	0.4462	0.0587	0.3285
Si	0.0000	0.9068	0.8150	Si	0.5000	0.9068	0.3150
Si	0.0000	0.8128	0.9096	Si	0.5000	0.8128	0.4096
O	0.0000	0.8863	0.7534	O	0.5000	0.8863	0.2534
O	0.0000	0.8554	0.8541	O	0.5000	0.8554	0.3541
O	0.0538	0.9414	0.8285	O	0.5538	0.9414	0.3285
Si	0.1850	0.0000	0.0932	Si	0.6850	0.0000	0.5932
Si	0.0904	0.0000	0.1872	Si	0.5904	0.0000	0.6872
O	0.2466	0.0000	0.1137	O	0.7466	0.0000	0.6137
O	0.1459	0.0000	0.1446	O	0.6459	0.0000	0.6446
O	0.1715	0.0538	0.0587	O	0.6715	0.0538	0.5586
Si	0.1850	0.0000	0.9068	Si	0.6850	0.0000	0.4068
Si	0.0904	0.0000	0.8128	Si	0.5904	0.0000	0.3129
O	0.2466	0.0000	0.8863	O	0.7466	0.0000	0.3863
O	0.1459	0.0000	0.8554	O	0.6459	0.0000	0.3554
O	0.1715	0.9462	0.9414	O	0.6715	0.9462	0.4414
Si	0.8150	0.0000	0.0932	Si	0.3150	0.0000	0.5932
Si	0.9096	0.0000	0.1872	Si	0.4096	0.0000	0.6872
O	0.7534	0.0000	0.1137	O	0.2534	0.0000	0.6137
O	0.8541	0.0000	0.1446	O	0.3541	0.0000	0.6446
O	0.8285	0.9462	0.0587	O	0.3285	0.9462	0.5586
Si	0.8150	0.0000	0.9068	Si	0.3150	0.0000	0.4068
Si	0.9096	0.0000	0.8128	Si	0.4096	0.0000	0.3129
O	0.7534	0.0000	0.8863	O	0.2534	0.0000	0.3863
O	0.8541	0.0000	0.8554	O	0.3541	0.0000	0.3554
O	0.8285	0.0538	0.9414	O	0.3285	0.0538	0.4414
Si	0.0932	0.1850	0.0000	Si	0.5932	0.1850	0.5000
Si	0.1872	0.0904	0.0000	Si	0.6872	0.0904	0.5000
O	0.1137	0.2466	0.0000	O	0.6137	0.2466	0.5000
O	0.1446	0.1459	0.0000	O	0.6446	0.1459	0.5000
O	0.0587	0.1715	0.0538	O	0.5586	0.1715	0.5538
Si	0.9068	0.1850	0.0000	Si	0.4068	0.1850	0.5000
Si	0.8128	0.0904	0.0000	Si	0.3129	0.0904	0.5000
O	0.8863	0.2466	0.0000	O	0.3863	0.2466	0.5000
O	0.8554	0.1459	0.0000	O	0.3554	0.1459	0.5000
O	0.9414	0.1715	0.9462	O	0.4414	0.1715	0.4462

To be continued on next page.

Si	0.0932	0.8150	0.0000	Si	0.5932	0.8150	0.5000
Si	0.1872	0.9096	0.0000	Si	0.6872	0.9096	0.5000
O	0.1137	0.7534	0.0000	O	0.6137	0.7534	0.5000
O	0.1446	0.8541	0.0000	O	0.6446	0.8541	0.5000
O	0.0587	0.8285	0.9462	O	0.5586	0.8285	0.4462
Si	0.9068	0.8150	0.0000	Si	0.4068	0.8150	0.5000
Si	0.8128	0.9096	0.0000	Si	0.3129	0.9096	0.5000
O	0.8863	0.7534	0.0000	O	0.3863	0.7534	0.5000
O	0.8554	0.8541	0.0000	O	0.3554	0.8541	0.5000
O	0.9414	0.8285	0.0538	O	0.4414	0.8285	0.5538
Si	0.5932	0.5000	0.3150	Si	0.0932	0.5000	0.8150
Si	0.6872	0.5000	0.4096	Si	0.1872	0.5000	0.9096
O	0.6137	0.5000	0.2534	O	0.1137	0.5000	0.7534
O	0.6446	0.5000	0.3541	O	0.1446	0.5000	0.8541
O	0.5586	0.5538	0.3285	O	0.0587	0.5538	0.8285
Si	0.4068	0.5000	0.3150	Si	0.9068	0.5000	0.8150
Si	0.3129	0.5000	0.4096	Si	0.8128	0.5000	0.9096
O	0.3863	0.5000	0.2534	O	0.8863	0.5000	0.7534
O	0.3554	0.5000	0.3541	O	0.8554	0.5000	0.8541
O	0.4414	0.4462	0.3285	O	0.9414	0.4462	0.8285
Si	0.5932	0.5000	0.6850	Si	0.0932	0.5000	0.1850
Si	0.6872	0.5000	0.5904	Si	0.1872	0.5000	0.0904
O	0.6137	0.5000	0.7466	O	0.1137	0.5000	0.2466
O	0.6446	0.5000	0.6459	O	0.1446	0.5000	0.1459
O	0.5586	0.4462	0.6715	O	0.0587	0.4462	0.1715
Si	0.4068	0.5000	0.6850	Si	0.9068	0.5000	0.1850
Si	0.3129	0.5000	0.5904	Si	0.8128	0.5000	0.0904
O	0.3863	0.5000	0.7466	O	0.8863	0.5000	0.2466
O	0.3554	0.5000	0.6459	O	0.8554	0.5000	0.1459
O	0.4414	0.5538	0.6715	O	0.9414	0.5538	0.1715
Si	0.5000	0.6850	0.4068	Si	0.0000	0.6850	0.9068
Si	0.5000	0.5904	0.3129	Si	0.0000	0.5904	0.8128
O	0.5000	0.7466	0.3863	O	0.0000	0.7466	0.8863
O	0.5000	0.6459	0.3554	O	0.0000	0.6459	0.8554
O	0.5538	0.6715	0.4414	O	0.0538	0.6715	0.9414
Si	0.5000	0.6850	0.5932	Si	0.0000	0.6850	0.0932
Si	0.5000	0.5904	0.6872	Si	0.0000	0.5904	0.1872
O	0.5000	0.7466	0.6137	O	0.0000	0.7466	0.1137
O	0.5000	0.6459	0.6446	O	0.0000	0.6459	0.1446
O	0.4462	0.6715	0.5586	O	0.9462	0.6715	0.0587
Si	0.5000	0.3150	0.4068	Si	0.0000	0.3150	0.9068
Si	0.5000	0.4096	0.3129	Si	0.0000	0.4096	0.8128
O	0.5000	0.2534	0.3863	O	0.0000	0.2534	0.8863
O	0.5000	0.3541	0.3554	O	0.0000	0.3541	0.8554
O	0.4462	0.3285	0.4414	O	0.9462	0.3285	0.9414
Si	0.5000	0.3150	0.5932	Si	0.0000	0.3150	0.0932
Si	0.5000	0.4096	0.6872	Si	0.0000	0.4096	0.1872
O	0.5000	0.2534	0.6137	O	0.0000	0.2534	0.1137
O	0.5000	0.3541	0.6446	O	0.0000	0.3541	0.1446
O	0.5538	0.3285	0.5586	O	0.0538	0.3285	0.0587
Si	0.6850	0.5932	0.5000	Si	0.1850	0.5932	0.0000
Si	0.5904	0.6872	0.5000	Si	0.0904	0.6872	0.0000
O	0.7466	0.6137	0.5000	O	0.2466	0.6137	0.0000
O	0.6459	0.6446	0.5000	O	0.1459	0.6446	0.0000
O	0.6715	0.5586	0.4462	O	0.1715	0.5586	0.9462
Si	0.6850	0.4068	0.5000	Si	0.1850	0.4068	0.0000
Si	0.5904	0.3129	0.5000	Si	0.0904	0.3129	0.0000
O	0.7466	0.3863	0.5000	O	0.2466	0.3863	0.0000
O	0.6459	0.3554	0.5000	O	0.1459	0.3554	0.0000

To be continued on next page.

O	0.6715	0.4414	0.5538	O	0.1715	0.4414	0.0538
Si	0.3150	0.5932	0.5000	Si	0.8150	0.5932	0.0000
Si	0.4096	0.6872	0.5000	Si	0.9096	0.6872	0.0000
O	0.2534	0.6137	0.5000	O	0.7534	0.6137	0.0000
O	0.3541	0.6446	0.5000	O	0.8541	0.6446	0.0000
O	0.3285	0.5586	0.5538	O	0.8285	0.5586	0.0538
Si	0.3150	0.4068	0.5000	Si	0.8150	0.4068	0.0000
Si	0.4096	0.3129	0.5000	Si	0.9096	0.3129	0.0000
O	0.2534	0.3863	0.5000	O	0.7534	0.3863	0.0000
O	0.3541	0.3554	0.5000	O	0.8541	0.3554	0.0000
O	0.3285	0.4414	0.4462	O	0.8285	0.4414	0.9462
O	0.9462	0.9414	0.8285	O	0.4462	0.9414	0.3285
O	0.0538	0.0587	0.8285	O	0.5538	0.0587	0.3285
O	0.0538	0.9414	0.1715	O	0.5538	0.9414	0.6715
O	0.9462	0.0587	0.1715	O	0.4462	0.0587	0.6715
O	0.8285	0.9462	0.9414	O	0.3285	0.9462	0.4414
O	0.8285	0.0538	0.0587	O	0.3285	0.0538	0.5586
O	0.1715	0.0538	0.9414	O	0.6715	0.0538	0.4414
O	0.1715	0.9462	0.0587	O	0.6715	0.9462	0.5586
O	0.9414	0.8285	0.9462	O	0.4414	0.8285	0.4462
O	0.0587	0.8285	0.0538	O	0.5586	0.8285	0.5538
O	0.9414	0.1715	0.0538	O	0.4414	0.1715	0.5538
O	0.0587	0.1715	0.9462	O	0.5586	0.1715	0.4462
O	0.4414	0.4462	0.6715	O	0.9414	0.4462	0.1715
O	0.5586	0.5538	0.6715	O	0.0587	0.5538	0.1715
O	0.4414	0.5538	0.3285	O	0.9414	0.5538	0.8285
O	0.5586	0.4462	0.3285	O	0.0587	0.4462	0.8285
O	0.4462	0.3285	0.5586	O	0.9462	0.3285	0.0587
O	0.5538	0.3285	0.4414	O	0.0538	0.3285	0.9414
O	0.5538	0.6715	0.5586	O	0.0538	0.6715	0.0587
O	0.4462	0.6715	0.4414	O	0.9462	0.6715	0.9414
O	0.3285	0.4414	0.5538	O	0.8285	0.4414	0.0538
O	0.3285	0.5586	0.4462	O	0.8285	0.5586	0.9462
O	0.6715	0.4414	0.4462	O	0.1715	0.4414	0.9462
O	0.6715	0.5586	0.5538	O	0.1715	0.5586	0.0538
Si	0.0000	0.5932	0.6850	Si	0.5000	0.5932	0.1850
Si	0.0000	0.6872	0.5904	Si	0.5000	0.6872	0.0904
O	0.0000	0.6137	0.7466	O	0.5000	0.6137	0.2466
O	0.0000	0.6446	0.6459	O	0.5000	0.6446	0.1459
O	0.0538	0.5586	0.6715	O	0.5538	0.5586	0.1715
Si	0.0000	0.4068	0.6850	Si	0.5000	0.4068	0.1850
Si	0.0000	0.3129	0.5904	Si	0.5000	0.3129	0.0904
O	0.0000	0.3863	0.7466	O	0.5000	0.3863	0.2466
O	0.0000	0.3554	0.6459	O	0.5000	0.3554	0.1459
O	0.9462	0.4414	0.6715	O	0.4462	0.4414	0.1715
Si	0.0000	0.5932	0.3150	Si	0.5000	0.5932	0.8150
Si	0.0000	0.6872	0.4096	Si	0.5000	0.6872	0.9096
O	0.0000	0.6137	0.2534	O	0.5000	0.6137	0.7534
O	0.0000	0.6446	0.3541	O	0.5000	0.6446	0.8541
O	0.9462	0.5586	0.3285	O	0.4462	0.5586	0.8285
Si	0.0000	0.4068	0.3150	Si	0.5000	0.4068	0.8150
Si	0.0000	0.3129	0.4096	Si	0.5000	0.3129	0.9096
O	0.0000	0.3863	0.2534	O	0.5000	0.3863	0.7534
O	0.0000	0.3554	0.3541	O	0.5000	0.3554	0.8541
O	0.0538	0.4414	0.3285	O	0.5538	0.4414	0.8285
Si	0.1850	0.5000	0.5932	Si	0.6850	0.5000	0.0932
Si	0.0904	0.5000	0.6872	Si	0.5904	0.5000	0.1872
O	0.2466	0.5000	0.6137	O	0.7466	0.5000	0.1137
O	0.1459	0.5000	0.6446	O	0.6459	0.5000	0.1446

To be continued on next page.

O	0.1715	0.5538	0.5586	O	0.6715	0.5538	0.0587
Si	0.1850	0.5000	0.4068	Si	0.6850	0.5000	0.9068
Si	0.0904	0.5000	0.3129	Si	0.5904	0.5000	0.8128
O	0.2466	0.5000	0.3863	O	0.7466	0.5000	0.8863
O	0.1459	0.5000	0.3554	O	0.6459	0.5000	0.8554
O	0.1715	0.4462	0.4414	O	0.6715	0.4462	0.9414
Si	0.8150	0.5000	0.5932	Si	0.3150	0.5000	0.0932
Si	0.9096	0.5000	0.6872	Si	0.4096	0.5000	0.1872
O	0.7534	0.5000	0.6137	O	0.2534	0.5000	0.1137
O	0.8541	0.5000	0.6446	O	0.3541	0.5000	0.1446
O	0.8285	0.4462	0.5586	O	0.3285	0.4462	0.0587
Si	0.8150	0.5000	0.4068	Si	0.3150	0.5000	0.9068
Si	0.9096	0.5000	0.3129	Si	0.4096	0.5000	0.8128
O	0.7534	0.5000	0.3863	O	0.2534	0.5000	0.8863
O	0.8541	0.5000	0.3554	O	0.3541	0.5000	0.8554
O	0.8285	0.5538	0.4414	O	0.3285	0.5538	0.9414
Si	0.0932	0.6850	0.5000	Si	0.5932	0.6850	0.0000
Si	0.1872	0.5904	0.5000	Si	0.6872	0.5904	0.0000
O	0.1137	0.7466	0.5000	O	0.6137	0.7466	0.0000
O	0.1446	0.6459	0.5000	O	0.6446	0.6459	0.0000
O	0.0587	0.6715	0.5538	O	0.5586	0.6715	0.0538
Si	0.9068	0.6850	0.5000	Si	0.4068	0.6850	0.0000
Si	0.8128	0.5904	0.5000	Si	0.3129	0.5904	0.0000
O	0.8863	0.7466	0.5000	O	0.3863	0.7466	0.0000
O	0.8554	0.6459	0.5000	O	0.3554	0.6459	0.0000
O	0.9414	0.6715	0.4462	O	0.4414	0.6715	0.9462
Si	0.0932	0.3150	0.5000	Si	0.5932	0.3150	0.0000
Si	0.1872	0.4096	0.5000	Si	0.6872	0.4096	0.0000
O	0.1137	0.2534	0.5000	O	0.6137	0.2534	0.0000
O	0.1446	0.3541	0.5000	O	0.6446	0.3541	0.0000
O	0.0587	0.3285	0.4462	O	0.5586	0.3285	0.9462
Si	0.9068	0.3150	0.5000	Si	0.4068	0.3150	0.0000
Si	0.8128	0.4096	0.5000	Si	0.3129	0.4096	0.0000
O	0.8863	0.2534	0.5000	O	0.3863	0.2534	0.0000
O	0.8554	0.3541	0.5000	O	0.3554	0.3541	0.0000
O	0.9414	0.3285	0.5538	O	0.4414	0.3285	0.0538
Si	0.5932	0.0000	0.8150	Si	0.0932	0.0000	0.3150
Si	0.6872	0.0000	0.9096	Si	0.1872	0.0000	0.4096
O	0.6137	0.0000	0.7534	O	0.1137	0.0000	0.2534
O	0.6446	0.0000	0.8541	O	0.1446	0.0000	0.3541
O	0.5586	0.0538	0.8285	O	0.0587	0.0538	0.3285
Si	0.4068	0.0000	0.8150	Si	0.9068	0.0000	0.3150
Si	0.3129	0.0000	0.9096	Si	0.8128	0.0000	0.4096
O	0.3863	0.0000	0.7534	O	0.8863	0.0000	0.2534
O	0.3554	0.0000	0.8541	O	0.8554	0.0000	0.3541
O	0.4414	0.9462	0.8285	O	0.9414	0.9462	0.3285
Si	0.5932	0.0000	0.1850	Si	0.0932	0.0000	0.6850
Si	0.6872	0.0000	0.0904	Si	0.1872	0.0000	0.5904
O	0.6137	0.0000	0.2466	O	0.1137	0.0000	0.7466
O	0.6446	0.0000	0.1459	O	0.1446	0.0000	0.6459
O	0.5586	0.9462	0.1715	O	0.0587	0.9462	0.6715
Si	0.4068	0.0000	0.1850	Si	0.9068	0.0000	0.6850
Si	0.3129	0.0000	0.0904	Si	0.8128	0.0000	0.5904
O	0.3863	0.0000	0.2466	O	0.8863	0.0000	0.7466
O	0.3554	0.0000	0.1459	O	0.8554	0.0000	0.6459
O	0.4414	0.0538	0.1715	O	0.9414	0.0538	0.6715
Si	0.5000	0.1850	0.9068	Si	0.0000	0.1850	0.4068
Si	0.5000	0.0904	0.8128	Si	0.0000	0.0904	0.3129
O	0.5000	0.2466	0.8863	O	0.0000	0.2466	0.3863

To be continued on next page.

O	0.5000	0.1459	0.8554	O	0.0000	0.1459	0.3554
O	0.5538	0.1715	0.9414	O	0.0538	0.1715	0.4414
Si	0.5000	0.1850	0.0932	Si	0.0000	0.1850	0.5932
Si	0.5000	0.0904	0.1872	Si	0.0000	0.0904	0.6872
O	0.5000	0.2466	0.1137	O	0.0000	0.2466	0.6137
O	0.5000	0.1459	0.1446	O	0.0000	0.1459	0.6446
O	0.4462	0.1715	0.0587	O	0.9462	0.1715	0.5586
Si	0.5000	0.8150	0.9068	Si	0.0000	0.8150	0.4068
Si	0.5000	0.9096	0.8128	Si	0.0000	0.9096	0.3129
O	0.5000	0.7534	0.8863	O	0.0000	0.7534	0.3863
O	0.5000	0.8541	0.8554	O	0.0000	0.8541	0.3554
O	0.4462	0.8285	0.9414	O	0.9462	0.8285	0.4414
Si	0.5000	0.8150	0.0932	Si	0.0000	0.8150	0.5932
Si	0.5000	0.9096	0.1872	Si	0.0000	0.9096	0.6872
O	0.5000	0.7534	0.1137	O	0.0000	0.7534	0.6137
O	0.5000	0.8541	0.1446	O	0.0000	0.8541	0.6446
O	0.5538	0.8285	0.0587	O	0.0538	0.8285	0.5586
Si	0.6850	0.0932	0.0000	Si	0.1850	0.0932	0.5000
Si	0.5904	0.1872	0.0000	Si	0.0904	0.1872	0.5000
O	0.7466	0.1137	0.0000	O	0.2466	0.1137	0.5000
O	0.6459	0.1446	0.0000	O	0.1459	0.1446	0.5000
O	0.6715	0.0587	0.9462	O	0.1715	0.0587	0.4462
Si	0.6850	0.9068	0.0000	Si	0.1850	0.9068	0.5000
Si	0.5904	0.8128	0.0000	Si	0.0904	0.8128	0.5000
O	0.7466	0.8863	0.0000	O	0.2466	0.8863	0.5000
O	0.6459	0.8554	0.0000	O	0.1459	0.8554	0.5000
O	0.6715	0.9414	0.0538	O	0.1715	0.9414	0.5538
Si	0.3150	0.0932	0.0000	Si	0.8150	0.0932	0.5000
Si	0.4096	0.1872	0.0000	Si	0.9096	0.1872	0.5000
O	0.2534	0.1137	0.0000	O	0.7534	0.1137	0.5000
O	0.3541	0.1446	0.0000	O	0.8541	0.1446	0.5000
O	0.3285	0.0587	0.0538	O	0.8285	0.0587	0.5538
Si	0.3150	0.9068	0.0000	Si	0.8150	0.9068	0.5000
Si	0.4096	0.8128	0.0000	Si	0.9096	0.8128	0.5000
O	0.2534	0.8863	0.0000	O	0.7534	0.8863	0.5000
O	0.3541	0.8554	0.0000	O	0.8541	0.8554	0.5000
O	0.3285	0.9414	0.9462	O	0.8285	0.9414	0.4462
O	0.9462	0.4414	0.3285	O	0.4462	0.4414	0.8285
O	0.0538	0.5586	0.3285	O	0.5538	0.5586	0.8285
O	0.0538	0.4414	0.6715	O	0.5538	0.4414	0.1715
O	0.9462	0.5586	0.6715	O	0.4462	0.5586	0.1715
O	0.8285	0.4462	0.4414	O	0.3285	0.4462	0.9414
O	0.8285	0.5538	0.5586	O	0.3285	0.5538	0.0587
O	0.1715	0.5538	0.4414	O	0.6715	0.5538	0.9414
O	0.1715	0.4462	0.5586	O	0.6715	0.4462	0.0587
O	0.9414	0.3285	0.4462	O	0.4414	0.3285	0.9462
O	0.0587	0.3285	0.5538	O	0.5586	0.3285	0.0538
O	0.9414	0.6715	0.5538	O	0.4414	0.6715	0.0538
O	0.0587	0.6715	0.4462	O	0.5586	0.6715	0.9462
O	0.4414	0.9462	0.1715	O	0.9414	0.9462	0.6715
O	0.5586	0.0538	0.1715	O	0.0587	0.0538	0.6715
O	0.4414	0.0538	0.8285	O	0.9414	0.0538	0.3285
O	0.5586	0.9462	0.8285	O	0.0587	0.9462	0.3285
O	0.4462	0.8285	0.0587	O	0.9462	0.8285	0.5586
O	0.5538	0.8285	0.9414	O	0.0538	0.8285	0.4414
O	0.5538	0.1715	0.0587	O	0.0538	0.1715	0.5586
O	0.4462	0.1715	0.9414	O	0.9462	0.1715	0.4414
O	0.3285	0.9414	0.0538	O	0.8285	0.9414	0.5538
O	0.3285	0.0587	0.9462	O	0.8285	0.0587	0.4462

To be continued on next page.

O	0.6715	0.9414	0.9462	O	0.1715	0.9414	0.4462
O	0.6715	0.0587	0.0538	O	0.1715	0.0587	0.5538

B.7 LTL from Barrer and Villiger

This structure was taken from Barrer and Villiger⁶³
 Note that the original monoclinic unit cell was converted
 to an orthorhombic unit cell for computational convenience;
 compare also Reference 127.

$$\hat{a}_0 = 3.1984 \text{ nm} \quad \hat{b}_0 = 1.8466 \text{ nm} \quad \hat{c}_0 = 0.7476 \text{ nm}$$

Si	0.0471	0.3112	0.5000	Si	0.3680	0.2737	0.5000
Si	0.5471	0.8112	0.5000	Si	0.8680	0.7737	0.5000
Si	0.0830	0.4159	0.2121	Si	0.3335	0.1675	0.7879
Si	0.5830	0.9159	0.2121	Si	0.8335	0.6675	0.7879
O	0.0000	0.2753	0.5000	O	0.3672	0.1015	0.7440
O	0.5000	0.7753	0.5000	O	0.8672	0.6015	0.7440
O	0.0829	0.2488	0.5000	O	0.3440	0.2418	0.6817
O	0.5829	0.7488	0.5000	O	0.8440	0.7418	0.6817
O	0.1328	0.3985	0.2560	O	0.2874	0.8623	0.7249
O	0.6328	0.8985	0.2560	O	0.7874	0.3623	0.7249
O	0.0511	0.3631	0.3183	O	0.3335	0.1893	0.0000
O	0.5511	0.8631	0.3183	O	0.8335	0.6893	0.0000
O	0.2125	0.6377	0.2751	Si	0.4529	0.8112	0.5000
O	0.7126	0.1377	0.2751	Si	0.9529	0.3112	0.5000
O	0.0721	0.4051	0.0000	Si	0.4170	0.9159	0.7879
O	0.5721	0.9051	0.0000	Si	0.9170	0.4159	0.7879
Si	0.3208	0.4151	0.5000	O	0.3672	0.8985	0.7440
Si	0.8208	0.9151	0.5000	O	0.8672	0.3985	0.7440
Si	0.2505	0.4165	0.2121	O	0.4489	0.8631	0.6817
Si	0.7505	0.9165	0.2121	O	0.9489	0.3631	0.6817
O	0.3623	0.3623	0.5000	O	0.2874	0.1377	0.7249
O	0.8623	0.8623	0.5000	O	0.7874	0.6377	0.7249
O	0.3341	0.5000	0.5000	O	0.4279	0.9051	0.0000
O	0.8341	0.0000	0.5000	O	0.9279	0.4051	0.0000
O	0.2343	0.5000	0.2560	Si	0.3208	0.5849	0.5000
O	0.7343	0.0000	0.2560	Si	0.8208	0.0849	0.5000
O	0.2929	0.3951	0.3183	Si	0.2505	0.5835	0.7879
O	0.7929	0.8951	0.3183	Si	0.7505	0.0835	0.7879
O	0.0749	0.5000	0.2751	O	0.2343	0.5000	0.7440
O	0.5749	0.0000	0.2751	O	0.7343	0.0000	0.7440
O	0.2614	0.4056	0.0000	O	0.2929	0.6049	0.6817
O	0.7614	0.9056	0.0000	O	0.7929	0.1049	0.6817
Si	0.1320	0.7737	0.5000	O	0.0749	0.5000	0.7249
Si	0.6320	0.2737	0.5000	O	0.5749	0.0000	0.7249
Si	0.1665	0.6675	0.2121	O	0.2614	0.5944	0.0000
Si	0.6665	0.1675	0.2121	O	0.7614	0.0944	0.0000
O	0.1377	0.8623	0.5000	Si	0.1320	0.2263	0.5000
O	0.6377	0.3623	0.5000	Si	0.6320	0.7263	0.5000
O	0.0829	0.7512	0.5000	Si	0.1665	0.3325	0.7879
O	0.5829	0.2512	0.5000	Si	0.6665	0.8325	0.7879
O	0.1328	0.6015	0.2560	O	0.1328	0.3985	0.7440

To be continued on next page.

O	0.6328	0.1015	0.2560	O	0.6328	0.8985	0.7440
O	0.1560	0.7418	0.3183	O	0.1560	0.2582	0.6817
O	0.6560	0.2418	0.3183	O	0.6560	0.7582	0.6817
O	0.2125	0.3623	0.2751	O	0.2125	0.6377	0.7249
O	0.7126	0.8623	0.2751	O	0.7126	0.1377	0.7249
O	0.1665	0.6893	0.0000	O	0.1665	0.3107	0.0000
O	0.6665	0.1893	0.0000	O	0.6665	0.8107	0.0000
Si	0.4529	0.1888	0.5000	Si	0.0471	0.6888	0.5000
Si	0.9529	0.6888	0.5000	Si	0.5471	0.1888	0.5000
Si	0.4170	0.0841	0.2121	Si	0.0830	0.5841	0.7879
Si	0.9170	0.5841	0.2121	Si	0.5830	0.0841	0.7879
O	0.0000	0.7247	0.5000	O	0.1328	0.6015	0.7440
O	0.5000	0.2246	0.5000	O	0.6328	0.1015	0.7440
O	0.4171	0.2512	0.5000	O	0.0511	0.6369	0.6817
O	0.9171	0.7512	0.5000	O	0.5511	0.1369	0.6817
O	0.3672	0.1015	0.2560	O	0.2125	0.3623	0.7249
O	0.8672	0.6015	0.2560	O	0.7126	0.8623	0.7249
O	0.4489	0.1369	0.3183	O	0.0721	0.5949	0.0000
O	0.9489	0.6369	0.3183	O	0.5721	0.0949	0.0000
O	0.2874	0.8623	0.2751	Si	0.4170	0.0841	0.7879
O	0.7874	0.3623	0.2751	Si	0.9170	0.5841	0.7879
O	0.4279	0.0949	0.0000	O	0.4489	0.1369	0.6817
O	0.9279	0.5949	0.0000	O	0.9489	0.6369	0.6817
Si	0.1792	0.0849	0.5000	Si	0.2495	0.0835	0.7879
Si	0.6792	0.5849	0.5000	Si	0.7495	0.5835	0.7879
Si	0.2495	0.0835	0.2121	O	0.2071	0.1049	0.6817
Si	0.7495	0.5835	0.2121	O	0.7071	0.6049	0.6817
O	0.1377	0.1377	0.5000	Si	0.3335	0.8325	0.7879
O	0.6377	0.6377	0.5000	Si	0.8335	0.3325	0.7879
O	0.1659	0.0000	0.5000	O	0.3440	0.7582	0.6817
O	0.6659	0.5000	0.5000	O	0.8440	0.2582	0.6817
O	0.2657	0.0000	0.2560	Si	0.0830	0.4159	0.7879
O	0.7657	0.5000	0.2560	Si	0.5830	0.9159	0.7879
O	0.2071	0.1049	0.3183	O	0.0511	0.3631	0.6817
O	0.7071	0.6049	0.3183	O	0.5511	0.8631	0.6817
O	0.4251	0.0000	0.2751	Si	0.2505	0.4165	0.7879
O	0.9251	0.5000	0.2751	Si	0.7505	0.9165	0.7879
O	0.2386	0.0944	0.0000	O	0.2929	0.3951	0.6817
O	0.7386	0.5944	0.0000	O	0.7929	0.8951	0.6817
Si	0.3680	0.7263	0.5000	Si	0.1665	0.6675	0.7879
Si	0.8680	0.2263	0.5000	Si	0.6665	0.1675	0.7879
Si	0.3335	0.8325	0.2121	O	0.1560	0.7418	0.6817
Si	0.8335	0.3325	0.2121	O	0.6560	0.2418	0.6817
O	0.3623	0.6377	0.5000	Si	0.2505	0.5835	0.2121
O	0.8623	0.1377	0.5000	Si	0.7505	0.0835	0.2121
O	0.4171	0.7488	0.5000	O	0.2929	0.6049	0.3183
O	0.9171	0.2488	0.5000	O	0.7929	0.1049	0.3183
O	0.3672	0.8985	0.2560	Si	0.1665	0.3325	0.2121
O	0.8672	0.3985	0.2560	Si	0.6665	0.8325	0.2121
O	0.3440	0.7582	0.3183	O	0.1560	0.2582	0.3183
O	0.8440	0.2582	0.3183	O	0.6560	0.7582	0.3183
O	0.2874	0.1377	0.2751	Si	0.0830	0.5841	0.2121
O	0.7874	0.6377	0.2751	Si	0.5830	0.0841	0.2121
O	0.3335	0.8107	0.0000	O	0.0511	0.6369	0.3183
O	0.8335	0.3107	0.0000	O	0.5511	0.1369	0.3183
Si	0.1792	0.9151	0.5000	Si	0.2495	0.9165	0.2121
Si	0.6792	0.4151	0.5000	Si	0.7495	0.4165	0.2121
Si	0.2495	0.9165	0.7879	O	0.2071	0.8951	0.3183
Si	0.7495	0.4165	0.7879	O	0.7071	0.3951	0.3183

To be continued on next page.

O	0.2657	0.0000	0.7440	Si	0.3335	0.1675	0.2121
O	0.7657	0.5000	0.7440	Si	0.8335	0.6675	0.2121
O	0.2071	0.8951	0.6817	O	0.3440	0.2418	0.3183
O	0.7071	0.3951	0.6817	O	0.8440	0.7418	0.3183
O	0.4251	0.0000	0.7249	Si	0.4170	0.9159	0.2121
O	0.9251	0.5000	0.7249	Si	0.9170	0.4159	0.2121
O	0.2386	0.9056	0.0000	O	0.4489	0.8631	0.3183
O	0.7386	0.4056	0.0000	O	0.9489	0.3631	0.3183

B.8 MFI from van Koningsveld *et al.*

This structure was taken from van Koningsveld *et al.*⁶⁴

$$\hat{a}_0 = 2.0022 \text{ nm} \quad \hat{b}_0 = 1.9899 \text{ nm} \quad \hat{c}_0 = 1.3383 \text{ nm}$$

Si	0.4224	0.0565	0.6640	O	0.6940	0.4993	0.9082
Si	0.3072	0.0277	0.8107	O	0.6951	0.6291	0.9190
Si	0.2791	0.0613	0.0312	O	0.4960	0.4575	0.7078
Si	0.1221	0.0630	0.0267	O	0.4960	0.6528	0.7078
Si	0.0713	0.0272	0.8145	O	0.9192	0.7500	0.8540
Si	0.1864	0.0590	0.6718	O	0.6884	0.7500	0.8538
Si	0.4227	0.8275	0.6728	O	0.7883	0.7500	0.4421
Si	0.3078	0.8698	0.8145	O	0.6085	0.7500	0.4389
Si	0.2755	0.8272	0.0311	Si	0.5776	0.9435	0.3360
Si	0.1206	0.8269	0.0298	Si	0.6928	0.9723	0.1893
Si	0.0704	0.8696	0.8180	Si	0.7209	0.9387	0.9688
Si	0.1871	0.8267	0.6807	Si	0.8779	0.9370	0.9733
O	0.3726	0.0534	0.7558	Si	0.9287	0.9728	0.1855
O	0.3084	0.0587	0.9211	Si	0.8136	0.9410	0.3282
O	0.2007	0.0592	0.0289	Si	0.5774	0.1725	0.3272
O	0.0969	0.0611	0.9144	Si	0.6922	0.1302	0.1855
O	0.1149	0.0541	0.7237	Si	0.7245	0.1728	0.9689
O	0.2435	0.0553	0.7540	Si	0.8794	0.1731	0.9702
O	0.3742	0.8439	0.7628	Si	0.9296	0.1304	0.1820
O	0.3085	0.8448	0.9272	Si	0.8129	0.1733	0.3193
O	0.1980	0.8446	0.0288	O	0.6274	0.9466	0.2442
O	0.0910	0.8386	0.9223	O	0.6916	0.9413	0.0789
O	0.1169	0.8422	0.7306	O	0.7993	0.9408	0.9711
O	0.2448	0.8406	0.7578	O	0.9031	0.9389	0.0856
O	0.3047	0.9490	0.8134	O	0.8851	0.9459	0.2763
O	0.0768	0.9481	0.8231	O	0.7565	0.9447	0.2460
O	0.4161	0.1276	0.6104	O	0.6258	0.1561	0.2372
O	0.4086	0.9983	0.5864	O	0.6915	0.1552	0.0728
O	0.4020	0.8686	0.5761	O	0.8020	0.1554	0.9712
O	0.1886	0.1298	0.6164	O	0.9090	0.1614	0.0777
O	0.1940	0.0007	0.5918	O	0.8831	0.1578	0.2694
O	0.1951	0.8709	0.5810	O	0.7552	0.1594	0.2422
O	0.9960	0.0425	0.7922	O	0.6953	0.0510	0.1866
O	0.9960	0.8472	0.7922	O	0.9232	0.0519	0.1769
O	0.4192	0.7500	0.6460	O	0.5839	0.8724	0.3896
O	0.1884	0.7500	0.6462	O	0.5914	0.0017	0.4136
O	0.2883	0.7500	0.0579	O	0.5980	0.1314	0.4239
O	0.1085	0.7500	0.0611	O	0.8114	0.8702	0.3836

To be continued on next page.

Si	0.0776	0.9435	0.1640	O	0.8060	0.9993	0.4082
Si	0.1928	0.9723	0.3107	O	0.8049	0.1291	0.4190
Si	0.2209	0.9387	0.5312	O	0.0040	0.9575	0.2078
Si	0.3779	0.9370	0.5267	O	0.0040	0.1528	0.2078
Si	0.4287	0.9728	0.3145	Si	0.9224	0.0565	0.8360
Si	0.3136	0.9410	0.1718	Si	0.8072	0.0277	0.6893
Si	0.0774	0.1725	0.1728	Si	0.7791	0.0613	0.4688
Si	0.1922	0.1302	0.3145	Si	0.6221	0.0630	0.4733
Si	0.2245	0.1728	0.5311	Si	0.5713	0.0272	0.6855
Si	0.3794	0.1731	0.5298	Si	0.6864	0.0590	0.8282
Si	0.4296	0.1304	0.3180	Si	0.9226	0.8275	0.8272
Si	0.3129	0.1733	0.1807	Si	0.8078	0.8698	0.6855
O	0.1274	0.9466	0.2558	Si	0.7755	0.8272	0.4689
O	0.1916	0.9413	0.4211	Si	0.6206	0.8269	0.4702
O	0.2993	0.9408	0.5289	Si	0.5704	0.8696	0.6820
O	0.4031	0.9389	0.4144	Si	0.6871	0.8267	0.8193
O	0.3851	0.9459	0.2237	O	0.8726	0.0534	0.7442
O	0.2565	0.9447	0.2540	O	0.8084	0.0587	0.5789
O	0.1258	0.1561	0.2628	O	0.7007	0.0592	0.4711
O	0.1915	0.1552	0.4272	O	0.5969	0.0611	0.5856
O	0.3020	0.1554	0.5288	O	0.6149	0.0541	0.7763
O	0.4090	0.1614	0.4223	O	0.7435	0.0553	0.7460
O	0.3831	0.1578	0.2306	O	0.8742	0.8439	0.7372
O	0.2552	0.1594	0.2578	O	0.8085	0.8448	0.5728
O	0.1953	0.0510	0.3134	O	0.6980	0.8446	0.4712
O	0.4232	0.0519	0.3231	O	0.5910	0.8386	0.5777
O	0.0839	0.8724	0.1104	O	0.6169	0.8422	0.7694
O	0.0914	0.0017	0.0864	O	0.7448	0.8406	0.7422
O	0.0980	0.1314	0.0761	O	0.8047	0.9490	0.6866
O	0.3114	0.8702	0.1164	O	0.5768	0.9481	0.6769
O	0.3060	0.9993	0.0918	O	0.9161	0.1276	0.8896
O	0.3049	0.1291	0.0810	O	0.9086	0.9983	0.9136
O	0.5040	0.9575	0.2922	O	0.9020	0.8686	0.9239
O	0.5040	0.1528	0.2922	O	0.6886	0.1298	0.8836
O	0.0808	0.2500	0.1460	O	0.6940	0.0007	0.9082
O	0.3116	0.2500	0.1462	O	0.6951	0.8709	0.9190
O	0.2117	0.2500	0.5579	O	0.4960	0.0425	0.7078
O	0.3915	0.2500	0.5611	O	0.4960	0.8472	0.7078
Si	0.5776	0.5565	0.3360	Si	0.4224	0.4435	0.6640
Si	0.6928	0.5277	0.1893	Si	0.3072	0.4723	0.8107
Si	0.7209	0.5613	0.9688	Si	0.2791	0.4387	0.0312
Si	0.8779	0.5630	0.9733	Si	0.1221	0.4370	0.0267
Si	0.9287	0.5272	0.1855	Si	0.0713	0.4728	0.8145
Si	0.8136	0.5590	0.3282	Si	0.1864	0.4410	0.6718
Si	0.5774	0.3275	0.3272	Si	0.4227	0.6725	0.6728
Si	0.6922	0.3698	0.1855	Si	0.3078	0.6302	0.8145
Si	0.7245	0.3272	0.9689	Si	0.2755	0.6728	0.0311
Si	0.8794	0.3269	0.9702	Si	0.1206	0.6731	0.0298
Si	0.9296	0.3696	0.1820	Si	0.0704	0.6304	0.8180
Si	0.8129	0.3267	0.3193	Si	0.1871	0.6733	0.6807
O	0.6274	0.5534	0.2442	O	0.3726	0.4466	0.7558
O	0.6916	0.5587	0.0789	O	0.3084	0.4413	0.9211
O	0.7993	0.5592	0.9711	O	0.2007	0.4408	0.0289
O	0.9031	0.5611	0.0856	O	0.0969	0.4389	0.9144
O	0.8851	0.5541	0.2763	O	0.1149	0.4459	0.7237
O	0.7565	0.5553	0.2460	O	0.2435	0.4447	0.7540
O	0.6258	0.3439	0.2372	O	0.3742	0.6561	0.7628
O	0.6915	0.3448	0.0728	O	0.3085	0.6552	0.9272
O	0.8020	0.3446	0.9712	O	0.1980	0.6554	0.0288

To be continued on next page.

O	0.9090	0.3386	0.0777	O	0.0910	0.6614	0.9223
O	0.8831	0.3422	0.2694	O	0.1169	0.6578	0.7306
O	0.7552	0.3406	0.2422	O	0.2448	0.6594	0.7578
O	0.6953	0.4490	0.1866	O	0.3047	0.5510	0.8134
O	0.9232	0.4481	0.1769	O	0.0768	0.5519	0.8231
O	0.5839	0.6276	0.3896	O	0.4161	0.3724	0.6104
O	0.5914	0.4983	0.4136	O	0.4086	0.5017	0.5864
O	0.5980	0.3686	0.4239	O	0.4020	0.6314	0.5761
O	0.8114	0.6298	0.3836	O	0.1886	0.3702	0.6164
O	0.8060	0.5007	0.4082	O	0.1940	0.4993	0.5918
O	0.8049	0.3709	0.4190	O	0.1951	0.6291	0.5810
O	0.0040	0.5425	0.2078	O	0.9960	0.4575	0.7922
O	0.0040	0.3472	0.2078	O	0.9960	0.6528	0.7922
O	0.5808	0.2500	0.3540	Si	0.0776	0.5565	0.1640
O	0.8116	0.2500	0.3538	Si	0.1928	0.5277	0.3107
O	0.7117	0.2500	0.9421	Si	0.2209	0.5613	0.5312
O	0.8915	0.2500	0.9389	Si	0.3779	0.5630	0.5267
Si	0.9224	0.4435	0.8360	Si	0.4287	0.5272	0.3145
Si	0.8072	0.4723	0.6893	Si	0.3136	0.5590	0.1718
Si	0.7791	0.4387	0.4688	Si	0.0774	0.3275	0.1728
Si	0.6221	0.4370	0.4733	Si	0.1922	0.3698	0.3145
Si	0.5713	0.4728	0.6855	Si	0.2245	0.3272	0.5311
Si	0.6864	0.4410	0.8282	Si	0.3794	0.3269	0.5298
Si	0.9226	0.6725	0.8272	Si	0.4296	0.3696	0.3180
Si	0.8078	0.6302	0.6855	Si	0.3129	0.3267	0.1807
Si	0.7755	0.6728	0.4689	O	0.1274	0.5534	0.2558
Si	0.6206	0.6731	0.4702	O	0.1916	0.5587	0.4211
Si	0.5704	0.6304	0.6820	O	0.2993	0.5592	0.5289
Si	0.6871	0.6733	0.8193	O	0.4031	0.5611	0.4144
O	0.8726	0.4466	0.7442	O	0.3851	0.5541	0.2237
O	0.8084	0.4413	0.5789	O	0.2565	0.5553	0.2540
O	0.7007	0.4408	0.4711	O	0.1258	0.3439	0.2628
O	0.5969	0.4389	0.5856	O	0.1915	0.3448	0.4272
O	0.6149	0.4459	0.7763	O	0.3020	0.3446	0.5288
O	0.7435	0.4447	0.7460	O	0.4090	0.3386	0.4223
O	0.8742	0.6561	0.7372	O	0.3831	0.3422	0.2306
O	0.8085	0.6552	0.5728	O	0.2552	0.3406	0.2578
O	0.6980	0.6554	0.4712	O	0.1953	0.4490	0.3134
O	0.5910	0.6614	0.5777	O	0.4232	0.4481	0.3231
O	0.6169	0.6578	0.7694	O	0.0839	0.6276	0.1104
O	0.7448	0.6594	0.7422	O	0.0914	0.4983	0.0864
O	0.8047	0.5510	0.6866	O	0.0980	0.3686	0.0761
O	0.5768	0.5519	0.6769	O	0.3114	0.6298	0.1164
O	0.9161	0.3724	0.8896	O	0.3060	0.5007	0.0918
O	0.9086	0.5017	0.9136	O	0.3049	0.3709	0.0810
O	0.9020	0.6314	0.9239	O	0.5040	0.5425	0.2922
O	0.6886	0.3702	0.8836	O	0.5040	0.3472	0.2922

B.9 SAS from IZA

This structure was taken from Baerlocher and McCusker²²

$$\hat{a}_0 = 1.4349 \text{ nm} \quad \hat{b}_0 = 1.4349 \text{ nm} \quad \hat{c}_0 = 1.0398 \text{ nm}$$

O	0.2418	0.0000	0.0000	O	0.8261	0.3629	0.3723
O	0.0000	0.2418	0.0000	O	0.6371	0.8261	0.3723
O	0.0000	0.7582	0.0000	O	0.3629	0.1739	0.3723
O	0.7582	0.0000	0.0000	O	0.8261	0.6371	0.6277
O	0.7418	0.5000	0.5000	O	0.1739	0.3629	0.6277
O	0.5000	0.7418	0.5000	O	0.1739	0.6371	0.3723
O	0.5000	0.2582	0.5000	O	0.3629	0.8261	0.6277
O	0.2582	0.5000	0.5000	O	0.6371	0.1739	0.6277
O	0.1690	0.1690	0.0000	O	0.1739	0.6371	0.6277
O	0.8310	0.1690	0.0000	O	0.3629	0.1739	0.6277
O	0.1690	0.8310	0.0000	O	0.6371	0.8261	0.6277
O	0.8310	0.8310	0.0000	O	0.1739	0.3629	0.3723
O	0.6690	0.6690	0.5000	O	0.8261	0.6371	0.3723
O	0.3310	0.6690	0.5000	O	0.8261	0.3629	0.6277
O	0.6690	0.3310	0.5000	O	0.6371	0.1739	0.3723
O	0.3310	0.3310	0.5000	O	0.3629	0.8261	0.3723
O	0.5000	0.8745	0.7865	Si	0.2662	0.8893	0.0000
O	0.1255	0.5000	0.7865	Si	0.1107	0.2662	0.0000
O	0.8745	0.5000	0.7865	Si	0.8893	0.7338	0.0000
O	0.5000	0.1255	0.2135	Si	0.2662	0.1107	0.0000
O	0.5000	0.8745	0.2135	Si	0.7338	0.8893	0.0000
O	0.5000	0.1255	0.7865	Si	0.7338	0.1107	0.0000
O	0.8745	0.5000	0.2135	Si	0.8893	0.2662	0.0000
O	0.1255	0.5000	0.2135	Si	0.1107	0.7338	0.0000
O	0.0000	0.3745	0.2865	Si	0.7662	0.3893	0.5000
O	0.6255	0.0000	0.2865	Si	0.6107	0.7662	0.5000
O	0.3745	0.0000	0.2865	Si	0.3893	0.2338	0.5000
O	0.0000	0.6255	0.7135	Si	0.7662	0.6107	0.5000
O	0.0000	0.3745	0.7135	Si	0.2338	0.3893	0.5000
O	0.0000	0.6255	0.2865	Si	0.2338	0.6107	0.5000
O	0.3745	0.0000	0.7135	Si	0.3893	0.7662	0.5000
O	0.6255	0.0000	0.7135	Si	0.6107	0.2338	0.5000
O	0.3261	0.8629	0.8723	Si	0.6090	0.8910	0.7500
O	0.1371	0.3261	0.8723	Si	0.1090	0.6090	0.7500
O	0.8629	0.6739	0.8723	Si	0.8910	0.3910	0.7500
O	0.3261	0.1371	0.1277	Si	0.6090	0.1090	0.2500
O	0.6739	0.8629	0.1277	Si	0.3910	0.8910	0.2500
O	0.6739	0.1371	0.8723	Si	0.3910	0.1090	0.7500
O	0.8629	0.3261	0.1277	Si	0.8910	0.6090	0.2500
O	0.1371	0.6739	0.1277	Si	0.1090	0.3910	0.2500
O	0.6739	0.1371	0.1277	Si	0.3910	0.1090	0.2500
O	0.8629	0.6739	0.1277	Si	0.8910	0.3910	0.2500
O	0.1371	0.3261	0.1277	Si	0.1090	0.6090	0.2500
O	0.6739	0.8629	0.8723	Si	0.3910	0.8910	0.7500
O	0.3261	0.1371	0.8723	Si	0.6090	0.1090	0.7500
O	0.3261	0.8629	0.1277	Si	0.6090	0.8910	0.2500
O	0.1371	0.6739	0.8723	Si	0.1090	0.3910	0.7500
O	0.8629	0.3261	0.8723	Si	0.8910	0.6090	0.7500

B.10 SAS from Patinec *et al.*

This structure was taken from Patinec *et al.*⁶⁶

$$\hat{a}_0 = 1.4322 \text{ nm} \quad \hat{b}_0 = 1.4322 \text{ nm} \quad \hat{c}_0 = 1.0424 \text{ nm}$$

Si	0.2689	0.1091	0.0000	O	0.6791	0.1397	0.1174
Si	0.8909	0.2689	0.0000	O	0.8603	0.6791	0.1174
Si	0.1091	0.7311	0.0000	O	0.1397	0.3209	0.1174
Si	0.7689	0.3909	0.5000	O	0.1791	0.3603	0.3826
Si	0.2311	0.6091	0.5000	O	0.8209	0.6397	0.3826
Si	0.7311	0.8909	0.0000	O	0.3209	0.8603	0.1174
Si	0.6091	0.7689	0.5000	O	0.6397	0.1791	0.3826
Si	0.3909	0.2311	0.5000	O	0.3603	0.8209	0.3826
Si	0.3907	0.8907	0.7500	O	0.5093	0.8722	0.7865
Si	0.1093	0.3907	0.7500	O	0.1278	0.5093	0.7865
Si	0.8907	0.6093	0.7500	O	0.8722	0.4907	0.7865
Si	0.6093	0.1093	0.7500	O	0.0093	0.6278	0.7135
Si	0.6093	0.1093	0.2500	O	0.9907	0.3722	0.7135
Si	0.8907	0.6093	0.2500	O	0.4907	0.1278	0.7865
Si	0.1093	0.3907	0.2500	O	0.3722	0.0093	0.7135
Si	0.3907	0.8907	0.2500	O	0.6278	0.9907	0.7135
Si	0.6101	0.8899	0.7500	O	0.4907	0.1278	0.2135
Si	0.1101	0.6101	0.7500	O	0.8722	0.4907	0.2135
Si	0.8899	0.3899	0.7500	O	0.1278	0.5093	0.2135
Si	0.3899	0.1101	0.7500	O	0.9907	0.3722	0.2865
Si	0.3899	0.1101	0.2500	O	0.0093	0.6278	0.2865
Si	0.8899	0.3899	0.2500	O	0.5093	0.8722	0.2135
Si	0.1101	0.6101	0.2500	O	0.6278	0.9907	0.2865
Si	0.6101	0.8899	0.2500	O	0.3722	0.0093	0.2865
Si	0.2666	0.8863	0.0000	O	0.1750	0.8339	0.0000
Si	0.1137	0.2666	0.0000	O	0.1661	0.1750	0.0000
Si	0.8863	0.7334	0.0000	O	0.8339	0.8250	0.0000
Si	0.7666	0.6137	0.5000	O	0.6750	0.6661	0.5000
Si	0.2334	0.3863	0.5000	O	0.3250	0.3339	0.5000
Si	0.7334	0.1137	0.0000	O	0.8250	0.1661	0.0000
Si	0.3863	0.7666	0.5000	O	0.3339	0.6750	0.5000
Si	0.6137	0.2334	0.5000	O	0.6661	0.3250	0.5000
O	0.2414	0.9886	0.0000	O	0.6683	0.8619	0.8614
O	0.0114	0.2414	0.0000	O	0.1381	0.6683	0.8614
O	0.9886	0.7586	0.0000	O	0.8619	0.3317	0.8614
O	0.7414	0.5114	0.5000	O	0.1683	0.6381	0.6386
O	0.2586	0.4886	0.5000	O	0.8317	0.3619	0.6386
O	0.7586	0.0114	0.0000	O	0.3317	0.1381	0.8614
O	0.4886	0.7414	0.5000	O	0.3619	0.1683	0.6386
O	0.5114	0.2586	0.5000	O	0.6381	0.8317	0.6386
O	0.3209	0.8603	0.8826	O	0.3317	0.1381	0.1386
O	0.1397	0.3209	0.8826	O	0.8619	0.3317	0.1386
O	0.8603	0.6791	0.8826	O	0.1381	0.6683	0.1386
O	0.8209	0.6397	0.6174	O	0.8317	0.3619	0.3614
O	0.1791	0.3603	0.6174	O	0.1683	0.6381	0.3614
O	0.6791	0.1397	0.8826	O	0.6683	0.8619	0.1386
O	0.3603	0.8209	0.6174	O	0.6381	0.8317	0.3614
O	0.6397	0.1791	0.6174	O	0.3619	0.1683	0.3614

B.11 SAS from Wragg *et al.*

This structure was taken from Wragg *et al.*⁶⁵

$$\hat{a}_0 = 1.4104 \text{ nm} \quad \hat{b}_0 = 1.4104 \text{ nm} \quad \hat{c}_0 = 1.0188 \text{ nm}$$

O	0.2386	0.0000	0.0000	O	0.0000	0.3739	0.2893
O	0.0000	0.2386	0.0000	O	0.6261	0.0000	0.2893
O	0.0000	0.7614	0.0000	O	0.3739	0.0000	0.2893
O	0.7614	0.0000	0.0000	O	0.0000	0.6261	0.7107
O	0.7386	0.5000	0.5000	O	0.0000	0.3739	0.7107
O	0.5000	0.7386	0.5000	O	0.0000	0.6261	0.2893
O	0.5000	0.2614	0.5000	O	0.3739	0.0000	0.7107
O	0.2614	0.5000	0.5000	O	0.6261	0.0000	0.7107
O	0.3255	0.8623	0.8735	O	0.1684	0.8316	0.0000
O	0.1377	0.3255	0.8735	O	0.1684	0.1684	0.0000
O	0.8623	0.6745	0.8735	O	0.8316	0.8316	0.0000
O	0.3255	0.1377	0.1265	O	0.8316	0.1684	0.0000
O	0.6745	0.8623	0.1265	O	0.6684	0.3316	0.5000
O	0.6745	0.1377	0.8735	O	0.6684	0.6684	0.5000
O	0.8623	0.3255	0.1265	O	0.3316	0.3316	0.5000
O	0.1377	0.6745	0.1265	O	0.3316	0.6684	0.5000
O	0.6745	0.1377	0.1265	Si	0.2658	0.1098	0.0000
O	0.8623	0.6745	0.1265	Si	0.8902	0.2658	0.0000
O	0.1377	0.3255	0.1265	Si	0.1098	0.7342	0.0000
O	0.6745	0.8623	0.8735	Si	0.2658	0.8902	0.0000
O	0.3255	0.1377	0.8735	Si	0.7342	0.1098	0.0000
O	0.3255	0.8623	0.1265	Si	0.7342	0.8902	0.0000
O	0.1377	0.6745	0.8735	Si	0.1098	0.2658	0.0000
O	0.8623	0.3255	0.8735	Si	0.8902	0.7342	0.0000
O	0.8255	0.3623	0.3735	Si	0.7658	0.6098	0.5000
O	0.6377	0.8255	0.3735	Si	0.3902	0.7658	0.5000
O	0.3623	0.1745	0.3735	Si	0.6098	0.2342	0.5000
O	0.8255	0.6377	0.6265	Si	0.7658	0.3902	0.5000
O	0.1745	0.3623	0.6265	Si	0.2342	0.6098	0.5000
O	0.1745	0.6377	0.3735	Si	0.2342	0.3902	0.5000
O	0.3623	0.8255	0.6265	Si	0.6098	0.7658	0.5000
O	0.6377	0.1745	0.6265	Si	0.3902	0.2342	0.5000
O	0.1745	0.6377	0.6265	Si	0.6090	0.8910	0.7500
O	0.3623	0.1745	0.6265	Si	0.1090	0.6090	0.7500
O	0.6377	0.8255	0.6265	Si	0.8910	0.3910	0.7500
O	0.1745	0.3623	0.3735	Si	0.6090	0.1090	0.2500
O	0.8255	0.6377	0.3735	Si	0.3910	0.8910	0.2500
O	0.8255	0.3623	0.6265	Si	0.3910	0.1090	0.7500
O	0.6377	0.1745	0.3735	Si	0.8910	0.6090	0.2500
O	0.3623	0.8255	0.3735	Si	0.1090	0.3910	0.2500
O	0.5000	0.8739	0.7893	Si	0.3910	0.1090	0.2500
O	0.1261	0.5000	0.7893	Si	0.8910	0.3910	0.2500
O	0.8739	0.5000	0.7893	Si	0.1090	0.6090	0.2500
O	0.5000	0.1261	0.2107	Si	0.3910	0.8910	0.7500
O	0.5000	0.8739	0.2107	Si	0.6090	0.1090	0.7500
O	0.5000	0.1261	0.7893	Si	0.6090	0.8910	0.2500
O	0.8739	0.5000	0.2107	Si	0.1090	0.3910	0.7500
O	0.1261	0.5000	0.2107	Si	0.8910	0.6090	0.7500

Continuum Calculations of Tracer Exchange

C

Appendix C describes numerical continuum calculations performed to mimic transient tracer exchange in AFI-type membranes. The procedure made possible the study of exchange kinetics with growing membrane thicknesses up to the micrometer scale.

The membranes were modeled as perfect single-crystals, geometrically resembling a plate of infinite cross section in x - y plane and of thickness δ in z direction.^{114,214} The plate was divided into N_{slabs} slabs (or sub-plates) each of width $l_{\text{zeol}} = 0.4242$ nm (= cage length), which has therefore maintained the most relevant AFI-structure characteristic. Because symmetry was assumed across the membrane, N_{slabs} corresponds in fact to half of the membrane ($\delta/2$).

As for the one-step exchange simulations, where molecules having reached the surface adsorption layer are being considered exchanged in case of tracer release, the *one* outermost slab was given a different width, l_{marg} . This was necessary for a realistic spatial description because free-energy profiles, as shown in Figure 10.2, evidence that the separation between the two maxima enclosing the marginal well is obviously larger than the typical innermost maxima separation (= cage length). As for the two-step exchange simulations, in which molecules are considered exchanged when they have left the surface adsorption layer for the gas phase in tracer-release situations, the *two* outermost slabs were given different widths, representing the extensions of the zeolite margin (second outermost slab), l_{marg} , and the surface adsorption layer width (outermost slab), l_{lay} , as highlighted in Figure C.1. Exchange of labeled molecules between the slabs was modeled with equilibrium fluxes, j_{eq} , prevailing at the window locations of the channels which were determined within the framework of dynamically-corrected transition

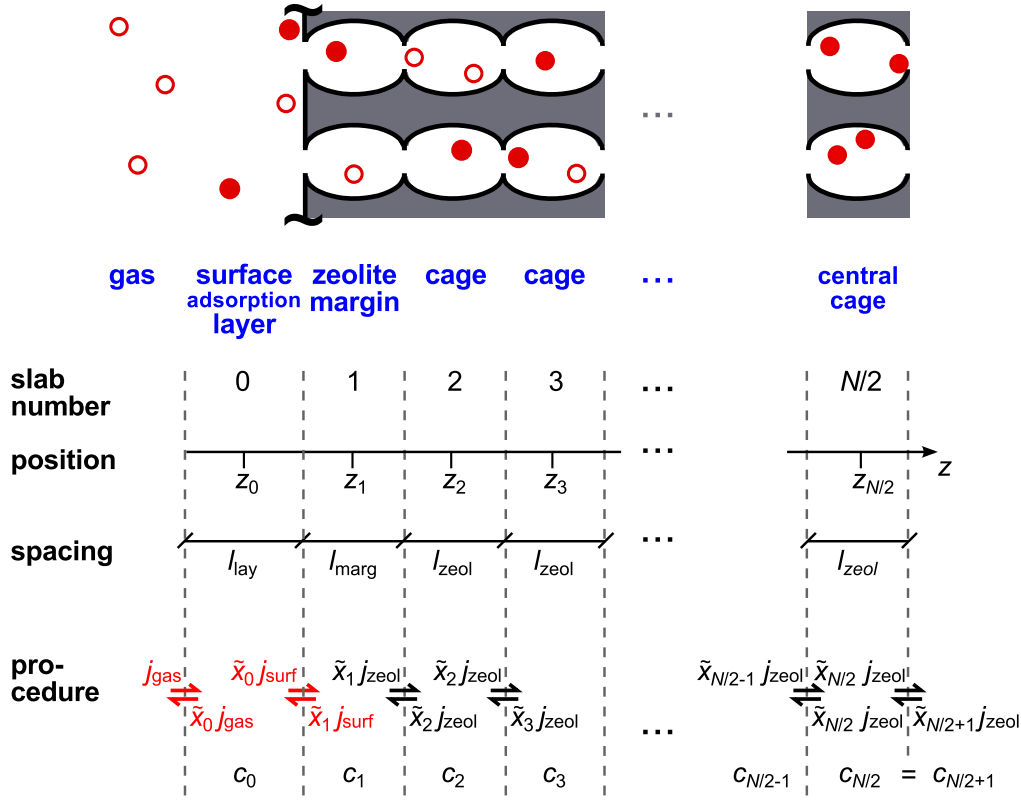


Figure C.1: Scheme of spatial set-up of the tracer-exchange continuum calculations. Note that 1) $\tilde{x}_i = \tilde{x}_i(t) = c_i(t)/c_{\text{eq},i} = c(t, z_i)/c_{\text{eq}}(z_i)$, 2) the fluxes are equilibrium fluxes (e.g. $j_{\text{gas}} = j_{\text{eq,gas}}$), as well as 3) $N_{\text{slabs}} = n/2$ and $N_{\text{slabs}} = n/2 + 1$ for the one-step and two-step simulations, respectively.

state theory^{109,114,214} from molecular simulations.

Following conditions apply in the case of tracer *release*:

1. all slabs were initialized with their respective equilibrium (i.e., saturation) concentrations, that is, the innermost slabs with $c_{\text{eq,zeol}}$ and the outermost slabs with $c_{\text{eq,marg}}$ and $c_{\text{eq,lay}}$;
2. the *entering* boundary equilibrium flux (one-step simulations: $j_{\text{eq,surf}}$; two-step simulations: $j_{\text{eq,gas}}$; cf., Figure C.1) was set to zero.

In the case of tracer *uptake*, these conditions are not applicable. Rather, all slabs were initialized with zero concentration and the entering boundary flux ($j_{\text{eq,surf}}$ and $j_{\text{eq,gas}}$, respectively) maintained its full magnitude throughout the calculation.

To evolve the systems in time the material balances are solved numeric-

ally. In general, the incremental change in concentration, $\Delta c_i(t + \Delta t)$, for slab number i at z_i is given by

$$\Delta c_i(t + \Delta t) = \frac{j_{\text{eq,zeol}} [c_{i-1}(t) - 2c_i(t) + c_{i+1}(t)]}{c_{\text{eq,zeol}} \cdot l_{\text{zeol}}} \cdot \Delta t, \quad (\text{C.1})$$

with $c_i(t) \equiv c(t, z_i)$ and Δt the time increment. Because of symmetry conditions the right-hand side boundary condition (Figure C.1) is:

$$\Delta c_{N_{\text{slabs}}}(t + \Delta t) = \frac{j_{\text{eq,zeol}} [c_{N_{\text{slabs}}-1}(t) - c_{N_{\text{slabs}}}(t)]}{c_{\text{eq,zeol}} \cdot l_{\text{zeol}}} \cdot \Delta t. \quad (\text{C.2})$$

As for the one-step exchange simulations, in which slab number 0 of Figure C.1 is not present, the left-hand side boundary condition reads:

$$\Delta c_1(t + \Delta t) = \frac{j_{\text{eq,surf}} \left[S_{\text{witch}} - \frac{c_1(t)}{c_{\text{eq,marg}}} \right] + j_{\text{eq,zeol}} \left[\frac{c_2(t)}{c_{\text{eq,zeol}}} - \frac{c_1(t)}{c_{\text{eq,marg}}} \right]}{l_{\text{marg}}} \cdot \Delta t. \quad (\text{C.3})$$

The parameter S_{witch} is zero in case of tracer release and unity in case of tracer uptake, thus reflecting the conditions described at the beginning. As for the two-step exchange simulations, the left-hand side boundary conditions (i.e., for the two outermost slabs) read:

$$\Delta c_0(t + \Delta t) = \frac{j_{\text{eq,gas}} \left[S_{\text{witch}} - \frac{c_0(t)}{c_{\text{eq,lay}}} \right] + j_{\text{eq,surf}} \left[\frac{c_1(t)}{c_{\text{eq,marg}}} - \frac{c_0(t)}{c_{\text{eq,lay}}} \right]}{l_{\text{lay}}} \cdot \Delta t, \quad \text{and} \quad (\text{C.4})$$

$$\Delta c_1(t + \Delta t) = \frac{j_{\text{eq,surf}} \left[\frac{c_0(t)}{c_{\text{eq,lay}}} - \frac{c_1(t)}{c_{\text{eq,marg}}} \right] + j_{\text{eq,zeol}} \left[\frac{c_2(t)}{c_{\text{eq,zeol}}} - \frac{c_1(t)}{c_{\text{eq,marg}}} \right]}{l_{\text{marg}}} \cdot \Delta t. \quad (\text{C.5})$$

Apart from the input obtained from the molecular simulations ($c_{\text{eq,zeol}}$, l_{zeol} , $j_{\text{eq,zeol}}$, etc.), a single tracer-exchange continuum calculation requires following data:

- number of slabs determining the membrane thickness in the end, N_{slabs} (= 5–3000);
- time-step size for the numerical integration of the material balances, Δt (= 0.01–1 ps);

- number of numerical integration steps, N_{steps} ($= 400\,000 - 2 \cdot 10^6$), determining, together with the time-step size, the total simulation time ($= N_{\text{steps}} \cdot \Delta t$);
- number of times of sampling the concentration profile, N_{samples} ($= 99$);
- fitting parameters, such as minimum relative precision of exchange curve per time instance ($= 10^{-12}$).

The transient concentration profiles obtained by this procedure were (numerically) integrated to yield, apart from a constant, the mass, $m(t)$, of tracer in the membrane at time t :

$$m(t) \propto \int_{-\delta/2}^{+\delta/2} c(t, z) \, dz. \quad (\text{C.6})$$

On the basis of these concentration integrals, the fractional exchange at time t was calculated by:⁹²

$$\frac{m(t)}{\lim_{t' \rightarrow \infty} m(t')} = \frac{\int_{-\delta/2}^{+\delta/2} c(t, z) \, dz}{\lim_{t' \rightarrow \infty} \int_{-\delta/2}^{+\delta/2} c(t', z) \, dz} \quad \text{in case of uptake;} \quad (\text{C.7})$$

$$\frac{m(0) - m(t)}{m(0)} = 1 - \frac{\int_{-\delta/2}^{+\delta/2} c(t, z) \, dz}{\int_{-\delta/2}^{+\delta/2} c(0, z) \, dz} \quad \text{in case of release.} \quad (\text{C.8})$$

Self-diffusion coefficients, D_S , and tracer-exchange permeabilities, α_S , could then be determined by fitting analytical solutions of the diffusion equations (Equations 3.4 and 3.7) to match the resulting exchange curve.

Bibliography

- [1] J. Kärger, D. M. Ruthven, D. N. Theodorou, *Diffusion in Nanoporous Materials*, vol. 1, Wiley-VCH Verlag, Weinheim **2012**.
- [2] J. Kärger, D. M. Ruthven, D. N. Theodorou, *Diffusion in Nanoporous Materials*, vol. 2, Wiley-VCH Verlag, Weinheim **2012**.
- [3] C. Chmelik, J. Kärger, In situ study on molecular diffusion phenomena in nanoporous catalytic solids, *Chem. Soc. Rev.* **2010**, 39, 4864–4884.
- [4] F. Hibbe, C. Chmelik, L. Heinke, S. Pramanik, J. Li, D. M. Ruthven, D. Tzoulaki, J. Kärger, The nature of surface barriers on nanoporous solids explored by microimaging of transient guest distributions, *J. Am. Chem. Soc.* **2011**, 133, 2804–2807.
- [5] L. Heinke, J. Kärger, Correlating surface permeability with intracrystalline diffusivity in nanoporous solids, *Phys. Rev. Lett.* **2011**, 106, 074501.
- [6] L.-C. Lin, A. H. Berger, R. L. Martin, J. Kim, J. A. Swisher, K. Jariwala, C. H. Rycroft, A. S. Bhowan, M. W. Deem, M. Haranczyk, B. Smit, *In silico* screening of carbon-capture materials, *Nat. Mater.* **2012**, 11, 633–641.
- [7] N. Hansen, F. J. Keil, Multiscale modeling of reaction and diffusion in zeolites: from the molecular level to the reactor, *Soft Mater.* **2012**, 10, 179–201.
- [8] D. A. Newsome, D. S. Sholl, Predictive assessment of surface resistances in zeolite membranes using atomically detailed models, *J. Phys. Chem. B* **2005**, 109, 7237–7244.
- [9] J. Gulín-González, A. Schüring, S. Fritzsche, J. Kärger, S. Vasenkov, The influence of the desorption barrier on the transport of molecules through the external surface of nanoporous crystals, *Chem. Phys. Lett.* **2006**, 430, 60–66.
- [10] E. Beerdsen, D. Dubbeldam, B. Smit, Loading dependence of the diffusion coefficient of methane in nanoporous materials, *J. Phys. Chem. B* **2006**, 110, 22754–22772.
- [11] J. Caro, M. Noack, Zeolite membranes—recent developments and pro-

- gress, *Microporous Mesoporous Mater.* **2008**, 115, 215–233.
- [12] M. Tsapatsis, Toward high-throughput zeolite membranes, *Science* **2011**, 334, 767–768.
- [13] C. M. Veziri, M. Palomino, G. N. Karanikolos, A. Corma, N. K. Kanellopoulos, M. Tsapatsis, Toward submicrometer *c*-oriented nanoporous films with unidimensional pore network: AFI film morphology control by precursor mixture manipulation, *Chem. Mater.* **2010**, 22, 1492–1502.
- [14] M. Choi, K. Na, J. Kim, Y. Sakamoto, O. Terasaki, R. Ryoo, Stable single-unit-cell nanosheets of zeolite MFI as active and long-lived catalysts, *Nature* **2009**, 461, 246–249.
- [15] J. Rouquerol, D. Avnir, C. W. Fairbridge, D. H. Everett, J. H. Haynes, N. Pernicone, J. D. F. Ramsay, K. S. W. Sing, K. K. Unger, Recommendations for the characterization of porous solids, *Pure Appl. Chem.* **1994**, 66, 1739–1758.
- [16] Z. Song, L. Chen, J. Hu, R. Richards, NiO(111) nanosheets as efficient and recyclable adsorbents for dye pollutant removal from wastewater, *Nanotechnology* **2009**, 20, 275707.
- [17] J. García-Martínez, K. Li, G. Krishnaiah, A mesostructured Y zeolite as a superior FCC catalyst—from lab to refinery, *Chem. Commun.* **2012**, 48, 11841–11843.
- [18] Y.-T. Cheng, J. Jae, J. Shi, W. Fan, G. W. Huber, Production of renewable aromatic compounds by catalytic fast pyrolysis of lignocellulosic biomass with bifunctional Ga/ZSM-5 catalysts, *Angew. Chem., Int. Ed.* **2012**, 51, 1387–1390.
- [19] Y.-T. Cheng, Z. Wang, C. J. Gilbert, W. Fan, G. W. Huber, Production of *p*-xylene from biomass by catalytic fast pyrolysis using ZSM-5 catalysts with reduced pore openings, *Angew. Chem., Int. Ed.* **2012**, 51, 11097–11100.
- [20] N. Hansen, R. Krishna, J. M. van Baten, A. T. Bell, F. J. Keil, Analysis of diffusion limitation in the alkylation of benzene over H-ZSM-5 by combining quantum chemical calculations, molecular simulations, and a continuum approach, *J. Phys. Chem. C* **2009**, 113, 235–246.
- [21] P. S. Wheatley, A. R. Butler, M. S. Crane, S. Fox, B. Xiao, A. G. Rossi, I. L. Megson, R. E. Morris, NO-releasing zeolites and their antithrombotic properties, *J. Am. Chem. Soc.* **2006**, 128, 502–509.
- [22] C. Baerlocher, L. B. McCusker, Database of zeolite structures, <http://www.iza-structure.org/databases/>, January 10, **2013**.
- [23] M. D. Foster, M. M. J. Treacy, Database of hypothetical zeolite materials, <http://www.hypotheticalzeolites.net/>, January 17, **2013**.
- [24] M. W. Deem, Database of hypothetical zeolite materials,

- <http://www.hypotheticalzeolites.net/DATABASE/DEEM/>, January 14, **2013**.
- [25] E. M. Flanigen, R. W. Broach, S. T. Wilson, *Zeolites in Industrial Separation and Catalysis*, chap. Introduction, Wiley-VCH Verlag, Weinheim **2010**, pp. 1–26.
- [26] L. B. McCusker, C. Baerlocher, *Introduction to Zeolite Science and Practice*, chap. Zeolite Structures, Elsevier, Amsterdam, 2nd ed. **2001**, pp. 37–67.
- [27] E. B. M. Doesburg, K. P. de Jong, J. H. C. van Hooff, *Catalysis: An Integrated Approach*, chap. Preparation of Catalyst Supports, Zeolites and Mesoporous Materials, Elsevier, Amsterdam, 2nd ed. **1999**, pp. 433–457.
- [28] E. M. Flanigen, *Introduction to Zeolite Science and Practice*, chap. Zeolites and Molecular Sieves. An Historical Perspective, Elsevier, Amsterdam, 2nd ed. **2001**, pp. 11–35.
- [29] A. D. McNaught, A. Wilkinson, *IUPAC. Compendium of Chemical Terminology*, Blackwell Scientific Publications, Oxford, 2nd ed. **1997**.
- [30] L. B. McCusker, F. Liebau, G. Engelhardt, Nomenclature of structural and compositional characteristics of ordered microporous and mesoporous materials with inorganic hosts (IUPAC recommendations 2001), *Pure Appl. Chem.* **2001**, 73, 381–394.
- [31] N. E. R. Zimmermann, *Molecular-Simulation Studies of Porous Materials*, Master's thesis, Hamburg University of Technology **2006**.
- [32] Wikimedia Foundation, Axel Fredrik Cronstedt, http://en.wikipedia.org/wiki/Axel_Fredrik_Cronstedt, January 11, **2013**.
- [33] A. Simmen, J. Patarin, C. Baerlocher, Rietveld refinement of F-containing GaPO₄-LTA, in *Proceedings from the 9th International Zeolite Conference I and II*, Butterworth-Heinemann, Boston, pp. 433–440.
- [34] R. Pophale, P. A. Cheeseman, M. W. Deem, A database of new zeolite-like materials, *Phys. Chem. Chem. Phys.* **2011**, 13, 12407–12412.
- [35] A. Corma, F. Rey, J. Rius, M. J. Sabater, S. Valencia, Supramolecular self-assembled molecules as organic directing agent for synthesis of zeolites, *Nature* **2004**, 431, 287–290.
- [36] J. J. Pluth, J. V. Smith, Accurate redetermination of crystal structure of dehydrated zeolite-A. Absence of near zero coordination of sodium. Refinement of Si,Al-ordered superstructure, *J. Am. Chem. Soc.* **1980**, 102, 4704–4708.
- [37] W. Loewenstein, The Distribution of Aluminum in the Tetrahedra of Silicates and Aluminates, *Am. Mineral.* **1954**, 39, 92–96.

- [38] Wikimedia Foundation, Fractional coordinates, http://en.wikipedia.org/wiki/Fractional_coordinates, January 16, **2013**.
- [39] D. Dubbeldam, *Computer-Simulation of Adsorption and Diffusion of Hydrocarbons in Zeolites*, Ph.D. thesis, University of Amsterdam **2005**.
- [40] E. Lehmann, C. Chmelik, H. Scheidt, S. Vasenkov, B. Staudte, J. Kärger, F. Kremer, G. Zadrozna, J. Kornatowski, Regular intergrowth in the AFI-type crystals: influence on the intracrystalline adsorbate distribution as observed by interference and FTIR-microscopy, *J. Am. Chem. Soc.* **2002**, 124, 8690–8692.
- [41] E. Beerdsen, D. Dubbeldam, B. Smit, Understanding diffusion in nanoporous materials, *Phys. Rev. Lett.* **2006**, 96, 044501.
- [42] D. W. Ming, J. B. Dixon, Quantitative Determination of Clinoptilolite in Soils by a Cation-exchange Capacity Method, *Clays Clay. Miner.* **1987**, 35, 463–468.
- [43] M. M. Bomgardner, Using Pore Power, *Chem. Eng. News* **2011**, 89, 20–21.
- [44] G. Steenbruggen, G. G. Hollman, The synthesis of zeolites from fly ash and the properties of the zeolite products, *J. Geochem. Explor.* **1998**, 62, 305–309.
- [45] R. Szostak, *Introduction to Zeolite Science and Practice*, chap. Secondary Synthesis Methods, Elsevier, Amsterdam, 2nd ed. **2001**, pp. 261–297.
- [46] Z. Lai, G. Bonilla, I. Diaz, J. G. Nery, K. Sujaoti, M. A. Amat, E. Kokkoli, O. Terasaki, R. W. Thompson, M. Tsapatsis, D. G. Vlachos, Microstructural optimization of a zeolite membrane for organic vapor separation, *Science* **2003**, 300, 456–460.
- [47] A. I. Lupulescu, J. D. Rimer, Tailoring silicalite-1 crystal morphology with molecular modifiers, *Angew. Chem., Int. Ed.* **2012**, 51, 3345–3349.
- [48] W. C. Yoo, J. A. Stoeger, P.-S. Lee, M. Tsapatsis, A. Stein, High-performance randomly oriented zeolite membranes using brittle seeds and rapid thermal processing, *Angew. Chem., Int. Ed.* **2010**, 49, 8699–8703.
- [49] J. García-Martínez, M. Johnson, J. Valla, K. Li, J. Y. Ying, Mesoporous zeolite Y—high hydrothermal stability and superior FCC catalytic performance, *Catal. Sci. Technol.* **2012**, 2, 987–994.
- [50] Y. Li, J. Yu, R. Xu, Criteria for zeolite frameworks realizable for target synthesis, *Angew. Chem., Int. Ed.* **2013**, 1673–1677.
- [51] M. E. Davis, Ordered porous materials for emerging applications, *Nature* **2002**, 417, 813–821.

- [52] J. Keller, R. Staudt, *Gas Adsorption Equilibria—Experimental Methods and Adsorption Isotherms*, Springer Science+Business Media, New York **2005**.
- [53] D. M. Ruthven, S. Farooq, K. S. Knaebel, *Pressure Swing Adsorption*, VCH Publishers, New York **1994**.
- [54] T. Maesen, B. Marcus, *Introduction to Zeolite Science and Practice*, chap. The Zeolite Scene—An Overview, Elsevier, Amsterdam, 2nd ed. **2001**, pp. 1–9.
- [55] S. E. Bailey, T. J. Olin, R. M. Bricka, D. D. Adrian, A review of potentially low-cost sorbents for heavy metals, *Water Res.* **1999**, *33*, 2469–2479.
- [56] The Associated Press, Levels of radioactive materials rise near Japanese plant, <http://www.nytimes.com/2011/04/17/world/asia/17nuke.html>, April 16, **2011**.
- [57] Green Dot Holdings, LLC, Green dot offers toy companies a safer more sustainable alternative to petroleum based soft plastic, <http://www.greendotpure.com/news>, October, **2012**.
- [58] T. C. T. Pham, H. S. Kim, K. B. Yoon, Growth of uniformly oriented silica MFI and BEA zeolite films on substrates, *Science* **2011**, *334*, 1533–1538.
- [59] K. J. Balkus, Jr., A. D. Sherry, S. W. Young, *U.S. Patent 5,122,363: Zeolite-enclosed Transistion and Rare Earth Metal Ions as Contrast Agents for the Gastrointestinal Tract* **1992**.
- [60] U. Vietze, O. Krauß, F. Laeri, G. Ihlein, F. Schüth, B. Limburg, M. Abraham, Zeolite-dye microlasers, *Phys. Rev. Lett.* **1998**, *81*, 4628–4631.
- [61] S. Qiu, W. Pang, H. Kessler, J.-L. Guth, Synthesis and structure of the $[\text{AlPO}_4]_{12}$, Pr_4NF molecular sieve with AFI structure, *Zeolites* **1989**, *9*, 440–444.
- [62] M. A. Camblor, A. Corma, P. Lightfoot, L. A. Villaescusa, P. A. Wright, Synthesis and structure of ITQ-3, the first pure silica polymorph with a two-dimensional system of straight eight-ring channels, *Angew. Chem., Int. Ed.* **1997**, *36*, 2659–2661.
- [63] R. M. Barrer, H. Villiger, Crystal structure of synthetic zeolite L, *Z. Kristallogr.* **1969**, *128*, 352–370.
- [64] H. van Koningsveld, H. van Bekkum, J. C. Jansen, On the location and disorder of the tetrapropylammonium (TPA) ion in zeolite ZSM-5 with improved framework accuracy, *Acta Crystallogr., Sect. B: Struct. Sci.* **1987**, *43*, 127–132.
- [65] D. S. Wragg, R. Morris, A. W. Burton, S. I. Zones, K. Ong, G. Lee, The synthesis and structure of SSZ-73: an all-silica zeolite with an unusual framework topology, *Chem. Mater.* **2007**, *19*, 3924–3932.

- [66] V. Patinec, P. A. Wright, P. Lightfoot, R. A. Aitken, P. A. Cox, Synthesis of a novel microporous magnesioaluminophosphate, STA-6, containing an unbound azamacrocyclic, *J. Chem. Soc., Dalton Trans.* **1999**, 3909–3911.
- [67] N. Wang, Z. K. Tang, G. D. Li, J. S. Chen, Materials science—single-walled 4 Å carbon nanotube arrays, *Nature* **2000**, 408, 50–51.
- [68] Wikimedia Foundation, Carbon nanotube, http://en.wikipedia.org/wiki/Carbon_nanotube, January 18, **2013**.
- [69] K. A. Mirica, J. G. Weis, J. M. Schnorr, B. Esser, T. M. Swager, Mechanical Drawing of Gas Sensors on Paper, *Angew. Chem., Int. Ed.* **2012**, 51, 10740–10745.
- [70] S. Jakobtorweihen, *Molecular Simulation of Technically Relevant Molecules in Nanoporous Materials—Carbon Nanotubes and Zeolites*, Ph.D. thesis, Hamburg University of Technology **2007**.
- [71] Wikimedia Foundation, Metal-organic framework, http://en.wikipedia.org/wiki/Metal-organic_framework, January 18, **2013**.
- [72] S. R. Batten, N. R. Champness, X.-M. Chen, J. Garcia-Martinez, S. Kitagawa, L. Öhrström, M. O’Keeffe, M. P. Suh, J. Reedijk, Terminology of metal-organic frameworks and coordination polymers (IUPAC provisional recommendation), *IUPAC—Inorganic Chemistry Division* **2012**.
- [73] F. H. Allen, The Cambridge Structural Database: a quarter of a million crystal structures and rising, *Acta Cryst.* **2002**, 58, 380–388.
- [74] The Cambridge Crystallographic Data Centre, The Cambridge structural database for organic molecules and metal-organic compounds, <http://www.ccdc.cam.ac.uk/products/csd/>, January 10, **2013**.
- [75] L. Pan, B. Parker, X. Huang, D. H. Olson, J. Lee, J. Li, Zn(tbip) (H(2)tbip=5-*tert*-butyl isophthalic acid): a highly stable guest-free microporous metal organic framework with unique gas separation capability, *J. Am. Chem. Soc.* **2006**, 128, 4180–4181.
- [76] K. Momma, F. Izumi, VESTA 3 for three-dimensional visualization of crystal, volumetric and morphology data, *J. Appl. Crystallogr.* **2011**, 44, 1272–1276.
- [77] S. R. Batten, N. R. Champness, X.-M. Chen, J. Garcia-Martinez, S. Kitagawa, L. Öhrström, M. O’Keeffe, M. P. Suh, J. Reedijk, Coordination polymers, metal-organic frameworks and the need for terminology guidelines, *CrystEngComm* **2012**, 14, 3001–3004.
- [78] L. J. Murray, M. Dincă, J. R. Long, Hydrogen storage in metal-organic frameworks, *Chem. Soc. Rev.* **2009**, 38, 1294–1314.
- [79] A. O. Yazaydin, R. Q. Snurr, T.-H. Park, K. Koh, J. Liu, M. D. LeVan,

- A. I. Benin, P. Jakubczak, M. Lanuza, D. B. Galloway, J. J. Low, R. R. Willis, Screening of metal-organic frameworks for carbon dioxide capture from flue gas using a combined experimental and modeling approach, *J. Am. Chem. Soc.* **2009**, 131, 18198–18199.
- [80] T. Ben, C. Lu, C. Pei, S. Xu, S. Qiu, Polymer-supported and free-standing metal-organic framework membrane, *Chem.—Eur. J.* **2012**, 18, 10250–10253.
- [81] W. L. McCabe, J. C. Smith, P. Harriott, *Unit Operations of Chemical Engineering*, McGraw-Hill, New York, 7th ed. **2005**.
- [82] Z. U. A. Warsi, *Fluid Dynamics—Theoretical and Computational Approaches*, CRC Press, Boca Raton, 2nd ed. **1999**.
- [83] R. B. Bird, W. E. Stewart, E. N. Lightfoot, *Transport Phenomena*, John Wiley & Sons, New York, 2nd ed. **2007**.
- [84] H. D. Baehr, K. Stephan, *Heat and Mass Transfer*, Springer-Verlag, Berlin, 2nd ed. **2006**.
- [85] I. Inzoli, J. M. Simon, D. Bedeaux, S. Kjelstrup, Thermal diffusion and partial molar enthalpy variations of n-butane in silicalite-1, *J. Phys. Chem. B* **2008**, 112, 14937–14951.
- [86] Wikimedia Foundation, Thermophoresis, <http://en.wikipedia.org/wiki/Thermophoresis>, January 23, **2013**.
- [87] S. Duhr, D. Braun, Why molecules move along a temperature gradient, *Proc. Natl. Acad. Sci. U. S. A.* **2006**, 103, 19678–19682.
- [88] Wikimedia Foundation, Microscale thermophoresis, http://en.wikipedia.org/wiki/Microscale_thermophoresis, January 23, **2013**.
- [89] M. Jerabek-Willemsen, C. J. Wienken, D. Braun, P. Baaske, S. Duhr, Molecular interaction studies using microscale thermophoresis, *Assay Drug Dev. Technol.* **2011**, 9, 342–353.
- [90] R. Krishna, Diffusion in porous crystalline materials, *Chem. Soc. Rev.* **2012**, 41, 3099–3118.
- [91] D. Frenkel, B. Smit, *Understanding Molecular Simulations—from Algorithms to Applications*, Academic Press, San Diego, 2nd ed. **2002**.
- [92] J. Crank, *The Mathematics of Diffusion*, Oxford University Press, New York, 2nd ed. **1975**.
- [93] Wikimedia Foundation, Adolf Eugen Fick, http://en.wikipedia.org/wiki/Adolf_Eugen_Fick, February 19, **2013**.
- [94] Wikimedia Foundation, Fick principle, http://en.wikipedia.org/wiki/Fick_principle, February 19, **2013**.
- [95] A. Fick, Ueber Diffusion, *Ann. Phys.* **1855**, 170, 59–86.
- [96] D. Chandler, *Introduction to Modern Statistical Mechanics*, Oxford University Press, New York **1987**.

- [97] Wikimedia Foundation, Ludwig Boltzmann, http://en.wikipedia.org/wiki/Ludwig_Boltzmann, February 18, **2013**.
- [98] Wikimedia Foundation, Monte Carlo method, http://en.wikipedia.org/wiki/Monte_Carlo_method, February 20, **2013**.
- [99] N. Metropolis, A. W. Rosenbluth, M. N. Rosenbluth, A. H. Teller, E. Teller, Equation of state calculations by fast computing machines, *J. Chem. Phys.* **1953**, 21, 1087–1092.
- [100] S. Jakobtorweihen, N. Hansen, F. J. Keil, Combining reactive and configurational-bias Monte Carlo: confinement influence on the propene metathesis reaction system in various zeolites, *J. Chem. Phys.* **2006**, 125.
- [101] W. Greiner, *Theoretische Physik 1: Mechanik I*, Verlag Harri Deutsch, Thun **1981**.
- [102] D. Frenkel, Simulations: the dark side, *arXiv:1211.4440* **2012**, [cond-mat.stat-mech].
- [103] S. Nosé, A unified formulation of the constant temperature molecular dynamics methods, *J. Chem. Phys.* **1984**, 81, 511–519.
- [104] W. G. Hoover, Canonical dynamics: equilibrium phase-space distributions, *Phys. Rev. A* **1985**, 31, 1695–1697.
- [105] G. J. Martyna, M. E. Tuckerman, D. J. Tobias, M. L. Klein, Explicit reversible integrators for extended systems dynamics, *Mol. Phys.* **1996**, 87, 1117–1157.
- [106] S. Jakobtorweihen, M. G. Verbeek, C. P. Lowe, F. J. Keil, B. Smit, Understanding the loading dependence of self-diffusion in carbon nanotubes, *Phys. Rev. Lett.* **2005**, 95, 044501.
- [107] S. Jakobtorweihen, C. P. Lowe, F. J. Keil, B. Smit, A novel algorithm to model the influence of host lattice flexibility in molecular dynamics simulations: loading dependence of self-diffusion in carbon nanotubes, *J. Chem. Phys.* **2006**, 124, 154706.
- [108] H. Eyring, The activated complex in chemical reactions, *J. Chem. Phys.* **1935**, 3, 107–115.
- [109] R. L. June, A. T. Bell, D. N. Theodorou, Transition-state studies of xenon and SF₆ diffusion in silicalite, *J. Phys. Chem.* **1991**, 95, 8866–8878.
- [110] D. Dubbeldam, E. Beerdsen, T. J. H. Vlugt, B. Smit, Molecular simulation of loading-dependent diffusion in nanoporous materials using extended dynamically corrected transition state theory, *J. Chem. Phys.* **2005**, 122, 224712.
- [111] C. H. Bennett, Molecular-dynamics calculation of isotope-effect for vacancy diffusion, *Thin Solid Films* **1975**, 25, 65–70.

- [112] D. Chandler, Statistical mechanics of isomerization dynamics in liquids and transition state approximation, *J. Chem. Phys.* **1978**, 68, 2959–2970.
- [113] N. E. R. Zimmermann, B. Smit, F. J. Keil, On the effects of the external surface on the equilibrium transport in zeolite crystals, *J. Phys. Chem. C* **2010**, 114, 300–310.
- [114] N. E. R. Zimmermann, S. P. Balaji, F. J. Keil, Surface barriers of hydrocarbon transport triggered by ideal zeolite structures, *J. Phys. Chem. C* **2012**, 116, 3677–3683.
- [115] A. Schüring, S. M. Auerbach, S. Fritzsche, A simple method for sampling partition function ratios, *Chem. Phys. Lett.* **2007**, 450, 164–169.
- [116] E. Beerdsen, B. Smit, D. Dubbeldam, Molecular simulation of loading dependent slow diffusion in confined systems, *Phys. Rev. Lett.* **2004**, 93, 248301.
- [117] C. A. Krishna, S. Yashonath, A. Schüring, S. Fritzsche, J. Kärger, Influence of the methane-zeolite A interaction potential on the concentration dependence of self-diffusivity, *Adsorpt. Sci. Technol.* **2011**, 29, 553–567.
- [118] N. E. R. Zimmermann, S. Jakobtorweihen, E. Beerdsen, B. Smit, F. J. Keil, Additions and corrections: In-depth study of the influence of host-framework flexibility on the diffusion of small gas molecules in one-dimensional zeolitic pore systems (vol. 111, pp. 17370–17381, 2007), *J. Phys. Chem. C* **2010**, 114, 15546.
- [119] H. Jobic, H. Ramanan, S. M. Auerbach, M. Tsapatsis, P. Fouquet, Probing cooperative jump-diffusion in zeolites: Neutron spin-echo measurements and molecular dynamics simulations of benzene in NaX, *Microporous Mesoporous Mater.* **2006**, 90, 307–313.
- [120] S. K. Bhatia, D. Nicholson, Anomalous transport in molecularly confined spaces, *J. Chem. Phys.* **2007**, 127, 124701.
- [121] D. S. Sholl, K. A. Fichthorn, Concerted diffusion of molecular clusters in a molecular sieve, *Phys. Rev. Lett.* **1997**, 79, 3569–3572.
- [122] R. Radhakrishnan, T. Schlick, Biomolecular free energy profiles by a shooting/umbrella sampling protocol, “BOLAS”, *J. Chem. Phys.* **2004**, 121, 2436–2444.
- [123] B. Peters, N. E. R. Zimmermann, G. T. Beckham, J. W. Tester, B. L. Trout, Path sampling calculation of methane diffusivity in natural gas hydrates from a water-vacancy assisted mechanism, *J. Am. Chem. Soc.* **2008**, 130, 17342–17350.
- [124] S. Thompho, R. Chanajaree, T. Remsungnen, S. Hannongbua, P. A. Bopp, S. Fritzsche, The permeation of methane molecules through

- silicalite-1 surfaces, *J. Phys. Chem. A* **2009**, 113, 2004–2014.
- [125] N. E. R. Zimmermann, T. J. Zabel, F. J. Keil, Transport into nano-sheets: diffusion equations put to test, *J. Phys. Chem. C* **2013**, DOI: 10.1021/jp400152q.
- [126] D. Dubbeldam, S. Calero, T. J. H. Vlugt, R. Krishna, T. L. M. Maesen, E. Beerdsen, B. Smit, Force field parametrization through fitting on inflection points in isotherms, *Phys. Rev. Lett.* **2004**, 93, 088302.
- [127] D. Dubbeldam, S. Calero, T. J. H. Vlugt, R. Krishna, T. L. M. Maesen, B. Smit, United atom force field for alkanes in nanoporous materials, *J. Phys. Chem. B* **2004**, 108, 12301–12313.
- [128] S. Fritzsche, M. Wolfsberg, R. Haberlandt, The importance of various degrees of freedom in the theoretical study of the diffusion of methane in silicalite-1, *Chem. Phys.* **2003**, 289, 321–333.
- [129] B. Smit, T. L. M. Maesen, Molecular simulations of zeolites: adsorption, diffusion, and shape selectivity, *Chem. Rev.* **2008**, 108, 4125–4184.
- [130] M. G. Martin, J. I. Siepmann, Transferable potentials for phase equilibria. 1. United-atom description of *n*-alkanes, *J. Phys. Chem. B* **1998**, 102, 2569–2577.
- [131] B. Liu, B. Smit, F. Rey, S. Valencia, S. Calero, A new united atom force field for adsorption of alkenes in zeolites, *J. Phys. Chem. C* **2008**, 112, 2492–2498.
- [132] D. Dubbeldam, R. Q. Snurr, Recent developments in the molecular modeling of diffusion in nanoporous materials, *Mol. Simul.* **2007**, 33, 305–325.
- [133] M. Fischer, R. G. Bell, Influence of zeolite topology on CO₂/N₂ separation behavior: force-field simulations using a DFT-derived charge model, *J. Phys. Chem. C* **2012**, 116, 26449–26463.
- [134] L. A. Clark, R. Q. Snurr, Adsorption isotherm sensitivity to small changes in zeolite structure, *Chem. Phys. Lett.* **1999**, 308, 155–159.
- [135] D. M. Ruthven, A. Vidoni, ZLC diffusion measurements: combined effect of surface resistance and internal diffusion, *Chem. Eng. Sci.* **2012**, 71, 1–4.
- [136] S. Han, T. M. Hermans, P. E. Fuller, Y. Wei, B. A. Grzybowski, Transport into metal-organic frameworks from solution is not purely diffusive, *Angew. Chem., Int. Ed.* **2012**, 51, 2662–2666.
- [137] L. Gueudré, N. Bats, E. Jolimaître, Effect of surface resistance on cyclohexane uptake curves in silicalite-1 crystals, *Microporous Mesoporous Mater.* **2012**, 147, 310–317.
- [138] U. Schemmert, J. Kärger, C. Krause, R. A. Rákoczy, J. Weitkamp, Monitoring the evolution of intracrystalline concentration, *Europhys.*

- Lett.* **1999**, 46, 204–210.
- [139] F. Hibbe, J. Caro, C. Chmelik, A. Huang, T. Kirchner, D. Ruthven, R. Valiullin, J. Kärger, Monitoring molecular mass transfer in cation-free nanoporous host crystals of type AlPO-LTA, *J. Am. Chem. Soc.* **2012**, 134, 7725–7732.
- [140] N. Hedin, G. J. DeMartin, W. J. Roth, K. G. Strohmaier, S. C. Reyes, PFG NMR self-diffusion of small hydrocarbons in high silica DDR, CHA and LTA structures, *Microporous Mesoporous Mater.* **2008**, 109, 327–334.
- [141] T. Binder, Z. Adem, C. B. Krause, M. Krutyeva, A. Huang, J. Caro, J. Kärger, Surface permeability on zeolite NaCaA enhanced by layer deposition, *Microporous Mesoporous Mater.* **2011**, 146, 151–157.
- [142] U. Schemmert, J. Kärger, J. Weitkamp, Interference microscopy as a technique for directly measuring intracrystalline transport diffusion in zeolites, *Microporous Mesoporous Mater.* **1999**, 32, 101–110.
- [143] L. Heinke, J. Kärger, Assessing one-dimensional diffusion in nanoporous materials from transient concentration profiles, *New J. Phys.* **2008**, 10, 023035.
- [144] F. Hibbe, J. M. van Baten, R. Krishna, C. Chmelik, J. Weitkamp, J. Kärger, In-depth study of mass transfer in nanoporous materials by micro-imaging, *Chem. Ing. Tech.* **2011**, 83, 2211–2218.
- [145] N.-K. Bär, J. Kärger, C. Krause, W. Schmitz, G. Seiffert, Pitfalls in PFG NMR self-diffusion measurements with powder samples, *J. Magn. Reson. A* **1995**, 113, 278–280.
- [146] N. E. R. Zimmermann, S. Jakobtorweihen, E. Beerdsen, B. Smit, F. J. Keil, In-depth study of the influence of host-framework flexibility on the diffusion of small gas molecules in one-dimensional zeolitic pore systems, *J. Phys. Chem. C* **2007**, 111, 17370–17381.
- [147] S. Fritzsche, R. Haberlandt, J. Kärger, H. Pfeifer, K. Heinzinger, On the diffusion mechanism of methane in a cation-free zeolite of type ZK4, *Chem. Phys.* **1993**, 174, 229–236.
- [148] N. Hedin, G. J. DeMartin, K. G. Strohmaier, S. C. Reyes, PFG NMR self-diffusion of propylene in ITQ-29, CaA and NaCaA: window size and cation effects, *Microporous Mesoporous Mater.* **2007**, 98, 182–188.
- [149] T. F. Willems, C. H. Rycroft, M. Kazi, J. C. Meza, M. Haranczyk, Algorithms and tools for high-throughput geometry-based analysis of crystalline porous materials, *Microporous Mesoporous Mater.* **2012**, 149, 134–141.
- [150] J. M. Castillo, D. Dubbeldam, T. J. H. Vlught, B. Smit, S. Calero, Evaluation of various water models for simulation of adsorption in hydrophobic zeolites, *Mol. Simul.* **2009**, 35, 1067–1076.

- [151] T. J. H. Vlugt, M. Schenk, Influence of framework flexibility on the adsorption properties of hydrocarbons in the zeolite silicalite, *J. Phys. Chem. B* **2002**, 106, 12757–12763.
- [152] M. W. Deem, J. M. Newsam, J. A. Creighton, Fluctuations in zeolite aperture dimensions simulated by crystal dynamics, *J. Am. Chem. Soc.* **1992**, 114, 7198–7207.
- [153] K. S. Smirnov, D. Bougeard, A molecular dynamics computer study of window fluctuations in zeolite A, *Zeolites* **1994**, 14, 203–207.
- [154] A. García-Sánchez, D. Dubbeldam, S. Calero, Modeling adsorption and self-diffusion of methane in LTA zeolites: the influence of framework flexibility, *J. Phys. Chem. C* **2010**, 114, 15068–15074.
- [155] R. Krishna, J. M. van Baten, Comment on “Modeling adsorption and self-diffusion of methane in LTA zeolites: the influence of framework flexibility”, *J. Phys. Chem. C* **2010**, 114, 18017–18021.
- [156] R. Krishna, J. M. van Baten, A molecular dynamics investigation of the diffusion characteristics of cavity-type zeolites with 8-ring windows, *Microporous Mesoporous Mater.* **2011**, 137, 83–91.
- [157] S. Jakobtorweihen, F. J. Keil, B. Smit, Temperature and size effects on diffusion in carbon nanotubes, *J. Phys. Chem. B* **2006**, 110, 16332–16336.
- [158] M. Palomino, A. Corma, F. Rey, S. Valencia, New insights on CO₂-methane separation using LTA zeolites with different Si/Al ratios and a first comparison with MOFs, *Langmuir* **2010**, 26, 1910–1917.
- [159] N. E. R. Zimmermann, M. Haranczyk, M. Sharma, B. Liu, B. Smit, F. J. Keil, Adsorption and diffusion in zeolites: the pitfall of isotypic crystal structures, *Mol. Simul.* **2011**, 37, 986–989.
- [160] J. Kärger, Comment on “PFG NMR self-diffusion of small hydrocarbons in high silica DDR, CHA and LTA structures” [Micropor. Mesopor. Mater. 109 (2008) 327], *Microporous Mesoporous Mater.* **2008**, 116, 715–717.
- [161] R. Bialek, W. M. Meier, M. Davis, M. J. Annen, The synthesis and structure of SSZ-24, the silica analog of AlPO₄-5, *Zeolites* **1991**, 11, 438–442.
- [162] F. Eder, J. A. Lercher, Alkane sorption on siliceous and aluminophosphate molecular sieves. A comparative study, *J. Phys. Chem.* **1996**, 100, 16460–16462.
- [163] C. Martin, J. P. Coulomb, Y. Grillet, R. Kahn, Measure of the translational mobility D_t of methane molecules sorbed in the one-dimensional micropore network of the AlPO₄-5 zeolite, in *Fundamentals of Adsorption*, Kluwer Academic Publishers, Boston, pp. 587–594.
- [164] C. Martin, N. Tosi-Pellenq, J. Patarin, J. P. Coulomb, Sorption prop-

- erties of $\text{AlPO}_4\text{-5}$ and SAPO-5 zeolite-like materials, *Langmuir* **1998**, 14, 1774–1778.
- [165] L. Song, Z. Sun, S. Duan, L. Jiang, L. V. C. Rees, Investigation of adsorption hysteresis in microporous materials, in *Recent Advances in the Science and Technology of Zeolites and Related Materials*, Elsevier, Amsterdam, pp. 1797–1803.
- [166] S. S. Nivarthi, A. V. McCormick, H. T. Davis, Diffusion anisotropy in molecular sieves. A Fourier transform PFG NMR study of methane in $\text{AlPO}_4\text{-5}$, *Chem. Phys. Lett.* **1994**, 229, 297–301.
- [167] H. Jobic, K. Hahn, J. Kärger, M. Bée, A. Tuel, M. Noack, I. Girnus, G. J. Kearley, Unidirectional and single-file diffusion of molecules in one-dimensional channel systems. A quasi-elastic neutron scattering study, *J. Phys. Chem. B* **1997**, 101, 5834–5841.
- [168] D. Tzoulaki, L. Heinke, M. Castro, P. Cubillas, M. W. Anderson, W. Zhou, P. A. Wright, J. Kärger, Assessing molecular transport properties of nanoporous materials by interference microscopy: remarkable effects of composition and microstructure on diffusion in the silicoaluminophosphate zeotype STA-7, *J. Am. Chem. Soc.* **2010**, 132, 11665–11670.
- [169] B. Hampson, H. F. Leach, B. M. Lowe, C. D. Williams, Degradation of $\text{AlPO}_4\text{-5}$ by aqueous salt solutions, *Zeolites* **1989**, 9, 521–525.
- [170] E. García-Pérez, D. Dubbeldam, B. Liu, B. Smit, S. Calero, A computational method to characterize framework aluminum in aluminosilicates, *Angew. Chem., Int. Ed.* **2007**, 46, 276–278.
- [171] L. Heinke, P. Kortunov, D. Tzoulaki, J. Kärger, Exchange dynamics at the interface of nanoporous materials with their surroundings, *Phys. Rev. Lett.* **2007**, 99, 228301.
- [172] G. Arya, E. J. Maginn, H.-C. Chang, Effect of the surface energy barrier on sorbate diffusion in $\text{AlPO}_4\text{-5}$, *J. Phys. Chem. B* **2001**, 105, 2725–2735.
- [173] M. G. Ahunbay, J. R. Elliott, Jr., O. Talu, The diffusion process of methane through a silicalite single crystal membrane, *J. Phys. Chem. B* **2002**, 106, 5163–5168.
- [174] E. B. Webb III, G. S. Grest, Interfaces between silicalite surfaces and liquid hexadecane: a molecular dynamics simulation, *J. Chem. Phys.* **2002**, 116, 6311–6321.
- [175] A. Schüring, S. Vasenkov, S. Fritzsche, Influence of boundaries of nanoporous crystals on molecular exchange under the conditions of single-file diffusion, *J. Phys. Chem. B* **2005**, 109, 16711–16717.
- [176] D. A. Newsome, D. S. Sholl, Atomically detailed simulations of surface resistances to transport of CH_4 , CF_4 , and C_2H_6 through silicalite

- membranes, *Microporous Mesoporous Mater.* **2008**, 107, 286–295.
- [177] G. Arya, H.-C. Chang, E. J. Maginn, A critical comparison of equilibrium, non-equilibrium and boundary-driven molecular dynamics techniques for studying transport in microporous materials, *J. Chem. Phys.* **2001**, 115, 8112–8124.
- [178] Y. S. Lin, I. Kumakiri, B. N. Nair, H. Alsyouri, Microporous inorganic membranes, *Sep. Purif. Methods* **2002**, 31, 229–379.
- [179] M. Kanezashi, Y. S. Lin, Gas permeation and diffusion characteristics of MFI-type zeolite membranes at high temperatures, *J. Phys. Chem. C* **2009**, 113, 3767–3774.
- [180] O. Terasaki, Fine structures of zeolites, *J. Electron Microsc.* **1994**, 43, 337–346.
- [181] E. Beerdsen, B. Smit, Diffusion in confinement: agreement between experiments better than expected, *J. Phys. Chem. B* **2006**, 110, 14529–14530.
- [182] A. Schüring, Analytical estimate of the entering probability of molecules into crystalline nanoporous materials, *J. Phys. Chem. C* **2007**, 111, 11285–11290.
- [183] T. Maris, T. J. H. Vlugt, B. Smit, Simulation of alkane adsorption in the aluminophosphate molecular sieve $\text{AlPO}_4\text{-5}$, *J. Phys. Chem. B* **1998**, 102, 7183–7189.
- [184] R. A. Kuharski, D. Chandler, J. A. Montgomery, F. Rabii, S. J. Singer, Stochastic molecular dynamics study of cyclohexane isomerization, *J. Phys. Chem.* **1988**, 92, 3261–3267.
- [185] E. Helfand, Brownian dynamics study of transitions in a polymer chain of bistable oscillators, *J. Chem. Phys.* **1978**, 69, 1010–1018.
- [186] D. Dubbeldam, E. Beerdsen, S. Calero, B. Smit, Molecular path control in zeolite membranes, *Proc. Natl. Acad. Sci. U. S. A.* **2005**, 102, 12317–12320.
- [187] R. Du, V. S. Pande, A. Y. Grosberg, T. Tanaka, E. S. Shakhnovich, On the transition coordinate for protein folding, *J. Chem. Phys.* **1998**, 108, 334–350.
- [188] P. G. Bolhuis, D. Chandler, C. Dellago, P. L. Geissler, Transition path sampling: throwing ropes over rough mountain passes, in the dark, *Annu. Rev. Phys. Chem.* **2002**, 53, 291–318.
- [189] D. A. Newsome, D. S. Sholl, Influences of interfacial resistances on gas transport through carbon nanotube membranes, *Nano Lett.* **2006**, 6, 2150–2153.
- [190] C. Chmelik, L. Heinke, R. Valiullin, J. Kärger, A new view of diffusion in nanoporous materials, *Chem. Ing. Tech.* **2010**, 82, 779–804.
- [191] A. F. Combariza, G. Sastre, Influence of zeolite surface in the sorption

- of methane from molecular dynamics, *J. Phys. Chem. C* **2011**, 115, 13751–13758.
- [192] B. E. Poling, J. M. Prausnitz, J. P. O’Connell, *The Properties of Gases and Liquids*, McGraw-Hill, New York, 5th ed. **2001**.
- [193] E. García-Pérez, S. K. Schnell, J. M. Castillo, S. Calero, S. Kjelstrup, D. Dubbeldam, T. J. H. Vlugt, External surface adsorption on silicalite-1 zeolite studied by molecular simulation, *J. Phys. Chem. C* **2011**, 115, 15355–15360.
- [194] S. Jakobtorweihen, N. Hansen, F. J. Keil, Molecular simulation of alkene adsorption in zeolites, *Mol. Phys.* **2005**, 103, 471–489.
- [195] O. K. Farha, I. Eryazici, N. C. Jeong, B. G. Hauser, C. E. Wilmer, A. A. Sarjeant, R. Q. Snurr, S. T. Nguyen, A. O. Yazaydin, J. T. Hupp, Metal–organic framework materials with ultrahigh surface areas: is the sky the limit?, *J. Am. Chem. Soc.* **2012**, 134, 15016–15021.
- [196] J. Kärger, P. Kortunov, S. Vasenkov, L. Heinke, D. R. Shah, R. A. Rakoczy, Y. Traa, J. Weitkamp, Unprecedented insight into diffusion by monitoring the concentration of guest molecules in nanoporous host materials, *Angew. Chem., Int. Ed.* **2006**, 45, 7846–7849.
- [197] J. Hafner, G. Kresse, D. Vogtenhuber, and M. Marsman, Vienna ab initio simulation package, <http://www.vasp.at/>, March 27 **2013**.
- [198] J. Hafner, *Ab-initio* simulations of materials using VASP: density-functional theory and beyond, *J. Comput. Chem.* **2008**, 29, 2044–2078.
- [199] M. Dion, H. Rydberg, E. Schröder, D. C. Langreth, B. I. Lundqvist, Van der Waals density functional for general geometries, *Phys. Rev. Lett.* **2004**, 92, 246401.
- [200] R. Krishna, Describing the diffusion of guest molecules inside porous structures, *J. Phys. Chem. C* **2009**, 113, 19756–19781.
- [201] D. S. Sholl, Understanding macroscopic diffusion of adsorbed molecules in crystalline nanoporous materials via atomistic simulations, *Acc. Chem. Res.* **2006**, 39, 403–411.
- [202] H. Jobic, D. N. Theodorou, Diffusion of long n-alkanes in silicalite. A comparison between neutron scattering experiments and hierarchical simulation results, *J. Phys. Chem. B* **2006**, 110, 1964–1967.
- [203] L. Gueudré, E. Jolimaîte, N. Bats, W. Dong, Diffusion in zeolites: is surface resistance a critical parameter?, *Adsorption* **2010**, 16, 17–27.
- [204] L. Whitmore, B. Slater, C. R. A. Catlow, Adsorption of benzene at the hydroxylated (111) external surface of faujasite, *Phys. Chem. Chem. Phys.* **2000**, 2, 5354–5356.
- [205] O. C. Gobin, S. J. Reitmeier, A. Jentys, J. A. Lercher, Role of the surface modification on the transport of hexane isomers in ZSM-5, *J. Phys. Chem. C* **2011**, 115, 1171–1179.

- [206] C. Chmelik, A. Varmla, L. Heinke, D. B. Shah, J. Kärger, F. Kremer, U. Wilczok, W. Schmidt, Effect of surface modification on uptake rates of isobutane in MFI crystals: an infrared microscopy study, *Chem. Mater.* **2007**, 19, 6012–6019.
- [207] A. Schüring, J. Gulín-González, S. Vasenkov, S. Fritzsche, Quantification of the mass-transfer coefficient of the external surface of zeolite crystals by molecular dynamics simulations and analytical treatment, *Microporous Mesoporous Mater.* **2009**, 125, 107–111.
- [208] F. Hibbe, V. R. R. Marthala, C. Chmelik, J. Weitkamp, J. Kärger, Micro-imaging of transient guest profiles in nanochannels, *J. Chem. Phys.* **2011**, 135, 184201.
- [209] J. Caro, M. Noack, P. Kölsch, R. Schäfer, Zeolite membranes—state of their development and perspective, *Microporous Mesoporous Mater.* **2000**, 38, 3–24.
- [210] N. E. R. Zimmermann, F. J. Keil, Transport barriers as triggered by the idealized microscopic crystal surface and the role of the evaluation protocol of diffusion experiments, *Diffus. Fundam.* **2011**, 16, 1–2.
- [211] J. S. Chen, Y. L. Tan, C. M. Li, Y. L. Cheah, D. Luan, S. Madhavi, F. Y. C. Boey, L. A. Archer, X. W. Lou, Constructing hierarchical spheres from large ultrathin anatase TiO₂ nanosheets with nearly 100% exposed (001) facets for fast reversible lithium storage, *J. Am. Chem. Soc.* **2010**, 132, 6124–6130.
- [212] L. Ren, Y. Liu, X. Qi, K. S. Hui, K. N. Hui, Z. Huang, J. Li, K. Huang, J. Zhong, An architected TiO₂ nanosheet with discrete integrated nanocrystalline subunits and its application in lithium batteries, *J. Mater. Chem.* **2012**, 22, 21513–21518.
- [213] J. N. Coleman, M. Lotya, A. O’Neill, S. D. Bergin, P. J. King, U. Khan, K. Young, A. Gaucher, S. De, R. J. Smith, I. V. Shvets, S. K. Arora, G. Stanton, H.-Y. Kim, K. Lee, G. T. Kim, G. S. Duesberg, T. Hallam, J. J. Boland, J. J. Wang, J. F. Donegan, J. C. Grunlan, G. Moriarty, A. Shmeliov, R. J. Nicholls, J. M. Perkins, E. M. Grieveson, K. Theuwissen, D. W. McComb, P. D. Nellist, V. Nicolosi, Two-dimensional nanosheets produced by liquid exfoliation of layered materials, *Science* **2011**, 331, 568–571.
- [214] N. E. R. Zimmermann, B. Smit, F. J. Keil, Predicting local transport coefficients at solid-gas interfaces, *J. Phys. Chem. C* **2012**, 116, 18878–18883.
- [215] B. J. Alder, T. E. Wainwright, Studies in molecular dynamics. 1. General method, *J. Chem. Phys.* **1959**, 31, 459–466.
- [216] J. Kärger, P. Demontis, G. B. Suffritti, A. Tilocca, “Two-step” model of molecular diffusion in silicalite, *J. Chem. Phys.* **1999**, 110, 1163–

- 1172.
- [217] M. Haranczyk, J. A. Sethian, Automatic structure analysis in high-throughput characterization of porous materials, *J. Chem. Theory Comput.* **2010**, 6, 3472–3480.
- [218] R. F. Cracknell, D. Nicholson, N. Quirke, Direct molecular-dynamics simulation of flow down a chemical-potential gradient in a slit-shaped micropore, *Phys. Rev. Lett.* **1995**, 74, 2463–2466.
- [219] R. Krishna, J. M. van Baten, Insights into diffusion of gases in zeolites gained from molecular dynamics simulations, *Microporous Mesoporous Mater.* **2008**, 109, 91–108.
- [220] H. Yucel, D. M. Ruthven, Diffusion in 4A zeolite. Study of the effect of crystal size, *J. Chem. Soc., Faraday Trans. I* **1980**, 76, 60–70.
- [221] S. Brandani, M. A. Jama, D. M. Ruthven, ZLC measurements under non-linear conditions, *Chem. Eng. Sci.* **2000**, 55, 1205–1212.
- [222] J. Kärger, The random walk of understanding diffusion, *Ind. Eng. Chem. Res.* **2002**, 41, 3335–3340.
- [223] M. K. F. Abouelnasr, B. Smit, Diffusion in confinement: kinetic simulations of self- and collective diffusion behavior of adsorbed gases, *Phys. Chem. Chem. Phys.* **2012**, 14, 11600–11609.
- [224] N. Hansen, T. Kerber, J. Sauer, A. T. Bell, F. J. Keil, Quantum chemical modeling of benzene ethylation over H-ZSM-5 approaching chemical accuracy: a hybrid MP2:DFT study, *J. Am. Chem. Soc.* **2010**, 132, 11525–11538.
- [225] P. M. Zimmerman, D. C. Tranca, J. Gomes, D. S. Lambrecht, M. Head-Gordon, A. T. Bell, Ab initio simulations reveal that reaction dynamics strongly affect product selectivity for the cracking of alkanes over H-MFI, *J. Am. Chem. Soc.* **2012**, 134, 19468–19476.

Publications

- **Nils E. R. Zimmermann**, Timm J. Zabel, and Frerich J. Keil, Transport into nanosheets: diffusion equations put to test, *J. Phys. Chem. C* **2013**, DOI: 10.1021/jp400152q.
- **Nils E. R. Zimmermann**, Berend Smit, and Frerich J. Keil, Predicting local transport coefficients at solid–gas interfaces, *J. Phys. Chem. C* **2012**, 116, 18878–18883.
- **Nils E. R. Zimmermann**, Sayee P. Balaji, and Frerich J. Keil, Surface barriers of hydrocarbon transport triggered by ideal zeolite structures, *J. Phys. Chem. C* **2012**, 116, 3677–3683.
- **Nils E. R. Zimmermann**, Maciej Haranczyk, Manju Sharma, Bei Liu, Berend Smit, and Frerich J. Keil, Adsorption and diffusion in zeolites: the pitfall of isotypic crystal structures, *Mol. Simul.* **2011**, 37, 986–989.
- **Nils E. R. Zimmermann**, Berend Smit, and Frerich J. Keil, On the effects of the external surface on the equilibrium transport in zeolite crystals, *J. Phys. Chem. C* **2010**, 114, 300–310.
- Baron Peters, **Nils E. R. Zimmermann**, Gregg T. Beckham, Jefferson W. Tester, and Bernhardt L. Trout, Path sampling calculation of methane diffusivity in natural gas hydrates from a water-vacancy assisted mechanism, *J. Am. Chem. Soc.* **2008**, 130, 17342–17350.

- **Nils E. R. Zimmermann**, Sven Jakobtorweihen, Edith Beerdsen, Berend Smit, and Frerich J. Keil,
In-depth study of the influence of host-framework flexibility on the diffusion of small gas molecules in one-dimensional zeolitic pore systems,
J. Phys. Chem. C **2007**, 111, 17370–17381.

Conferences

- **N. E. R. Zimmermann**, B. Smit, and F. J. Keil, “Predicting surface permeabilities via molecular simulations”, talk at *The 35th Annual British Zeolite Association Meeting*, Chester, U. K., July 15–20, 2012.
- **N. E. R. Zimmermann**, M. Haranczyk, M. Sharma, B. Liu, B. Smit, and F. J. Keil, “How sensitive are adsorption and diffusion of guest molecules in zeolites towards small changes in the crystal structure?”, poster at *24th German Zeolite Meeting*, Magdeburg, Germany, March 7–9, 2012.
- **N. E. R. Zimmermann** and F. J. Keil, “Transport barriers as triggered by the idealized microscopic crystal surface and the role of the evaluation protocol of diffusion experiments”, poster at *Diffusion Fundamentals IV*, Troy, New York, U. S. A., August 21–24, 2011, and at *Molecular Modeling of Thermophysical Properties—Science Meets Engineering*, Dortmund, Germany, September 15–16, 2011.
- **N. E. R. Zimmermann**, S. P. Balaji, and F. J. Keil, “How do chain length and pore type influence tracer transport of hydrocarbons at zeolite surfaces?”, talk at *23rd German Zeolite Meeting*, Erlangen-Nuremberg, Germany, March 2–4, 2011.
- **N. E. R. Zimmermann**, B. Smit, and F. J. Keil, “Crystal surface influence on equilibrium transport of guest molecules in zeolites”, poster at *Mini Statistical Mechanics Meeting*, Berkeley, California, U. S. A., January 8–10, 2010.
- **B. Peters**, **N. E. R. Zimmermann**, G. T. Beckham, J. W. Tester, and B. L. Trout, “Path sampling calculation of methane diffusivity in natural gas hydrates”, poster at *Foundations of Molecular Modeling and Simulation*, Blaine, Washington, U. S. A., July 9–14, 2009, and talk at *2008 AIChE Annual Meeting*, Philadelphia, Pennsylvania, U. S. A., November 16–21, 2008.

-
- **N. E. R. Zimmermann**, B. Smit, and F. J. Keil, “The influence of surface barriers on diffusion of alkane-zeolite systems—a molecular dynamics study”, talk at *2008 AIChE Annual Meeting*, Philadelphia, Pennsylvania, U. S. A., November 16–21, 2008.
 - **N. E. R. Zimmermann**, S. Jakobtorweihen, B. Smit, and **F. J. Keil**, “In-depth study of the influence of host-framework flexibility on the diffusion of small gas molecules in one-dimensional zeolitic pore systems”, talk at *DECHEMA Meeting: Molecular Modeling*, Frankfurt on Main, Germany, March 10–11, 2008.

Lebenslauf

Persönliche Daten

Name	Nils Edvin Richard Zimmermann
Geburtsdatum	24.05.1979
Geburtsort	Buchholz in der Nordheide

Schulbildung

1985 – 1989	Grundschule Elstorf
1989 – 1991	Orientierungsstufe Neu Wulmstorf
1991 – 1998	Gymnasium Neu Wulmstorf
06/1998	Abitur

Studium

10/1999 – 07/2003	Allgemeine Ingenieurwissenschaften an der TU Hamburg-Harburg
08/2003 – 06/2006	Process Engineering an der TU Hamburg-Harburg
08/2004 – 12/2004	Chemical Engineering am Royal Institute of Technology, Stockholm, Schweden
06/2006	Abschluss: Master of Science

Wissenschaftliche Tätigkeit

09/2006 – 09/2007	Wissenschaftlicher Mitarbeiter an der Ecole Normale Supérieure, Lyon, Frankreich, Centre Européen de Calcul Atomique et Moléculaire
-------------------	--

Fortsetzung auf der nächsten Seite.

11/2007 – 03/2013 Wissenschaftlicher Mitarbeiter an der
TU Hamburg-Harburg,
Institut für Chemische Reaktionstechnik

09/2008 – 11/2008, Forschungsaufenthalte an der University of
10/2009 – 02/2010 California, Berkeley, U. S. A.

